



UNIVERSIDAD  
**NACIONAL**  
DE COLOMBIA

**DIAGNOSIS OF INCIPIENT  
FAILURES IN ROLLING ELEMENT  
BEARINGS UNDER NON-  
STATIONARY OPERATION  
CONDITIONS BY VIBRATION  
ANALYSIS.**

**Juan David Arango Castrillón**

Universidad Nacional de Colombia  
Facultad de Minas  
Departamento de Ingeniería Mecánica  
Medellín, Colombia

2023



# **DIAGNOSIS OF INCIPIENT FAILURES IN ROLLING ELEMENT BEARINGS UNDER NON- STATIONARY OPERATION CONDITIONS BY VIBRATION ANALYSIS.**

**Juan David Arango Castrillón**

Tesis o trabajo de investigación presentada(o) como requisito parcial para optar al título de:

**Magister en Ingeniería Mecánica**

Director (a):

Ph.D. Alejandro Restrepo Martínez

Codirector (a):

Ph.D. Fernando Jesús Guevara Carazas

Universidad Nacional de Colombia

Facultad de Minas

Departamento de Ingeniería Mecánica

Medellín, Colombia

2023





*(Dedicatoria o lema)*

*A mis padres. En especial a mi madre, quien durante el desarrollo de esta tesis falleció vibrando en la frecuencia más alta, la frecuencia del amor.*



## **Declaración de obra original**

Yo declaro lo siguiente:

He leído el Acuerdo 035 de 2003 del Consejo Académico de la Universidad Nacional. «Reglamento sobre propiedad intelectual» y la Normatividad Nacional relacionada al respeto de los derechos de autor. Esta disertación representa mi trabajo original, excepto donde he reconocido las ideas, las palabras, o materiales de otros autores.

Cuando se han presentado ideas o palabras de otros autores en esta disertación, he realizado su respectivo reconocimiento aplicando correctamente los esquemas de citas y referencias bibliográficas en el estilo requerido.

He obtenido el permiso del autor o editor para incluir cualquier material con derechos de autor (por ejemplo, tablas, figuras, instrumentos de encuesta o grandes porciones de texto).

Por último, he sometido esta disertación a la herramienta de integridad académica, definida por la universidad.



Juan David Arango Castrillón.

Fecha 31/01/2023

## **Agradecimientos**

Quisiera agradecer en primera instancia a mi núcleo familiar, a mi madre y a mi padre por haberme brindado tal acompañamiento en este proceso. En especial, rescatar la paciencia de mi madre, quien durante el desarrollo de este trabajo falleció debido a una serie de complicaciones asociadas a un tumor cancerígeno. Agradecer al grupo GOMAC por su apoyo, en cabeza del profesor Fernando Guevara y su familia, a quien quisiera extender mi más sentido mensaje de gratitud. Adicionalmente, agradecer al profesor Alejandro Restrepo por la paciencia y la dedicación que tuvo durante el desarrollo de este trabajo.

## Resumen (Abstract)

### DIAGNÓSTICO DE FALLAS INCIPIENTES EN RODAMIENTOS BAJO CONDICIONES DE OPERACIÓN NO ESTACIONARIAS MEDIANTE ANÁLISIS DE VIBRACIONES.

Los rodamientos, son una parte fundamental de la mayoría de máquinas rotativas, consecuentemente, la detección de fallas y el diagnóstico temprano de estos elementos son de gran interés para incrementar los niveles de confiabilidad y mantenibilidad de los equipos rotativos. El análisis de vibraciones es la herramienta más utilizada para el diagnóstico de rodamientos. Pese a los avances en los algoritmos y procesamiento digital de señales para el diagnóstico, es común encontrar grandes avances para casos en los cuales las condiciones operativas se mantienen estacionarias. Este no es el caso de muchos equipos rotativos, donde la velocidad angular puede resultar variable en el tiempo. En general, la operación bajo condiciones de velocidad variable genera respuestas vibratorias en las cuales se combinan fenómenos ángulo-periódicos con fenómenos tiempo-periódicos.

Este trabajo presenta un método para el diagnóstico de fallas en rodamientos, utilizando algoritmos de “*Computer Order Tracking*”, análisis de Ciclo-No-Estacionareidad y análisis de Kurtosis Espectral. El método fue evaluado utilizando una serie de señales capturadas bajo condiciones de velocidad variable y una serie de señales simuladas, bajo diferentes condiciones de carga y velocidad. Adicionalmente se propone una estrategia para la demodulación de señales, y se presenta un clasificador, entrenado con una combinación entre señales simuladas y señales capturadas para el diagnóstico de tipos de fallas.

**Palabras clave:** Rodamiento, Análisis de Vibraciones, Velocidad variable, Cyclo-No Estacionareidad, Order Tracking Computarizado, Kurtosis Espectral.

## Abstract

### **DIAGNOSIS OF INCIPIENT FAILURES IN ROLLING ELEMENT BEARINGS UNDER NON-STATIONARY OPERATION CONDITIONS BY VIBRATION ANALYSIS.**

Rolling Element Bearings –REB are a fundamental part of most of rotating machines. Consequently, their fault detection and timely diagnosis are of great interest to improve the reliability and maintainability of rotational equipment. Vibration analysis is the most widely used tool for bearing diagnostics. Despite advances in algorithms and digital signal processing for diagnosis, it is common to find great advances for cases in which operating conditions remain stationary. This is not the case with many rotating equipment, where the angular velocity can be variable over time. In general, operation under variable speed conditions generates vibratory responses at which angle-periodic phenomena are combined with time-periodic phenomena.

This work presents a method for the diagnosis of bearing failures, using "Computer Order Tracking" algorithms, Cycle-Non-Stationarity analysis and Spectral Kurtosis analysis. The method was evaluated using a series of signals captured under variable speed conditions and a series of simulated signals, under different load and speed conditions. Additionally, a signal demodulation strategy is proposed, and a classifier is presented, trained with a combination between simulated signals and captured signals for the diagnosis of types of failures.

**Keywords:** Rolling Element Bearing, Vibration Analysis, non-stationary Speed, Cyclo-non-stationary analysis, Computer order tracking, Spectral Kurtosis.

# Content

	<b>Pág.</b>
<b>Resumen (Abstract) .....</b>	<b>IX</b>
<b>Figures list.....</b>	<b>XIII</b>
<b>Symbols and Abbreviations List .....</b>	<b>XVI</b>
<b>1. Introduction.....</b>	<b>19</b>
1.1 Background and Context.....	19
1.2 Justification .....	24
1.3 Research Aim.....	25
<b>2. Theoretical Framework.....</b>	<b>27</b>
2.1 Rolling Element Bearing Diagnosis – Benchmark method.....	27
2.2 Kurtosis, Spectral Kurtosis and Fast Kurtogram.....	30
2.3 Second-Order Cyclostationary Analysis for Rolling Element Bearing.....	36
2.4 Analysis of Square Envelope Spectrum.....	40
2.4.1. Demodulation Band .....	41
2.5 Variable Speed Order Tracking.....	45
2.5.1. Order Tracking Approaches .....	45
2.6 Variable Speed Bearing Diagnosis State of Art.....	52
<b>3. Experimental Setup.....</b>	<b>56</b>
3.1 Rolling Element Bearing Characterization .....	57
3.2 Test Rig Critical Speed .....	61
3.2.1. Critical Speed Model Estimation .....	61
3.3 Other notorious spectral components.....	62
<b>4. Model for Rolling Element Bearing Diagnosis under variable Speed.....</b>	<b>63</b>
4.1 NewIESfogram.....	71
<b>5. Simulated Experimental Results.....</b>	<b>74</b>
5.1 Simulation Model.....	74
5.1.1. Outer Race Amplitude Modulation Function.....	76
5.1.2. Inner Race Amplitude Modulation Function .....	77
5.1.3. Rolling Element Amplitude Modulation Function.....	78
5.1.4. Nominal Parameters for Simulated Signals.....	79
5.2 Simulated Faults Results .....	82
5.2.1. Outer Race Simulated Fault .....	83
5.2.2. Inner Race Simulated Fault.....	87
5.2.3. Ball Simulated Fault.....	91

---

5.2.4. Simulated Combination Fault .....	96
5.3 Other Effects Observables on Simulated Signals.....	101
5.3.1. Effect of Signal to noise ratio .....	101
5.3.2. Effect of Impulse distribution .....	102
5.3.3. Effect of Random Slippage .....	106
<b>6. Experimental Tests. ....</b>	<b>109</b>
6.1 Outer Race Fault. ....	110
6.2 Inner Race Fault. ....	116
6.3 Rolling Element Fault. ....	123
6.4 Combination Fault.....	127
6.5 Conclusions of chapter.....	132
6.6 Classification Algorithm. ....	132
<b>7. Conclusions and Recommendations .....</b>	<b>135</b>
<b>8. References.....</b>	<b>137</b>
<b>9. Annex .....</b>	<b>141</b>
9.1 Annex: Spectral Correlation Estimators.....	142
9.2 Annex: Spectral Correlation Statistical Threshold.....	143
9.3 Annex: Chapter 5 - Outer Race Simulated Signals Summary. ....	145
9.4 Annex: Chapter 5 - Inner Race Simulated Signals Summary. ....	147
9.5 Annex: Chapter 5 – Ball Fault Simulated Signals Summary. ....	149
9.6 Annex: Chapter 6 - Outer Race Faults Summary.....	151
9.7 Annex: Chapter 6 - Inner Race Faults Summary. ....	154
9.8 Annex: Chapter 6 – Rolling Element Faults Summary. ....	157
9.9 Annex: Chapter 6 – Combination Faults Summary. ....	160



## Figures list

Figure 1-1. Vibration response in a faulty Rolling Element Bearing - Illustration.....	20
Figure 1-2. Illustration for vibrational response in time domain and angular domain.....	22
Figure 1-3. Vibrational response in REB under variable speed [10]. .....	23
Figure 2-1. Typical REB fault waveform and Envelope. Vibrational response against angular position.....	28
Figure 2-2. Rolling Element Bearing Diagnosis by Squared Envelope Spectral Analysis – Two methods [25]. .....	29
Figure 2-3. Sample kurtosis illustration.....	31
Figure 2-4 Illustration of Spectral Kurtosis Estimator.....	32
Figure 2-5. Window length dependence of spectral kurtosis. ....	33
Figure 2-6. Kurtogram .....	34
Figure 2-7. Kurtogram Binary Tree. ....	35
Figure 2-8. Fast Kurtogram.....	35
Figure 2-9. Illustration of Spectral Correlation for strictly Second-Order Cyclostationary.....	37
Figure 2-10. 'Signal 1' Power Spectral Density.....	37
Figure 2-11. Power Spectral Density vs. $\alpha$ -shifted Power Spectral Density.....	38
Figure 2-12. 'Signal 1' Simulated Outer Race Fault Spectral Correlation .....	39
Figure 2-13 'Signal 1' Simulated Outer Race Fault Spectral Correlation Color-map .....	39
Figure 2-14. simulated Outer Race Fault 'signal 1' Waveform .....	40
Figure 2-15. 'Signal 1' Squared Envelope Spectrum.....	41
Figure 2-16. 'Signal 1' Spectral Correlation averaging over spectral frequency axis. ....	41
Figure 2-17. Simulated Outer Race Fault 'Signal 2' Kurtogram demodulation. ....	43
Figure 2-18. Simulated Outer Race Fault 'Signal 2' Spectral Correlation.....	44
Figure 2-19. Simulated Outer Race Fault 'Signal 2' Spectral Correlation Demodulation.....	44
Figure 2-20 Variable Speed Conceptualization. ....	45
Figure 2-21 Illustration for Order Tracking Approaches .....	46
Figure 2-22 Theoretical Tacho Encoder Signal for Increasing Rotational Speed.....	47
Figure 2-23 Phase demodulation illustration .....	48
Figure 2-24. Simulated Spectrogram for illustration of MOPA.....	50
Figure 2-25 Instantaneous Spectrum at time step $t_i$ .....	50
Figure 2-26 Shrunked Instantaneous Spectrum under the harmonics set H. ....	51
Figure 2-27. Probability distribution map for instantaneous angular speed.....	52
Figure 3-1. Test Rig .....	56
Figure 3-2. Magnitude Spectrum Raw Vibration Response. ....	57
Figure 3-3 Modulations in resonance regions for Outer Race Fault REB 1450-1850 Hz. ....	58
Figure 3-4.Outer-Race Fault waveform. ....	59

Figure 3-5. Outer Race Faulty Bearing – Kurtogram. ....	59
Figure 3-6. Raw signal vs Kurtogram filtered signal waveforms. ....	60
Figure 3-7. Spectral Correlation for Outer Race Fault Bearing .....	60
Figure 3-8. Discrete Random Separation filter magnitude spectrum.....	62
Figure 4-1. Procedure for REB Diagnosis under variable speed. ....	63
Figure 4-2. Procedure for REB Diagnosis illustration. ....	64
Figure 4-3 Waveform of variable speed vibration response. A) Time domain signal. B) Short Time Fourier Representation.....	66
Figure 4-4. Instantaneous Rotational Speed from MOPA approach.....	67
Figure 4-5. Phase demodulation order tracking. ....	68
Figure 4-6. Angle domain waveform. ....	68
Figure 4-7. GSA illustration .....	69
Figure 4-8. Order-Frequency Spectral Coherence - OFSCoh.....	69
Figure 4-9. Enhanced Envelope Order Spectrum .....	70
Figure 4-10. Illustration of IES and Ind-metric computation. A) Spectral Coherence Representation. B) IES representation. ....	72
Figure 4-11. Ind-metric computation comparison. A) <i>ind</i> illustration for low SNR Improved Envelope Spectrum. B) <i>ind</i> illustration for high SNR Improved Envelope Spectrum .....	73
Figure 4-12 Sample correlation computation comparison. A) Low sample correlation case. B) High sample correlation case. ....	73
Figure 5-1. Amplitude Modulation Function.....	75
Figure 5-2. Loads for the case of localized faulty on outer race.....	76
Figure 5-3. Loads for the case of localized faulty on inner race.....	77
Figure 5-4 Loads for the case of localized faulty on rolling element .....	78
Figure 5-5 Illustration of slippage.....	80
Figure 5-6. Components of simulated signals and rotation speed. ....	81
Figure 5-7. Simulated Signals for OR fault. ....	84
Figure 5-8. 'S-OR7' signal OFSC and IES .....	85
Figure 5-9. 'S-OR2' signal OFSC and IES.....	86
Figure 5-10. IES comparison for Inner Race Simulations Signals. ....	88
Figure 5-11. 'S-IR-1' signal OFSC and IES. ....	89
Figure 5-12. 'S-IR-1' signal OFSC and IES. ....	90
Figure 5-13. IES comparison for Rolling Element Faults Simulations Signals.....	92
Figure 5-14. IES for Rolling Element Faults Simulations Signals – Horizontal Comparison.....	93
Figure 5-15. 'S-BF-4' signal OFSC and IES. ....	94
Figure 5-16. 'S-BF-6' signal OFSC and IES. ....	94
Figure 5-17. IES comparison for Combination Fault Simulations Signals.....	96
Figure 5-18. 'S-CF-6' signal OFSC and IES. ....	97
Figure 5-19. 'S-CF-8' signal OFSC and IES. ....	98
Figure 5-20. Order Frequency Spectral Coherence Map for Combination Fault S-CF-9.....	99
Figure 5-21. IES at different spectral frequency bands for S-CF-9. A) Demodulation for Ball Fault. B) Demodulation for Outer Race Fault. C) Demodulation for Inner Race Fault. D) EES.....	100
Figure 5-22. Effect on Signal to Noise Ratio.....	101
Figure 5-23. Effect of spall size on vibration generated .....	102

Figure 5-24. IES for different spall extension..... 103

Figure 5-25. Effect on Spall Percentage – Loads similar to S-BF-2..... 104

Figure 5-26. Effect on Spall Percentage – Loads similar to S-BF-7..... 105

Figure 5-27. Effect of random slippage. .... 107

Figure 6-1 Run OR-3 B1 signal. A. OFSCoh Map B. Enhanced Envelope Order Spectrum. .... 111

Figure 6-2. Run OR-3 B1 A. IESFOgram B. IESFO..... 112

Figure 6-3. Run OR-3 B1. A. newIESFOgram, B. newIESFO..... 112

Figure 6-4. Run OR-5 B1 signal. A. OFSCoh Map B. Enhanced Envelope Order Spectrum. .... 113

Figure 6-5. Run OR-5 B1 signal. A. IESFOgram B. newIESFOgram. C. Improved Envelope Order Spectrum. .... 114

Figure 6-6. Run OR-6 B1 signal. A. OFSCoh Map B. Enhanced Envelope Order Spectrum ..... 115

Figure 6-7. Run OR-6 B1 signal. A. IESFOgram B. newIESFOgram C. IESFO D. newIESFO .. 116

Figure 6-8. Run IR-1 B1 signal. A. OFSCoh Map B. Enhanced Envelope Order Spectrum..... 117

Figure 6-9 Run IR-1 B1 signal. A. IESFO. B. newIESFO ..... 118

Figure 6-10. Run IR-1 B2 signal. A. OFSCoh Map B. Enhanced Envelope Order Spectrum..... 119

Figure 6-11. Run IR-1 B2 signal. A. IESFO. B. newIESFO. .... 120

Figure 6-12. Run IR-2 B1 signal. A. OFSCoh Map B. Enhanced Envelope Order Spectrum..... 121

Figure 6-13. Run IR-2 B2 signal. A. OFSCoh Map B. Enhanced Envelope Order Spectrum..... 122

Figure 6-14. Run IR-2 B2 signal. A. IESFO. B. newIESFO. .... 122

Figure 6-15 Run BF-1 B1 signal. A. OFSCoh Map B. Enhanced Envelope Order Spectrum..... 124

Figure 6-16 Run BF-1 B2 signal. newIESFO. .... 124

Figure 6-17. Run BF-2 B2 signal. newIESFO ..... 125

Figure 6-18 Different newIESFO for ball fault case, signals sampled on B2..... 126

Figure 6-19 Run CF-2 B2 signal. A. OFSCoh Map B. Enhanced Envelope Order Spectrum..... 128

Figure 6-20. Run CF-2 B2 newIESFO for Inner-Race fault search..... 129

Figure 6-21. Run CF-2 B2 newIESFO for Outer-Race fault search ..... 129

Figure 6-22. Run CF-3 B2 signal. Enhanced Envelope Order-Spectrum ..... 130

Figure 6-23. Run CF-6 B2 signal. Enhanced Envelope Order-Spectrum ..... 130

Figure 6-24. Run CF-8 B2 signal. Enhanced Envelope Order-Spectrum ..... 131

Figure 6-25. Data Set Estructure..... 133

Figure 6-26. Confusion matrix for validation data..... 134

Figure 6-27. ROC Performance illustration. .... 134

## Symbols and Abbreviations List

### Latin Symbols

Symbol	Term	Unit SI
$f$	Spectral Frequency	Hz
$h$	System's Impulse Response – Time representation of discrete filter	[-]
$t$	Time variable	s
$x$	Vibrational Response / Vibration Signal	$\text{m s}^{-2}$
$Mg$	Rotor weight	N
$m$	Unbalance equivalent mass	kg
$e$	Unbalance equivalent eccentricity	m
$me$	Unbalance weight	kg m
$A(t)$	Amplitude Modulation Function	$\text{m s}^{-2}$

### Greek Symbols

Symbol	Term	Unit SI
$\alpha$	Cyclic frequency	revolution <sup>-1</sup>
$\theta$	Angular shaft position	rad
$\dot{\theta}$	Angular shaft speed	s <sup>-1</sup>
$\ddot{\theta}$	Angular shaft acceleration	s <sup>-2</sup>

### Abbreviations

Abbreviation	Term
<i>REB</i>	Rolling Element Bearing
<i>F<sub>s</sub></i>	Frequency of Sampling [samples/s]
<i>O<sub>s</sub></i>	Order sampling (similar to <i>F<sub>s</sub></i> but in angular domain) [samples/revolution]
<i>STFT</i>	Short Time Fourier Transform
<i>BPOO</i>	Ball Pass Order Outer-Race [event / revolution]
<i>BPOI</i>	Ball Pass Order Inner-Race [event / revolution]
<i>BSO</i>	Ball Spin Order [event / revolution]
<i>FCO</i>	Fault Characteristic Order [event / revolution]
<i>FTO</i>	Fundamental Train Order [event / revolution]
<i>BPFO</i>	Ball Pass Outer-Race Frequency [Hz]
<i>BPFI</i>	Ball Pass Inner-Race Frequency [Hz]

**AbbreviationTerm**

---

<i>BSF</i>	Ball Spin Frequency [Hz]
<i>FTF</i>	Fundamental Train Frequency [Hz]
<i>SC</i>	Spectral Correlation [ $U^4 \text{ Hz}^{-2}$ ]
<i>SCoh</i>	Spectral Coherence [-]
<i>PSD</i>	Power Spectral Density [ $U^2 \text{ Hz}^{-1}$ ]
<i>SES</i>	Squared Envelope Spectrum
<i>EES</i>	Enhanced Envelope Spectrum
<i>EEOS</i>	Enhances Envelope Order Spectrum
<i>IES</i>	Improved Envelope Spectrum
<i>IEOS</i>	Improved Envelope Order Spectrum
<i>MOPA</i>	Multi Order Probabilistic Analysis
<i>PDF</i>	Probability Distribution Function
<i>SNR</i>	Signal to Noise Ratio
<i>OR</i>	Outer Race
<i>IR</i>	Inner Race
<i>RE</i>	Rolling Element
<i>BF</i>	Ball Fault



# 1. Introduction

## 1.1 Background and Context

The Rolling Element Bearing (REB) diagnosis is of particular interest for condition based maintenance. The aim of the diagnosis by mechanical vibrations consists in the identification of anomalies in the vibratory response of a particular equipment, identifying if such anomaly comes from a change in the driving source, or some physical change in the equipment of interest. The above is illustrated in Equation 1-1, in this model the vibratory response  $x(t)$  results as the output of a lineal time invariant system with time transfer response function  $h(t)$ , when an external stimulus or drive force  $f(t)$ , taking into account the noise or others vibration sources  $n(t)$ .

Equation 1-1 
$$x(t) = h(t) * f(t) + n(t)$$

For the particular case of vibrations in rotary machinery, it is intuitive to assume that the external driving force presents a periodic behavior as a function of the angular position of the shaft  $\theta$ . As a result, it is expected that the vibratory response will also show some kind of periodical behavior in the angular domain. However, in most cases, the transfer function does not depend on the angular position of the axis, therefore, without incurring in rigorous math's, Equation 1-1 can be rewritten as follows.

Equation 1-2 
$$x(t, \theta) = h(t) * f(\theta) + n(t)$$

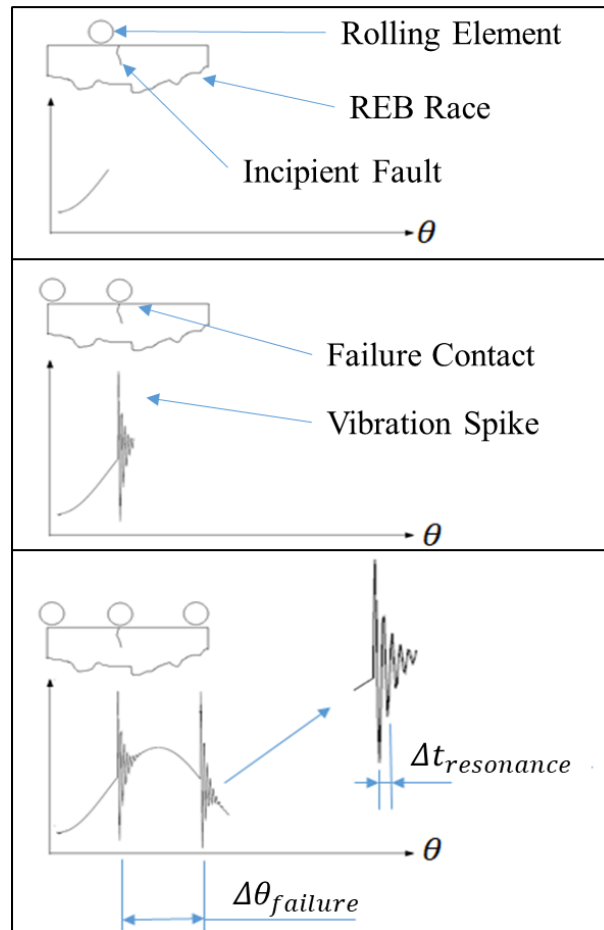
In order to express the vibratory response in the angular domain, different techniques have been developed [1]–[4]. These authors have mainly taken advantage from the different advances in digital signal processing. Among those techniques the Computer Order Tracking (COT) is maybe the most used [5]. The Computer Order Tracking identify the angular position of the shaft by referencing in the pulses series emitted by a tachometer or encoder. By this, is possible to obtain a signal sampled at instants, which correspond to equally angular spans.

Particularly for the Rolling Element Bearing diagnosis, the interaction between time periodical and angular periodical phenomenons has been exposed by different authors [2], [6]. To exemplify this, consider the presence of a brief crack in the outer race of a bearing, as shown in Figure 1-1. This crack will generate contact with the rolling elements as the shaft continues rotating. This situation would be present at equally-spaced angular intervals according to the geometry of the bearing. In this sense, the contacts will occur at periods dictated by the Fault Characteristics Frequencies –FCF of the rolling element bearing, named BPFI, BPFO, BSF and FTF. Those frequencies are broadly exposed and discussed in literature [7].

Each time crack and rolling elements are in contact, occurs an impulsive force, which generates a vibration response in the resonance frequencies of the REB. Resonance frequencies usually belong to 2000 – 10000 Hz [8], and they are dictated mainly by dynamic conditions, i.e. dictated by the mass, restrictions, stiffness and damping characteristics of REB. This has an important implication,

which is that instantaneous vibrational response generated by those impacts are mainly time-dependent, as it is illustrated in Figure 1-1.

Figure 1-1. Vibration response in a faulty Rolling Element Bearing - Illustration.



The situation illustrated in Figure 1-1 and the previous paragraph, could be summarized by the fact that the impacts periodicity are dictated by the geometry of the REB and the shaft rotational speed. On the other hand, the behaviour of the vibrational response at impacts is mainly dictated by dynamics characteristics and is usually associated with high frequencies energy.

The simplistic model of Equation 1-2, also could explain the situation previously seen. The impulsive force generated by the contact between rolling elements and race is represented by the force  $f(\theta)$ . This force is dictated by the kinematic characteristics of the ensemble, i.e. geometry and rotational speed. On the other side, the path between race and the vibration sensor corresponds to the function  $h(t)$ , which is a transfer function dictated by the dynamic characteristic i.e. mass, stiffness and



damping, and consequently, will determine the resonance frequencies of the REB. In this sense,  $f(\theta)$  represents the periodic forces while the  $h(t)$  represents the system dynamic.

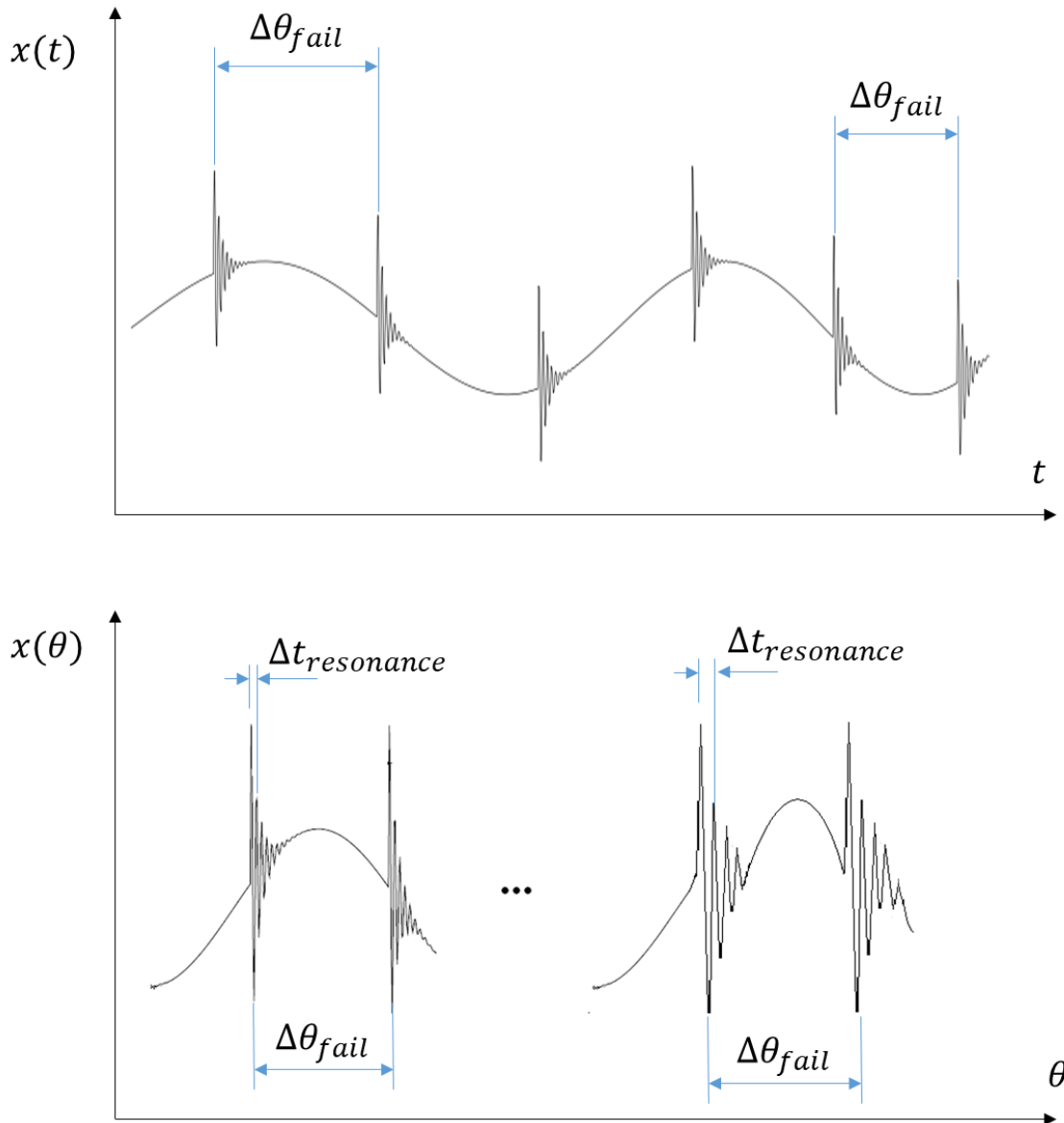
The previous discussion shows the linkage between angular position dependency and time phenomenon dependency for REB diagnosis. The first one governs the periodicity forces while the second one represents the system dynamics.

If the angular velocity keeps constant, the duality between time variable  $t$  and angular position  $\theta$  is easily solved since the proportional relation for both variables. In this sense, the vibrational response would have periodicity in both domains. In general, it is preferred to perform the REB diagnosis in angular domain, analyzing the spectral behaviour of the signal envelope in terms of 'orders', which is the analogue to frequency in time domain.

In many applications it is reasonable to assume the angular velocity keeps stationary, i.e. nearly constant. However, it is common to find diverse situations at which this assumption does not result reasonable. In such situations, the interaction between kinematics (angular domain) and dynamics (time domain) matter, since vibrational response signal contains valuable information in both domains.

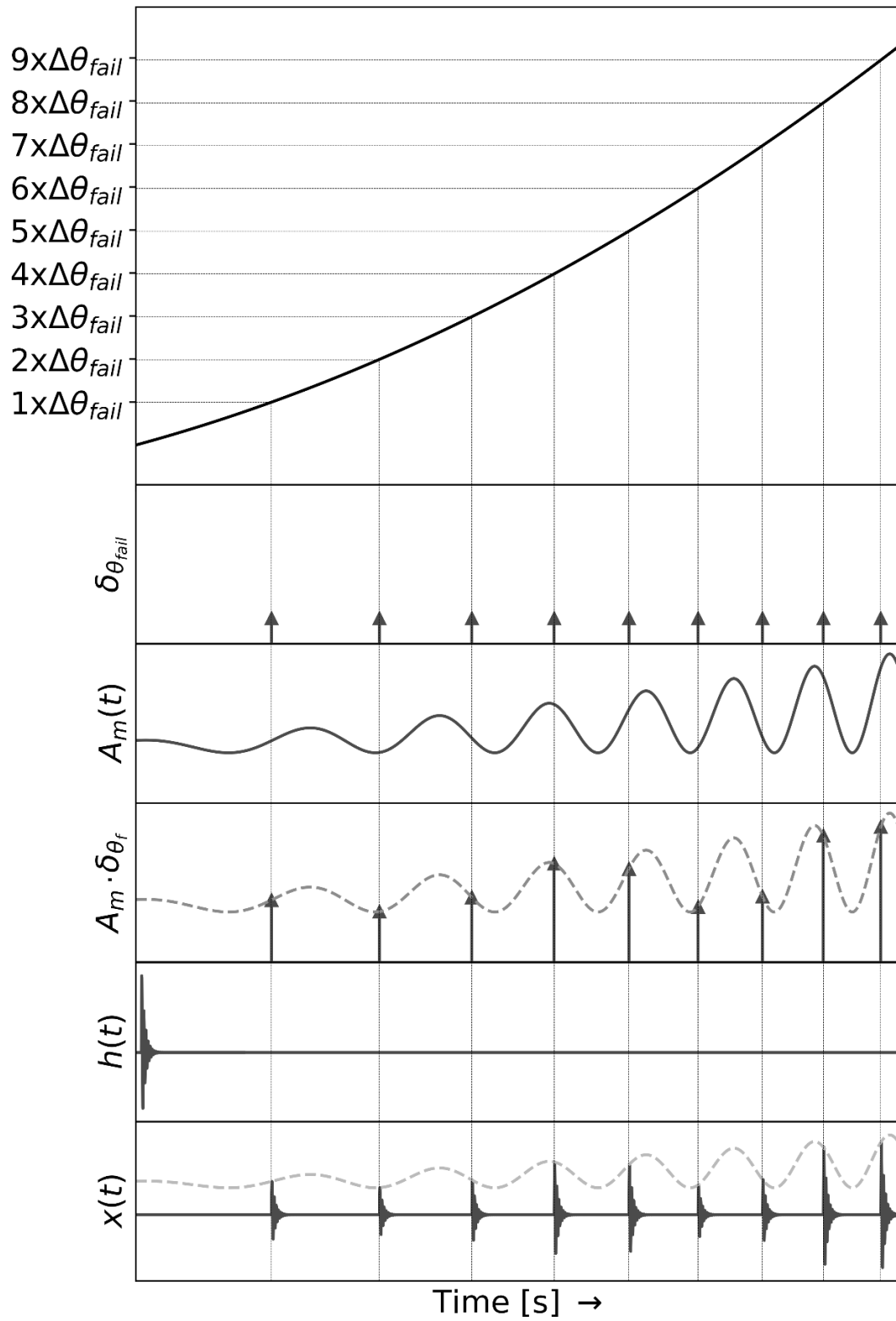
To explain the interaction between both domains, in nonstationary angular speed, let us consider again the rolling element bearing exposed in previous paragraphs and illustrated in Figure 1-1. Consider a "run-up" situation at which the angular speed is increasing. Under this situation, the impulses generated due to contact with failure surface conserve periodicity in angular domain. However, this periodicity is not conserved in time domain since the time-intervals at which impacts are generated would be reducing as angular velocity increases. Accordingly, this indicates that if the vibrational response is expressed as a time function, the impacts would not seem periodical. This situation is illustrated in Figure 1-2. On the other hand, the behaviour of the signal just at instants when impacts occur, is mainly governed by time domain, i.e. when vibrational response is represented in angular domain, the time periodicities at impact instants do not seem periodical, as it is illustrated in the lower part of Figure 1-2. From REB diagnostic perspective, this duality generates the necessity of implementing a method which allows to extract periodic information related with angular domain, but also, consider the frequencies associated with the ensemble dynamics [9].

Figure 1-2. Illustration for vibrational response in time domain and angular domain.



Additionally to the duality on time and angular dependencies, it should be added that the amplitude could be modulated as consequence of angular speed changes. From an energetic perspective, this velocity increasing (decreasing) could be represented as an increase in kinetic energy, transmitted to REB and generating increases (decreases) in the energy of elastic deformation. To illustrate this, consider the model presented by [10], illustrated in Figure 1-3.

Figure 1-3. Vibrational response in REB under variable speed [10].



In this model the force is represented as an angular periodic pulse train  $\delta_{\theta_f}$ , which activate the REB transfer function  $h(t)$ . Those pulses are modulated in amplitude by the function  $A_m(t)$  because of kinetic energy increasing.

This modulation  $A_m(t)$  could have other additional causes different from kinetic energy increase, including for example natural frequencies excitations associated with shaft or rotors supported by the REB. This excitations are probable because the temporal changes in the IX during acceleration run-up. Equally to resonance frequencies associated with REB, the resonance frequencies of the shaft, rotor, and other elements present are mainly time dependent, establishing a linkage between vibrational response of REB and dynamical behaviour of other elements arranged in the assembly.

Through this section, a general discussion of the aspects related with the diagnosis of REB under variable speed has been discussed. As previously discussed, results important to build models which results able to detect the presence of periodicity of vibration spikes while catching the dynamic behaviour of the system.

For the following sections of this chapter, a brief justification of this work and a summary of the research aim is presented.

## 1.2 Justification

The condition-based maintenance represents an interesting strategy for many of industrial and productive process since their benefits in reducing operative costs and increase equipment's reliability. By this approximation many logistics and monetary benefits could be achieved [11], [12]. Particularly, the mechanical vibration analysis and vibration based condition monitoring are one of the most useful techniques in CBM [13]. By vibration, analysis is possible to capture symptoms of early failures, which could also aid the detection, diagnostic and eventual prognostic of the indication.

Vibration-based condition monitoring is intended to capture the vibrational response of particular equipment by the use of vibration sensors. This is done to identify if an eventual change in the vibrational response is either due to any change in equipment structure or is due to any change in excitation source or drive mechanism [14].

In some situations, the criticality of the equipment in question induces the need for permanent and online monitoring of mechanical vibrations. A need that can be reinforced when the mechanisms contain elements such as bearings, gears or blades, since detection under such conditions is made more sensitive by using accelerometers [14], [15]. The above, in conjunction with the nowadays context of Industry 4.0, the wide availability of sensors and acquisition systems at more accessible prices, the accelerated increase in computing capacity, and the availability of algorithms and frameworks for digital signal processing, lead the use of online vibration monitoring.

One of the great challenges for online vibration monitoring lies in the variability that can arise in the operating conditions of the different rotating equipment. This gives rise to non-stationary vibrations that can significantly alter the vibratory response and in consequently make it difficult to detect, classify and diagnostic faults [16]. The non-stationarity of the vibratory response can occur by the

variation in the operating speeds or external loads under which equipment is subject. In the first case, the nature of the vibrations in the frequency domain is highly altered, and consequently, the fault diagnosis may lose precision. Therefore, the analysis of vibrations in rotary machinery under variable speed conditions is a problem of nowadays interest [17].

In particular, bearing failure detection and diagnosis is one of the areas of greatest interest for Vibration-based condition monitoring. These elements are of great interest since most rotating machines are present but it is estimated that only 10% reach the L10 life expectancy [8]. In many applications, REB are the components of major spare replacement and even with biggest failure rate as illustrated by [18], where it is reported that REB cover until 6.77 % of electric motors. Being the biggest percentage of mechanical failures. Other sources as [19], [20] indicate that 40 % of failures of induction motors are associated with REB failures. Additionally, it is estimated that 76 % of wind turbines fails in their gearbox as a consequence of REB failure [21]. This latter case resulting of great interest as rotational speed presents high variation as consequence of wind currents randomness.

### 1.3 Research Aim

In the present work, it is intended to give an evaluation of diagnosis process of rolling element bearings when they are subjected to non-stationary conditions implying variable rotation speed. Under those situations, the vibrational responses associated with failures in REB are of special interest, by some important aspects such as the ones described in section 1.1.

In this sense, this work is aimed under the research question established as follows.

Under variable speed conditions, the presence of bearing failures and variable speed, added to amplitude modulation, can be diagnosed through the following techniques: Envelope spectral analysis, Order tracking techniques, Cycle stationarity analysis and Filtering for maximization of spectral kurtosis?

Using the following hypothesis.

Early diagnosis of bearing failures can be made under variable speed conditions using techniques of Spectral Envelope Analysis, Order Tracking Techniques, Cyclostationary Analysis and Filtering to maximize spectral kurtosis.

Accordingly, this thesis is formulated by using the following objectives.

As general objective has been declared.

- To evaluate the diagnosis of incipient failures in Rolling Element Bearings using mechanical vibration analysis.

For specific objectives, it has been declared.

- To design strategy for the simulation and acquisition of signals with bearing failures operating under variable speed conditions.

- To develop a model for the diagnosis of incipient failures in bearings, under variable speed conditions, using spectral envelope analysis, order tracking techniques, cyclo-stationarity analysis and filtering to maximize spectral kurtuosis.
- To evaluate the detection capacity of Cyclo-stationarity models and spectral kurtuosis filtering for cases of bearing failures.

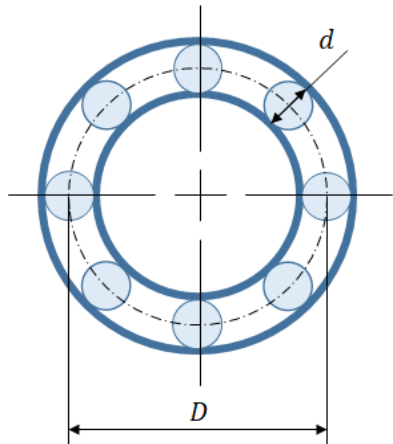
During the development of this work, a model for the simulation of REB fault signals is used. Also, a model for the REB diagnosis under non stationary rotational speed is proposed and the results of their usage for simulated signals and experimental signals are shown. Also a learning algorithm for the classification and diagnosis of REB faults is exposed. Accordingly, the document is organized as follows. On chapter 2 a theoretical framework with the main algorithms available on literature is exposed and their usage is briefly illustrated by a practical case. Section 3 describes the test rig used for capturing experimental dataset. At chapter 4 the model proposed for REB diagnosis is presented. The chapter 5 describes the model used for simulating REB fault signals. Finally, on chapter 6 the experimental data is shown and the result of using the model proposed on chapter 4 is also exposed. Chapter 7 presents conclusions and future works.

## 2. Theoretical Framework

### 2.1 Rolling Element Bearing Diagnosis – Benchmark method

For REB failure diagnosis in past decades, important advances have been shown. Maybe the most effective techniques to perform REB diagnosis is based on analyzing vibrational response envelope. Specifically, this technique relies on take the spectral content of the signal envelope and verify if there is information of Fault Characteristic Orders –FCO [2], [22]–[24]. The Fault Characteristic Orders are based on kinematic relations between the different elements of the REB, and their geometry. In the most common case, at which the outer race speed keeps static, the Table 2-1 summarize the relations for the FCO.

Table 2-1 Fault Characteristics Orders Relations

FAULT CHARACTERISTIC ORDER	MATHEMATICAL RELATION
Ball-Pass Inner Race Order: <i>BPOI</i>	$\frac{N}{2} \left( 1 + \frac{d}{D} \cos(\theta) \right)$
Ball-Pass Outer Race Order: <i>BPOO</i>	$\frac{N}{2} \left( 1 - \frac{d}{D} \cos(\theta) \right)$
Fundamental Train Order: <i>FTO</i>	$\frac{1}{2} \left( 1 - \frac{d}{D} \cos(\theta) \right)$
Ball Spin Order: <i>BSO</i>	$\frac{D}{2d} \left[ 1 - \left( \frac{d}{D} \cos(\theta) \right)^2 \right]$
<p><i>N</i>: Number of rolling elements.  <i>d</i>: Rolling Element Diameter.  <i>D</i>: Pitch Diameter.  <i>θ</i>: Contact Angle.</p>	 <p>The diagram illustrates a cross-section of a bearing with an outer race, an inner race, and several rolling elements (balls). The pitch diameter is labeled as <i>D</i>, the diameter of a single rolling element is labeled as <i>d</i>, and the contact angle is labeled as <i>θ</i>. The diagram shows the relative positions of the balls and the races, with dashed lines indicating the pitch circle and the contact points.</p>

Typical vibrational response of incipient failures have been modeled for faults on different components according to load distribution and kinematic relations. The most common patterns and envelopes for incipient failures are briefly illustrated on Figure 2-1. Although those waveforms correspond to most common failures, there are situation at which modulations could be different, mainly depending on the loads imposed to REB. The relation between modulations and type of loads are summarized on Table 2-2 [7].

Figure 2-1. Typical REB fault waveform and Envelope. Vibrational response against angular position

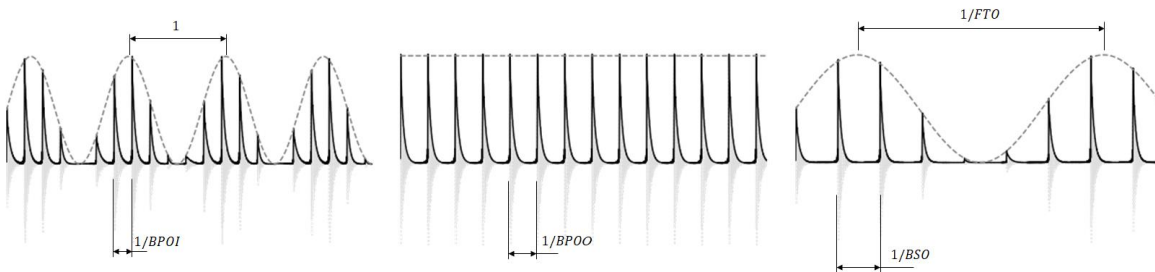


Table 2-2. Periodic characteristics of bearings with defects under various loadings and path effect

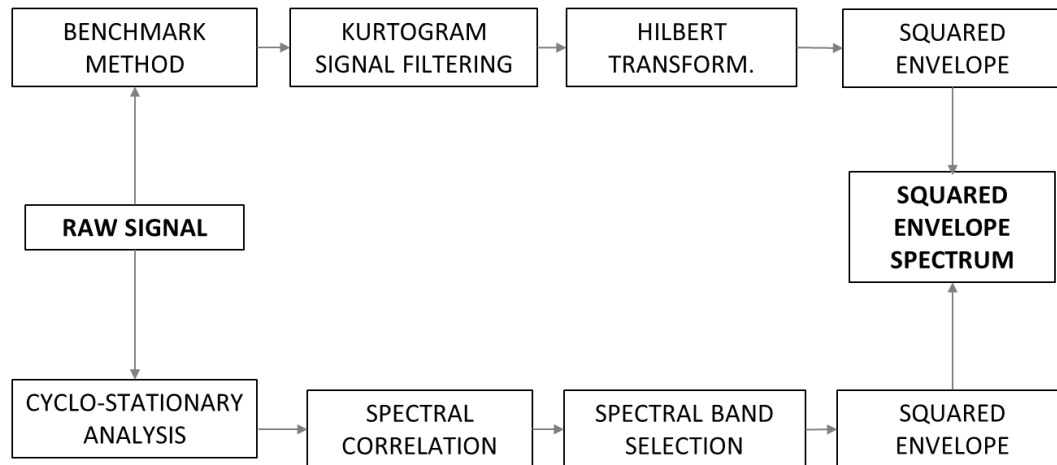
CAUSE OF PERIODICITY	PRACTICAL EXAMPLES	OUTER RACE DEFECT	INNER RACE DEFECT	ROLLING ELEMENT DEFECT
Static Load*	Misalignments. Dead Weight	No Effect	1×	FTO
Shaft Unbalance	High Unbalance High Speed Regimes	1×	No Effect	1-FTO
REB Diameter Variations	Mounting	1×FTO	1-FTO	No Effect
Transmission Path Effect	Cracks on shaft	No Effect	1×	FTO BSO

\*Static Load represents the case commonly exposed on literature and illustrated in Figure 2-1.

During the last decades, two methods for the analysis of the envelope have been highlighted, as illustrated in Figure 2-2. To describe those methods consider the angular speed keeps near constant. The first method consists of the use of a band-pass filter, which limits the content of the vibratory response to the resonance frequencies of the bearing. Usually the band-pass frequencies lies in the range of 2000 - 12000 Hz. Once the signal is filtered, an analytic version of this signal is obtained by the use of Hilbert transform. By taking the square magnitude of analytic signal, the squared envelope is obtained and results possible to analyze it, either in order or frequency domain.



Figure 2-2. Rolling Element Bearing Diagnosis by Squared Envelope Spectral Analysis – Two methods [25].



The first method consists of the use of a band-pass filter, which limits the content of the vibratory response to the resonance frequencies of the bearing. Usually the band-pass frequencies lies in the range of 2000 - 12000 Hz. Once the signal is filtered, an analytic version of this signal is obtained by the use of Hilbert transform. By taking the square magnitude of analytic signal, the squared envelope is obtained and results possible to analyze it, either in order or frequency domain. The band pass filter was usually selected by experience of analyst. However, some works describe a benchmark method to select the range of filter. This is made based on the fact that resonance frequencies are stimulated by impulsive forces resulting from contract with incipient fault, By the fact statistical kurtosis is a clear descriptor for impulsive behaviour, this method relies in selecting the range of frequencies for which kurtosis is maximized.

The second method uses the Cyclo-stationarity model. With this model, it is intended to extract the periodic information of the variation of the vibratory response. Particularly, it has been shown REB failure give rise to second order cyclostationary signals, which mean the autocorrelation function of the vibrational response has a periodical behaviour with respect time delay. To describe the behaviour of second order Cyclo-stationary the spectral correlation is an useful information. Spectral correlation is a bi-variable function which would depend on the spectral frequency  $-f$ , and the cyclic frequency  $-\alpha$ . Broadly, for the REB diagnosis, the spectral frequency would contain the information related with the dynamic characteristic of the ensemble, whereas the cyclic frequency would contains the information related with the kinematics. By have estimating spectral correlation, the square envelope spectrum could be obtained straightforward by averaging over the spectral frequency. Once square envelope is plotted, the idea is to search peaks at fault characteristics orders. Spectral correlation would be explained with more detail in section 2.3.

Recently other methods based on automatic learning algorithms has been [26]–[28]. Although there are many advantages associated with their utilization, at industrial level, they are limited mainly by the amount of failure data available, the labeling and the highlighted unbalance of failure data in contrast to normal operation. These automatic learning diagnosis methods have enormous potential, but results difficult to generalize at industrial environments.

The strategies exposed on Figure 2-2 have been broadly studied and developed for the case at which rotational speed keeps constant. For the case at which rotational speed does not keep constant, the Squared Envelope Order Spectrum –SEOS should be obtained instead of Squared Envelope Spectrum –SES. To obtain the SEOS, some different process should be done for obtaining the Squared Envelope Order Spectrum, such as order tracking, Cyclo non-stationarity analysis and different approach for demodulation should be used, as it will be discussed on section 4.

## 2.2 Kurtosis, Spectral Kurtosis and Fast Kurtogram.

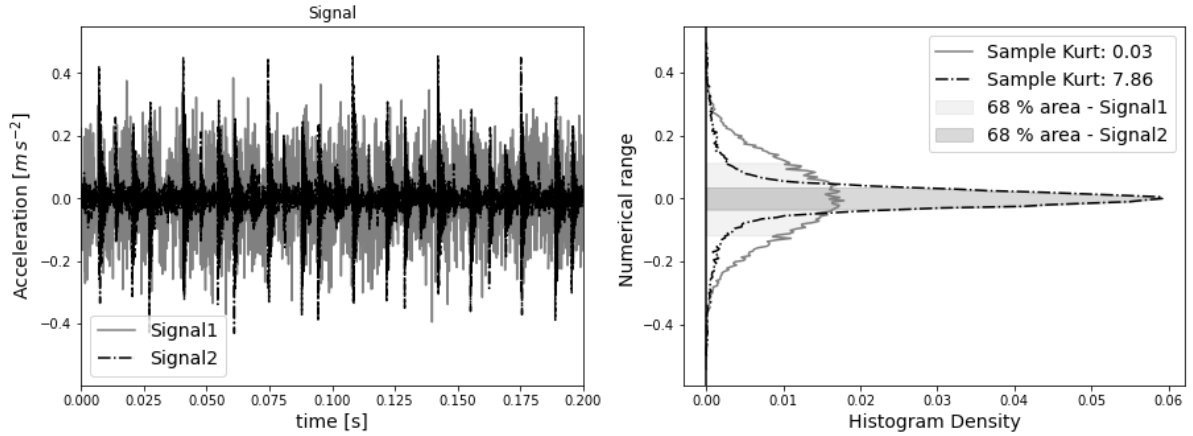
The kurtosis is a fourth moment descriptor for a random variable. It establish information related with the shape of probability distribution function. It is generally expressed as the relation between fourth moment and fourth power of standard deviation as it illustrated in Equation 2-1. Kurtosis is commonly estimated by the sample kurtosis as defined in Equation 2-2, where  $\bar{X}, S$  represent the average and the sampled standard deviation, while  $x_i$  and  $N$  represent the realizations and number of realizations respectively.

$$\text{Equation 2-1} \quad Kurt[X] = \frac{E[(X-\mu)^4]}{\sigma^4} - 3$$

$$\text{Equation 2-2} \quad \widehat{Kurt}[X] = \frac{1}{N} \frac{\sum_i (x_i - \bar{X})^4}{S^4} - 3$$

This definition is known as Pearson definition, also called excess kurtosis. The “3” scalar subtraction is done with the aim a random variable X normally distributed have a null kurtosis. It should be noticed than kurtosis takes measure of the weight of tails in the distribution of random variable X. To further illustrates consider the realization of two simulated signals illustrated in Figure 2-3. Note although both signals have the same range of numerical values, the backward signal, drawn with gray tone, seems normally distributed as their tails are not far separated from the  $\pm 1$  standard deviation region\*, (drawn in shadow gray region in right plot of Figure 2-3). In fact, each realization in signal 1 has been built as a stationary Gaussian noise, which explain the fact its sample kurtosis is near zero, as indicated by the labels of Figure 2-3.

Figure 2-3. Sample kurtosis illustration



On the other hand, signal 2 seems like if periodically, sudden transient events occurs and consequently realizations reach a high numerical value. This behaviour is further illustrated in the histogram of right side, since the major part of signal 2 realizations lies in a narrower region than signal 1, although both have the same range. Signal 2 in fact simulates a REB faulty vibrational response, as the transients previously discussed represents a periodical impact generated by faulty surface contact. It should also noticed signal 2 reaches a higher kurtosis value than signal 1.

Discussion until now allow illustrating the concept of kurtosis and their appliance on temporal realizations. It also illustrates the fact Gaussian distributed realizations are characterized by null kurtosis. Also, for the REB fault signal, the kurtosis value could be considered as and indicative of presence of anomalies which give raise to transients effects. Kurtosis in fact could be considered as a valuable descriptor of transient anomalies, which for our interest is interesting to characterize in frequency domain. To perform the characterization of transients in frequency domain, the spectral kurtosis is defined as the relation between the fourth cumulant and the squared second moment of signal at frequency  $f$ , i.e. equivalent to filter signal realizations at a particular frequency  $-f$ . Under the assumption of ergodicity spectral kurtosis could be defined as indicates Equation 2-3, where  $|H(t, f)|^2$  is the power spectrum at time  $t$ , and the  $\langle \cdot \rangle$  indicates averaging along time. The subtraction of “2” in contrast to “3” previously discussed is explained because  $H(t, f)$  represents a complex envelope, as it was shown by [29].

$$\text{Equation 2-3} \quad SK[X](f) = \frac{\langle |H(t, f)|^4 \rangle}{\langle |H(t, f)|^2 \rangle^2} - 2$$

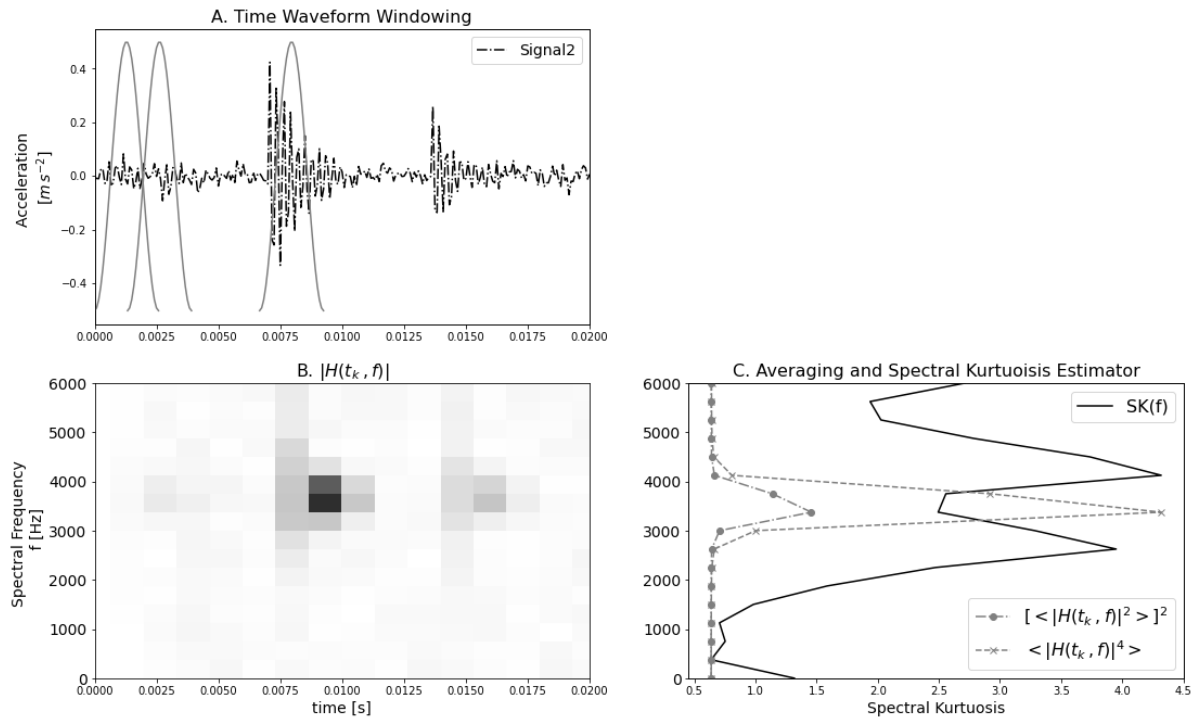
Spectral kurtosis could be estimated from the Short Time Fourier Transform – STFT, by consider a window slice tap along the time axis, taking the power spectrum at each tap and taking time averages on windowing taps according to Equation 2-4. Where  $N_w$  represents the length of window and  $|H_w|$  the windowed magnitude spectrum.

$$\text{Equation 2-4} \quad \widehat{SK}[X](f; N_w) = \frac{\langle |H_w(t_k, f)|^4 \rangle}{\langle |H_w(t_k, f)|^2 \rangle^2} - 2$$

To illustrate the estimator of spectral kurtosis described by Equation 2-4, consider the STFT of signal2 previously discussed, shown in Figure 2-4. In this figure a fraction of time has been plotted to illustrate the windowing process (Figure 2-4 – A). By slice the windows, and taking the Fourier

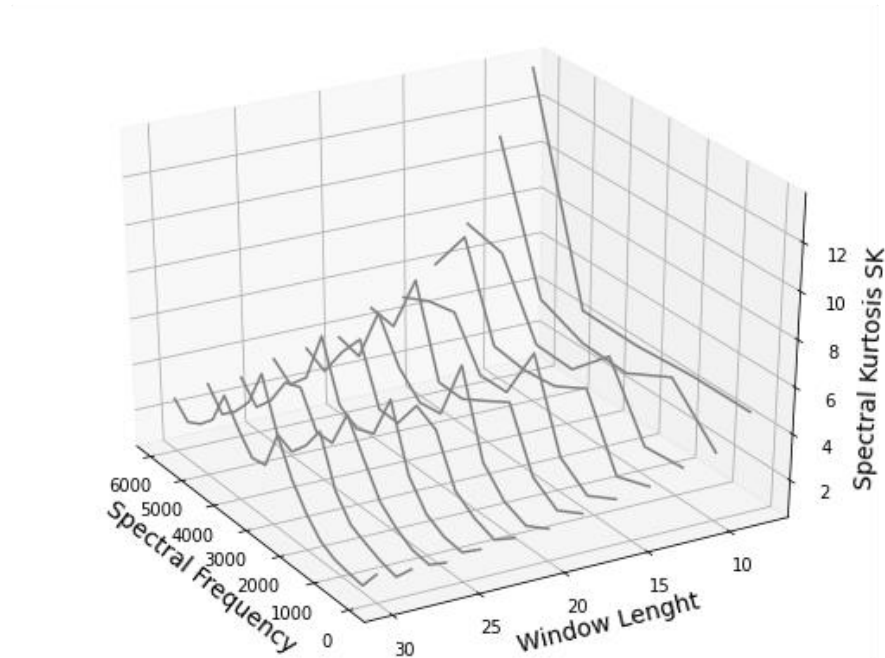
transform on each window the spectrogram is built as illustrates (Figure 2-4-B). Notice the compromise between time and frequency resolution as well established by uncertainty principle. On each row of the spectrogram averaging of the square magnitude and fourth power of magnitude are computed as illustrates the gray tone curves of Figure 2-4 – C. By taking the division between both curves, and subtracting 2 units, the spectral kurtosis is estimated, as illustrates the curve drawn in black continuous line. This estimator in fact could be seen as a welch estimator, since it replaces the ensemble averaging, by average over the time axis on STFT.

Figure 2-4 Illustration of Spectral Kurtosis Estimator



In previous illustration, should be noticed an important detail which is related with the role of the length of windows. The window length should be as short as possible to allow the correct identification of two transient effects (refers to Figure 2-4A) but should also be large enough to capture the entire transient effect. For the window illustrated in Figure 2-4A it could be noticed that the window length selected allows to separately identify two transients but is no large to capture the time duration of first transient. The so-called Kurtogram further explores the window length dependence of spectral kurtosis estimator. In the Kurtogram, the spectral kurtosis is plotted against the window length and spectral frequency, similar to the 3D projection plot illustrated in Figure 2-5.

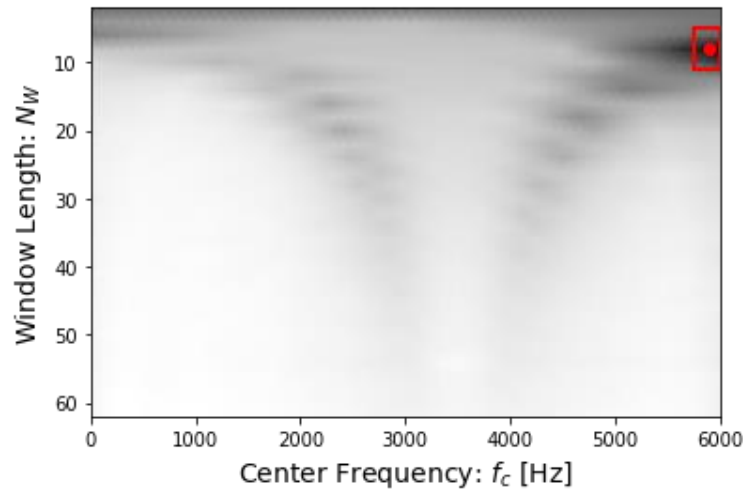
Figure 2-5. Window length dependence of spectral kurtosis.



The interest of spectral kurtosis relies on the fact it could indicate at which range of frequency the signal presents its maximum impulsiveness. The aforementioned results extremely useful for REB diagnosis as it could separate the frequency at which transient occurs. This suggest spectral kurtosis in fact could be taken as a filter which maximize the signal impulsivity, as it was demonstrated in [30].

In fact, for practices, is desirable to generate a passband filter, which allows maximizing the kurtosis of the resulting envelope. This filter should be centered in the frequency at which spectral kurtosis is maximum. However, considering spectral kurtosis is window-length dependent, the bandwidth is a parameter to concern. In this sense, to select the optimal filter, which maximizes the kurtosis of envelope, a bi-map of spectral kurtosis against window length and center frequency is usually plotted. The optimal filter to proceed the envelope spectrum analysis is selected as the combination of frequency bandwidth  $\Delta f \sim F_s/N_w$ , and center frequency  $f_c$ . This is illustrated in Figure 2-6.

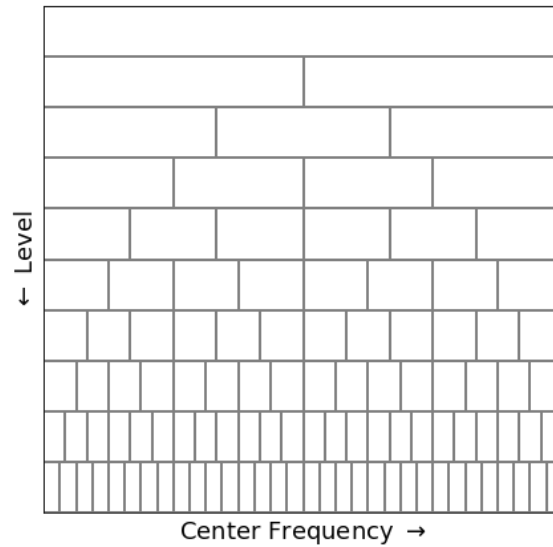
Figure 2-6. Kurtogram



This indicates that a filter, which maximizes kurtosis of envelope, should be centered near 6000 Hz, considering a window of near four (4) samples. Two appreciations should be considered, the first is computation of Kurtogram results computational costly, since it is necessary to compute STFT by each window length. Additionally, although it results clear the center frequency, the filter realization results in a bandwidth near to  $1.5 \times 10^3$  Hz, which is considerably wide, and do not result easy to obtain such a narrow window without ripple effects.

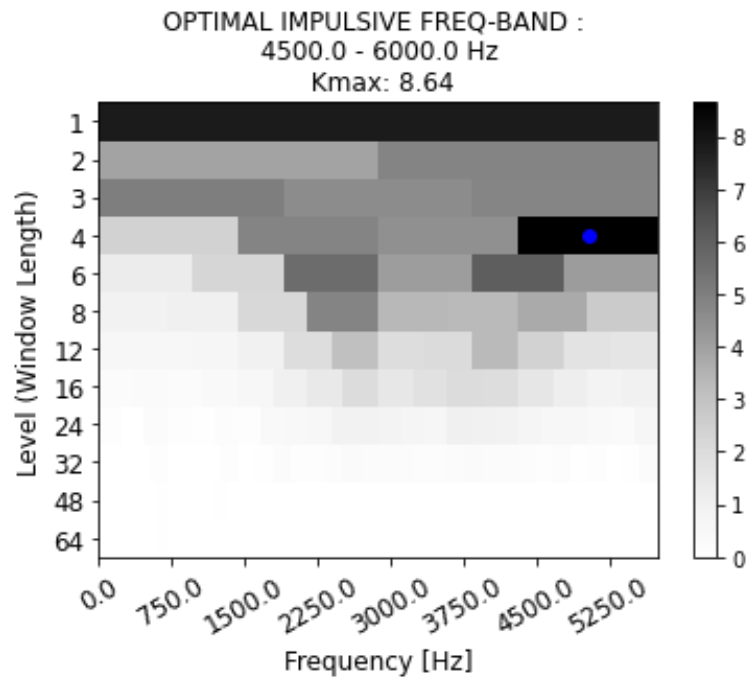
In a manner to overcome those appreciations, the fast Kurtogram is defined by [31]. This Kurtogram approximation is based on a binary tree search, partially inspired in Wavelet Packet transform. It divides the bandwidths and center frequencies in a binary-three map such as the ones drawn in Figure 2-7, using a bank of filters separating detail and residuals for each level (i.e. to analyze higher frequency resolution), instead of computing STFT for each window length.

Figure 2-7. Kurtogram Binary Tree.



The kurtosis of the envelope is represented by color map for each of pair of center frequency  $f_c$  and bandwidth  $\Delta f$  represented by the binary-tree grid. The pass-band filter is selected by taking the couple of center frequency and bandwidth, in which kurtosis rise is maximum value. As illustrated in Figure 2-2, once signal is filtered, the square envelope spectrum analysis proceeds. The fast Kurtogram for the previous ‘Signal 2’ is drawn in Figure 2-8.

Figure 2-8. Fast Kurtogram.



The Fast Kurtogram illustrated in Figure 2-8 highly coincides with the complete Kurtogram drawn in Figure 2-6. Although there is more clear resolution in the complete Kurtogram, the simplicity of the Fast Kurtogram and the savings in computational costs are extremely valuable for applications in REB diagnosis.

## 2.3 Second-Order Cyclostationary Analysis for Rolling Element Bearing.

As illustrated in Figure 2-2, the Square Envelope Spectrum, could be obtained by carrying a cyclostationary analysis, as exposed in [32]. The cyclostationary analysis were applied to REB, near two decades ago, where [33] shown that an anomaly in a REB give raise to a second order cyclostationary signal. Accordingly, the vibration response of a REB fault is non-stationary but hides a periodic behaviour in its variance. To characterize this, the Spectral Correlation representation has been shown extremely useful. Usually a bi-spectrum map is analyzed, where the Spectral Correlation (SC) is plotted against Spectral Frequency  $-f$  and Cyclic Frequency  $-\alpha$ . The earlier represents the dynamic characteristics of the REB i.e. their resonance frequencies, whereas the second one represents the periodic behave of the fault [23].

To define the concept of second order cyclostationarity, it is important to define the autocorrelation function, as it is defined in Equation 2-5, where  $E[\cdot]$  denotes the expectancy operator and the  $*$  indicates complex conjugate. In this equation results important to note the fact that autocorrelation depends on two variables, the instantaneous time  $t$ , and time lag  $\tau$ .

$$\text{Equation 2-5} \quad R_{xx}(t, \tau) = E[ x(t)x^*(t - \tau)]$$

A second order cyclostationary signal is defined as a signal in which their autocorrelation function keeps periodical with respect instantaneous time, i.e. it should exist a fundamental period  $T$ , such as  $R_{xx}(t + T, \tau) = R_{xx}(t, \tau)$ . To characterize the spectrum of a second order cyclostationary signal, Spectral Correlation is defined as the double Fourier transform of autocorrelation function as it is expressed in Equation 2-6. Where  $\alpha$ , and  $f$ , denote the Cyclic Frequency and Spectral Frequency.

$$\text{Equation 2-6} \quad SC_{2x}(\alpha, f) = \mathfrak{F}_{t \rightarrow \alpha} \{ \mathfrak{F}_{\tau \rightarrow f} \{ R_{xx}(t, \tau) \} \}$$

Cyclic frequency  $-\alpha$ , maps the instantaneous time, and usually contains information on modulation frequencies. Spectral frequency maps the time delay to the spectral domain and represents the spectral content of carrier frequencies. Particularly, for the case of REB fault signals,  $\alpha$  is mainly related to the periodicity of occurrence of impacts i.e. the cinematic characteristics of the REB ensemble (as discussed in section 2.1). On the other hand,  $f$  details the dynamic characteristic of the ensemble, which is contained in the carrier frequencies spectrum.

The name ‘Spectral Correlation’ is not fortuitous, in fact, from the previous definition expressed in Equation 2-6, it has been shown that this expression could be transformed in a correlation between

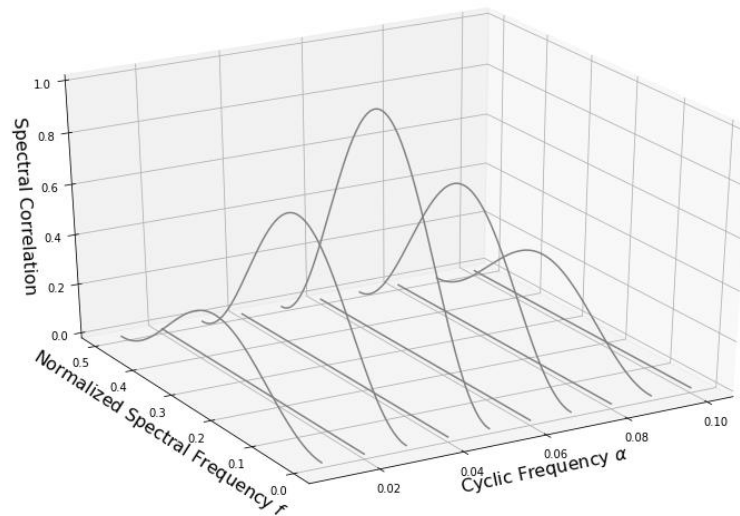


power spectral density of vibrational response, with their  $\alpha$  – delayed version, as it is shown in Equation 2-7.

$$\text{Equation 2-7} \quad SC_x(f, \alpha) = E[X(f)X^*(f - \alpha)]$$

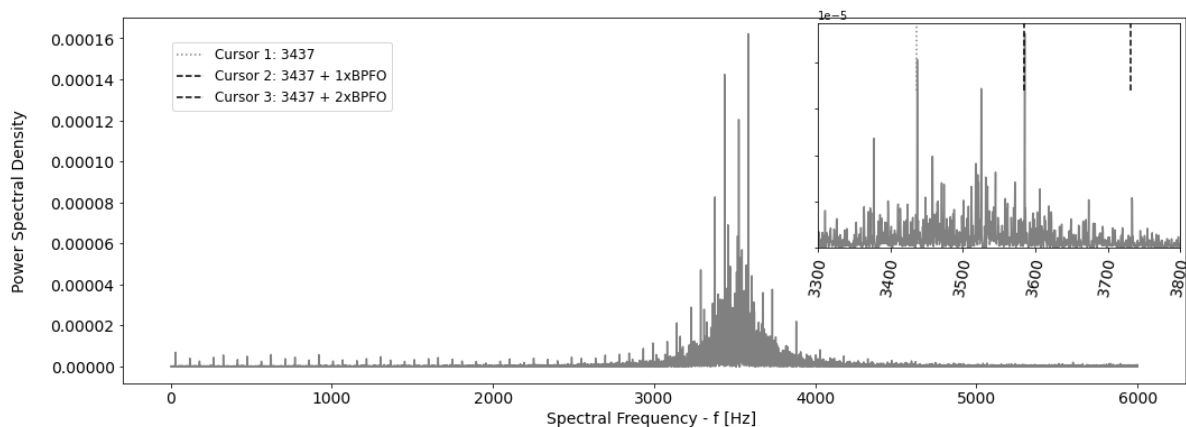
In fact, when a signal is strictly second order cyclostationary, the spectral correlation would be zero in whichever cyclic frequency, except in those in which the signal shows periodicity in its spectral correlation. Accordingly, the spectral correlation bi-map would seem similar to the one illustrated in Figure 2-9.

Figure 2-9. Illustration of Spectral Correlation for strictly Second-Order Cyclostationary.



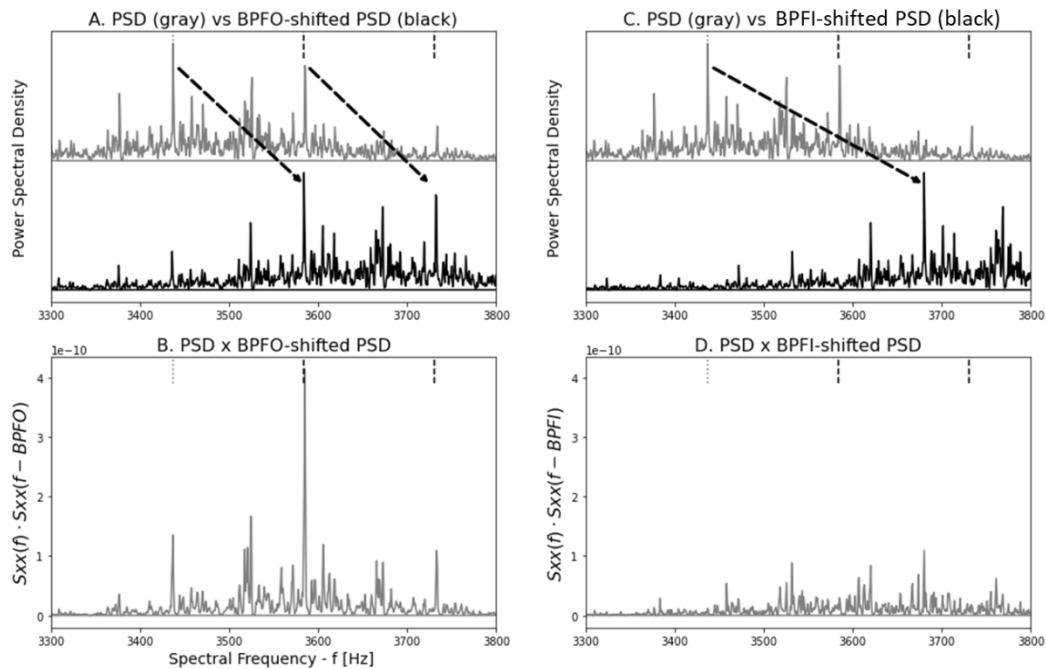
To illustrate the concept of spectral correlation, consider the simulated Outer Race Fault, named ‘Signal 1’, which was previously analyzed in section 2.2. The power spectral density –PSD, is shown in Figure 2-10. The power of the signal is mostly concentrated in the range of 3000 – 4000 Hz. In fact, the zoomed region located at the upper right corner, plots the PSD in the range of 330-3800 Hz.

Figure 2-10. 'Signal 1' Power Spectral Density



In Figure 2-10, the dotted cursor line, drawn in gray tone (Cursor 1) is located at 3437 Hz. The cursors drawn in black dashed line (Cursor 2 and Cursor 3), are distanced by exactly  $1 \times \text{BPOF}$  and  $2 \times \text{BPOF}$  from the Cursor 1. Now, let imagine the PSD curve is shifted by  $1 \times \text{BPOF}$  to the right, i.e. consider the PSD displaced by  $\text{BPOF}$ . By doing this displacement, the peak marked with the Cursor 1 will lie in the position marked by Cursor 2. Similarly, the peak marked with Cursor 2 will coincide with the position marked with Cursor 3. This situation is illustrated in Figure 2-11 A. where the zoomed (3300 Hz to 3800 Hz) is drawn in gray tone, while the  $1 \times \text{BPFO}$  shifted PSD is drawn in black tone.

Figure 2-11. Power Spectral Density vs.  $\alpha$ -shifted Power Spectral Density.

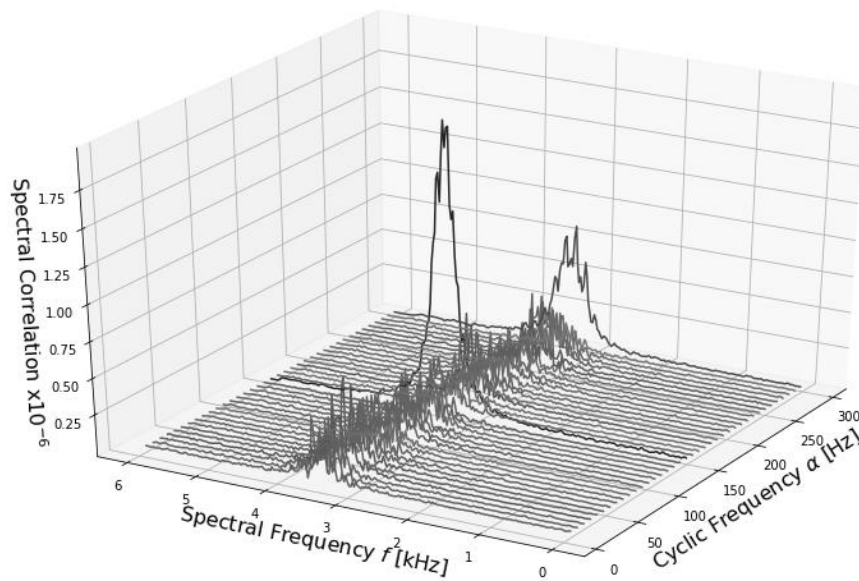


From the previous discussion, and the situation illustrated in Figure 2-11-A. and Figure 2-11-B., is straightforward to notice that if the product of both curves is computed, it will rise a considerably high value curve. To further discussion, consider the case where PSD is delayed by  $\text{BPFI}$  illustrated in Figure 2-11-C. As could be noticed, the peaks previously marked by cursors, do not coincide and subsequently, the product would of the PSD and  $\text{BPFI}$ -shifted PSD be a near to zero curve, as it is shown in Figure 2-11-D.

As would be discussed in section 2.4, the fact that the curve in Figure 2-11-B is numerically greater than Figure 2-11-D, indicates that high spectral correlation is raised when  $\alpha$  is set equal to  $\text{BPFO}$ , whereas is low when  $\alpha$  is set to  $\text{BPFI}$ .

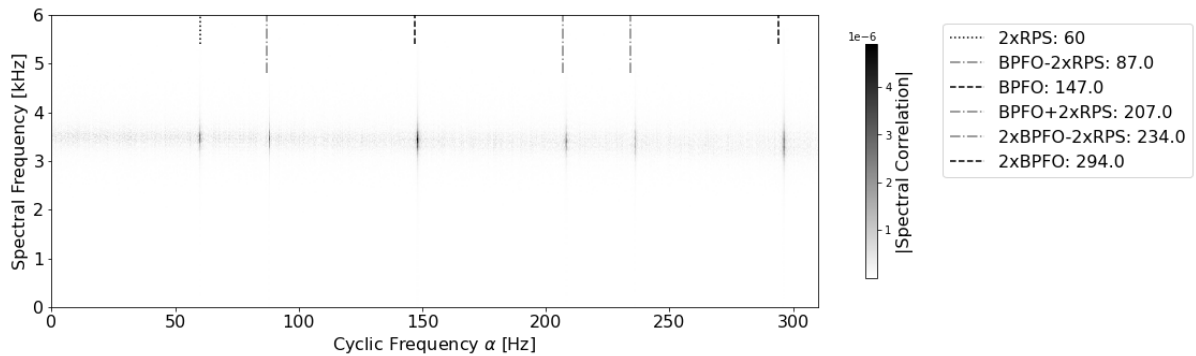
Spectral Correlation is the result to shift the Power Spectral Density among the  $\alpha$ -axis, and so, plotting the bi-spectral map  $f$ - $\alpha$  vs  $SC$ , in a similar manner as illustrated in Figure 2-9. For the previous worked 'signal 1', the spectral correlation bi-map is shown in Figure 2-12. It is notorious for the high value raised around  $\alpha = 140$  Hz, which is the value for  $\text{BPFO}$  in simulated signal.

Figure 2-12. ‘Signal 1’ Simulated Outer Race Fault Spectral Correlation



Usually, spectral correlation is plotted in a color-map, as the ones illustrated in Figure 2-13. As could be noticed, the vertical line pattern highly marked inside the spectral frequency range of 3000 – 4000 Hz, is an indicative of high second order cyclostationary and consequently, indication of fault in REB.

Figure 2-13 ‘Signal 1’ Simulated Outer Race Fault Spectral Correlation Color-map



Some quotations should be done respecting the Spectral Correlation estimator. The illustration worked on Figure 2-11 only intends to exemplify the principle of spectral correlation expressed in Equation 2-7, but the estimator for the Spectral Correlation has been subject to diverse discussion as has been synthesized by [34]. In Annex 9.1, the most common and useful estimators are listed.

## 2.4 Analysis of Square Envelope Spectrum.

To explore the concept of envelope function, and discuss it as a demodulation tool, let consider the analytic signal from  $x(t)$  as indicates Equation 2-8

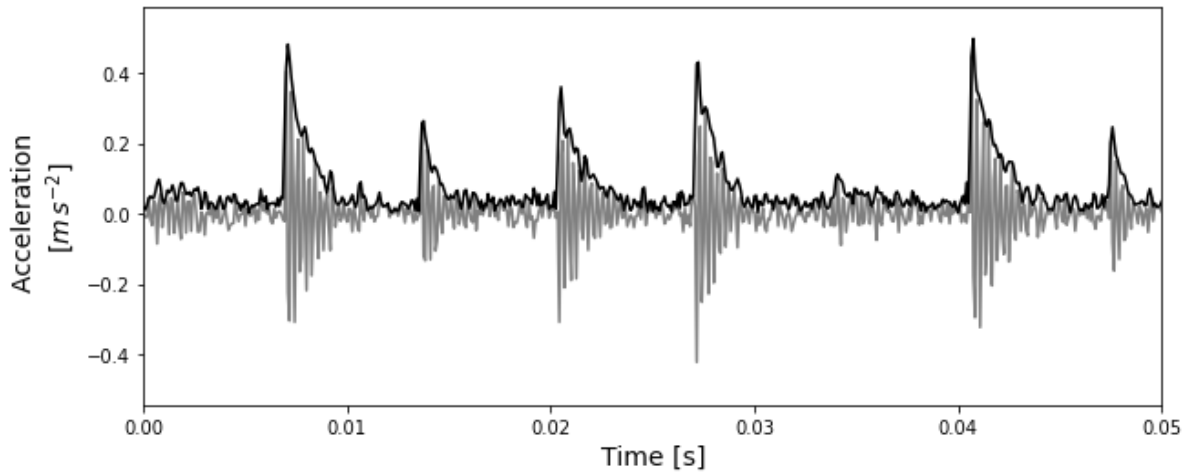
$$\text{Equation 2-8} \quad x_a(t) = x(t) + jx_h(t)$$

Where  $x_h(t)$  is obtained from taking Hilbert transform on  $x(t)$ . The analytic signal has the interesting property of having zero spectrum at negative frequencies. By taking the magnitude of the analytic signal, the envelope signal is obtained.

$$\text{Equation 2-9} \quad Env_x(t) = [x^2(t) + x_h^2(t)]^{\frac{1}{2}}$$

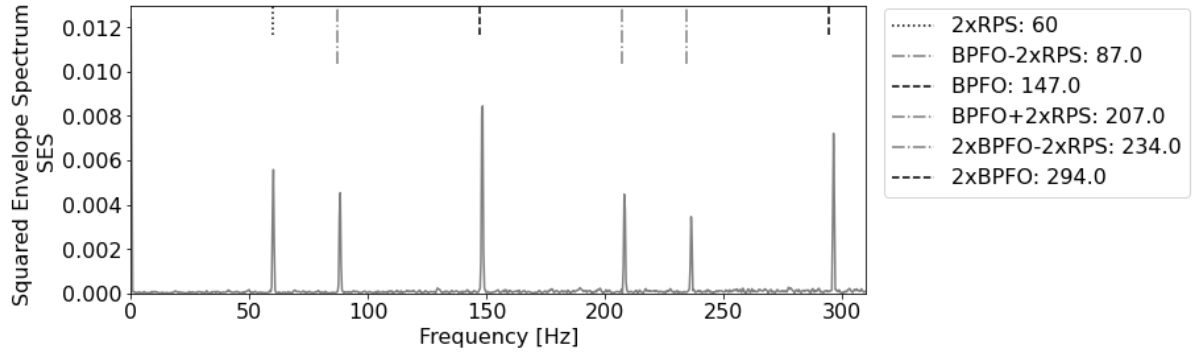
To illustrate the role of the envelope, consider again the simulated REB Outer Race fault signal, named 'signal 1'. The waveform is illustrated in Figure 2-14 (as previously zoomed in Figure 2-3). The black line represents the envelope of the signal, obtained as expressed in Equation 2-9.

Figure 2-14. simulated Outer Race Fault 'signal 1' Waveform



As it could be seen, the envelope is manner to demodulate the spectrum of original signal  $x$ , since the envelope draw the occurrence of impacts generated by contact with faulty surfaces. This in fact is the reason why the Envelope Spectrum Analysis is the most widely tool used for REB diagnosis. An important quotation should be mentioned, for smoothness in behaviour of spectrum, the Square Envelope Spectrum – SES is preferred rather the Envelope Spectrum. 'Signal 1' Square Envelope Spectrum is plotted in Figure 2-15.

Figure 2-15. 'Signal 1' Squared Envelope Spectrum

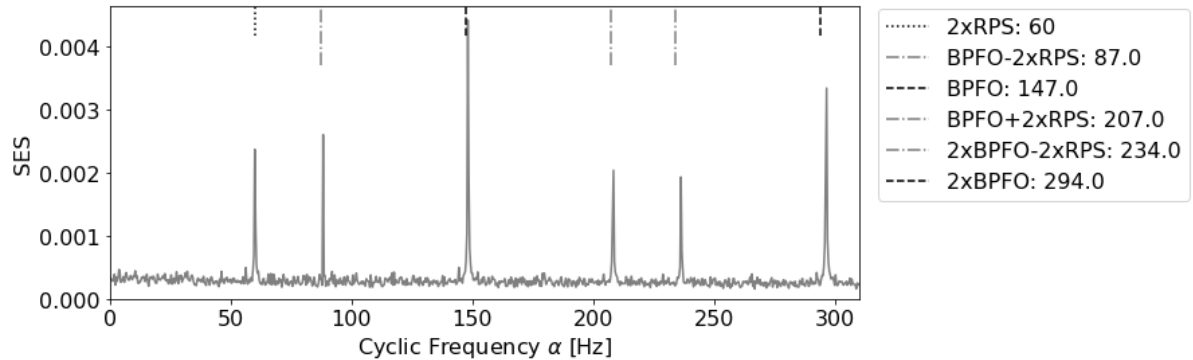


In fact, SES, could also be obtained from Spectral Correlation as it has been shown in. It is done by taking the average of SC over the spectral frequency  $f$  axis, i.e. integrating over the vertical direction in Figure 2-13. This idea is expressed in Equation 2-11, where  $F_s$  denotes the sampling frequency. Figure 2-16 illustrates the SES obtained from averaging the spectral correlation.

$$\text{Equation 2-10} \quad SES_x(\alpha) = \frac{1}{F_s} \int_0^{F_s} |SC(\alpha, f)| df$$

$$\text{Equation 2-11} \quad SES_x(\alpha; f_1, f_2) = \frac{1}{f_2 - f_1} \int_{f_1}^{f_2} |SC(\alpha, f)| df$$

Figure 2-16. 'Signal 1' Spectral Correlation averaging over spectral frequency axis.



### 2.4.1. Demodulation Band

Notorious similitude is evidenced in Figure 2-15 and Figure 2-16. This in fact was previously exposed in Figure 2-2, where both approaches ends up with the analysis of SES. In this particular case, there is clear evidence of high peaks at the Fault Characteristic Frequency, i.e. BPFO, indicating the presence of Outer Race in REB. However, the raw SES does not always reveal high peaks at the fault characteristic frequency, even if the fault has occurred.

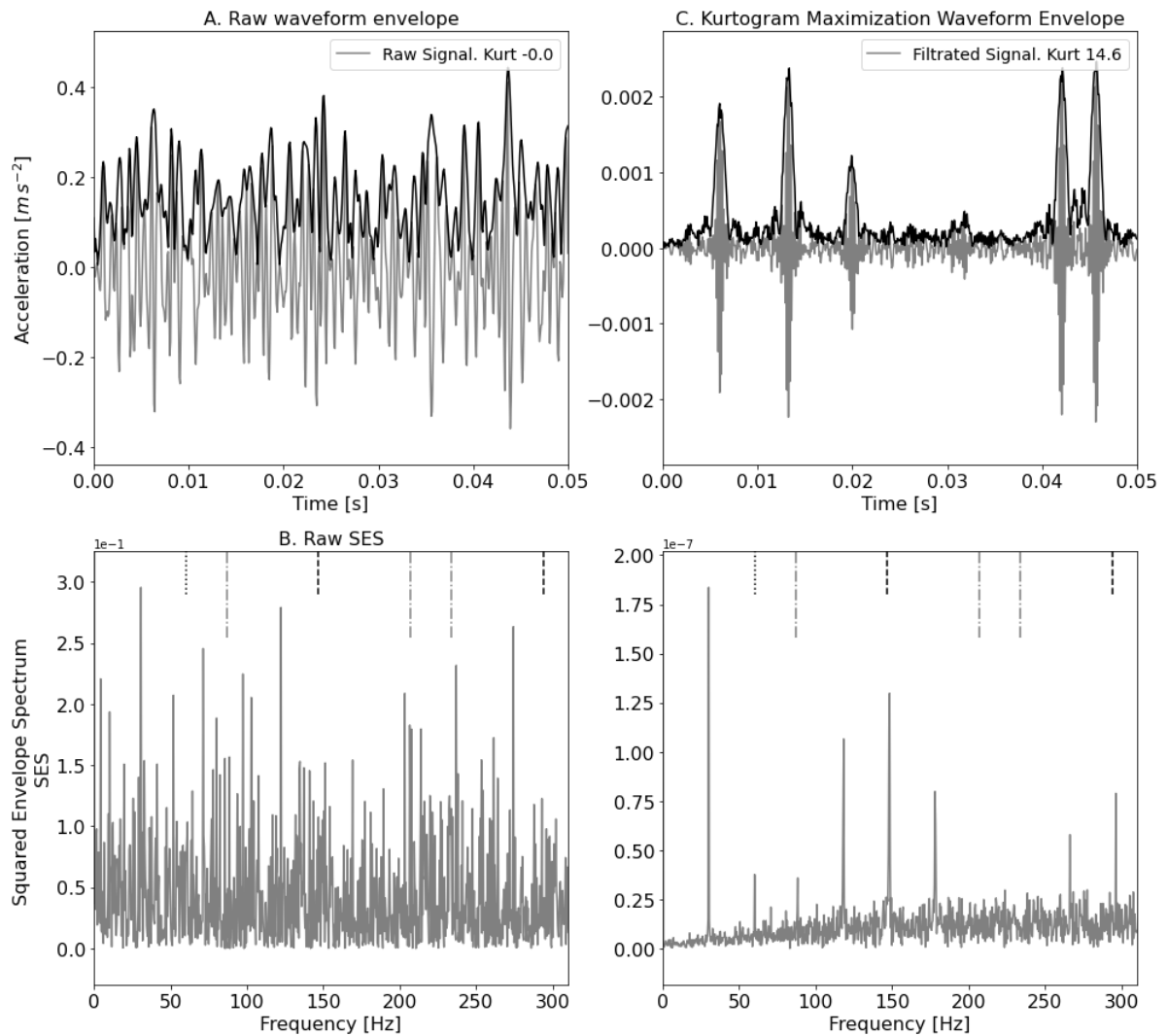
One way to improve the SES is to demodulate the signal. Whichever the two methods described in Figure 2-2, contemplates this procedure. In the called benchmark method, demodulation is done by

---

the use of Kurtogram, previously discussed in section 2.2. By the use of the Kurtogram is possible to determine the most useful filter bandwidth in which kurtosis is maximized, i.e. the one which maximizes the signal impulsivity. To exemplify this, consider the simulated Outer Race Fault signal named 'Signal 2', which was previously illustrated in gray tone in Figure 2-3. The raw envelope is illustrated in Figure 2-17-A. Their corresponding raw SES is shown in Figure 2-17-B, the cursors shown are set as in legend of Figure 2-15. By visualizing the SES, does not result possible to diagnosis an Outer Race Fault, since there is no evidence of markable peaks in the at the BPFO (Black-dotted lines). The reason of this particular case is explained because originally 'Signal 2' is highly corrupted by colored noise, further explained by its near zero kurtosis, as discussed in Figure 2-3.

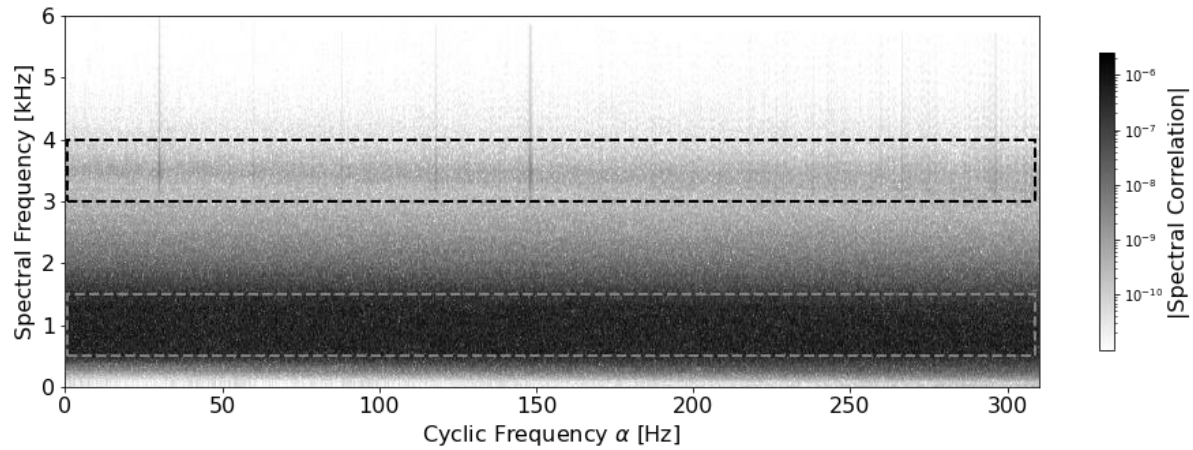
By the use of fast Kurtogram (Not illustrated for 'Signal 2'), is possible to determine the optimal kurtosis bandwidth is estimated in the range of 5004 - 6000.0 Hz. By filtering the signal using a linear FIR filter, the waveform shown in Figure 2-17-C is obtained. As it is illustrated, the kurtosis of filtered signal is highly increased in comparison with the kurtosis of raw signal, reaching a numerical value of 14.6. The demodulated waveform, shown a typical pattern of REB fault, characterized by periodical impacts, where periodicity is governed by fault characteristic frequency BPFO, as further shown in the SES of Figure 2-17-D. In this latter figure, noticeable peaks are reached at BPFO and sideband modulations around the shaft speed rotation in revolution per second (cursors set as in Figure 2-15).

Figure 2-17. Simulated Outer Race Fault 'Signal 2' Kurtogram demodulation.



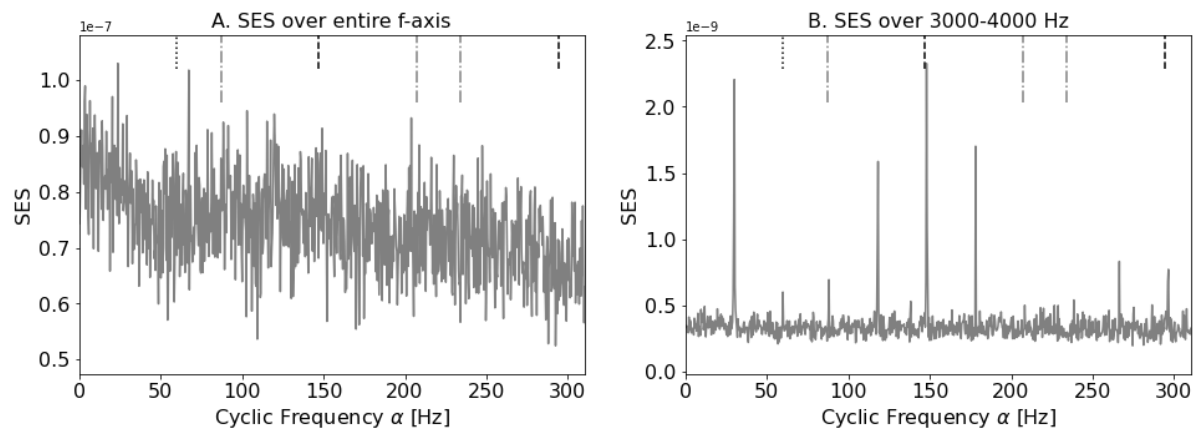
Similarly, SES could also be obtained by averaging the Spectral Correlation over the spectral frequency axis. However, a demodulated SES, could be obtained if the range of frequency being averaged is selected, as expressed in Equation 2-11. By selecting a correct demodulation band, clear symptoms of its second order cyclostationary at the specified Fault Characteristic Frequency, i.e. REB fault symptoms, could be evidenced. To exemplify this idea, consider the Spectral Correlation of simulated outer race fault 'Signal 2', shown in Figure 2-18 (Note the log-scale).

Figure 2-18. Simulated Outer Race Fault 'Signal 2' Spectral Correlation



In the range of 500 - 1500 Hz (Grey dashed rectangle), a high spectral density is evidenced. However, there in this region there is no vertical lines pattern, which indicates there is no evidence of second order cyclostationary. This high spectral density is product of the colored noise corruption intentionally added to 'Signal 2'. However, in the range of 3000 – 4000 Hz (Black dashed rectangle), notorious vertical patterns are evidenced. This is even more clear by consider the SES shown in Figure 2-19-A<sup>1</sup>, where the SC is averaged over the entire spectral frequency axis, i.e. 0 – 6000 Hz. In the SES there is no evidence of peaks at BPFO. In contrast, consider the SES averaged over the range 3000 – 4000 Hz shown in Figure 2-19-B. In this latter figure, clear evidence of Outer Race REB fault is evidenced, in a similar manner than exposed in Figure 2-17-D.

Figure 2-19. Simulated Outer Race Fault 'Signal 2' Spectral Correlation Demodulation



<sup>1</sup> Cursors are set as Figure 2-17



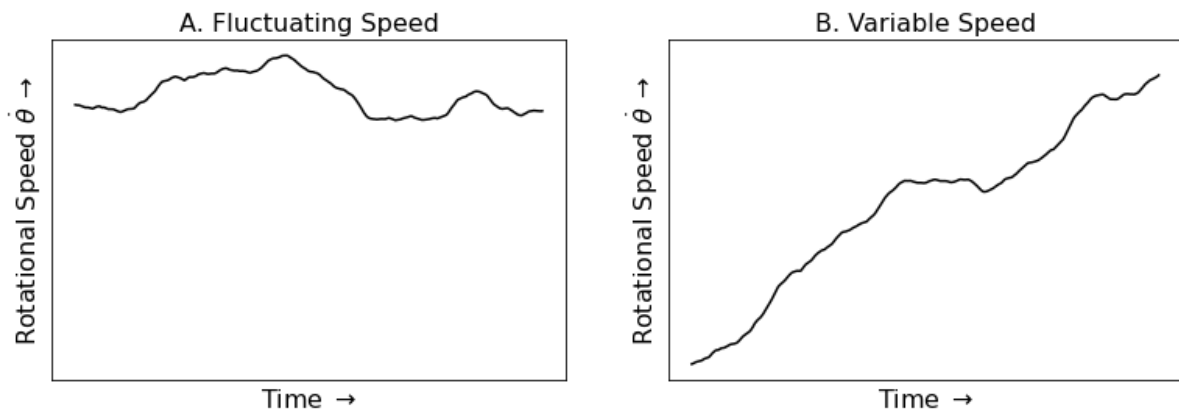
## 2.5 Variable Speed Order Tracking

As discussed, the periodicity of occurrence of impacts generated by REB fault are linked to angular shaft position, while the transient vibration at impact moments depends mainly to time domain. If angular speed is constant, this duality is straightforward managed, because direct and proportional relation between angular domain and time domain, as has been managed until now. However when rotational speed do not keeps constant, approaches to solve this duality are necessary to achieve a correct SES analysis, i.e. achieve a correct diagnosis.

Let classify the variable rotational speed in two categories. The first one, illustrated in Figure 2-20-A, occurs when rotation speed keeps nominally constant, but suffer fluctuations, mainly due to slippage, randomness, load changes, etc. As rotational fluctuations do not exceed 20% (1:5 relation) [35], is possible to assume that vibrational response could be analyzed entirely in angular domain. This implies that, by expressing the vibrational response in angular domain is possible to use the techniques previously exemplified to manage REB diagnosis.

Consider the second variable rotational speed case, in which the speed changes their numerical nominal value, as occurs in a run-up case, for example. In this case, illustrated in Figure 2-20-B, the linkage between angle dependence and time dependence should be considered as would be described in section 5.1.

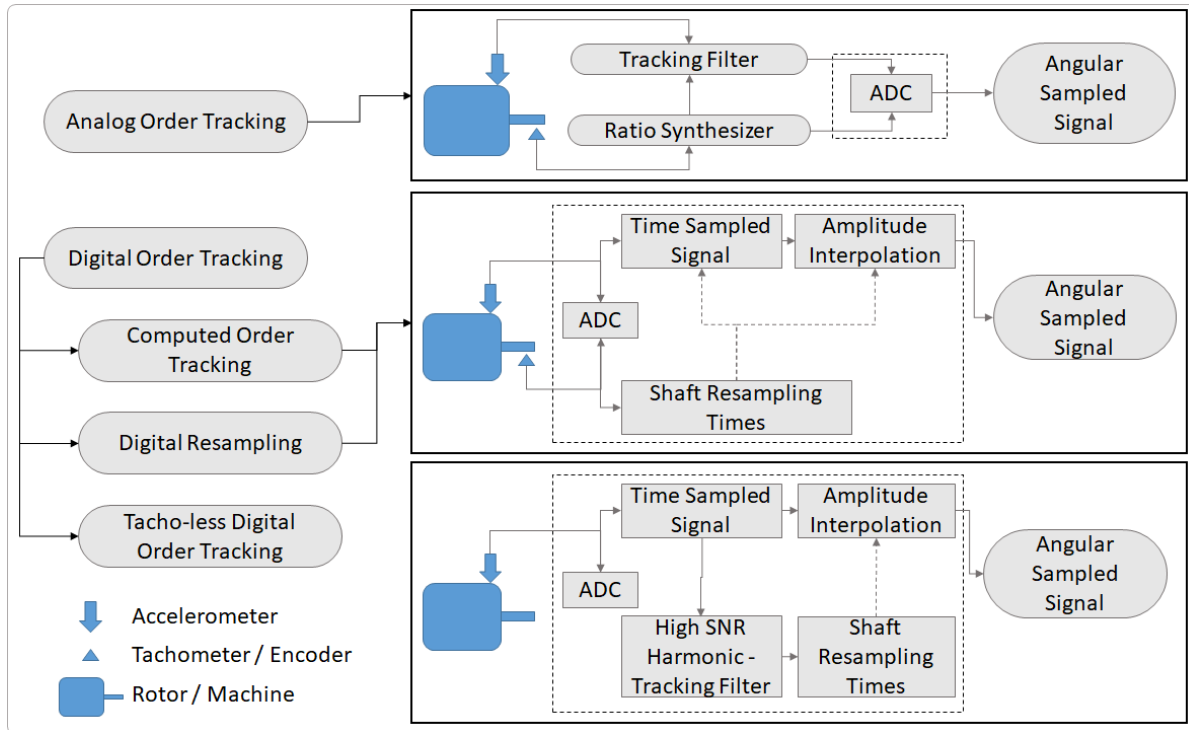
Figure 2-20 Variable Speed Conceptualization.



### 2.5.1. Order Tracking Approaches

In both variable rotational speed cases, illustrated in Figure 2-20, do result imperative get the angular position, rotational speed and vibrational response as function of angular position. By tracking the spectrum of vibrational response as function of orders, which is the equivalent to frequency in angular domain (measured in event per revolution), the smearing of synchronous components in vibrational response could be avoided. This process has been named Order Tracking in literature. Usually, Order Tracking relies on the use of different approaches, which are briefly illustrated in Figure 2-21.

Figure 2-21 Illustration for Order Tracking Approaches



The analog order tracking is the oldest approach. Consists in governing the sampling periods with a key-phasing signal, which generates a synchronous pulse, each time the shaft position rotates a constant angle. The sampling system then reads the numerical voltage of vibration sensor, generating a signal sampled at equally spaced angular positions. This procedure however does not result totally synchronous, since the lapses time between governing signal and sampling the sensor voltage could lose information about random speed fluctuations. The use of analog devices would result in costly devices and their use is fairly limited when there is no physical access to the rotor or the shaft to be tracked.

Second approach, takes advantage of digital signal processing. The idea is to sample (at equi-spaced times, as usual) the signal of vibration sensor and the signal generated by a tachometer or shaft encoder. This latter allows knowing the angular shaft position sampled in time domain, and so, does result possible to estimate the vibrational response at equally spaced angular periods. This approach is usually referred as Digital Order Tracking, and since the evolution of digital systems, is the most common used approach.

Digital Order Tracking techniques could be categorized in two approaches, Computed Order Tracking, and Digital Resampling Method. Although apparently both techniques are apparently equivalent, the procedure is slightly different.

- *Computed Order Tracking - COT:*

In Computed Order Tracking –COT, is done with the aid of a tacho or shaft encoder and the usual accelerometer. Both signals, generated by accelerometer and tacho are sampled

simultaneously at constant times, as usual in common ADC system. By the signal sampled on the shaft encoder, is possible to determine the time in which shaft rotation advances by the encoder ratio ( $\Delta\theta$ ). As it is illustrated in Figure 2-22.

Figure 2-22 Theoretical Tacho Encoder Signal for Increasing Rotational Speed

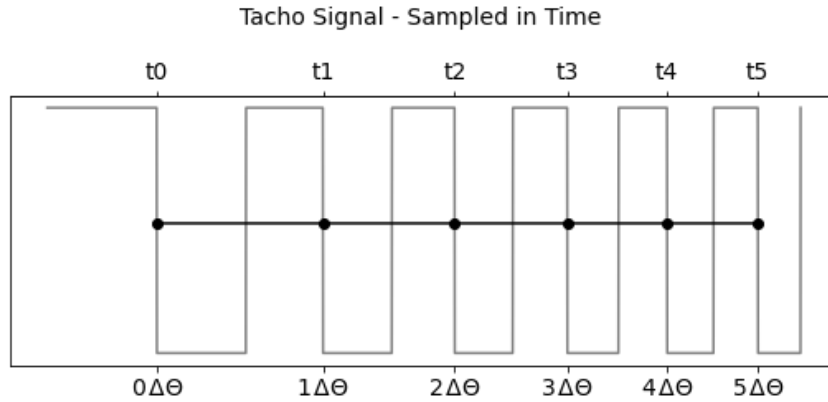


Figure 2-22 illustrates the usual tacho waveform when speed is variable. In this illustration, the width of pulses is decreasing indicating the rotational speed increases. The “circular marks” indicate the time arrivals at which shaft advances the angular position dictated by the resolution of tacho ( $\Delta\theta$ ). Knowing three consecutive time arrivals, does result possible to estimate a quadratic polynomial which interpolates angular position with time. This is illustrated in Equation 2-12 and Equation 2-13.

$$\text{Equation 2-12} \quad \theta^{<i>}(t) = b_0^{<i>} + b_1^{<i>}t + b_2^{<i>}t^2$$

Where  $\theta^{<i>}(t)$  indicates the angular position as function of time, in the interval which lies in  $[0.5i\Delta\theta ; 1.5i\Delta\theta]$ . The coefficients  $b_0, b_1, b_2$  are determined between three consecutive sections by solving the equations shown in Equation 2-13.

$$\text{Equation 2-13} \quad \begin{bmatrix} (i-1)\Delta\theta \\ i\Delta\theta \\ (i+1)\Delta\theta \end{bmatrix} = \begin{bmatrix} 1 & t_{i-1} & t_{i-1}^2 \\ 1 & t_i & t_i^2 \\ 1 & t_{i+1} & t_{i+1}^2 \end{bmatrix} \begin{bmatrix} b_0 \\ b_1 \\ b_2 \end{bmatrix}^{<i>}$$

Determining angular position as function of time, it is also possible to establish the time as function of angular positions. This could be estimated by the use of Equation 2-14.

$$\text{Equation 2-14} \quad t_k^{<i>} = \left[ \frac{1}{2b_2} \left( \sqrt{b_1^2 - 4b_2(\theta_k - b_0)^2} - b_1 \right) \right]^{<i>}$$

By taking a series of  $\{\theta_k\}$  equally sampled, do result possible to interpolate the vibration amplitude and so completing the COT process. This final step is easily done by the use of cubic splines. The COT process is detailed discussed in [1], [36].

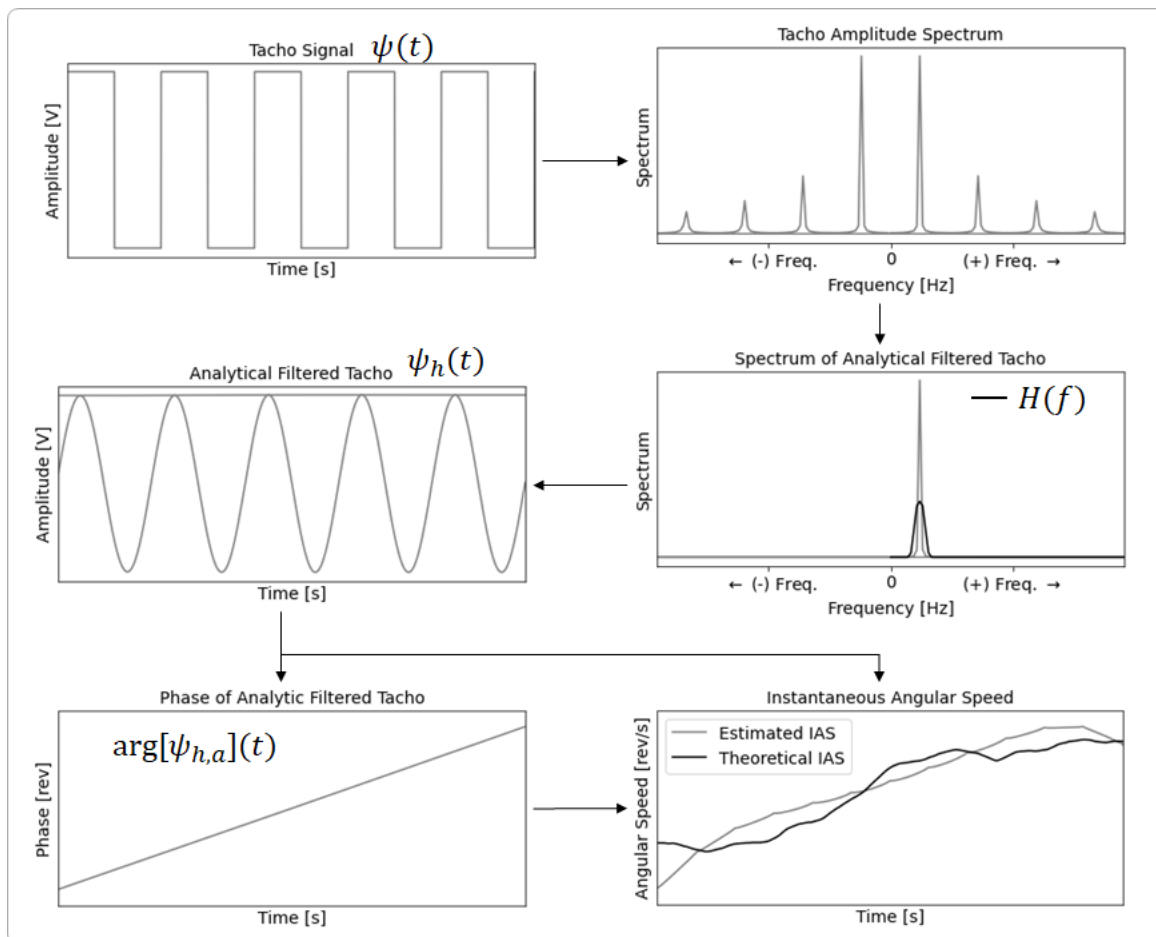
- *Angular Digital Resampling:*

This approach is quite similar to COT, however a difference should be remarked in the process. In Digital Resampling the tacho signal is not used to estimate the angular positions, but is used to

estimate the instantaneous angular speed  $-IAS$  curve. From the angular speed, the angular position curve is determined (easily made by integration over time). With angular position as function of time, is possible to determine the interpolation times, i.e. time instants at which angular increments results constant. On the other hand, the vibration signal (sampled in time) is Up-sampled, to increase time resolution. With the Up-sampled signal, the amplitude interpolation is achieved. To finish the order tracking process, a down-sampling process is done in order to reduce unusable computational cost. Up-sampling and Down-sampling process should be companied low pass-filter to avoid aliasing. This process is further discussed in [37].

In the Digital Resampling Order Tracking, the Phase Demodulation Approach should be highlighted. Phase demodulation has been reported as a valuable tool for Order Tracking, and is maybe the most used technique to determine the instantaneous angular speed [5]. Phase demodulation relies on extracting the phase of the first harmonic in the tachometer signal. Precisely, it extracts the phase of first harmonic for analytic tacho signal. From the phase extracted, a curve for angular position vs time is build and afterwards is used for determining the times to resample, such signal result sampled at constant angular increments [35]. Phase demodulation process is briefly illustrated in Figure 2-23.

Figure 2-23 Phase demodulation illustration



Phase demodulation process starts with the tacho signal sampled in time  $\psi(t)$ . By the analysis of their spectrum, the first harmonic is selected. Then a filter centered in the first harmonic is built ( $h(t)$ ). The bandwidth of the filter should not exceed the  $\pm 20\%$  of nominal center frequency, since filter could overlap with modulation side-bands or even higher harmonics. After the tacho signal is filtered ( $\psi_h(t)$ ), their analytic version is taken ( $\psi_{h,a}(t)$ ), i.e. one side spectrum is built. This step could be done by taking Hilbert transform on filtered signal as defined in Equation 2-15.

$$\text{Equation 2-15} \quad \psi_{h,a} = \psi_h + j\mathcal{H}[\psi_h]$$

where the sub-index  $h$  and  $a$ , denote the filtered version and the analytic version,  $j$  denotes the imaginary part and  $\mathcal{H}[\cdot]$  denote the Hilbert Transform.

From the analytic filtered, does result possible to extract the phase, which could be seen as the angular shaft position. At the same time, from the phase derivative, the instantaneous angular speed could be estimated, as exposed in Equation 2-16 and Equation 2-17.

$$\text{Equation 2-16} \quad \theta = \arctan\left(\frac{\Im[\psi_{h,a}]}{\Re[\psi_{h,a}]}\right)$$

$$\text{Equation 2-17} \quad \dot{\theta}(t) = \frac{1}{2\pi} \frac{d\theta}{dt}$$

Does result important to annotate that correction from the quadrant on the use of  $\arctan(\cdot)$  function should be taken. Also the unwrapped phase should be use when estimating instantaneous angular speed, i.e. when the phase derivative is taken.

- *Tacholless Digital Order Tracking*

In some situations, the use of tachometer or shaft encoder would require a physical access to desired shaft, increase the cost of acquisition system, or simply would be incompatible with operational conditions such as dust, humidity or high temperatures. Even so, in many practical situations, Order Tracking is a fundamental part of vibration monitoring. Recently high interest has been focus on achieve order tracking by using the vibrational response itself instead of using an external reference tacho. Tacholless order tracking could be applied where synchronous components are clearly separated from the main signal, i.e. synchronous orders and their harmonics are strong enough in the signal.

Tacholless order tracking could rely on diverse principles, such as, Time-Frequency representation, Adaptive filters harmonics Tracking, Multi-harmonics Time-Frequency representation, Probabilistic methods, Phase demodulation, Data-driven methods, among others [5], [38], [39]. Particularly, results interesting to discuss in brief detail the Multi Order Probabilistic Analysis –MOPA and the Phase demodulation approach.

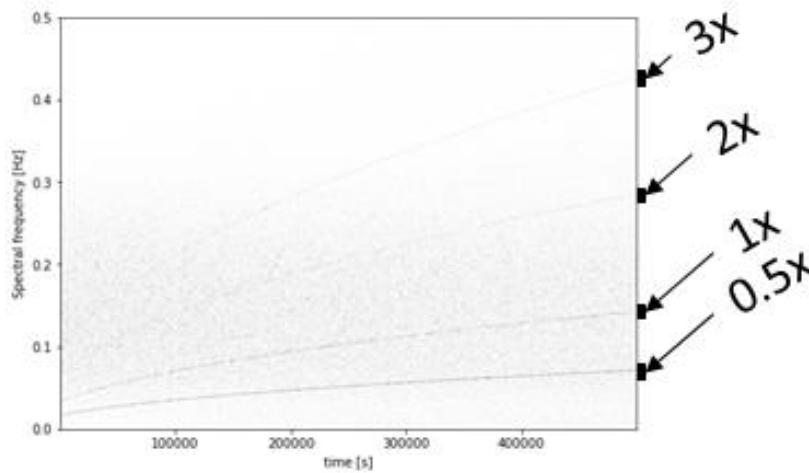
- *Multi Order Probabilistic Analysis.*

This approach results advantageous when a complex system with multiple harmonics is intend to be analyzed. Whereas many of Tacholless order tracking approach require that the user select the correct harmonic to be tracked, MOPA approach try to use the big part of synchronic harmonics available information, avoiding the user necessity to select the suitable harmonic. This approach build a

probability distribution function from the time frequency representation, as for example the classical Short Time Fourier Transform –STFT.

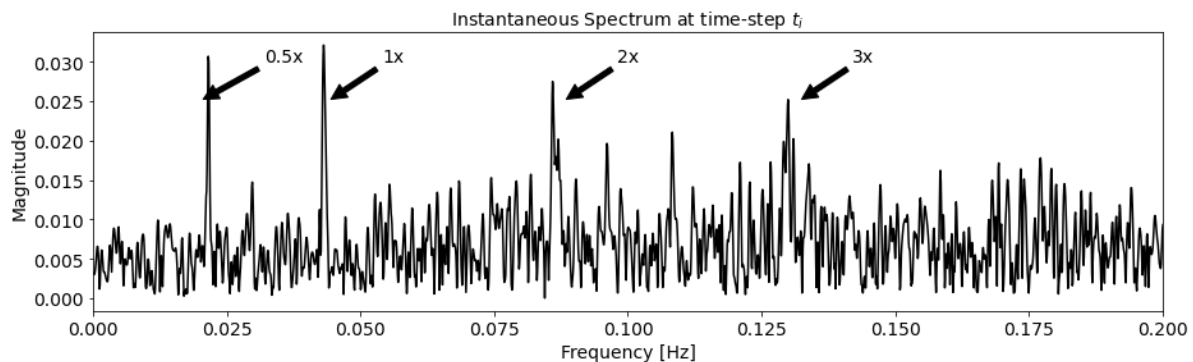
In this section the concept behind MOPA approach would be illustrated, however the detail would not be covered but could be found in the original paper [40]. Let consider the spectrogram shown in Figure 2-24. This signal was built by adding a colored noise with spectral content in the bandwidth [0.05 ; 0.25] Hz with a series of Synchronus harmonics with variable speed.

Figure 2-24. Simulated Spectrogram for illustration of MOPA



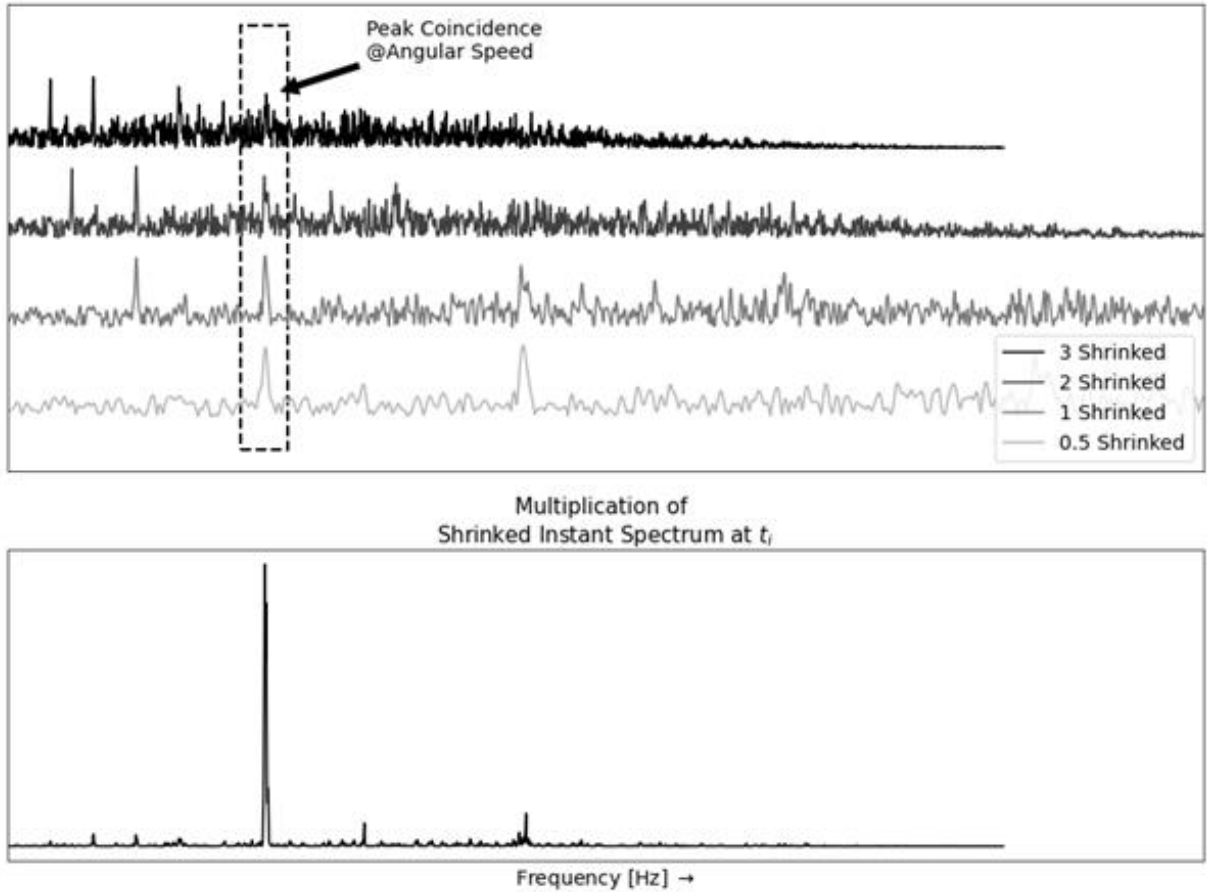
Consider now the frequency magnitude spectrum at some time step  $t_i$ . If the signal to noise ratio of each Synchronus component is considerable high, a clear peak at the corresponding harmonic would be noticeable, as illustrated in Figure 2-25.

Figure 2-25 Instantaneous Spectrum at time step  $t_i$



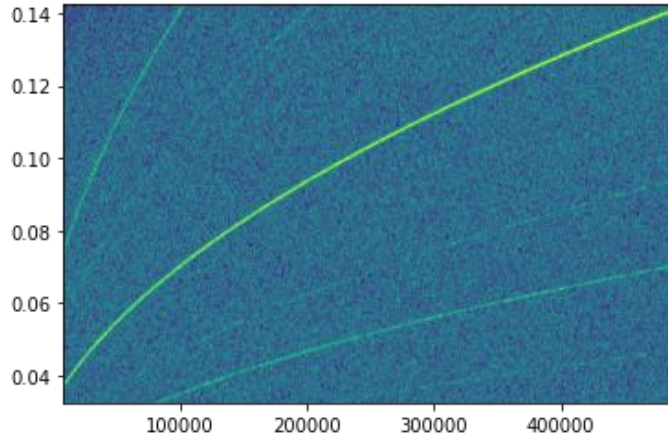
Consider a set of order harmonics  $\{H_i\}$  as for example illustrated in Figure 2-25,  $\{0.5, 1, 2, 3\}$ . If the magnitude spectrum is shrunk by each  $H_i$ , a coincidence of peaks at 1X is expected. This is illustrated in Figure 2-26. Given the coincidence of peaks at the corresponding synchronous frequency (1x), if the multiplication of those shrunk spectrum is computed, a high peak is expected as illustrates the bottom part of Figure 2-26.

Figure 2-26 Shrunk Instantaneous Spectrum under the harmonics set H.



Now, if the process illustrated above is made upon all the time steps, a time-frequency distribution is obtained, where the synchronous 1x curve should be highlighted. This time frequency representation could be seen as the evolution of probability distribution function –pdf, for angular speed at each time step, and finally, instantaneous angular speed could be computed by tacking the expectancy in such probability distribution function. Time-frequency probability density is illustrated in Figure 2-27.

Figure 2-27. Probability distribution map for instantaneous angular speed



A note of caution should be made at this point. To build the mentioned probability distribution function, a series of steps and mathematical rigor is needed. For example, normalization should be made prior to shrunk spectrums multiplication in order to guarantee the resulting representation will represent a probability. Additionally, a pre-whitening step is recommended in order to avoid distortions in the resulting pdf. Another important point is to pre-select the maximum frequency to be analyzed avoiding interferences with different spectral contents. All those details should be carefully taken into account and are clearly defined and explained in the original paper. The reader should be free to consult the original paper [40].

## 2.6 Variable Speed Bearing Diagnosis State of Art

Through sections 2.1 to 2.4 a series of algorithms and techniques related to REB diagnosis are described. However, the REB diagnosis under variable speed suffer from different aspects worth to mention.

As previously discussed, a simplistic model for REB- fault could be modeled as illustrated on Equation 2-18. The vibrational response for a REB result from the response of a LTI system, until the excitations generated periodically on angular domain.

Equation 2-18 
$$x = h(t) * f(\theta)$$

In this sense, to achieve an adequate diagnosis, three aspects could result important. The first one, as described in section 2.5, is the capability of identify a precise order tracking. The Order Tracking, and the estimation of accurate instantaneous angular speed becomes an edge for REB diagnosis under non-stationary conditions. As previously discussed, Tachless order tracking are become the most investigated approach. In such way, techniques such as MOPA and Phase Demodulation becomes extremely useful for. However, as limitation of such techniques are related to large speed fluctuations and crossing orders in time frequency representation.



The discrete-random separation process is also an important part of the REB diagnosis. REB fault generates vibrational responses characterized by the random occurrence of strikes. Thus, the deterministic components speed should compromise the SES and the ability of achieve REB diagnosis. Deterministic components are usually associated with gearboxes, misalignments, unbalance, etc., synchronized with shaft speed orders and their respective harmonics, the table below list some of the resent algorithms developed to achieve DRS.

Table 2-3. State of art strategies for discrete random separation

Author	Method	Description	Advantage	Disadvantage
Abboud 2016 [41]	GSA – Generalized Synchronous Average	It takes Synchronous Average at defined rotational speed regimes	Captures large fraction of energy on discrete components energy.  Synchronous components are almost removed from blind.	Unstable at lower rotational Speed.  Inability to separate discrete components present on time representation (such as PWM switching frequency)
Borghesani 2013 [42]	CEPSTRUM Prewhitening.	Removes quefrencies different from zero and utilize it as a whitening factor.	Facilitates the demodulation band selection.  There is not hyper-parameters involved	Limited to fluctuating speed cases.
Bonnardot 2004 [3]	E-SANC	Estimate the deterministic part of a signal by using a Self Adaptive filter after doing angular resampling.	Easy implementation	Filter function is mainly defined in time domain but does not track variations in angular domain.

As the last point, a correct way to obtain the SES should be consider. The focus should be pointed on the way that allows demodulating the signal in spectral frequency domain, in such a way the periodicity of fault contact strikes could be observed on order domain. The table below summarize the strategies most useful (According to author point of view).

Table 2-4. State of art for obtaining Squared Envelope Spectrum SES.

Author	Method	Description	Advantage	Disadvantage
Abboud 2015 [43]	OFSC-ACP	It is defined as the double Fourier transform on auto-correlation function. Is an extension of Spectral Correlation but taking one of the Fourier transforms on angular domain.	Captures the information related to time domain and angular domain in a correct manner.	Computational cost.  Dependent on selection of hyper parameters
D'Elia [44]	OFSC - CMS	It is defined as the double Fourier transform on auto-correlation function. Is an extension of Spectral Correlation but taking one of the Fourier transforms on angular domain.	Straightforward to select frequency demodulation bands  Low computational Cost	Limitation in the amount of order to be analyzed
Smith 2015 [45]	Benchmark-method extended	Filter the signal as dictated by Kurtogram on time domain. Followed by Hilbert transform SES		Kurtogram could raise to miss-interpretation of demodulation bands
Berntsen 2022 [46]	Demodulation based on OMA Analysis (Operational Mode Analysis)	Filter signal according to the pre-captured resonance frequencies		Implies prior characterization of all bearings to be diagnosed.

Mauricio 2022 [47]	Generalization of indicators of cyclo-nonstationarity			
Mauricio 2020 [48]	IESFOgram demodulation	Represent the IES as function of frequency bands, in a 1/3-binary tree for maximizing a metric	Improves demodulations.  Allows getting convenient IES for a desirable fault characteristic order	The metric proposed does not evaluate the behaviour of IES but the magnitude at desired Fault characteristic order.

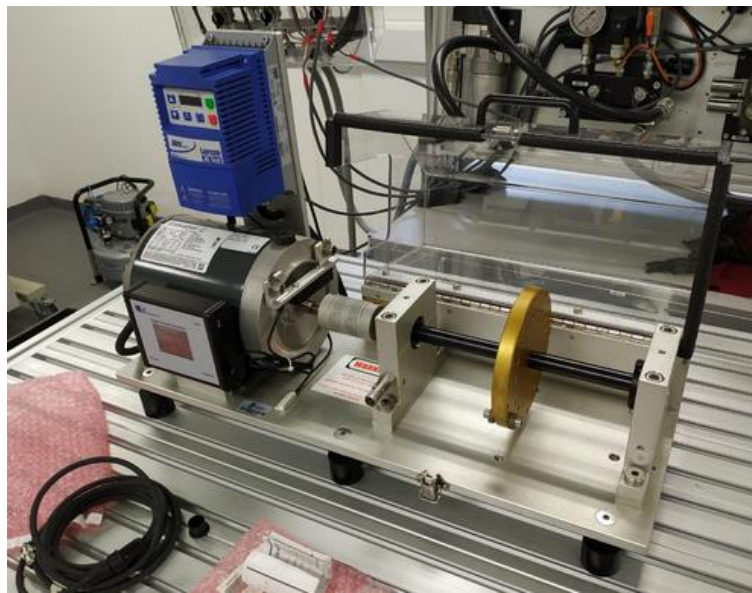
In the literature described in this section, it is not exposed a structured method that explicitly integrates the algorithms available for REB diagnosis in the case of variable speed conditions. It was also difficult to find a clear guide for the tuning of the parameters implied at each one of those algorithms. In this sense, the idea exposed in section 4 tries to structure some of the algorithms available and bring an explanation for the parameter selections. A method for demodulation is also exposed in section 4. From the author's perspective, the demodulation strategies could be susceptible to improvements.

Finally, according to the literature search, it is not usual to find classification algorithms based directly on the Improved Envelope Spectrum –IES (Or the similar version Improved Envelope Order Spectrum). The use of IES as the input for a classification algorithm rises as an interesting strategy, of the great understanding it brings about the vibrational response and could be interesting for the generalization of classification algorithms.

### 3. Experimental Setup

Experimentation was conducted on Test-Rig SpectraQuest Bearing Balance Fault Simulator BBFS, system shown in Figure 3-1. BBFS system consists of a 0.5 HP three phase induction motor with VFD-Lenze ESV251. The motor is coupled to a 5/8” diameter steel shaft, supported on two REB, with a span of 400 mm. In the middle of the span, a rotor of 5 kg weight is fit. Bearings with pre-fabricated faults are originally installed. The faults were generated by the use of electro-erosion methods. Commercial reference for bearing are Rexnord ER-16K.

Figure 3-1. Test Rig



Vibrations on horizontal and vertical direction were sampled in both REB pedestals. Signal were record using a NI9234 DAQ with a sampling frequency of 52 kHz. REB fault characteristic order are as indicated by Table 3-1.

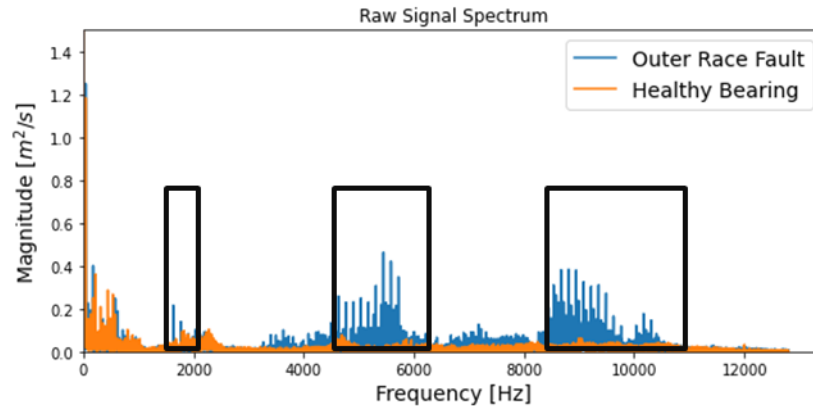
Table 3-1 Fault Characteristic Orders

<b>REB COMMERCIAL REFERENCE: Rexnord ER-16K</b>		
	<b>ABBREVIATION</b>	<b>FAULT CHARACTERISTIC ORDER</b>
Inner Race	BPOI	5.430
Outer Race	BPOO	3.572
Rolling Element	BSO	2.322
Cage	FTO	0.402

### 3.1 Rolling Element Bearing Characterization

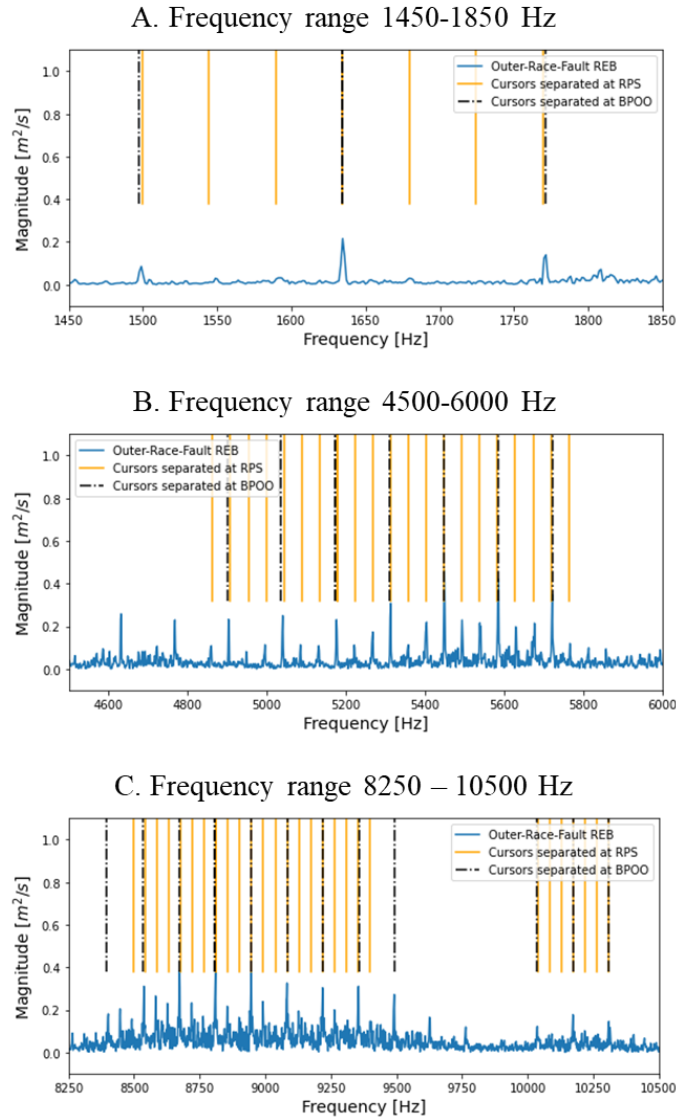
In order to achieve a first characterization of the vibrational response, the vibration signal measured in the motor-side pedestal for a Healthy bearing and a Bearing with Outer-Race induced fault are compared. The rotational speed keeps nominally constant at 45 Hz and both measured are taken with the same charge. The magnitude spectrum of both cases is illustrated in Figure 3-2.

Figure 3-2. Magnitude Spectrum Raw Vibration Response.



It results notorious the rise in spectral energy contained in the range of 4500 – 10500 Hz, as it has been highlighted on Figure 3-2. This effect can be seen with more detail in Figure 3-3 where the magnitude spectrum is zoomed in regions between 1450-1850 Hz, 4500 – 6000 Hz and 8250 – 10500 Hz. In the 4500 – 6000 Hz and 8250 – 10500 Hz regions, the spectrum reach peaks at frequencies equally spaced by entire multiples of the rotational speed – RPS. This behaviour is marked by the Orange-continuous cursors.

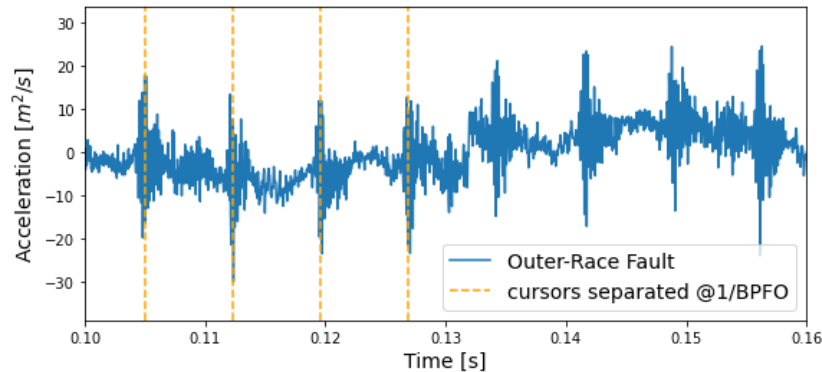
Figure 3-3 Modulations in resonance regions for Outer Race Fault REB 1450-1850 Hz.



It results of particular interest the peak raised at 1634.4 Hz illustrated in Figure 3-3-A, since similar test rig has been reported with REB resonance at 2000 Hz [49]. However, there is no clear evidence of harmonics multiples of this discrete frequency. According to this reasoning, the understudy REB appears to have resonance frequencies in some of the ranges marked previously discussed.

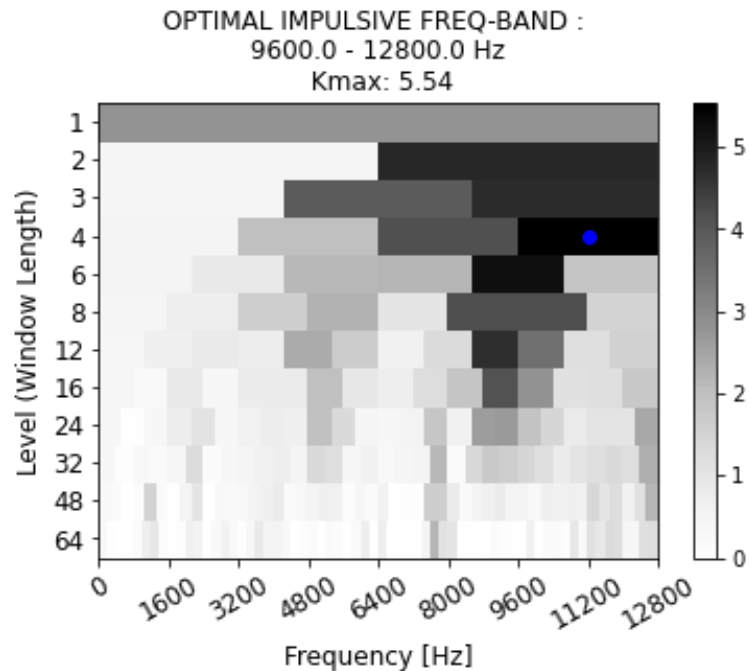
This is clarified if the waveform of the vibrational response is analyzed as it illustrated in Figure 3-4. The waveform is composed by a series of vibrations generated by the contact of the outer race fault surface and the rolling element, generating an impact on the REB body. Those impacts occurs periodically according to the fault characteristic order (or similarly called Fault Characteristic Frequency). Clearly, it indicates that the strong modulations occurring in the high frequency ranges, previously analyzed in Figure 3-3, are explained by the contact of surface faults.

Figure 3-4. Outer-Race Fault waveform.



Although results evident the presence of high impulsivity modulated at the Fault Characteristic Order BPOO, the focus in this section is to characterize the spectral behavior of the REB. For this reason, it results important to determine in which of the frequency range belong the most impulsive frequency i.e. tend to determine which is the most probable resonance frequency band excited by the shocks generated by fault surfaces contact. To explore this, consider Figure 3-5, which illustrates the fast Kurtogram. This is a representation of the spectral kurtosis by using a binary-three representation. This representation allows for identifying the band in which the most impulsive noise is generated.

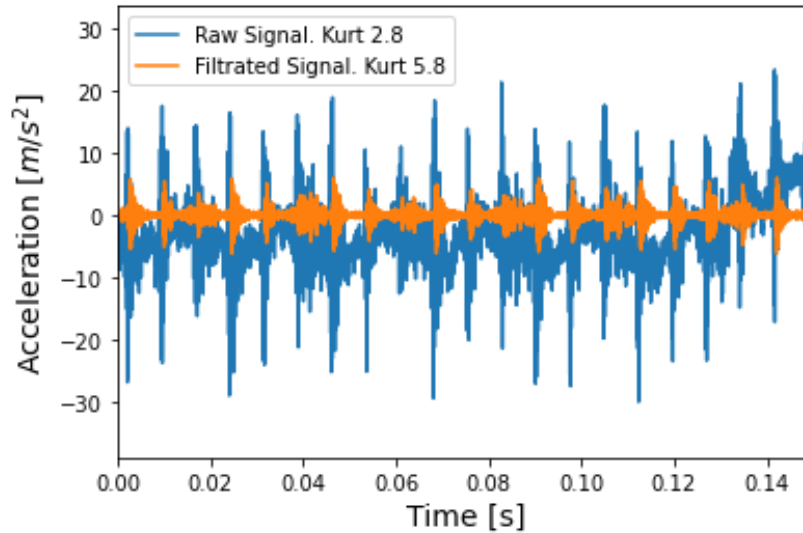
Figure 3-5. Outer Race Faulty Bearing – Kurtogram.



According to fast Kurtogram representation, the most impulsive bandwidth belongs to 9.600 – 12800 Hz. This is in accordance with the magnitude spectrum previously discussed. To discuss in more detail this, consider Figure 3-6, which plots the raw signal waveform and the waveform of the signal

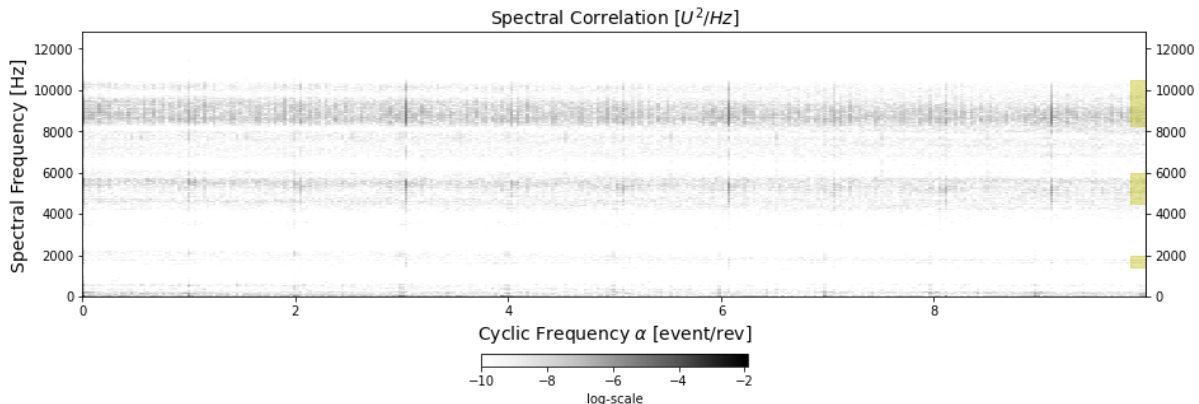
filtered at the maximum kurtosis bandwidth. As can be seen, the filtered signal shows a more impulsive behavior, dictated mainly by the occurrence of fault surfaces contact. This in fact is emphasized by the kurtosis descriptor of this second case.

Figure 3-6. Raw signal vs Kurtogram filtered signal waveforms.



The spectral content of the signal is also shown in the bi-spectral map shown in Figure 3-7. It displays the spectral correlation of the faulty outer race REB as a function of the spectral frequency  $f$  (Vertical axis expressed in Hz) and the cyclic frequency  $\alpha$  (Horizontal axis expressed in orders). The span cursors in the right part of the figure illustrate the spectral frequency bands analyzed previously in Figure 3-3. In those ranges, a notorious increase in the spectral correlation is raised. In the figures, a vertical line pattern is also notorious, especially in the cyclic frequencies  $\alpha$  equivalent to BPOO (nearest to  $3x$  rotational speed harmonic). The beforehand described behavior indicates the signal presents high cyclostationarity in the band selected, reinforcing the hypothesis of finding spectral resonance in those ranges.

Figure 3-7. Spectral Correlation for Outer Race Fault Bearing





## 3.2 Test Rig Critical Speed

In this section, a pre-characterization of the test-rig is achieved. This is done by a simplified model and is also verified by a transient speed run-up vibration analysis. Both results are presented separately.

### 3.2.1. Critical Speed Model Estimation

Considering the overall equivalent lumped mass on a simply rotor, located at the center of the shaft. The critical speed is dictated by Equation 3-1.

$$\text{Equation 3-1} \quad \omega_c = \sqrt{\frac{g}{W_{TL}\delta_{cc}}}$$

Where  $\delta_{cc}$  represents the influence coefficient of a load located at the center of the rotor, in the deflection measured at the center of the rotor. For a simple supported rotor, it is determined according to Equation 3-2.

$$\text{Equation 3-2} \quad \delta_{cc} = \frac{\frac{L^4}{8}}{6EIL} = \frac{L^3}{48EI}$$

The  $W_{TL}$  stand for the total equivalent lumped weight, which results as an equivalent load located at the center of the rotor. For this particular case, the rotor weight is located at the center of the shaft, with a numerical value of 5kg. The terms of Equation 3-2, are summarized in Table 3-2. A critical speed is estimated with a value of 1089.2 Hz.

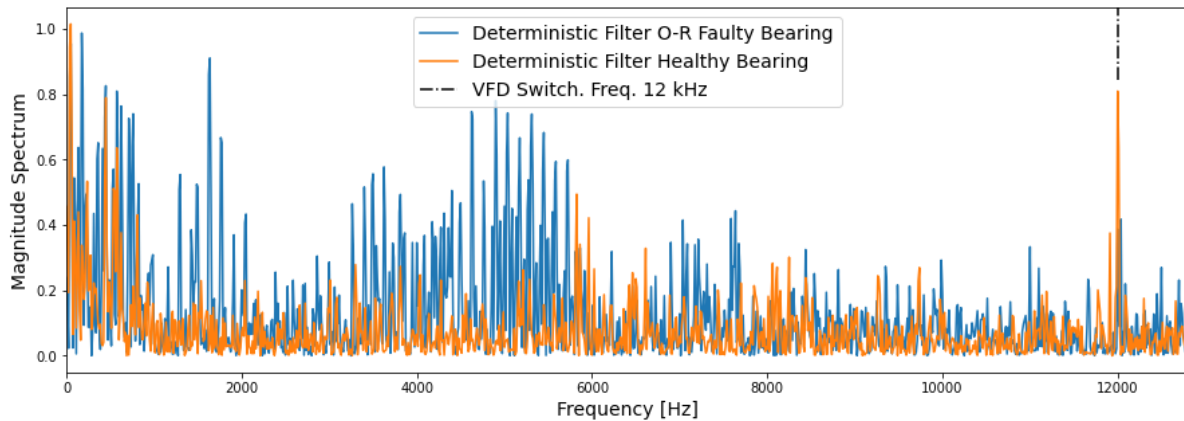
Table 3-2 Numerical Estimation of Test Rig Critical Speed.

Shaft Diameter	$D$	m	0.0254
Shaft radius	$R$	m	0.0127
Aluminium Rotor Weight	$Mr$	kg	5.0
Young Modulus	$E$	Pa	$2.00 \times 10^{11}$
Area - Inertia Moment	$I_{xx} = I_{yy}$	m <sup>4</sup>	$2.04 \times 10^{-8}$
Span - Shaft supports distance	$L$	m	0.3966
Gravity acceleration	$g$	m.s <sup>-2</sup>	9.785
Total Lumped Weight	$W_{TL}$	N	48.9
Influence coefficient cc	$\delta_{cc}$	m/N	$3.18 \times 10^{-7}$
Angular critical speed	$\omega_c$	rad.s <sup>-1</sup>	$7.93 \times 10^2$
Rotational critical frequency	$f_c$	Hz	126.2

### 3.3 Other notorious spectral components

As notated earlier, the AC motor is driving by a VFD. In those cases, they commonly produce electromechanical interactions, which could even generate torsional vibrations. VFD system try to control the phase frequency by switching the voltage and controlling the time-lapse of those switches inside an alternator. The switching frequency can vary in the range of 2 kHz to 16 kHz depending of the continuity required in the electrical connection. As more high, the switching frequency more smoothness is perceived in the AC wave. This type of devices usually generates high impulsive noise in a similar way than REB faults produce. In this sense, a prior identification of electromagnetic interactions should be carried in the Test characterization. For this particular case, happens that during the discrete random separation process, a notable peak is identified at the frequency of 12 kHz, as it is shown in Figure 3-8.

Figure 3-8. Discrete Random Separation filter magnitude spectrum.



In Figure 3-8, the DRS process has been done for the case of a healthy bearing and a faulty bearing. It is noticeable the 12000 Hz peak, which indicates the presence of a discrete component just in the switching frequency of the VFM.

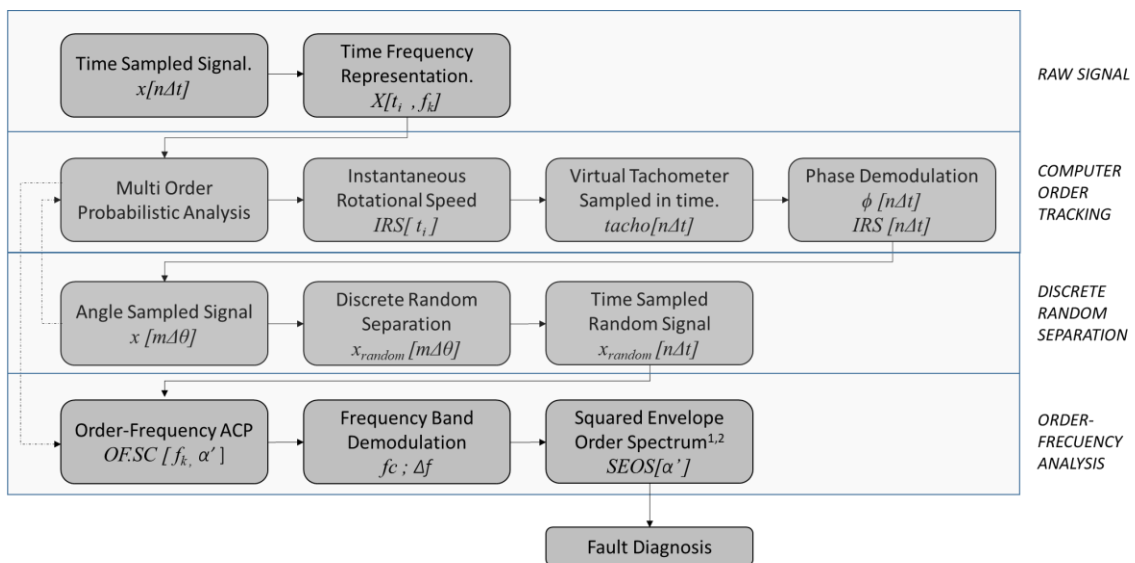
For the exposed in previous sections, some aspects should be highlighted. At first, the critical speed is far from the speed ranges at which the experiments were done, as it will be exposed in section 6, since the maximum rotational frequency is around 40 Hz while the critical speed is estimated at 126 Hz. There are three plausible ranges from resonance frequencies, i.e. (1.4-1.9 kHz, 4.5-6 kHz, and 8-11 kHz), which have been identified from the SC bi-spectral map and the Kurtogram. In addition, there is evidence of discrete components dictated by interference with the VFM shifting frequency, i.e. 12 kHz.

## 4. Model for Rolling Element Bearing Diagnosis under variable Speed

In this chapter, a model for the REB diagnosis under variable speed is presented. Many of the algorithms described in section 2 are integrated in the model presented. A particular case is exposed, corresponding to a signal sampled on the test rig described in section 3, at which the bearing far from motor (B2) is subject to Inner Race Fault, while rotational speed varies in the range 15 – 30 Hz.

The procedure is briefly summarized in Figure 4-1, and is further illustrated on Figure 4-2. The procedure is structured in four main steps, the capture of raw signal, computer order tracking, discrete random separation and the order-frequency analysis.

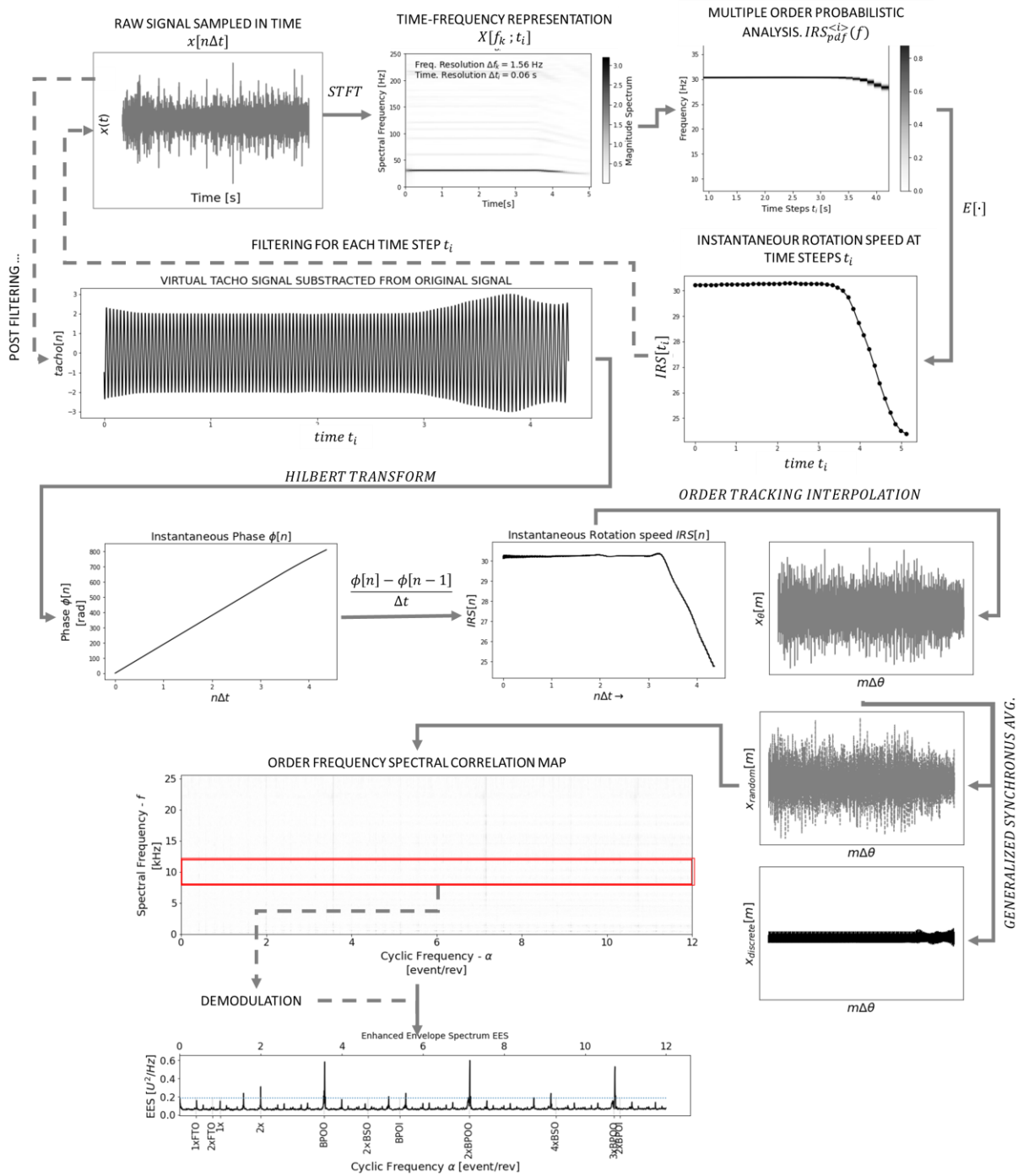
Figure 4-1. Procedure for REB Diagnosis under variable speed.



<sup>1</sup> This would be referred as IEOS (Improved Envelope Order Spectrum) for the case at which a demodulation band has been previously selected. If the demodulation band is selected as the entire frequency band  $[0; F_s/2]$  it would be referred as EEOS (Enhanced Envelope Spectrum).

<sup>2</sup> At literature is sometimes common to omit the "Order label", so, IES is used interchangeably with IEOS and similar occurs for EES and EEOS.

Figure 4-2. Procedure for REB Diagnosis illustration.



The method starts with the raw signal sampled in time domain, at a constant time step  $\Delta t = 1/F_s$ , where  $F_s$  corresponds to the sampling frequency of the ADC system. To perform order tracking using a Tachless strategy, the Short Time Fourier Transform –STFT is used to obtain a time-

frequency representation. Since the test rig do not owns element such as gears or blades, the synchronous orders are located in the bottom part of spectrum. This explains why other time-frequency representations such as wavelet transform was not considered for this case, once it would imply lower time resolution.

An adequate trade-off between time resolution and frequency resolution should be established. As a good recommendation, it is not desirable to allow frequency resolution to exceed 10% of the nominal speed (since speed variations between 10% to 25% could be predicted by time synchronous average [35]). While the minimum speed during experimental practice is around 15 Hz, the frequency resolution should not exceed 1.5 Hz.

From Time-Frequency representation and the use of Multi-Order-Probabilistic analysis, the instantaneous Rotational speed is estimated. Once the instantaneous rotational speed is determined, the MOPA strategy was used by the fact that no gears or blade elements are in the test rig, which becomes difficult to track a particular order different from the synchronous ones. Also, the maximum tracking of STFT usually generates distortions on the  $IRS[t_i]$ . By the experimental result, MOPA gives a good approximation during the experimental setup.

The reconstruction of instantaneous rotation speed  $IRS[t_i]$  could be achieved by taking the expected value of MOPA at each time step  $t_i$ , as it is exposed on Equation 4-1.

$$\text{Equation 4-1} \quad IRS[t_i] = E[ MOPA[\omega; t_i] ]$$

By taking the value of  $IRS[t_i]$ , a band-pass filter centered at  $IRS[t_i]$  is built. The previous time-frequency representation  $X[f_k, t_i]$  could be filtered and consequently, a virtual tachometer  $tacho[n]$  is obtained by synthesis. Popular synthesis method Overlap-add – OLA is adequate. OLA method results appropriately since it's relative simply implementation. It is also important to argue that the real attention for virtual tacho is focused on their phase, as is exposed in Figure 4-1 and Figure 4-2. Note that by using this procedure, virtual tacho is sampled on time domain, and consequently, instantaneous phase  $\phi[n]$  and instantaneous rotational speed  $irs[n]$  are obtained on time domain.

For discrete random separation, the GSA method proposed on [41] is proposed. Mainly, the use of GSA is preferred over the other methods exposed on Table 2-3 by the fact it could detect other synchronous components different from the synchronous ones. GSA was used with a speed resolution of 0.5 Hz, regimen increments of 0.5 Hz, and a kernel lambda  $\lambda$  of  $1.2 \times$  the speed resolution.

However, some limitations have been recognized for the use of GSA. For example, at signals with low rotational frequency, i.e. near 12-14 Hz, control over the frequency detail should be paid because the method tends to be unstable. For those situations, longer processing times were expected. Even an increase in frequency detail should be necessary. Additional steps are necessary from the use of GSA since order tracking interpolation is necessary to change to angular domain sampling (i.e  $x[m] = x(m\Delta\theta)$ , where 'm' indicates the index for angular domain sampling). This point is a future work proposal, based on how to properly set a method, which allows discrete random separation at variable speed conserving sampling on time domain.

Finally, the order-frequency analysis is made based on Cyclo-Nonstationary Representation. The OFSC bi-spectral map is obtained by the use of Average Cyclic Periodogram (Annex 4). This representation is interesting since it allows to identify periodical information related with cyclic order  $\alpha$  and spectral frequency  $f$ . The OFSC map was generated using the parameters described on Table 4-1.

Hann window is used since the spectral content of the signal is for many cases unknown and it results satisfactory for the major part of cases. In addition, Hann window owns good trade-off between frequency and amplitude accuracy.

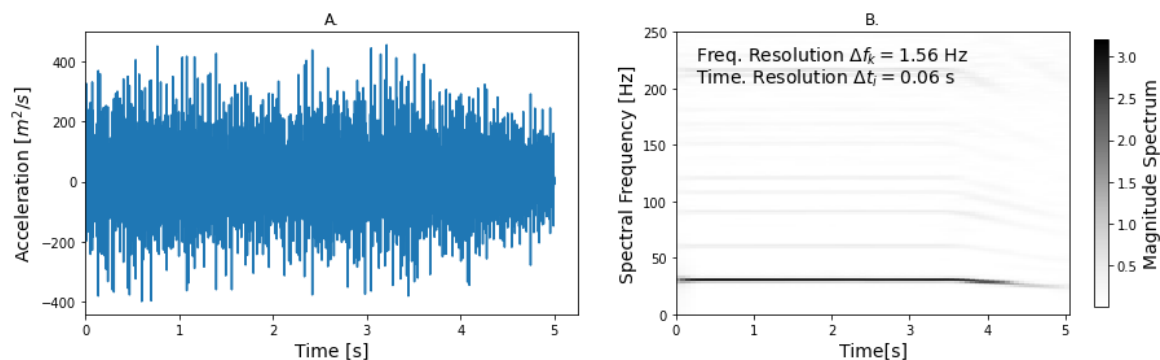
Table 4-1. Parameters for OFSC-ACP

<b>SIGNAL</b>		
Sampling time	Duration of signal in seconds	5 s
Sampling Frequency	Fs	51200 Hz
<b>DIGITAL SIGNAL PROCESSING</b>		
Window length $N_w$	Number of samples on window	$2^{11}$
Window	Type of window used	Hann
FFT length $N_{FFT}$	Number of samples to use in FFT	$2^{11}$
$c_w$	Noise Bandwidth Correction Coefficient	1.5
$\Delta f$	Spectral frequency resolution: $F_s/2N_w$	12.5 Hz
$c_w \Delta f$	Effective Spectral Frequency	18.75 Hz
Overlap Percentage	Overlapping between consecutive windows	75 %
$\alpha'$ range	Range of study for cyclic orders	0 – 12 [revolution <sup>-1</sup> ]
$\alpha'$ resolution	Space between consecutive $\alpha$ values	0.005

The next part of the section, the method is applied to a particular signal, which is the vibrational response for an outer race fault case. All steps related in Figure 4-1 and Figure 4-2 are further illustrated.

The Figure 4-3A illustrates the waveform of vibrational response sampled on test rig, while running at a variable speed between 15 and 30 Hz. The corresponding spectrogram is illustrated on Figure 4-3B.

Figure 4-3 Waveform of variable speed vibration response.  
A) Time domain signal. B) Short Time Fourier Representation.



From the Multi-Order Probabilistic Analysis, a Probability Distribution Function – pdf for the instantaneous rotational speed –IRS is obtained. The IRS is obtained for time steps  $t_i$ , with a resolution  $\Delta t_i$  dictated by the time frequency representation previously discussed. In this sense, at each time step a pdf for the IRS is represented (named IRS[f,  $t_i$ ] on Figure 4-2). By using of expected operator the Instantaneous Rotation Speed could be estimated at time steps  $t_i$ . This is illustrated in Figure 4-4. The MOPA results shown utilizes the first 3 harmonics, with a time step of 0.06 s. The hyper-parameters utilized are shown in Figure 4-4.

Figure 4-4. Instantaneous Rotational Speed from MOPA approach.

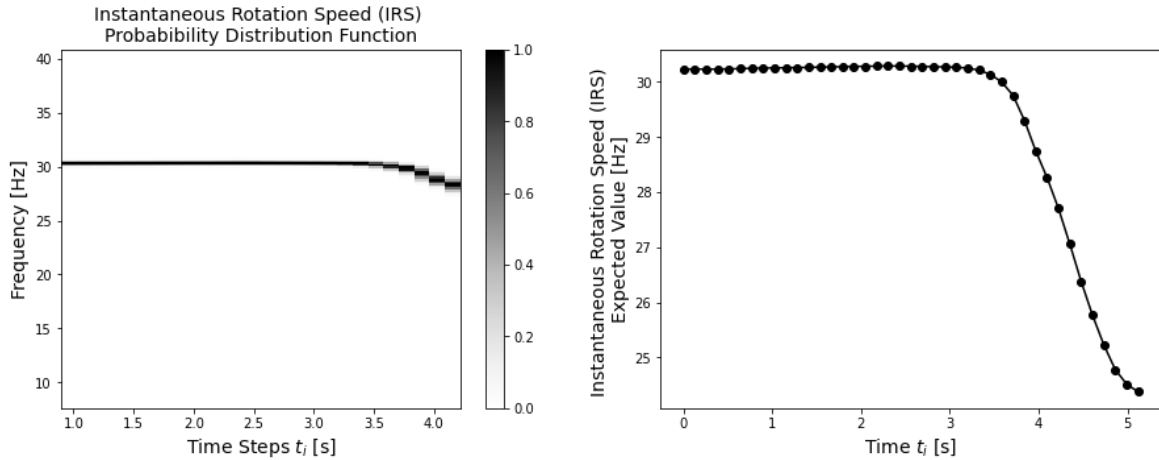
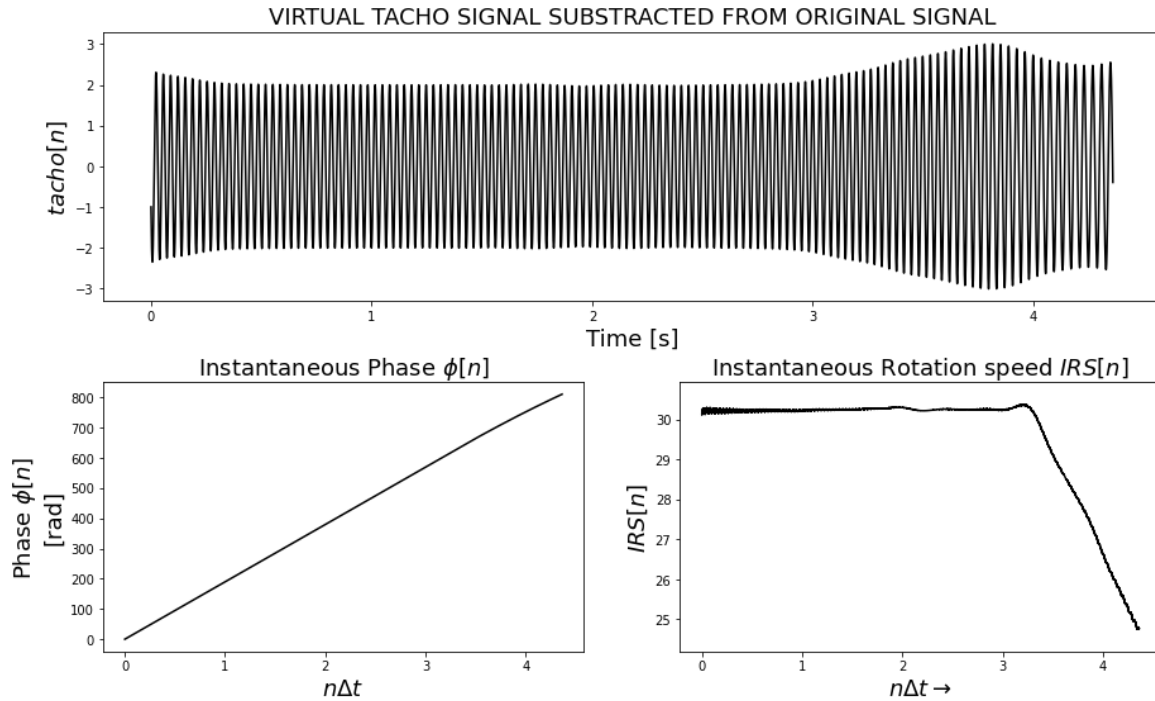


Table 4-2. Hyper-Parameter used for MOPA.

Hyperparameter	Nomenclature	
Sampling Frequency	$F_s$	51200 Hz
STFT window samples	$N_w$	$2^{15}$
STFT Overlap Percentage	[-]	90 %
STFT type window	[-]	Hanning
STFT num. of FFT samples	$N_{fft}$	$2^{17}$
Harmonics	$\{H_j\}$	{1,2,3}
Dim. Kernel	[-]	$2^6$
Number of Kernels	K	5
Gamma	[-]	17438 Hz/s

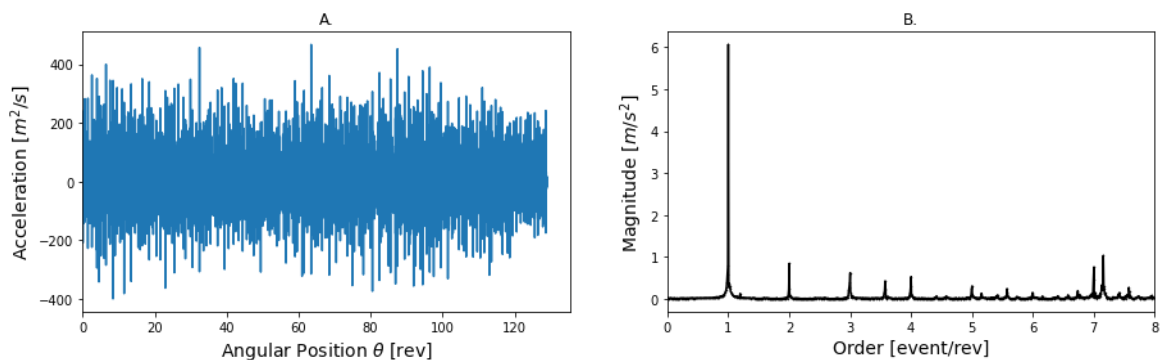
At each time step, a zero-phase filter is built. The filter is built with center frequency at the estimated IRS, with a bandwidth of 10 % around IRS, i.e.  $[0.9 \cdot IRS_i ; 1.1 \cdot IRS_i]$ . This filter is applied to original Time Frequency representation followed by normalization step. This normalization is done with the intention to avoid any kind of amplitude modulation in the virtual tacho signal but keeping the phase modulations as desired in virtual tacho signal. The synthesized virtual tacho and the subtracted phase and IRS are plotted in Figure 4-5.

Figure 4-5. Phase demodulation order tracking.



The angle resampled signal and their order spectrum are shown in Figure 4-6. Clear peaks at shaft rotation harmonics are revealed, which in fact indicates the resampling process has been achieved correctly. A second phase demodulation is recommended in cases where clear peak at shaft rotation harmonics are spread and do not result clear. This phase demodulation step could be made in angular domain by a similar way than exposed in section 2.5.

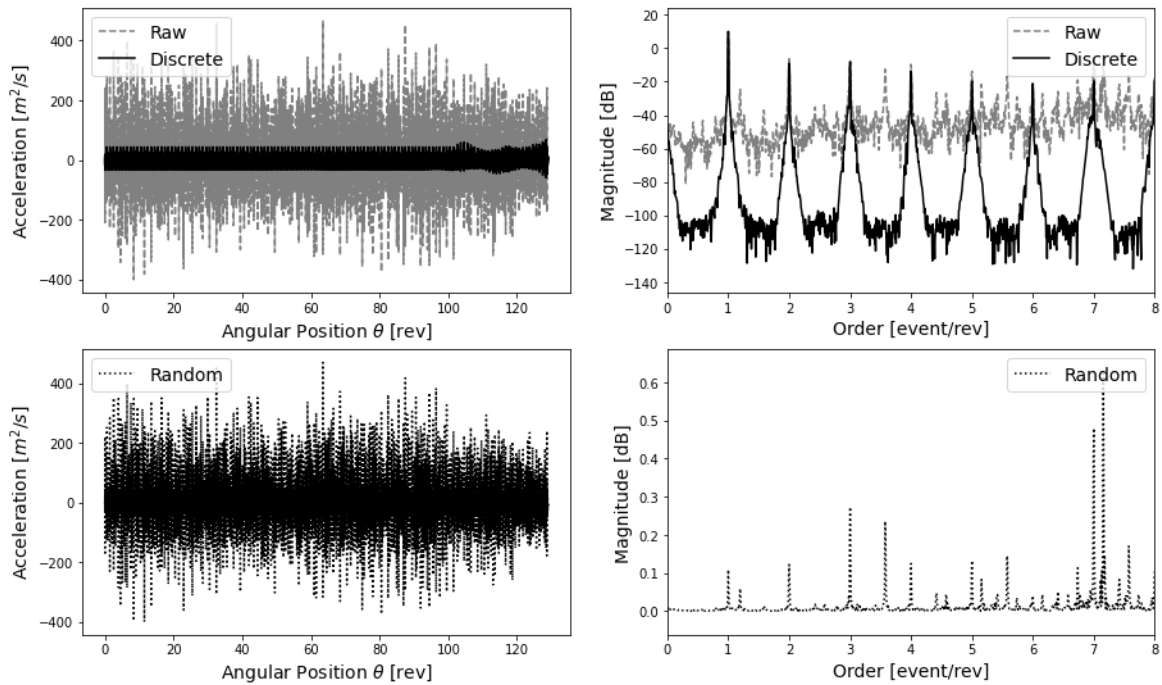
Figure 4-6. Angle domain waveform.





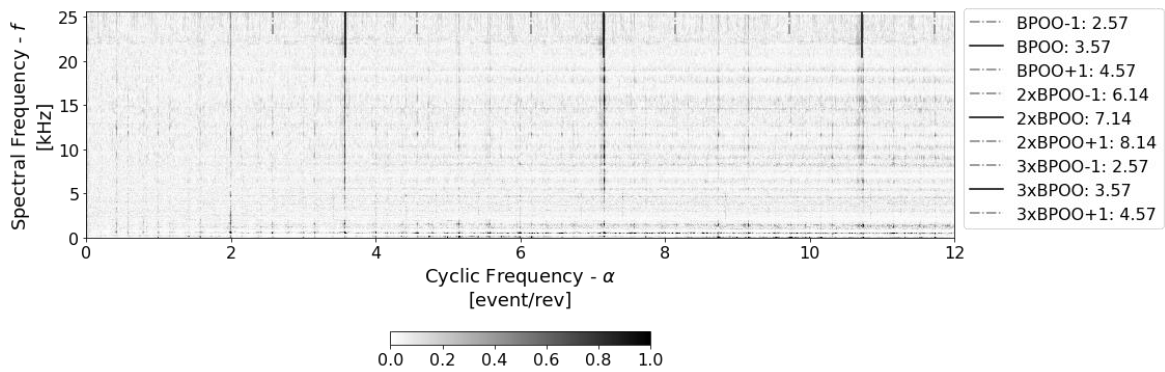
By the use of the Generalized Synchronous Average, a prior Discrete Random Separation could be achieved. The use of GSA is illustrated in Figure 4-7. Does result evident the energy loosed at the discrete synchronous orders 1x, 2x and 3x once the GSA is done.

Figure 4-7. GSA illustration



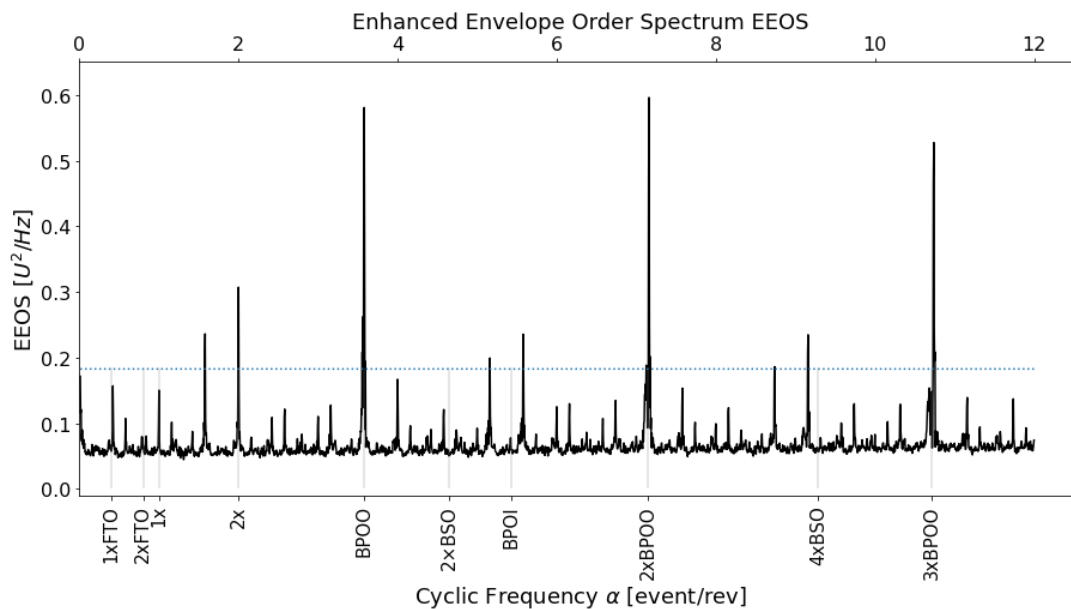
By using the random component obtained after GSA process, the Order-Frequency Spectral Coherence could be obtained as exposed in Figure 4-8. The parameters used were previously exposed on Table 4-1. Clear vertical patterns are observed at fault characteristic order of BPOO, 2xBPOO and 3xBPOO. Those vertical lines are visible on all the spectral frequency range between 0 to  $F_s/2$  which makes it straightforward to establish a diagnosis (Outer Race Fault Diagnosis).

Figure 4-8. Order-Frequency Spectral Coherence - OFSCoh



For the most part of cases, it results more convenient to analyze the Squared Envelope Order Spectrum (as discussed on section 2.4). At this point, there are many ways to build SEOS versions. For example, from OFSCoh map the Enhanced Envelope Order Spectrum could be obtained by averaging the OSFCoh map over the vertical axis. Former, mean integrating over the vertical axis and plotting the result as a function of  $\alpha$ . This is plotted on Figure 4-9. Dashed blue line stands for the statistical threshold, with a 95% Confidence Interval, for which the signal could be considered to own second-order cyclo-stationarity. To make the previous statement clear, consider the 1xBPOO cyclic order ( $\alpha = \text{BPOO}$ ). Since the EEOS overcome the statistical threshold represented by dashed blue line, it could be considered that signal owns a second order cyclostationary component at BPOO. Similar cases for orders such as 2x, 2xBPOO, and 3xBPOO. With previous results, it is clear the diagnosis of outer race fault.

Figure 4-9. Enhanced Envelope Order Spectrum



For the particular case studied on previous paragraph (case exposed on Figure 4-9) results in a clear diagnosis using EEOS, i.e. averaging over the spectral frequency range. However, this is not the general case. In many situations is not as straightforwardly as the case previously illustrated. Demodulation is usually necessary for obtaining convenient Order Spectrum, i.e. an order-spectrum useful for diagnosis. By the use of OFSCoh map, demodulation could be achieved by averaging (integrating) over a convenient spectral frequency band. When a particular spectral frequency band is selected, the result is usually called as IEOS, which stands for Improved Envelope Order Spectrum. For example, if a spectral frequency band comprehended

For this particular case, application of model previously summarized on Figure 4-1 allows to determine the Instantaneous rotational speed, separate the Random and Deterministic parts and so, obtain cyclic frequency representation by the use of Enhanced Envelope Spectrum. At EES clear peaks at Fault Characteristic Frequency could be obtained and so generate a Diagnosis. This procedure would be followed by the rest experimental setups.

In this section, the method NewIESfogram [50] is exposed. The NewIESfogram is a strategy for demodulation, i.e. selecting a convenient spectral frequency range to analyze the resulting IES. The

main idea with his method is to define a new metric, which can measure the convenience of selecting a spectral range to generate an IES and subsequently made a diagnosis based on such IES. The metric is exposed as a function of spectral frequency band.

The results exposed in [50] show that for the case of a constant speed, the diagnosis process could be improved with respect to similar strategy previously exposed on [48]. In section 6, the extension of that method for the case of variable speed would be exposed.

## 4.1 NewIESfogram

As it was mentioned, usually is common to try to represent the cyclic frequencies on a one-dimensional spectrogram. In fact, the IES has been proved to represent a valuable tool for REB fault diagnosis. The use of Improved Envelope (Order) Spectrum in place of Enhanced Envelope (Order) Spectrum, stands by the fact that commonly the fault characteristic frequencies do not modulate all the spectral content, but modulates selected frequency ranges. The latter indicates that an adequate selection of  $f_c$  and  $\Delta f$  for the IES determination could improve notoriously the one-dimensional spectrum representation, and so on the diagnosis process.

Recently, [51] has proposed a method for the semi-automatic selection of the optimal frequency band for the IES computation. The resulting IES is namely IESFO standing for Improved Envelope Spectrum Frequency Optimization. This method was applied to REB diagnosis under high impulsive noise coming for Pulse-Width Modulation (PWM). In this approach, a metric is represented as a function of the spectral frequency band. The metric selected in this proposed method correspond to the sum of the IES evaluated over a set of cyclic frequencies previously selected, as it is shown in Equation 4-2.

$$\text{Equation 4-2} \quad \text{Ind} = \sum_k \text{IES}(\alpha_k; f_c, \Delta f)$$

where  $\alpha_k$  could represents the  $k^{\text{TH}}$  candidate of cyclic frequency in which a track of fault should appear. It is important to mention that probably the set of cyclic frequencies correspond to the harmonics of the fault characteristic frequency prior selected.

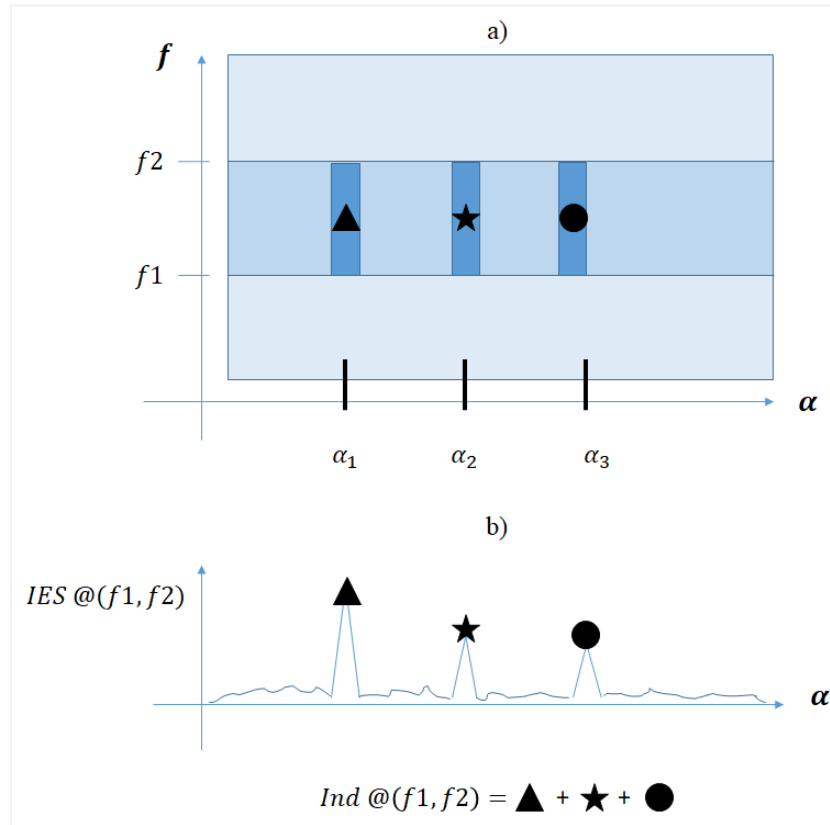
In this sense, optimal frequency band is done by representing the *Ind*-metric in a 1/3-binary tree, in a similar manner as Kurtogram is presented. The optimal spectral frequency band is then selected by maximum value observing in which center frequency and frequency bandwidth the *Ind*-metric reaches the. This approach has been named IESFOgram.

To further exploration of IES computation from the use of IESFOgram and the *Ind* computation let's analyze the Figure 4-9. A set of three cyclic frequencies are prior selected  $\{\alpha_1, \alpha_2, \alpha_3\}$ . Additionally let's suppose that a spectral frequency band ( $f_1$  and  $f_2$ ) is also prior selected by the use of IESFOgram. From the Spectral Coherence (refer to Figure 2-18) the Improved Envelope Spectrum is computed by the integration between  $f_1$  and  $f_2$  over the  $f$ -axis as it is illustrated on Equation 4-3.

$$\text{Equation 4-3} \quad IES(\alpha; f_c, \Delta f) = \frac{1}{\Delta f} \int_{f_1}^{f_2} SCOh(\alpha, f) df$$

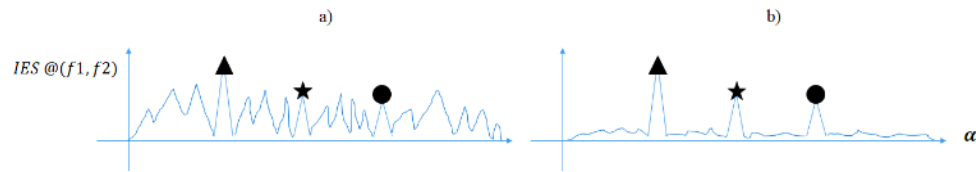
The IES is then evaluated at the set of cyclic frequencies, and the magnitudes obtained are added to compute the *Ind* metric as it is shown in Equation 4-2 process is schematized in the Figure 4-10.b.

Figure 4-10. Illustration of IES and Ind-metric computation. A) Spectral Coherence Representation. B) IES representation.



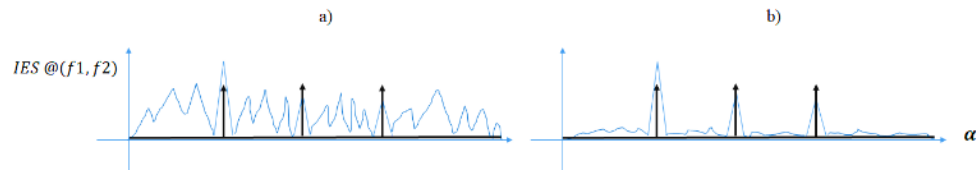
For REB diagnosis, it is desirable to obtain a spectrogram where the magnitude of the IES looks as close as possible to delta functions in the FCF. It means the desired shape of the IES is reaches high magnitude value in those FCF frequencies whereas the neighbor magnitudes keep close to zero. From the last idea, it results important to explore the nature of the metric used in the IESFOgram. Although the metric intends to maximize the amplitude on the selected FCF, it do not evaluate the IES on the neighbor cyclic frequencies. This is illustrated in Figure 4-11, where two IES generates the same *Ind* despite of their noticeable differences on their behaviour. In Figure 4-11.a. the IES do not keep zero at the neighbors of the selected fault characteristics frequencies, whereas the IES shown in Figure 4-11.b does.

Figure 4-11. Ind-metric computation comparison. A) *ind* illustration for low SNR Improved Envelope Spectrum. B) *ind* illustration for high SNR Improved Envelope Spectrum



In order to generate another metric, which evaluates a high peak in the selected FCF, but at the same time evaluates the neighbor behavior, the Sample Correlation Coefficient between the IES and a hypothetical IES equivalent to the sum of delta functions on the FCF is proposed. This idea is illustrated in Figure 4-12 and described by Equation 4-4. In Figure 4-12.a, an IES has small sample correlation with respect to the hypothetical IES, this is because the magnitude of IES on neighbor cyclic frequencies has considerable magnitude. In contrast, Figure 4-12.b has big sample correlation because of their similitude with the desired delta function.

Figure 4-12 Sample correlation computation comparison. A) Low sample correlation case. B) High sample correlation case.



Equation 4-4

$$r = \frac{\sum_k (IES[k] - \overline{IES})(IES_{desired}[k] - \overline{IES_{desired}})}{\sqrt{\sum_k (IES[k] - \overline{IES})^2 (IES_{desired}[k] - \overline{IES_{desired}})^2}}$$

where the  $\bar{\cdot}$  stands for the mean operator.

The optimal spectral frequency band could also be obtained by the 1/3-binary tree search in a similar way than an IESFOgram or a Kurtogram. With the only aim of simplicity, this approach is named newIESFOgram. The resulting IES generated is named newIESFO in analogous manner.

During this chapter, the method proposed has been described and exemplified. The algorithm's parameters employed in each of the steps of the method are exposed and their selection has been briefly discussed. Some improvement points on the method were mentioned and some control aspects have been exposed. Finally, in section 4.1 a new method for demodulation based on OFSCoh is introduced in a previous author's work.

## 5. Simulated Experimental Results

For validation of method exposed on section 4, a series of experiments are proposed. At first, a series of simulated signals are considered. The model for simulating those signals is described on section 5.1, and the different considerations for each of the type of failure are detailed in sections 5.1.1 to 5.1.4. In section 5.2 results of experiments on simulated signals are exposed and discussed for the different type of faults and the loads applied. Additionally, on section 5.3 the effect of random slippage, Signal to Noise Ratio and the spread on impulses are analyzed.

### 5.1 Simulation Model

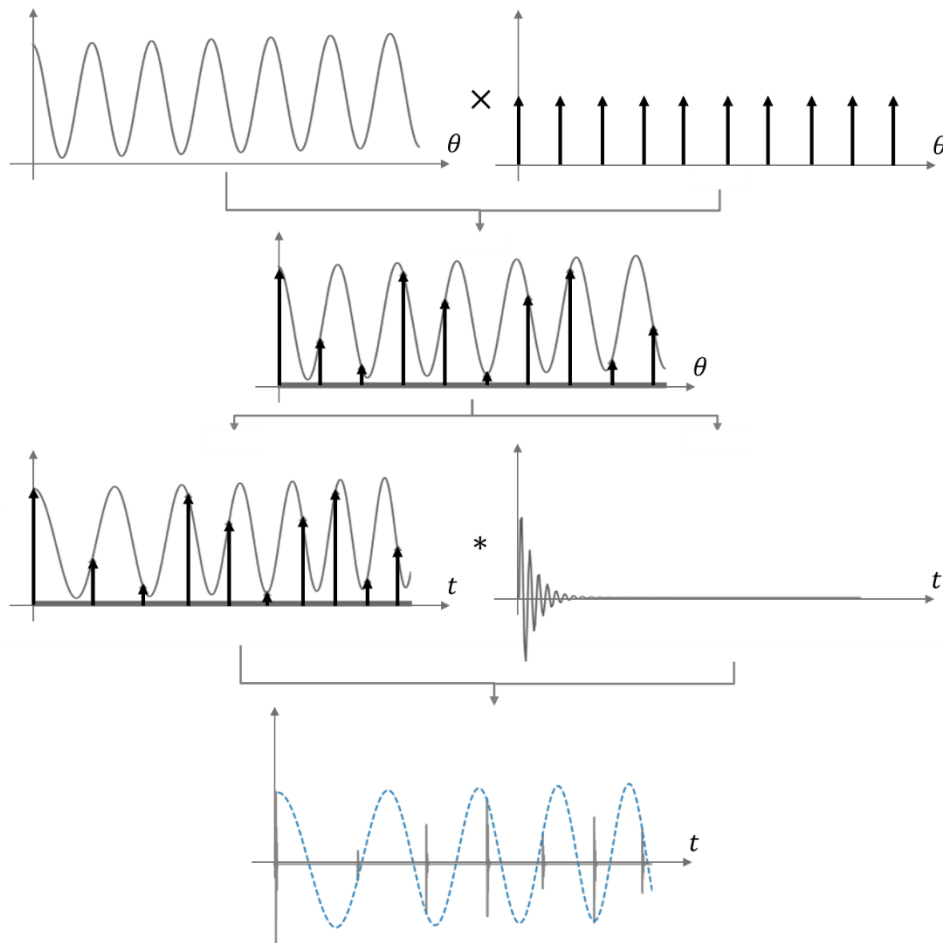
From this point, the interest is to achieve a classification according to angular acceleration and diverse type of charges. In this sense, an incipient fault in a REB could be simulated as a discrete train pulse, modulated by the load according to the nature of them. To further consider the behaviour and relations between the type of loads, modulations and pulse trains, consider the Equation 5-1.

Equation 5-1 
$$x(t) = [A(\theta(t)) \sum_k \delta_k^{\Theta_0}(\theta(t))] * h(t)$$

$$\delta_k^{\Theta_0}(\theta) = \begin{cases} 1 & \text{if } \theta = k\Theta_0 \\ 0 & ; \text{ otherwise} \end{cases}$$

Where  $x(t)$  denotes the acceleration, the \* operator denotes the convolution,  $h(t)$  represents the impulse response of REB body,  $A(\theta(t))$  represent the amplitude modulation function, and  $\delta_k^{\Theta_0}(\theta(t))$  represent an impulse located at an entire multiple of angular periodicity  $\Theta_0$ . Angular periodicity  $\Theta_0$  results as the inverse of Fault Characteristic Orders (BPOO, BPOI, BSO), depending of type of fault to be simulated. The terms of Equation 5-1 are illustrated on Figure 5-1.

Figure 5-1. Amplitude Modulation Function



For convenience,  $A$  and  $\delta_k^{\theta_0}$  would be expressed as function of angular domain, since it represents the direct relation between input force and angular position. On the other hand, the impulse response  $h(t)$  is strictly time dependent as described on section 1. Note the similarity between Equation 5-1 and Equation 1-2.

The modulation function  $A(t)$  would result from the combination of different load, as exposed on Table 2-2. Similar models were presented by [52], for the case of Outer Race and Inner Race defects, under constant speed regime. For the purpose of this section the amplitude load would be described for the three types of faults and a discussion about the implications of variable speed on their behaviour. For the rest of the chapter, the results of apply the method proposed on section 4 are exposed. Additionally, the effect of randomness are briefly discussed. For the particular analysis of this section, only radial loads are considered, and axial load effect is discarded.

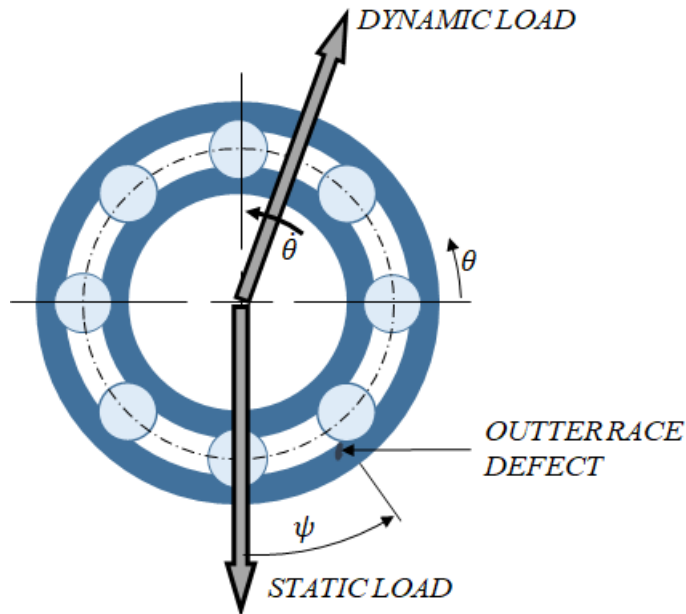
Table 5-1 Factor and levels from simulated signals.

FACTOR	SYMBOL	LOW LEVEL	HIGH LEVEL
Dynamic Load (unbalance)	$me$	0.00015 kg·m	0.015 kg·m
Static Load (Dead weight)	$Mg$	1 kg (9.8 N)	6 kg (58.8 N)
Rotational Speed Run up: 0 to 5 seconds.	$\dot{\theta}$	10 – 25 Hz	10 – 40 Hz
Fault type	[-]	IR – OR – BF – Healthy	

### 5.1.1. Outer Race Amplitude Modulation Function

As most common case, the Outer race is fixed without movement, whereas inner race rotates at synchronous speed with shaft at the Instantaneous Rotation Speed. Consequently, If a small defect is present on the outer race, it would keep on the same position, usually located on the bottom part of Outer Race. The Static load and dynamic loads are illustrated on Figure 5-2.

Figure 5-2. Loads for the case of localized faulty on outer race



As rolling element pass through the load zone and the defect, an impact would be generated. Note the static load does not generate any modulation as the distance between defect and static load keeps constant. On the other hand, dynamic load is synchronous with inner race and their effect would be seen as a modulation at the IRS frequency. The Equation 5-2 summarizes this situation [52].



Equation 5-2

$$A(\theta(t)) = \rho[Mg \cos \psi + m\theta\dot{\theta}(t)^2 \cos(2\pi\theta(t))]$$

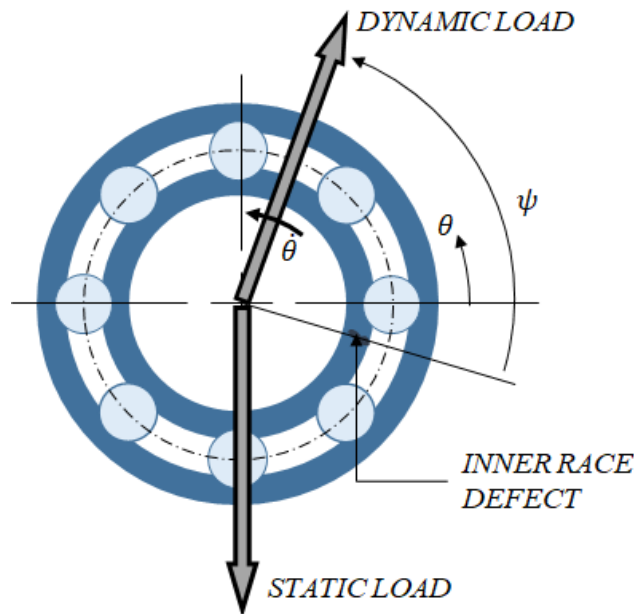
$$\theta^0 = \frac{1}{\text{BPOO}}$$

Notice the static load component does not have any relation with the angular domain. In fact, if static load is considerable with respect dynamic load a constant modulation function is expected. On the other hand, the dynamic load would not only depend on the angular position, but also would be amplified by the rotational speed. This situation results from particular interest on the case of variable speed, since the ration between static load and dynamic load changes over time. If the dynamic load is considerable, the envelope spectrum should be composed of discrete peaks at BPOO and harmonics of BPOO, accompanied with sidebands at  $1\times$ .

### 5.1.2. Inner Race Amplitude Modulation Function

In contrast to the Outer Race Fault case, if a small defect were present on the inner race, the location of defect would be displacing synchronously with shaft. This situation is illustrated on Figure 5-3.

Figure 5-3. Loads for the case of localized faulty on inner race



The static load would generate an amplitude modulation dictated by the difference between angular position of defect and static load. As angular position of the defect is displacing at shaft speed, a modulation of  $1\times$  is expected for the case of static load. On the other hand, as both, dynamic load

and defect position, rotates at the same angular speed (shaft speed), their relative position does not change and consequently any modulation is expected. The impact periodicity, is dictated by the Ball Pass Inner Race Order BPOI. The amplitude modulation function is expressed in Equation 5-3 [52].

$$\text{Equation 5-3} \quad A(\theta(t)) = \rho[Mg\cos(2\pi\theta(t)) + 4\pi^2me\dot{\theta}(t)^2 \cos(\psi)]$$

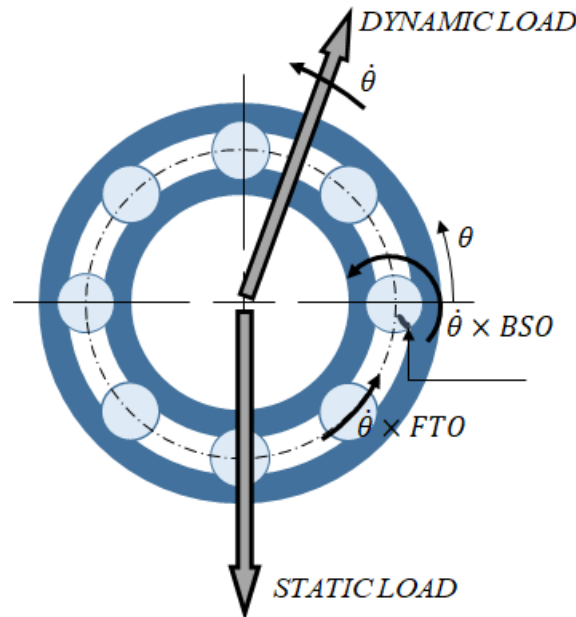
$$\theta^0 = \frac{1}{BPOI}$$

It is important to annotate that although in previous paragraph it has been said that any modulation is expected from dynamic load, it is only true for the case of constant angular speed. Notice the amplitude of dynamic load is proportional to square of Instantaneous Rotational Speed. The latter means for the case of variable speed, an amplitude modulation is expected from the increase in kinetic energy of the system.

### 5.1.3. Rolling Element Amplitude Modulation Function

For the case of rolling element failure, various modulations are expected. First, consider the situation illustrated on Figure 5-4 at which a fault is drawn in one of the rolling elements. The figure illustrates that the rolling element rotates at a speed equivalent to the product of BSO and shaft speed ( $\dot{\theta} \times BSO$ ). Whereas, the cage is rotating at an angular speed equivalent to the product of FTO and shaft speed ( $\dot{\theta} \times FTO$ ). As usual, the dynamic load is rotating synchronously with the shaft, i.e. at an angular speed of  $\dot{\theta}$  whereas the static load does not move.

Figure 5-4 Loads for the case of localized faulty on rolling element



To understand the model proposed, it is important to describe the effect of static load. The rolling element with failure would be located at the static load zone once per rotation of the cage. This means an amplitude modulation is expected in function of the angular distance between static load and the position of the cage with the rolling element failed rolling. The former, means that static load would generate an amplitude modulation at FTO order.

On the other hand, it is important to note the dynamic load rotates at different angular speed than the cage. In this sense, a modulation is expected from the relative positions between the faulty rolling, and the dynamic load. The before mentioned implies that a modulation is expected at (1-FTO) order as consequence of dynamic load. The magnitude of dynamic load could be modeled as proportional to square instantaneous angular speed. The Equation 5-4 models the vibrational response for the case of a localized fault on a rolling element.

$$\text{Equation 5-4} \quad A(\theta(t)) = \rho [Mg \cos(2\pi FTO \theta(t)) + me\dot{\theta}^2 \cos(2\pi(1 - FTO)\theta(t) + \psi_o)]$$

$$\theta^0 = 1/BSO$$

Notice in this case, amplitude modulations are expected from both contributions, static and dynamic load. Similar to previous cases, the dependence between dynamic load and angular speed generates additional amplitude modulation from the variations of the kinetic energy of the ensemble.

### 5.1.4. Nominal Parameters for Simulated Signals.

Signals for different type of faults were simulated according to amplitude modulation functions exposed through sections 5.1.1 to 5.1.4 and the model exposed on Equation 5-1. The impulse response function  $h(t)$  was modeled as an all poles, second order, 1 DOF system, with a damping coefficient  $\zeta = 0.01$ , a natural frequency of  $\Omega_N = 8000\pi \text{ rad s}^{-1}$ . The equivalent impulse response on digital domain was obtained by impulse invariance method.

Rotational speed was set as a linear-run up. With an initial rotation frequency of 10 Hz and an acceleration was a factor with levels at 3 Hz/s and 6 Hz/s. 5 seconds signals where simulated, at a sampling frequency of 25600 Hz.

The fault characteristic orders are set equal to the ones of the Test Rig described on section 3, in Table 3-1. To simulate the effect of progressive faults, and the randomness associated with strikes generated by the contact between faulty surfaces, a random slippage was added to the angular distance between pulses. This slippage is set as a random value in the range of -5% and 5% for each pulse, with an uniform probability distribution. This situation is illustrated on Figure 5-5.

Figure 5-5 Illustration of slippage

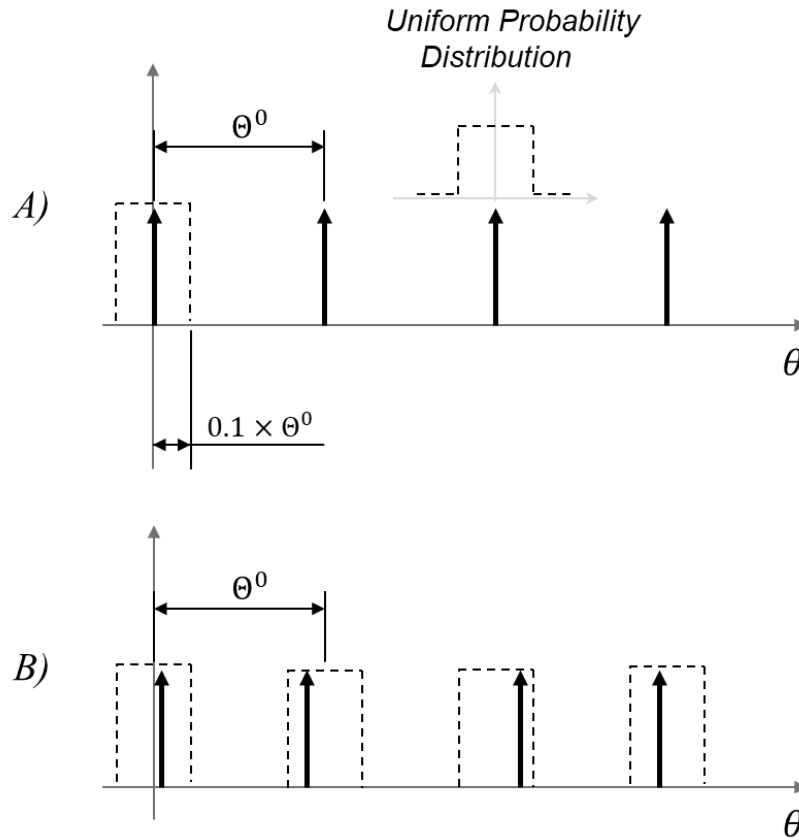


Figure 5-5-A illustrates the nominal position of pulse and the possible range at which the impulse could lie. As there is no information of probability of slippage, an uniform probability distribution is considered between the limits previously discussed ( $\pm 5\%$ ). Figure 5-5-B schematize a realization of the process and the multiplication with the corresponding amplitude modulation function  $A(\theta(t))$ , as previously discussed.

For making the simulation process more realistic, additional signals are added to build the simulated signal  $y(t)$ . The output signal is estimated as the sum of three different signals. The non-cyclostationarity signal,  $x(t)$ , simulated with the model exposed on Equation 5-1, additive white Gaussian noise,  $n(t)$ , and the effect of some discrete components  $d(t)$ . Each of the one signals are normalized between -0.5 and 0.5, and weighted prior to summation. This is exposed on Equation 5-5, and summarized on Table 5-2.

Equation 5-5

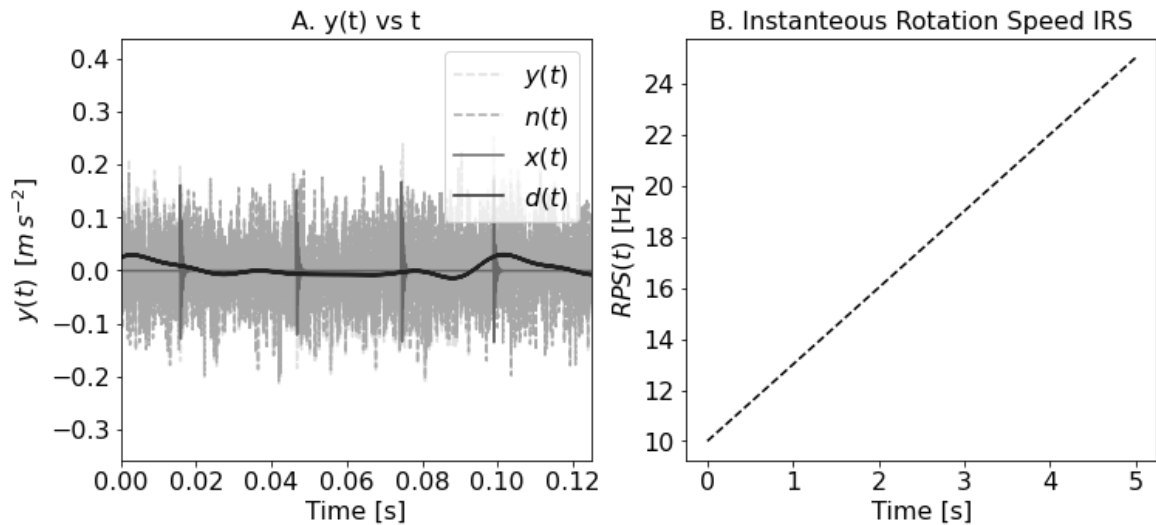
$$y(\theta, t) = x(\theta, t) + n(t) + d(\theta(t))$$

Table 5-2 Composition of simulated signals

TYPE OF SIGNAL	RELATION	WEIGHT FACTOR
Cyclo-Non Stationary	$x(\theta, t) = \left[ A(\theta(t)) \sum_k \delta^{\theta_0}(\theta(t)) \right] * h(t)$	$c_x = 0.40$
Additive White Noise	$n(t) ; n(t_i) \sim \mathcal{N}(\mu = 0, \sigma = 0.5)$	$c_n = 0.55$
Discrete components	$d(t) =$ $0.15 \sin\left(2\pi\theta(t) + \frac{\pi}{3}\right) +$ $0.10 \sin\left(4\pi\theta(t) + \frac{\pi}{4}\right) +$ $0.05 \sin\left(6\pi\theta(t) + \frac{\pi}{7}\right) +$ $0.05 \sin\left(8\pi\theta(t) + \frac{\pi}{5}\right) +$ $0.05 \sin\left(10\pi\theta(t) + \frac{\pi}{2}\right) +$ $0.05 \sin(60 \times 2\pi t) +$ $0.05 \sin(6000 \times 2\pi t)$	$c_n = 0.05$

To exemplify the previous paragraphs, consider a fault on Outer Race, for the case of low angular acceleration. The cyclo-nonstationary part, the white noise and discrete contributions are illustrated on Figure 5-6-A. The Figure 5-6-B illustrates the instantaneous angular speed.

Figure 5-6. Components of simulated signals and rotation speed.



The parameters for static load, unbalance, acceleration and dynamic load range are summarized on Table 5-3. For each case, the signal was scaled between 0 and 1. Those parameters have been selected aiming to simulate the conditions of test rig exposed on section 3.

Table 5-3. Parameters for Simulation Signals

	Static Load [N]	Unbalance [kg m]	Acceleration Freq. range	Range of Dynamic Load [N]
Run 1	9.8	$1.5 \times 10^{-4}$	$3 \text{ Hz s}^{-1}$ 10 – 25 Hz	0.6 – 3.7
Run 2	58.8	$1.5 \times 10^{-4}$	$3 \text{ Hz s}^{-1}$ 10 – 25 Hz	0.6 – 3.7
Run 3	9.8	0.015	$3 \text{ Hz s}^{-1}$ 10 – 25 Hz	59.2 – 370.1
Run 4	58.8	0.015	$3 \text{ Hz s}^{-1}$ 10 – 25 Hz	59.2 – 370.1
Run 5	9.8	$1.5 \times 10^{-4}$	$6 \text{ Hz s}^{-1}$ 10 – 40 Hz	0.6 – 9.5
Run 6	58.8	$1.5 \times 10^{-4}$	$6 \text{ Hz s}^{-1}$ 10 – 40 Hz	0.6 – 9.5
Run 7	9.8	0.015	$6 \text{ Hz s}^{-1}$ 10 – 40 Hz	59.2 – 947.5
Run 8	58.8	0.015	$6 \text{ Hz s}^{-1}$ 10 – 40 Hz	59.2 – 947.5

## 5.2 Simulated Faults Results

In this section, the simulated signals results are illustrated for each case of fault, with the parameters previously exposed on Table 5-3. The combination fault case is also considered. In general, after applying the model described on section 4, the diagnosis results satisfactory. In addition, the relation between dynamic loads and static loads results important for the behaviour on the Envelope Order Spectrum analysis.

The discrete components at IES are compared with respect to statistical threshold. In this sense, if a discrete cyclic frequency overcomes the statistical threshold is it possible to affirm that at such discrete cyclic frequency the signal has a second order cyclo-stationary behavior, with a p-value of 95% [34]. The statistical threshold comes from the Equation 9-8 described on annex 9.2

### 5.2.1. Outer Race Simulated Fault

Table 5-4 summarizes the result obtained on the different experimental simulations for the case of Outer Race Fault. In the last columns (shadow columns), the discrete cyclic orders of  $\alpha = 1, 2, BPOO$ , and  $2 \times BPOO$  were labeled as ‘N’ or ‘Y’ as follows. If those discrete components exceed the statistical threshold they were labeled as Y, in the opposite case were labeled as N.

A high correlation between the discrete components exceeding the statistical threshold and the modulation coefficient (Column  $\bar{R}$ ) is observed. The mean modulation coefficient  $\bar{R}$  is defined from the Amplitude modulation function, exposed on section 5.1.1. In the case of Outer Race Fault, it becomes the relation between static load  $Mg \cos(\psi)$  and dynamic load  $me\dot{\theta}^2$ . As shaft rotation speed does not keep constant, the modulation coefficient does not keep constant. For the previous reason, an average modulation coefficient is taken, as it is exposed on Equation 5-6.

$$\text{Equation 5-6} \quad \bar{R} = \frac{Mg \cos(\psi)}{4\pi^2 me \theta_1 \dot{\theta}_2}$$

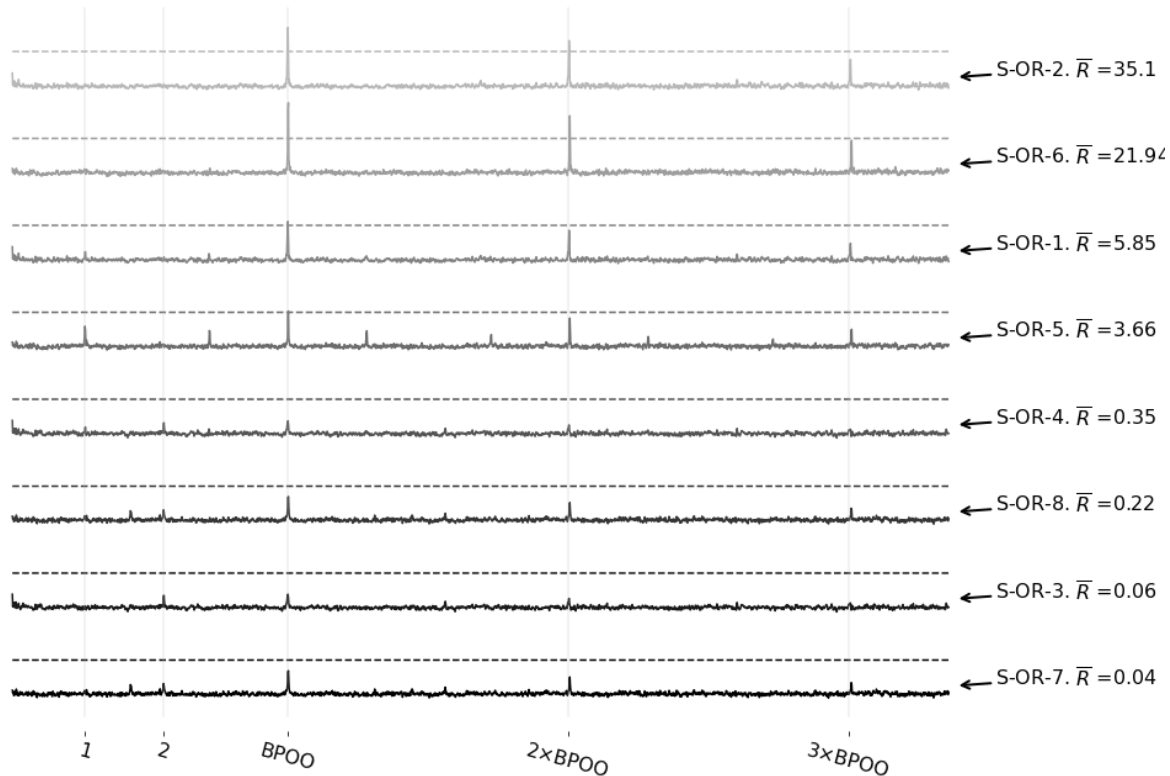
where  $Mg$  stands for the Rotor and shaft weight,  $me$  stands for the unbalance charge, and  $\dot{\theta}$  stands for instantaneous rotational speed, as it was exposed on Table 5-1.

Table 5-4. Summary of loads for Outer Race Simulated signals.

Run Label	Static Load [N]	Static Unbalance [kg m]	Acceleration Freq. range	Range of Dynamic Load [N]	$\bar{R}$	1x	2x	1xBPOO	2xBPOO
S-OR-1	9.8	$1.5 \times 10^{-4}$	3 rev/s <sup>2</sup> 10 – 25 Hz	0.6 – 3.7	5.85	N	N	Y	N
S-OR-2	58.8	$1.5 \times 10^{-4}$	3 rev/s <sup>2</sup> 10 – 25 Hz	0.6 – 3.7	35.10	N	N	Y	Y
S-OR-3	9.8	0.015	3 rev/s <sup>2</sup> 10 – 25 Hz	59.2 – 370.1	0.06	N	N	N	N
S-OR-4	58.8	0.015	3 rev/s <sup>2</sup> 10 – 25 Hz	59.2 – 370.1	0.35	N	N	N	N
S-OR-5	9.8	$1.5 \times 10^{-4}$	6 rev/s <sup>2</sup> 10 – 40 Hz	0.6 – 9.5	3.66	N	N	N	N
S-OR-6	58.8	$1.5 \times 10^{-4}$	6 rev/s <sup>2</sup> 10 – 40 Hz	0.6 – 9.5	21.94	N	N	Y	Y
S-OR-7	9.8	0.015	6 rev/s <sup>2</sup> 10 – 40 Hz	59.2 – 947.5	0.04	N	N	N	N
S-OR-8	58.8	0.015	6 rev/s <sup>2</sup> 10 – 40 Hz	59.2 – 947.5	0.22	N	N	N	N

Figure 5-7 illustrates the IES obtained from signals S-OR-1 to S-OR-8. Similarly. The statistical threshold (95% CI) is plotted for each case with a dashed line. Additional view of those results are presented on annex of section 9.3.

Figure 5-7. Simulated Signals for OR fault.



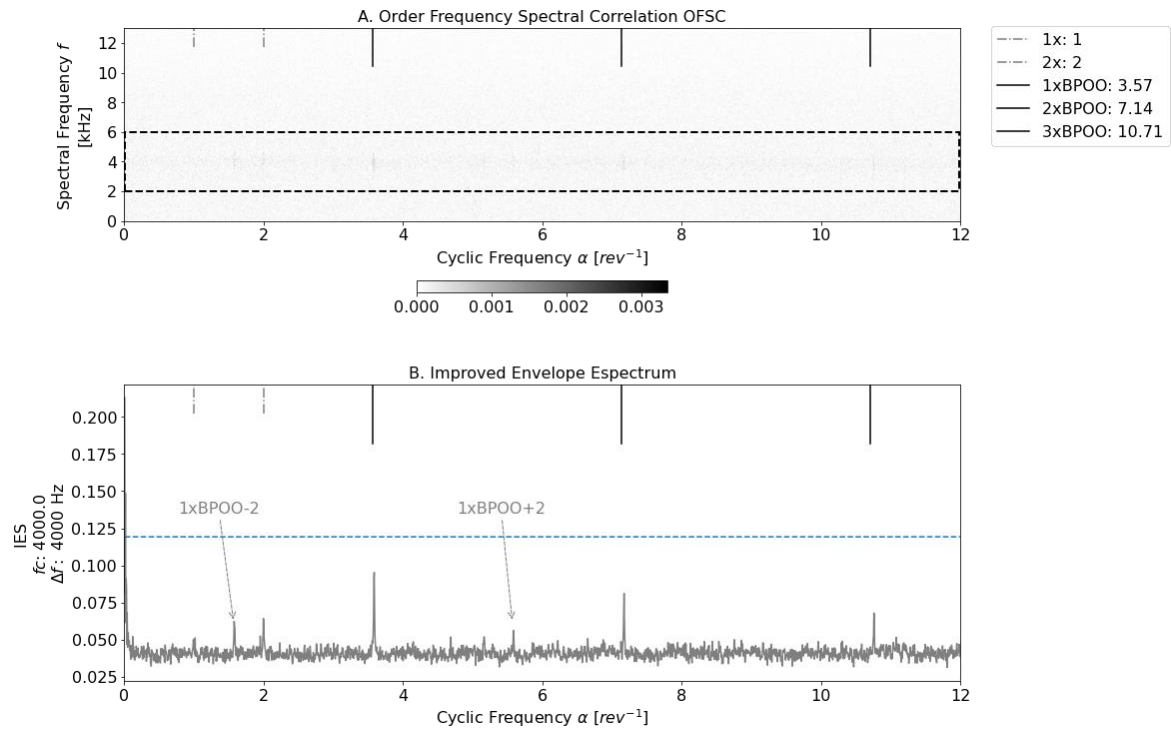
In general, for the case of Outer Race fault, when the dynamic load is considerably stronger than static load, the diagnosis process is difficult since the modulation generated by synchronous components spread the energy of strikes. On the other hand, when static load is the dominant component, diagnosis is more straightforward and the peaks at BPOO exceed statistical threshold.

To further illustrates this idea, let consider the signal S-OR-7, which is the one with the minimum modulation coefficient. The OFSC map is shown in Figure 5-8-A. The Figure 5-8-B, shows the IES estimated from the spectral range between 2 and 6 kHz. Although a clear discrete component is observed at cyclic frequency of BPOO, the energy of this discrete component does not overcome the hypothesis threshold. It is worth to note the presence of some discrete peaks on the at cyclic order  $2\times$ , and modulation sidebands at  $BPOO - 2x$ . Although his energy is so low, there are an effect of Synchronous modulations (Dynamic Load Effect). The fact it appears at  $2\times$ , instead of  $1x$ , is explainable given the extreme low modulation coefficient. The reader could be free to consult the



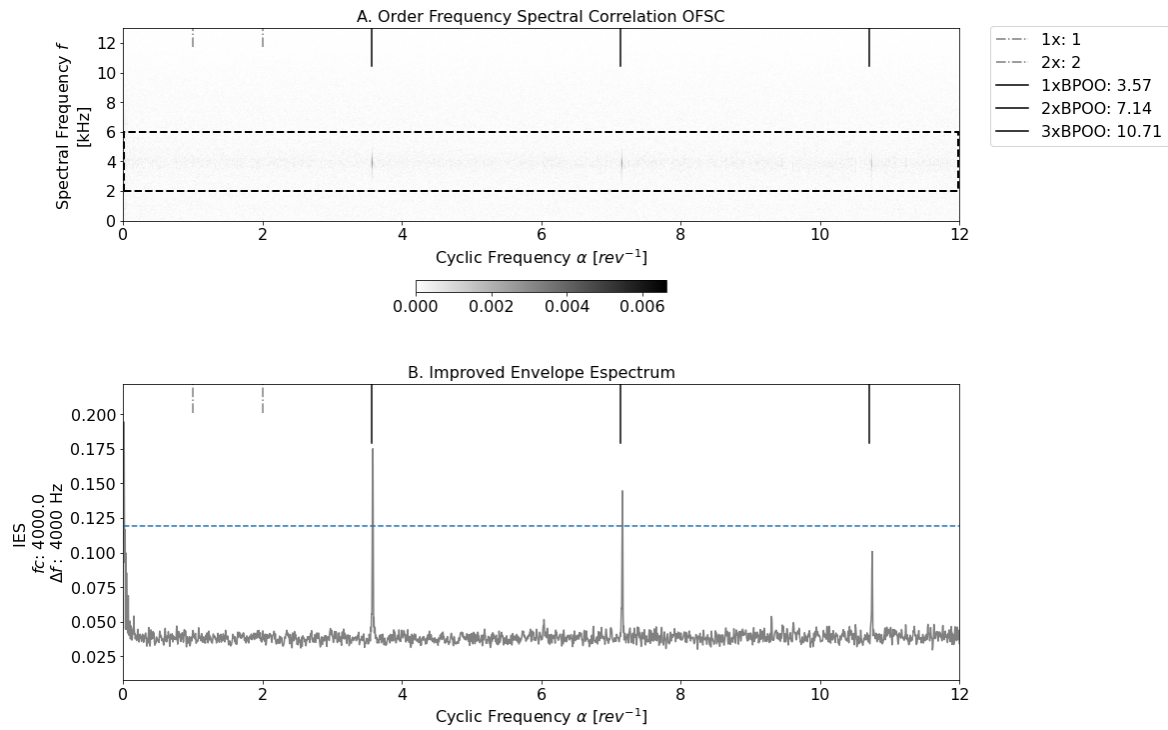
Appendix 9.2 and see the IES for the signal S-OR-4 and 5, in such cases modulations at  $1\times$  occurs, maybe because modulation coefficient are near to 1.

Figure 5-8. 'S-OR7' signal OFSC and IES



Now, consider the results for Signal S-OR-2, which is the case one with major modulation coefficient, this is illustrated on Figure 5-9, which illustrates the Order Frequency Spectral Correlation and the IES estimated at a spectral frequency between 2 and 6 kHz. A clear diagnosis could be established from the results shown in Figure 5-9, since clear peaks at BPOO are evidenced. Also is noticeable that those peaks exceed statistical threshold.

Figure 5-9. 'S-OR2' signal OFSC and IES.



In contrast with the exposed on Figure 5-8, for the IES in Figure 5-9 there is no evidence of peaks at any synchronous discrete component ( $1\times$  or  $2\times$ ), neither any modulation sideband. The former is in accordance with the exposed on Equation 5-2, since the static load is predominant over dynamic one.

## 5.2.2. Inner Race Simulated Fault

The Table 5-5 summarizes the result obtained for experimental simulations in the case of Inner Race Fault. If the cyclic orders  $\alpha = 1, 2, BPOI$  and  $2 \times BPOI$  exceed the statistical threshold they were labeled as ‘Y’ in the latest columns of Table 5-5. In the opposite case were labeled as ‘N’. The modulation coefficient  $\bar{R}$  is estimated as indicates Equation 5-7. This is defined as the quotient between the dynamic load and static load, i.e. the relation between term  $me(2\pi\dot{\theta})^2 \cos(\psi)$  and term  $Mg$  of Equation 5-3.

$$\text{Equation 5-7} \quad \bar{R} = \frac{4\pi^2 me \cos(\psi) (\dot{\theta}_2^2 + \dot{\theta}_2 \dot{\theta}_1 + \dot{\theta}_1^2)}{Mg}$$

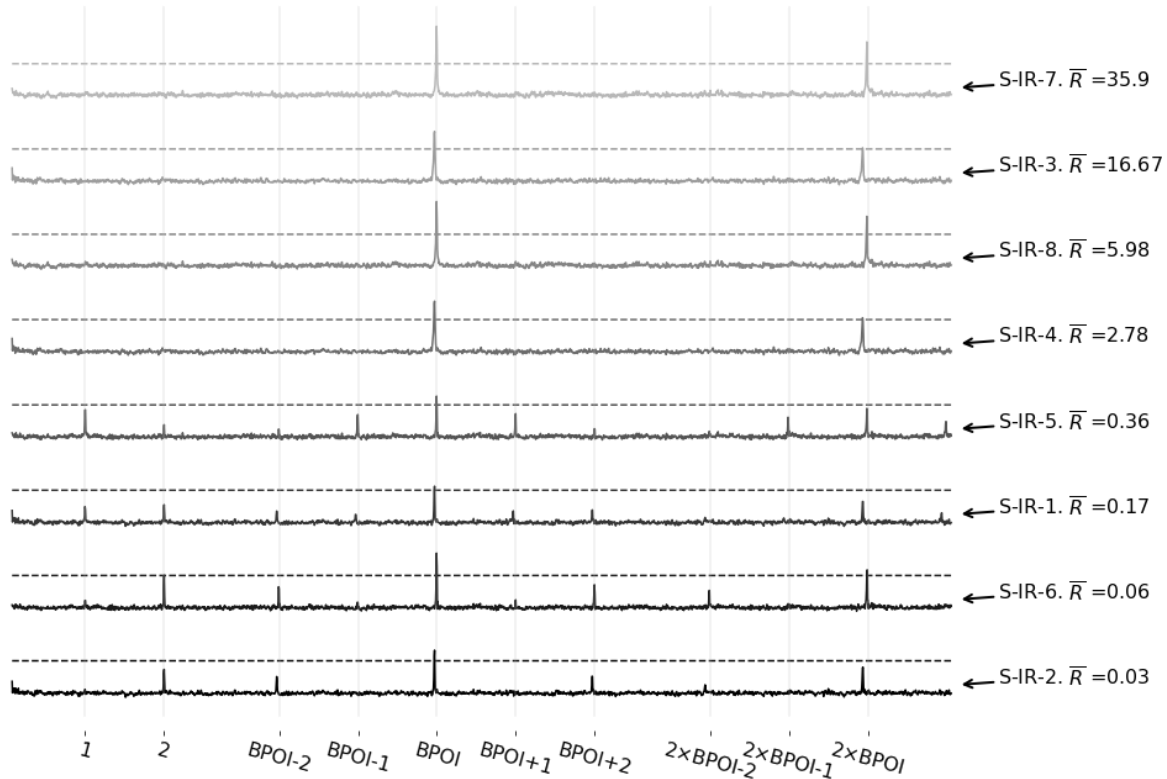
where  $Mg$  stands for the Rotor and shaft weight,  $me$  stands for the unbalance charge, and  $\dot{\theta}$  stands for instantaneous rotational speed, as it was exposed on Table 5-1.

Table 5-5. Summary of loads for Inner Race Simulated signals

Run Label	Static Load [N]	Static Unbalance [kg m]	Acceleration Freq. range	Range of Dynamic Load [N]	$\bar{R}$	1x	2x	1xBPOI	2xBPOI
S-IR-1	9.8	$1.5 \times 10^{-4}$	3 rev/s <sup>2</sup> 10 – 25 Hz	0.5 – 3.2	0.17	N	N	Y	N
S-IR-2	58.8	$1.5 \times 10^{-4}$	3 rev/s <sup>2</sup> 10 – 25 Hz	0.5 – 3.2	0.03	N	N	Y	Y
S-IR-3	9.8	0.015	3 rev/s <sup>2</sup> 10 – 25 Hz	51.3 – 320.5	16.67	N	N	Y	Y
S-IR-4	58.8	0.015	3 rev/s <sup>2</sup> 10 – 25 Hz	51.3 – 320.5	2.78	N	N	Y	Y
S-IR-5	9.8	$1.5 \times 10^{-4}$	6 rev/s <sup>2</sup> 10 – 40 Hz	0.5 – 8.2	0.36	N	N	Y	N
S-IR-6	58.8	$1.5 \times 10^{-4}$	6 rev/s <sup>2</sup> 10 – 40 Hz	0.5 – 8.2	0.06	N	Y	Y	Y
S-IR-7	9.8	0.015	6 rev/s <sup>2</sup> 10 – 40 Hz	51.3 – 820.5	35.90	N	N	Y	Y
S-IR-8	58.8	0.015	6 rev/s <sup>2</sup> 10 – 40 Hz	51.3 – 820.5	5.98	N	N	Y	Y

The Figure 5-10 illustrates the IES obtained from signals S-IR-1 to S-IR-8, ordered according to modulation coefficient  $\bar{R}$ . Each signal IES, and their corresponding statistical threshold are drawn with different gray tone. Particular cyclic orders are labeled on horizontal axis. Additional view of those results are presented on annex in section 9.4.

Figure 5-10. IES comparison for Inner Race Simulations Signals.

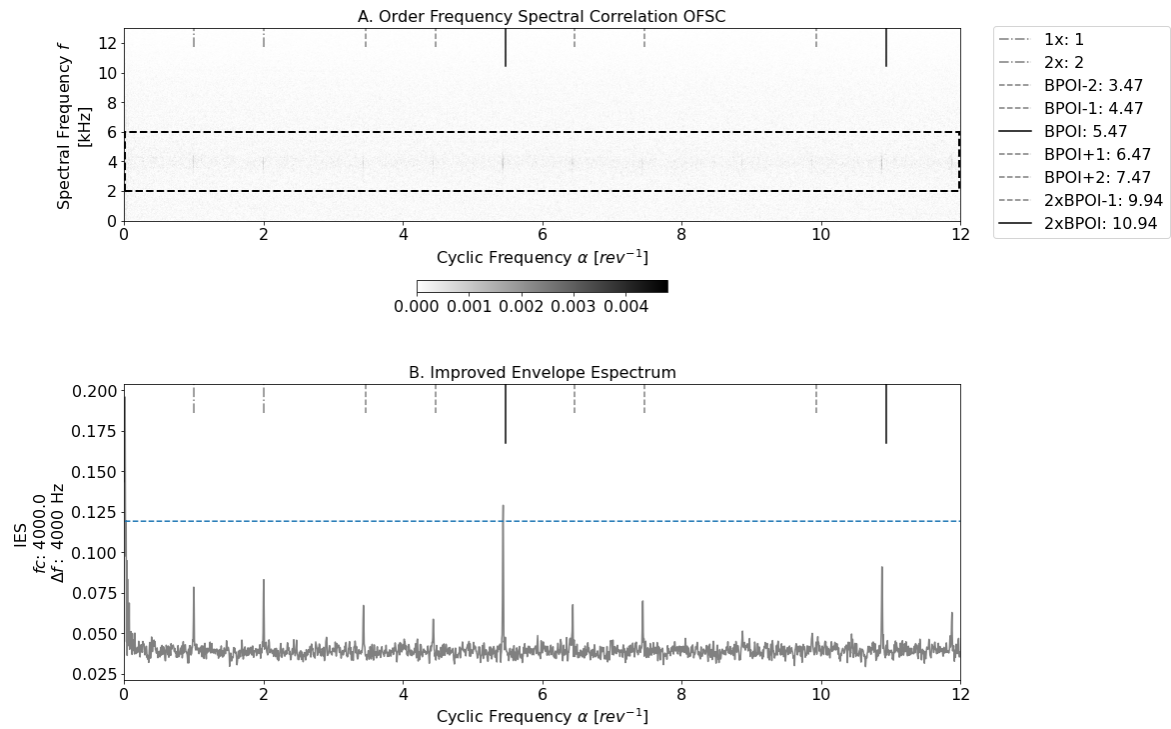


In Figure 5-10, all the cases presented the  $1xBPOI$  order exceeds the statistical threshold. It is noticeable the effect of modulation coefficient on the behaviour of the IES. As bigger the modulation coefficient, the peaks at  $BPOI$  and  $2xBPOI$  exceed in major proportions the statistical threshold (drawn with dashed lines for each case). It is also noticeable the fact that side bands tends to disappear as  $\bar{R}$  increases. This latest behaviour is in accordance with exposed on Equation 5-3, since, as  $\bar{R}$  is higher, indicates the term  $Mg$  is low in comparison with  $me\dot{\theta}^2 \cos(\psi)$  term. The former implies that sidebands at synchronous orders are decimated.

From previous observations, when an Inner Race fault occurs, higher static load leads to sidebands, which reduce the peaks at  $BPOI$ .

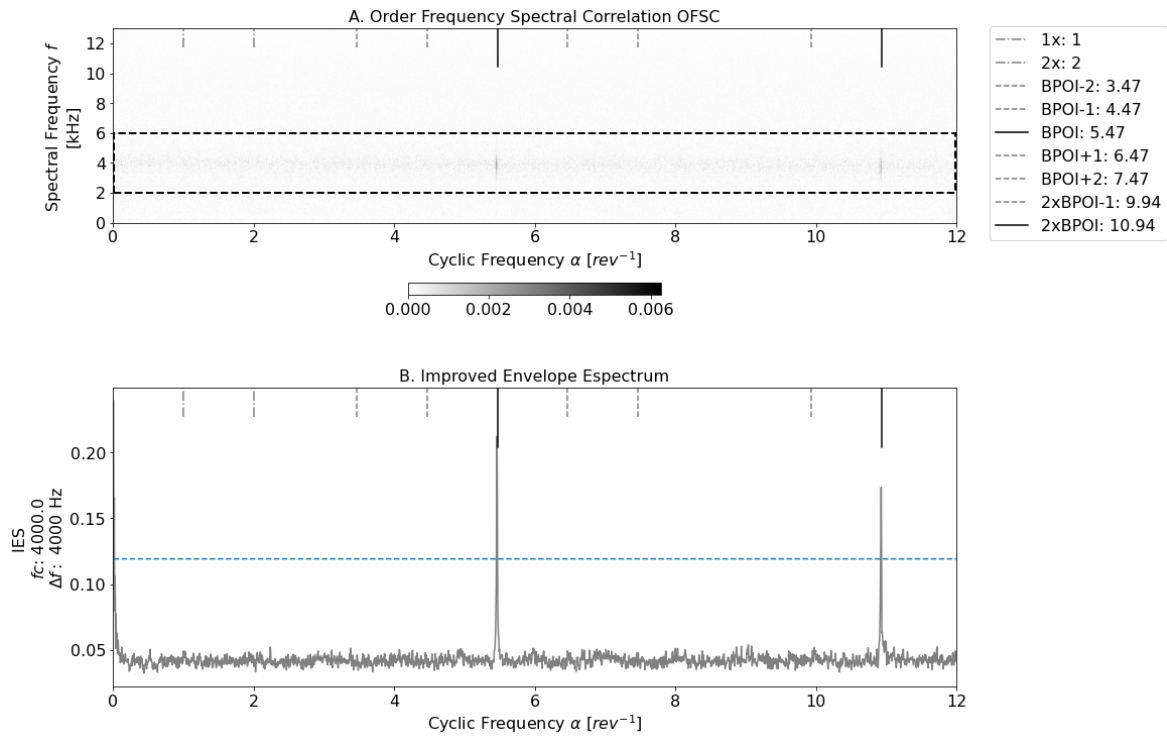
Signal S-IR-1 appears to be the one with a less confidence about cyclostationary behaviour at  $BPOI$ . To further exemplify this, consider the OFSC map for S-IR-1 shown in Figure 5-11-A and the IES estimated from the spectral range between 2 and 6 kHz shown in Figure 5-11-B. A clear peak exceeding statistical threshold is observed at  $1xBPOI$ . Peaks at  $1x$ ,  $2x$ ,  $2xBPOI$  and some synchronous sidebands are noticeable although they do not exceed statistical threshold.

Figure 5-11. ‘S-IR-1’ signal OFSC and IES.



On the other hand, from Figure 5-10, it is possible to observe the signal with major cyclostationary behaviour is the S-IR-7. In fact, that is the one with the biggest modulation coefficient  $\bar{R}$ . The OFSC map is illustrated in Figure 5-12-A and the IES is illustrated in Figure 5-12-B. Clear peaks at discrete cyclic frequencies of BPOI and 2xBPOI are evident. Those peaks exceed the statistical threshold considerably. It is also worth to note that no modulation sidebands are recognized, neither peaks at synchronous components such as 1x and 2x. The former is explained by the dominant effect of dynamic load, i.e. high modulation coefficient.

Figure 5-12. ‘S-IR-1’ signal OFSC and IES.



In general, the performance of method shows a good result for the case of inner race fault. The behaviour of the results are in accordance with the amplitude modulation function used to simulate the IR fault signals.

### 5.2.3. Ball Simulated Fault

Table 5-6 shows the results obtained for the case of Rolling Element (Ball) Fault simulation signals. In this case, it results important to search for orders such as  $\alpha = FTO, 2 \times FTO, 3 \times FTO$  and even harmonics of BSO such as  $2 \times BSO$  and  $4 \times BSO$ . The results of IES on those orders are summarized on right columns of Table 5-6. Similar to the previous cases, if the IES exceed the statistical threshold at those orders, they were labeled as ‘Y’. In the opposite case were labeled as ‘N’. Additional results of this table can be seen on annex of section 9.5.

The modulation coefficient  $\bar{R}$  is estimated as indicates Equation 5-8. This is defined as the quotient between the dynamic load and static load, i.e. the relation between term  $4\pi^2 me\dot{\theta}^2 \cos(\psi)$  and term  $Mg$  of Equation 5-4.

$$\text{Equation 5-8} \quad \bar{R} = \frac{Mg \cos(\psi)}{me\dot{\theta}_1\dot{\theta}_2}$$

where  $Mg$  stands for the Rotor and shaft weight,  $me$  stands for the unbalance charge, and  $\dot{\theta}$  stands for instantaneous rotational speed, as it was exposed on Table 5-1.

The interest on even multiples of BSO is reasonable, since per each revolution on rolling element, the defect would make double contact and so double strike, corresponding to contact with inner and outer race.

Table 5-6. Summary of loads for Rolling Element Fault Simulated signals

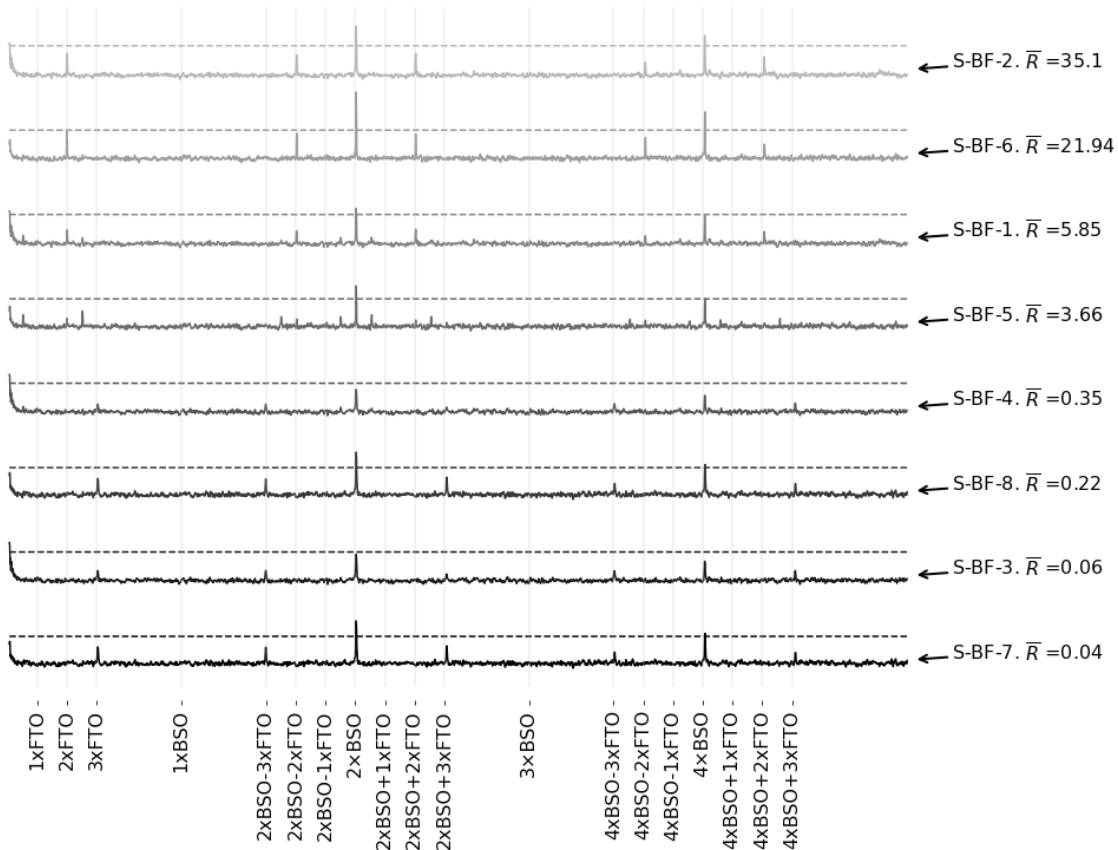
Run Label	Static Load [N]	Static Unbalance [kg m]	Acceleration Freq. range	Range of Dynamic Load [N]	$\bar{R}$	1xFTO	2xFTO	3xFTO	2xBSO	4xBSO
S-BF-1	9.8	$1.5 \times 10^{-4}$	3 rev/s <sup>2</sup> 10 – 25 Hz	0.5 – 3.2	5.85	N	N	N	Y	Y
S-BF-2	58.8	$1.5 \times 10^{-4}$	3 rev/s <sup>2</sup> 10 – 25 Hz	0.5 – 3.2	35.10	N	N	N	Y	Y
S-BF-3	9.8	0.015	3 rev/s <sup>2</sup> 10 – 25 Hz	51.3 – 320.5	0.06	N	N	N	N	N
S-BF-4	58.8	0.015	3 rev/s <sup>2</sup> 10 – 25 Hz	51.3 – 320.5	0.35	N	N	N	Y	Y
S-BF-5	9.8	$1.5 \times 10^{-4}$	6 rev/s <sup>2</sup> 10 – 40 Hz	0.5 – 8.2	3.66	N	N	N	Y	Y
S-BF-6	58.8	$1.5 \times 10^{-4}$	6 rev/s <sup>2</sup> 10 – 40 Hz	0.5 – 8.2	21.94	N	N	N	Y	Y
S-BF-7	9.8	0.015	6 rev/s <sup>2</sup> 10 – 40 Hz	51.3 – 820.5	0.04	N	N	N	Y	Y
S-BF-8	58.8	0.015	6 rev/s <sup>2</sup> 10 – 40 Hz	51.3 – 820.5	0.22	N	N	N	Y	Y

To discuss the modulation coefficient  $\bar{R}$ , is important to note the fact that amplitude modulation function of Equation 5-4, does not represent a typical case, since both components are associated to a periodical function. For convenience, the modulation coefficient was defined in a similar manner than the case exposed on Equation 5-6, i.e. similar to the Outer Race fault case. This definition is made based on the similitude between function exposed of Equation 5-4 and Amplitude Modulation from Single Side Band, usually called as SSB in literature [53]. In such case, the carrier order corresponds to 1-FTO, while modulation order corresponds to 1-2FTO.

In Figure 5-13 the IES from simulated ball fault signals are shown. Statistical thresholds are drawn for each case with horizontal dashed lines. Vertical cursors at harmonics of FTO, harmonics of BSO, and FTO sidebands are also drawn.

Although modulation coefficient does not represent a good descriptor for the behaviour of IES, the results on Figure 5-13 are organized according to modulation coefficient  $\bar{R}$  to save uniformity with respect other cases.

Figure 5-13. IES comparison for Rolling Element Faults Simulations Signals.

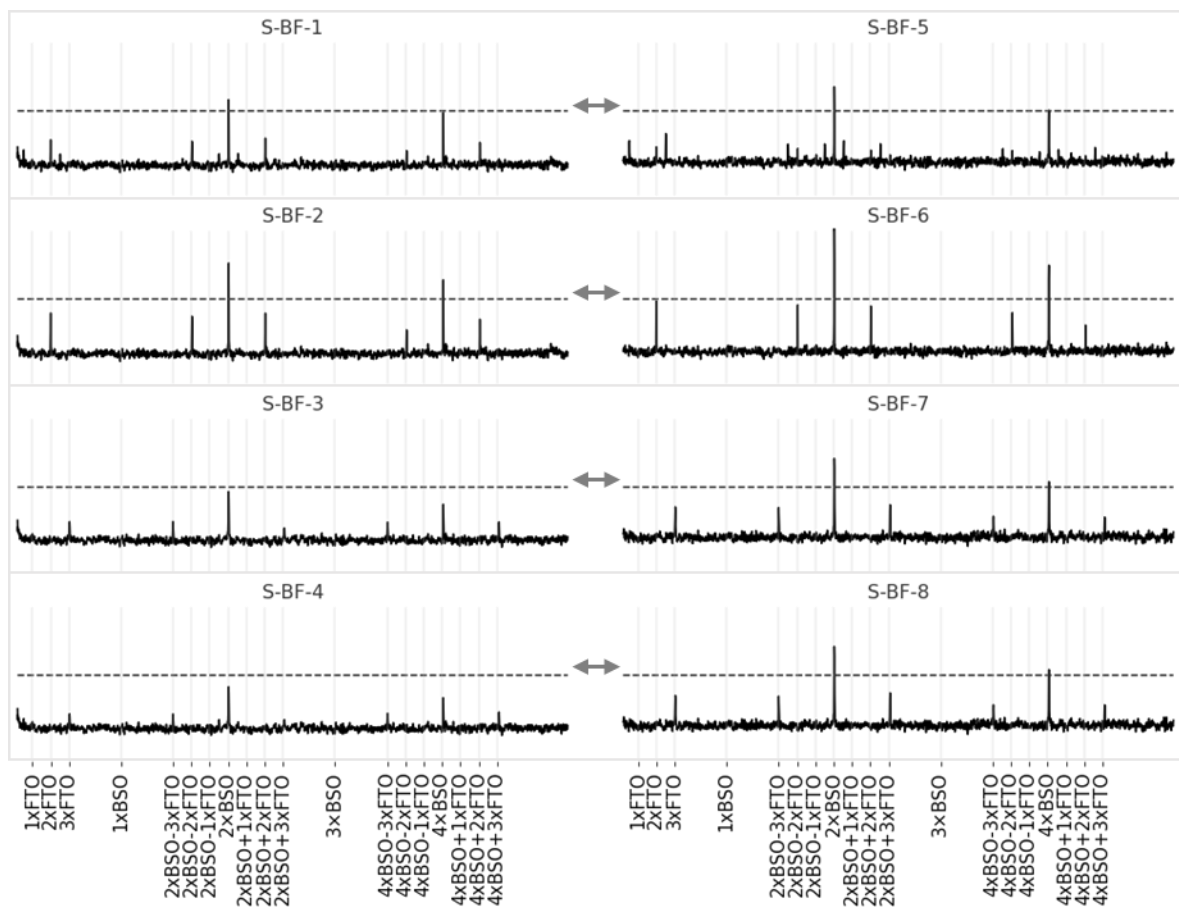




Even if modulation coefficient is not a good descriptor, a pattern could be observed if comparisons are carried out between signals with the same loads but with different dynamic ranges (see Table 5-6). To illustrate this, consider Figure 5-14 at which the results previously exposed on Figure 5-13 are reorganized.

For instance, consider the results of signals S-BF-1 and S-BF-5, both have been generated with the same loads, but S-BF-5 is modeled with higher acceleration. For the S-BF-5 the diagnosis is more straightforward since the peaks are higher at  $2xBSO$ . Similar conclusions could be seen for pairs such as S-BF-2 and S-BF-6, and so on.

Figure 5-14. IES for Rolling Element Faults Simulations Signals – Horizontal Comparison.



For the case of Rolling Element Fault (Ball fault), the case S-BF-4 is the one with less evidence of fault, i.e. with less evidence of cyclo-stationarity at  $2xBSO$ . The OFSC map and the IES for S-BF-4 are illustrated in Figure 5-15. Cursors at  $2xBSO$ ,  $4xBSO$  and FTO sidebands are drawn. Although IES at  $2xBSO$  does not exceed threshold, it is a notorious peak on IES for this particular case. Not considerable components at FTO appear on Figure 5-15.

Figure 5-15. 'S-BF-4'signal OFSC and IES.

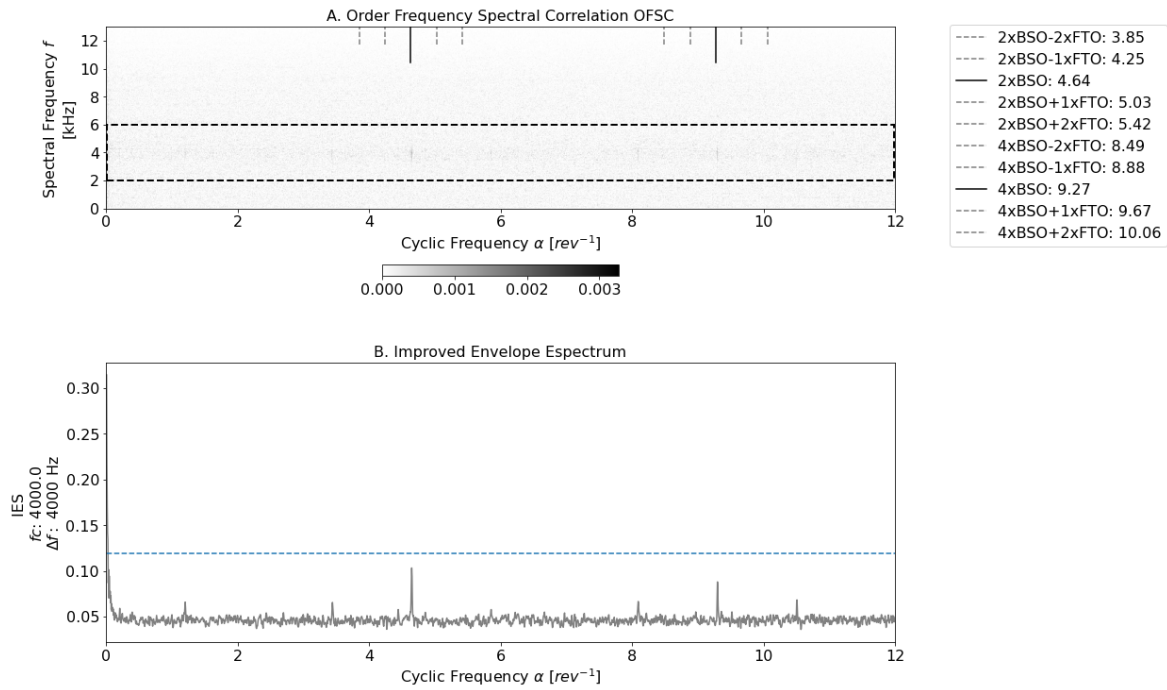
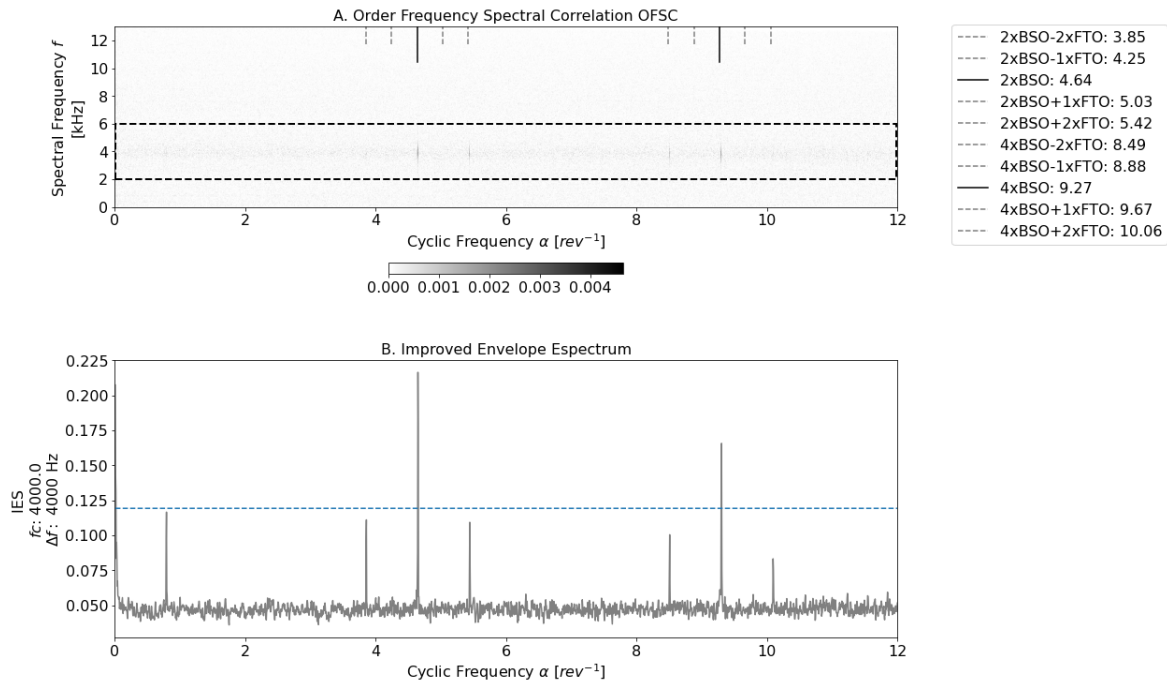


Figure 5-16. 'S-BF-6'signal OFSC and IES.

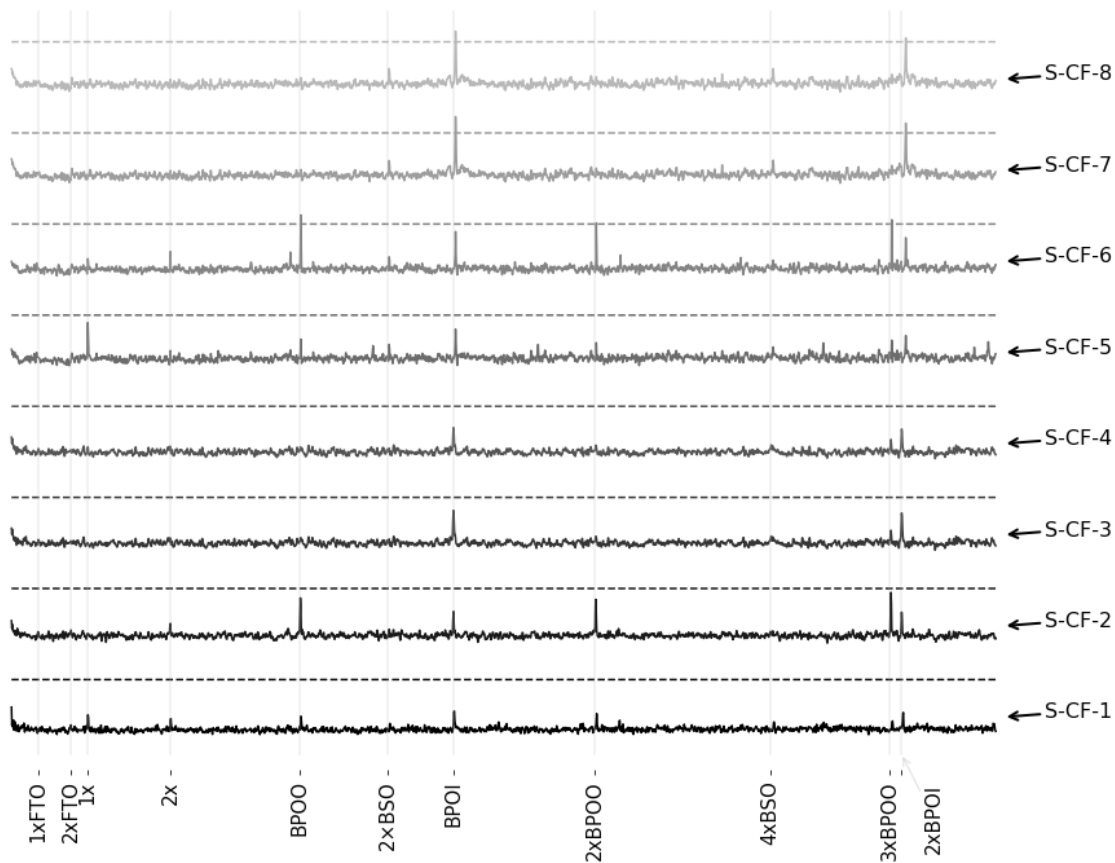


On the other hand, the case with higher level of cyclostationarity at  $2xBSO$  is the S-BF-6. The results for this case are further illustrated on Figure 5-16, where the OFSC map and the IES have been drawn. Clear peaks at cyclic orders  $2xBSO$  and  $4xBSO$  are evident since they exceed the threshold. In addition, FTO sidebands are evident on Figure 5-16-B.

## 5.2.4. Simulated Combination Fault

In this section, results of simulations for combination faults are presents. Simulations were carried considering the presence of faults on outer race, inner race and rolling element at same time. The loads, acceleration and rotational speed kept equal to the previous cases, i.e. similar to exposed on Table 5-3. Results obtained from combination fault are shown in Figure 5-17, where the IES is plotted against cyclic order  $\alpha$ . The statistical thresholds are plotted with horizontal dashed lines. Vertical cursors at harmonic of BPOO, BPOI, 2xBPO and FTO are drawn. In addition, cursors at 1x and 2x are also drawn.

Figure 5-17. IES comparison for Combination Fault Simulations Signals.

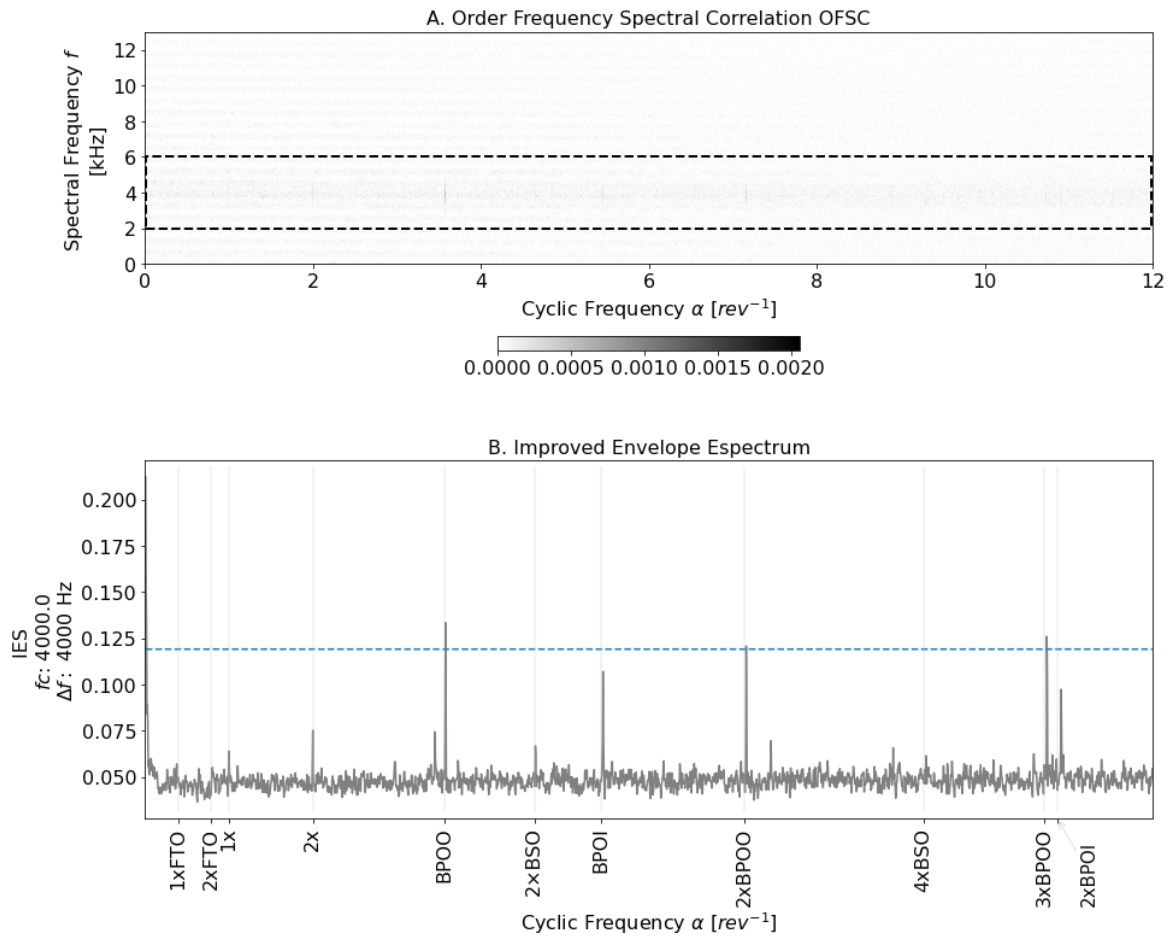


Is worth noting the fact, that across the IES shown in Figure 5-17 the major part of signals does not have any cyclic frequency with statistical evidence of cyclo-stationarity. Only for cases S-CF-6, S-CF-7 and S-CF-8 there is some cyclic order which exceeds the statistical threshold. However, clear peaks at BPOO and BPOI are evident across many of the signals analyzed. On the other hand, across all the cases simulated with combination faults, Cyclostationarity at BSO and FTO is difficult to be

established, which in fact shows that diagnosis of rolling element is the most difficult case. This situation was also presented during experimental test.

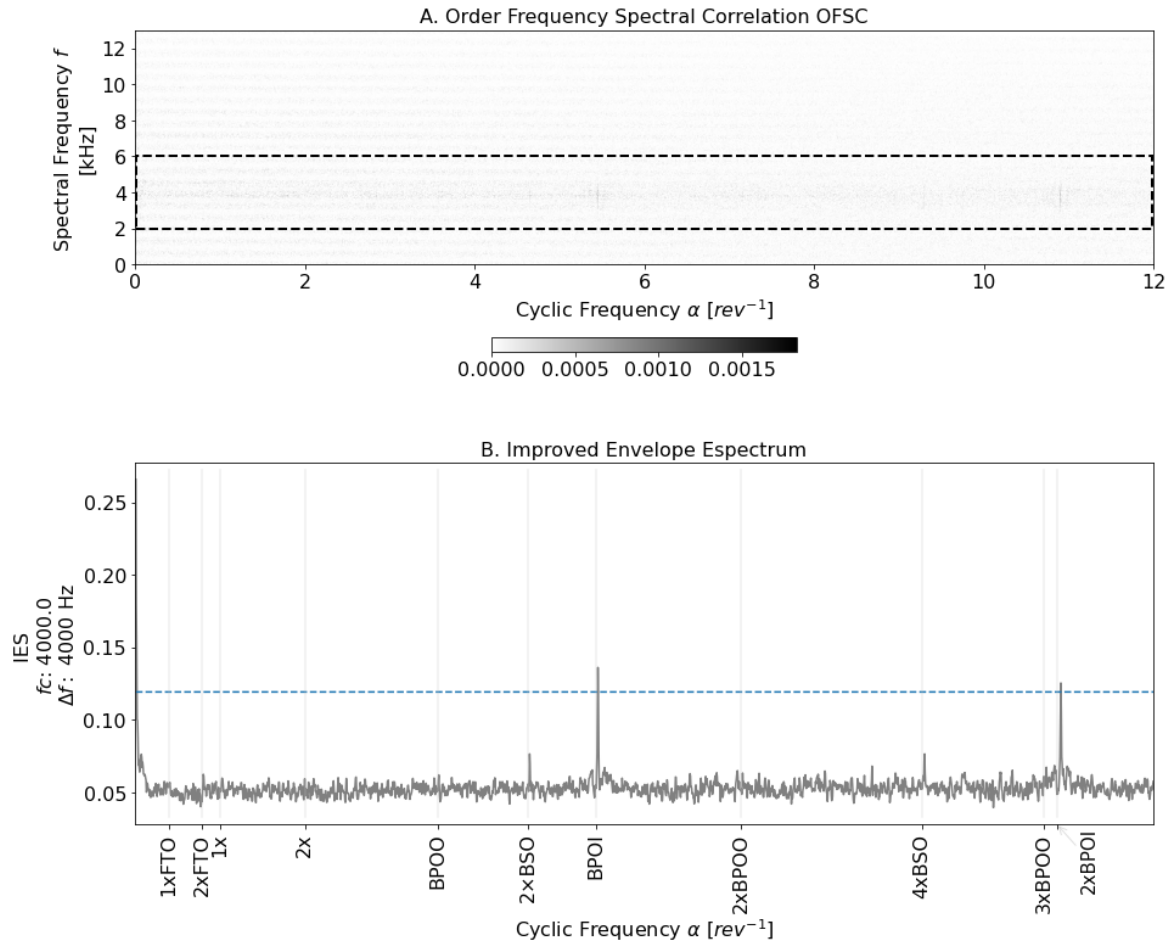
To illustrate some of the results previously presented, consider the case S-CF-6, for which the OFSC map and IES are illustrated in Figure 5-18. Cursors are settled similarly to the ones in Figure 5-17. Is observable than little peak arrive at order  $2xBSO$ , but their magnitude are not relevant.

Figure 5-18. 'S-CF-6'signal OFSC and IES.



The case S-CF-8 is illustrated in Figure 5-19. Similar to the S-CR-6 case. In this case, clear peaks are evident at BPOI and  $2xBPOI$  but, although there is a little peak at  $2xBSO$  it is no relevant.

Figure 5-19. ‘S-CF-8’ signal OFSC and IES.



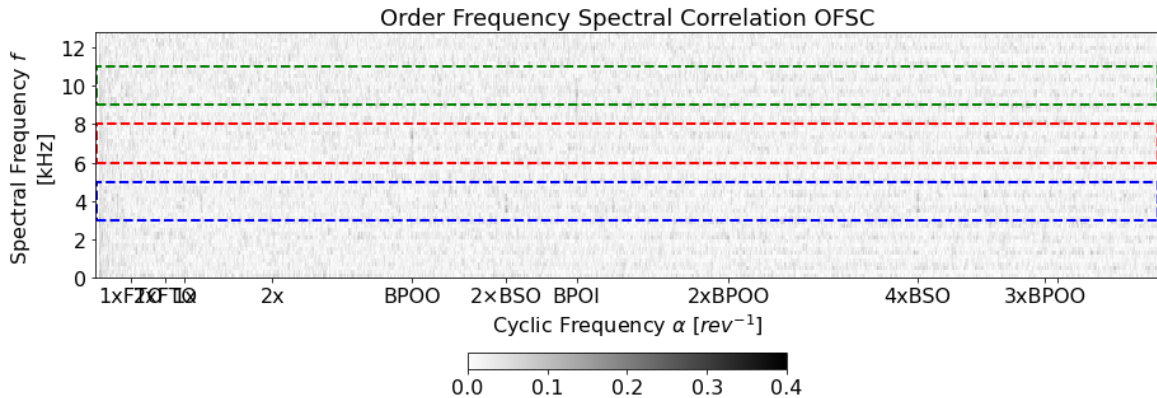
At this point, considering a combination of fault case results interesting to explore the role of the demodulation band. In this sense, consider an additional simulated signal, the one consisting of a combination of faults, but with the particular behavior that each one of the faults was simulated using different impulse response function  $h(t)$  through Equation 5-1. For instance, the Rolling Element Fault was simulated with an expected resonance frequency of 4 kHz, whereas Outer Race and Inner race were simulated with resonance frequencies of 7 kHz and 10 kHz respectively, as it is described in Table 5-7.

Table 5-7. S-CF-9 Signal Description.

Label	S-CF-9
Type Fault	Combination Fault
Load and Speed Conditions	Similar to run 4 on Table 5-3
Ball Fault Resonance Frequency [kHz]	~ 4
Outer Race Resonance Frequency [kHz]	~ 7
Inner Race Resonance Frequency [kHz]	~ 10

For the previously introduced signal S-CF-9, the Order Frequency Spectral Coherence OFSCoh map is shown in Figure 5-19. Some vertical patterns could be observed, but is noticeable those patterns are at different spectral frequency locations, as it is highlighted by the three rectangles drawn on the figure.

Figure 5-20. Order Frequency Spectral Coherence Map for Combination Fault S-CF-9.

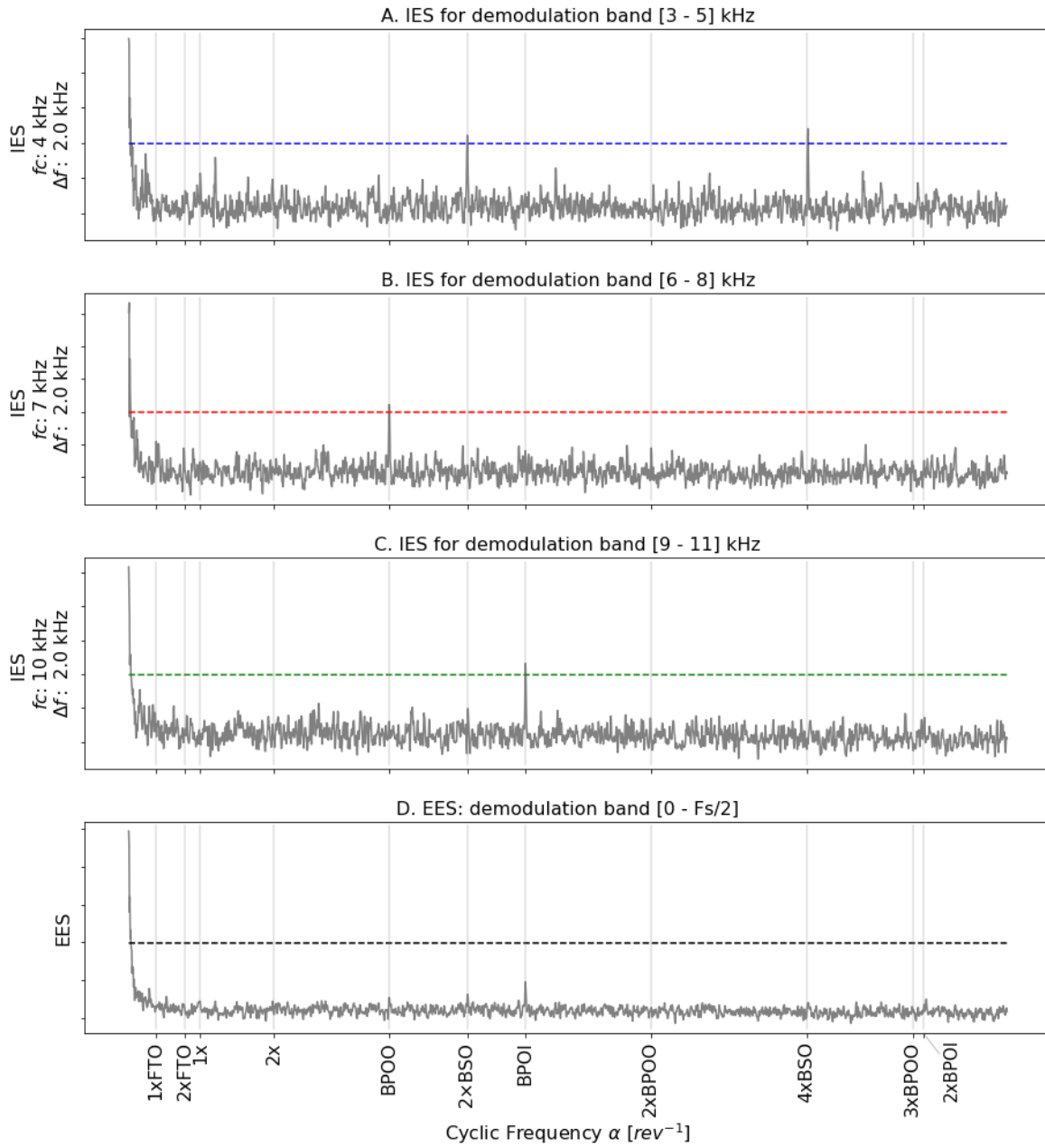


The three rectangles drawn in Figure 5-19 are centered at spectral frequencies of 4, 7, and 10 kHz, which are the resonance frequencies for each type of fault, as exposed in Table 5-7. If each one of the frequency bands, illustrated by the three rectangles, is considered for demodulation, the obtained IES would be as illustrated in Figure 5-21-A to Figure 5-21-C. The EES is also plotted in Figure 5-21-D, which is the equivalent of IES when the entire spectral frequency axis is considered.

In Figure 5-21-A, a clear sign of Rolling Element (Ball) fault is evident, once a peak at  $2xBPOO$  is exceeding the threshold. This was expected since the demodulation band contains the simulated resonance frequency. Similarly happens for Figure 5-21-B and Figure 5-21-C, showing signs of faults at outer race and inner race respectively. However, is worth noting that for Figure 5-21-D demodulation is not accurately enough to show any significant sign of fault.

From the previous discussion, it is important to highlight that when an adequate demodulation band is used, the diagnosis could be improved.

Figure 5-21. IES at different spectral frequency bands for S-CF-9. A) Demodulation for Ball Fault. B) Demodulation for Outer Race Fault. C) Demodulation for Inner Race Fault. D) EES.





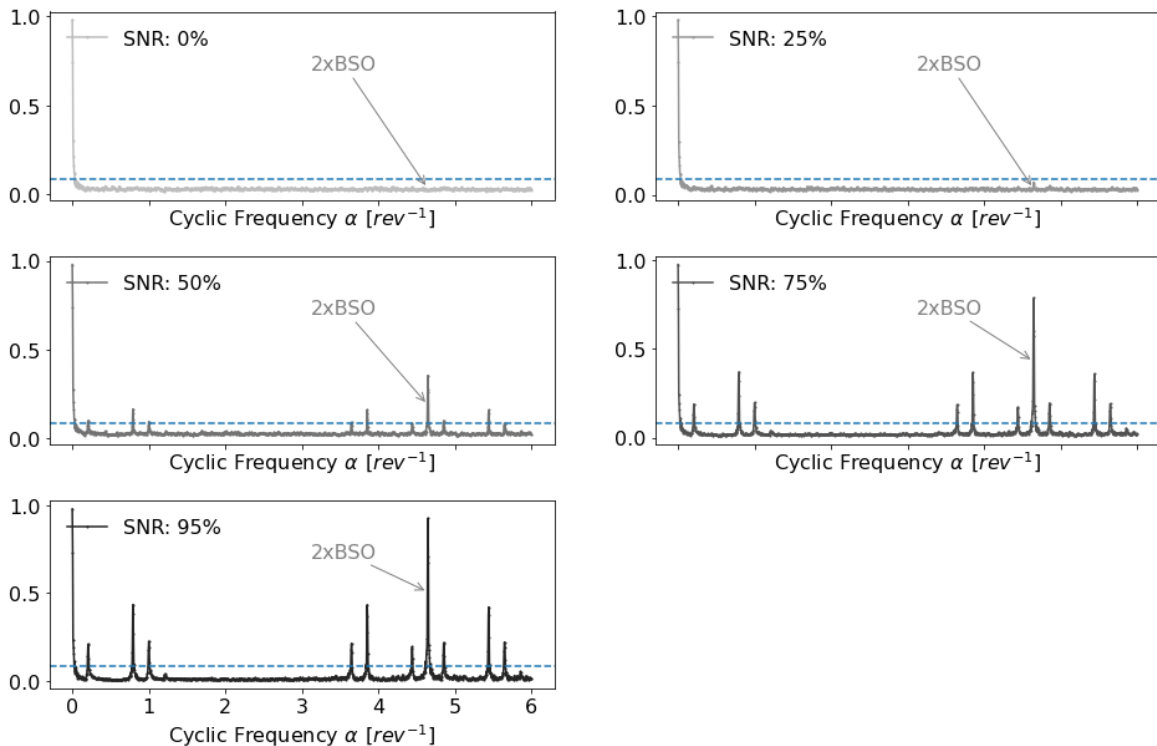
### 5.3 Other Effects Observables on Simulated Signals.

On this section, some parameters used for the simulation signals are discussed and their effect is exposed. In particular, it results from interest to discuss about signal to noise ratio, the effect of slippage and what is the effect generated when a surface defect is spalled rather than an incipient defect.

#### 5.3.1. Effect of Signal to noise ratio

As it is expected, the diagnosis by IES is improved when the signal to noise ratio is high. To illustrate this, consider Figure 5-22, which shows the IES for a ball fault, under load conditions similar to prior simulated signal ‘S-BF-01’ (See section 5.2.3 and Table 5-6). On Figure 5-22, the IES is shown for different levels of signal to noise ratio –SNR.

Figure 5-22. Effect on Signal to Noise Ratio.

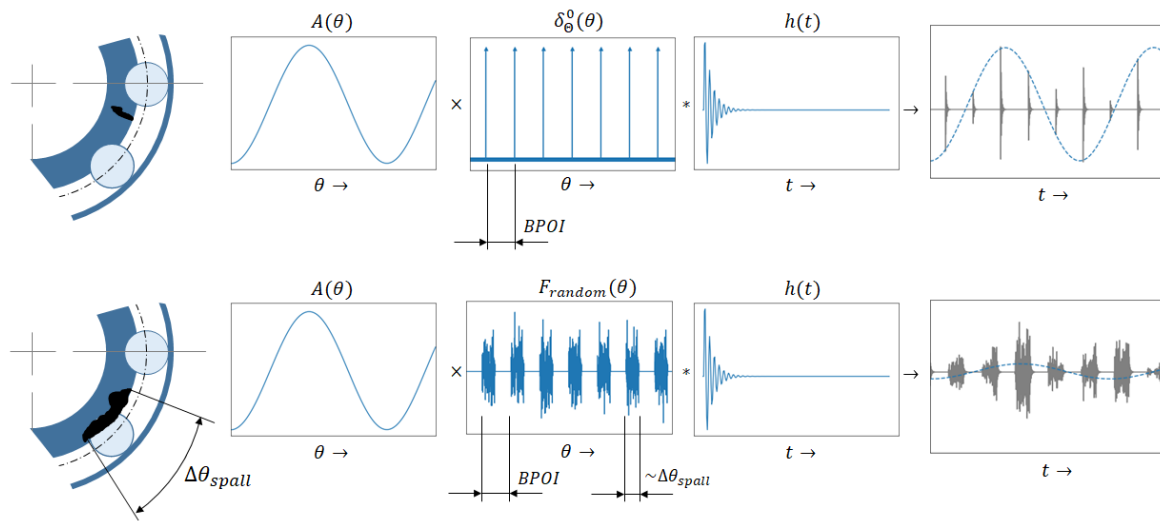


It results interesting to note that as noise is increased, the IES merges to a delta on the zero-cyclic frequency. This behaviour indicates there is no presence of any cyclostationarity and their spectral representation is well defined by their Power Spectral Density, i.e.  $SC(0, f)$ .

### 5.3.2. Effect of Impulse distribution

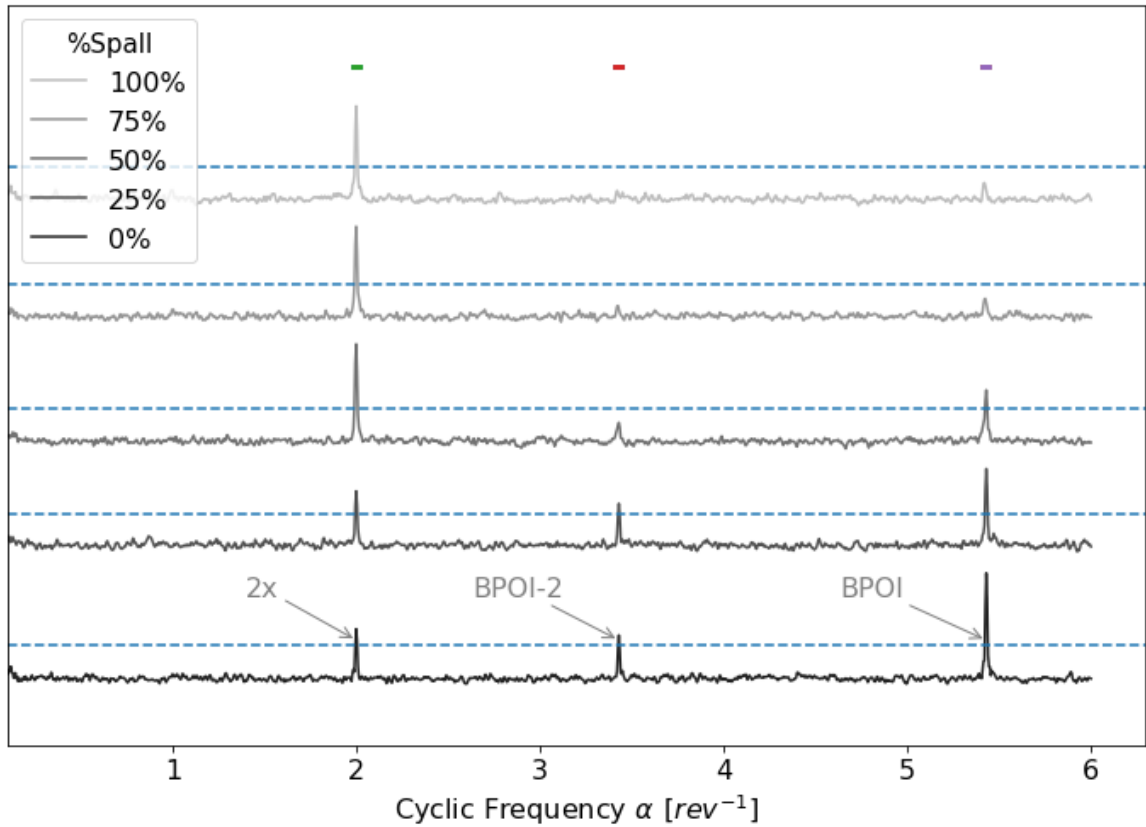
On the model exposed in section 5.1, described by Equation 5-1, the vibration is mainly the response of a series of periodical strikes, accompanied by an amplitude modulation signal. In this sense, the periodical strikes are modeled as a series of periodical delta functions. However, if the failure is not an incipient fault, i.e. their length has increased or it have been growth among the race, the vibration that is generated just at failed surface contact could not be modeled as a delta. In contrast, it more convenient to model it as a random force, generated by excessive friction and contact stresses. This situation is illustrated on Figure 5-23 for the case of an inner race fault.

Figure 5-23. Effect of spall size on vibration generated



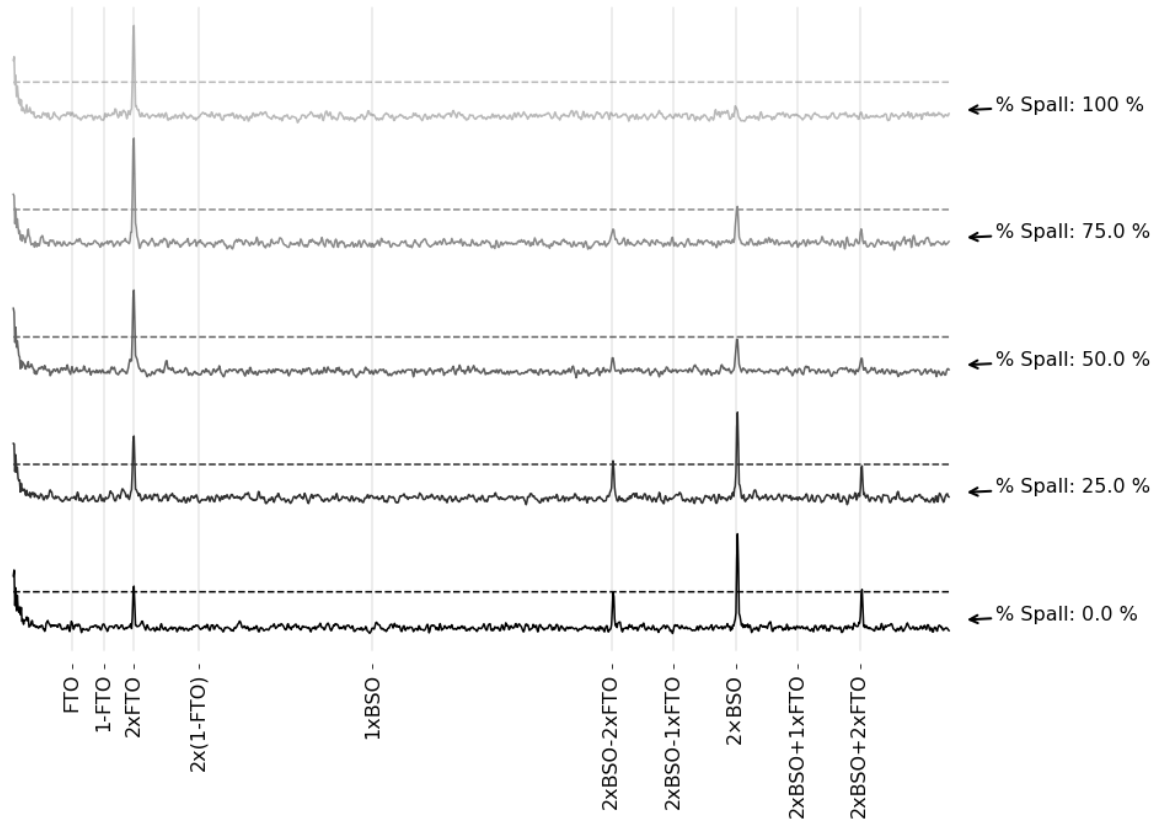
For the case illustrated, the periodicity of excitations is preserved, since the spall size is not large enough to capture two or more consecutive rolling elements. However this is not the most general case, in such case, the spall size could be sufficiently large to capture the position of various rolling elements. In those cases, is highly probably the BPOI order periodicity would be loosed by the combination of random forces generated by the various rolling elements captured by spall. To exemplify this, consider the Figure 5-24, where the IES is plotted against the spall size. The spall size is modeled as a percentage of  $1/BPOI$ , as illustrated in Figure 5-24.

Figure 5-24. IES for different spall extension.



A similar situation is observed if the case of ball defect is considered. For example, consider Figure 5-25, in which the case of rolling element fault is simulated under different spall percentages. Particularly, for this case, loads are loads similar to S-BF-2 (see Table 5-6). As spall percentages increases the fault characteristic order  $2 \times \text{BSO}$  lose their relevance, but at the same time, exists an increase on orders such as  $2 \times \text{FTO}$ . This is explainable because the periodicity of surface impacts get loosed but the amplitude modulation is conserved. In this sense, this behaviour indicates as spall is increased the modulations orders, i.e. the orders that governs  $A(\theta(t))$  of Equation 5-4 are increased, but the periodical impacts are loosed.

Figure 5-25. Effect on Spall Percentage – Loads similar to S-BF-2.



To further illustrates the discussion on prior paragraph, consider the simulated fault on rolling under conditions equal to ‘S-BF-7’. The behaviour of IES against spall percentages is shown on Figure 5-26. Vertical cursors are settled and the results are organized according to spall percentage. Similar to previous discussion, as spall percentages increase, the cyclostationarity of fault characteristic order  $2xBSO$  is loosed, while the cyclostationary at orders such as  $2x(1-FTO)$  is increased. To conclude the comparison between Figure 5-25 and Figure 5-26, let discuss about the static load and dynamic load effect. Table 5-8 presents a comparison between values of IES for different spall percentages, according to dynamic and static loads. For the case in which statistic threshold is overcome, the value is underlined and highlighted.

Figure 5-26. Effect on Spall Percentage – Loads similar to S-BF-7.

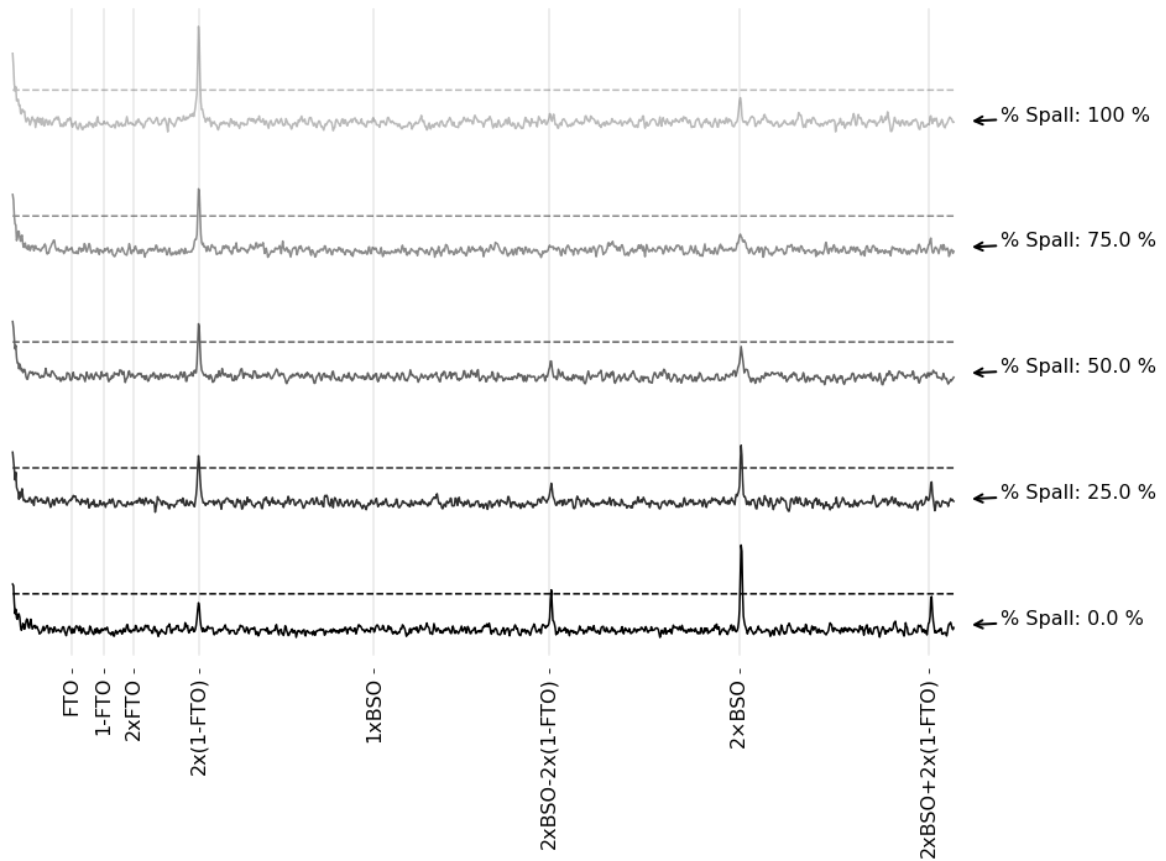


Table 5-8. Spall-percentage comparison between load conditions.

Equation 5-4 $A_{(\theta(t))} = \rho[Mg \cos(2\pi FTO \theta(t)) + me(2\pi\dot{\theta})^2 \cos(2\pi(1 - FTO)\theta(t) + \psi_o)]$							
% Spall	Run	Average Dynamic Load [N]:	Static Load [N]: $Mg$	Statistical Threshold	2xBSO	2xFTO	2x(1-FTO)
0 %	Run 2	1.93	58.8	0.084	<b><u>0.171</u></b>	<b><u>0.092</u></b>	0.034
0 %	Run 7	414.5	9.8	0.084	<b><u>0.150</u></b>	0.041	0.072
25 %	Run 2	1.93	58.8	0.084	<b><u>0.162</u></b>	<b><u>0.126</u></b>	0.038
25 %	Run 7	414.5	9.8	0.084	<b><u>0.114</u></b>	0.039	<b><u>0.100</u></b>
50 %	Run 2	1.93	58.8	0.084	0.080	<b><u>0.154</u></b>	0.032
50 %	Run 7	414.5	9.8	0.084	0.078	0.041	<b><u>0.108</u></b>
75 %	Run 2	1.93	58.8	0.084	0.088	<b><u>0.191</u></b>	0.039
75 %	Run 7	414.5	9.8	0.084	0.059	0.043	<b><u>0.121</u></b>
100 %	Run 2	1.93	58.8	0.084	0.048	<b><u>0.169</u></b>	0.036
100 %	Run 7	414.5	9.8	0.084	0.073	0.042	0.170

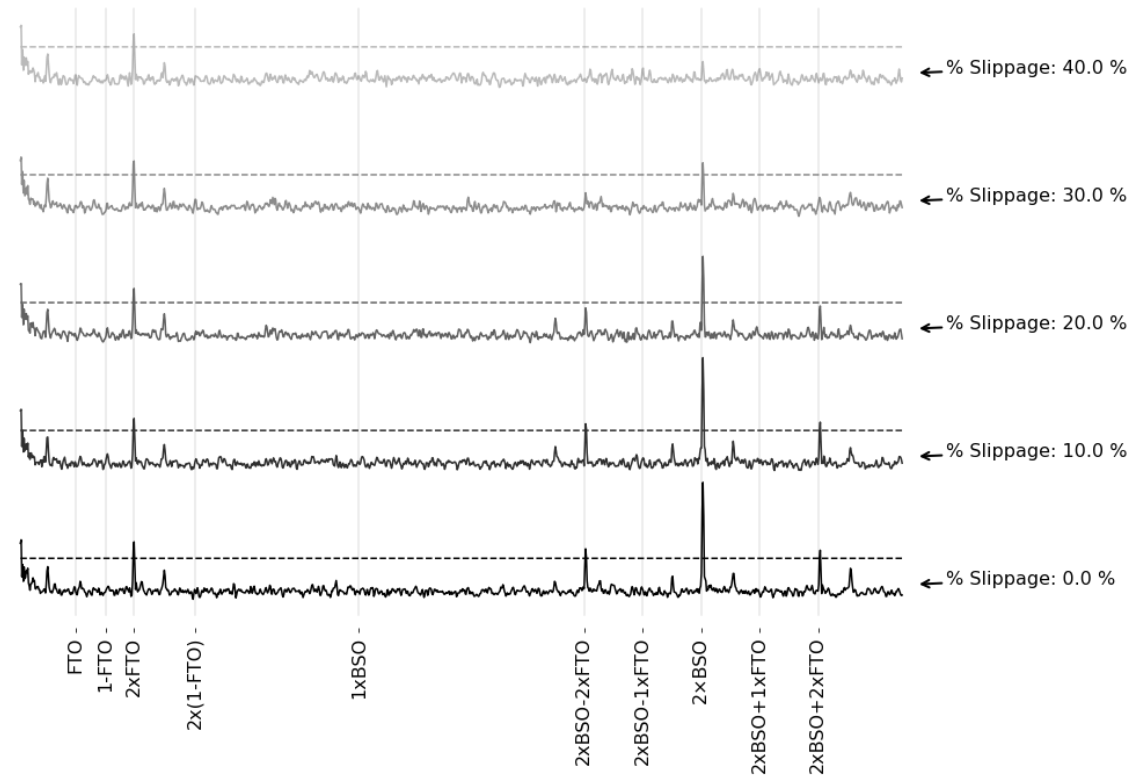
In Table 5-8, as previously discussed, modulations orders such as  $2 \times \text{FTO}$  and  $2 \times (1 - \text{FTO})$  becomes notorious and even the dominant orders for the cases at which spall percentage is big enough. Cases where loads are as 'Run2', in such case the static load is greater than dynamic load, the governing order becomes  $2 \times \text{FTO}$ , as is dictated by Equation 5-4. On the other hand, if we consider the case for which loads are similar to 'Run7', i.e. dynamic load bigger than static load, the dominant order becomes  $2 \times (1 - \text{FTO})$ , in accordance with exposed on Equation 5-4.

### **5.3.3.Effect of Random Slippage**

The model exposed in Equation 5-1 establish the vibrational response of a faulty bearing is composed by a series of periodical strikes. The periodicity of those strikes is determined by the kinematic relations of the bearing ensemble, i.e., mainly by the geometric relations of the REB. However, the periodicity of such strikes are not strictly periodic, in fact the periodical arrive of those strikes are susceptible to stochastic process, mainly by the slippage of the rolling element. The slippage could be product of ruptures in oil film formed between surfaces, changes between radial and axial loads ratios, among others.

In this section, the effect of random slippage is briefly discussed. Consider Figure 5-27, in which a simulated rolling element fault is considered under different percentages of slippage, as it was briefly explained in Figure 5-5. For this case, loads are similar to S-BF-1 (see Table 5-6).

Figure 5-27. Effect of random slippage.



In Figure 5-27, as slippage increases, at the  $2xBSO$  order, the IES is less conclusive, since the fault characteristic order tends to lose cyclostationarity, and tends to decrease until the threshold is not exceeded. Although slippage has a negative effect on the diagnosis, it seems to be less detrimental than other effects such as spall percentages and noise, as have been discussed in sections 5.3.1 and 5.3.2.

During this chapter, a model for simulating fault signals under variable speed has been exposed. The method exposed in section 4 has been applied to a series of simulated fault signals, considering four cases (Outer race fault, Inner race fault, Ball fault, and Combination of faults).

The method proposed shows good performance establishing diagnosis through the simulated signals, however it shows great dependency on the ratio between static loads and dynamic loads, called modulation coefficient depending of the case. In this sense, important quotations related with to modulation coefficient have been established. The importance of demodulation and spectral frequency band is also shown for the case of combination faults.

A discussion of the effect of signal-to-noise ratio, random slippage, and spall percentage is also presented. Some relevant aspects have been highlighted. It was shown that random slippage could be considerably high, and the method still being able to capture peaks in IES at fault characteristic

orders. This in fact is an advantage of using the Second Order Cyclostationary analysis. On the other hand, it was shown that the spall percentage tends to favor the apparition of peaks at the orders dictated by the amplitude modulation function  $A(t)$ , i.e. synchronous orders for Outer and Inner Race cases, and harmonics of FTO for Rolling Element Faults (Ball Fault).



## 6. Experimental Tests.

In this chapter, the results of experimentation done on the Test-Rig (previously introduced in chapter 3) is exposed. Four different defects, under different load conditions, acceleration conditions, and speed regimes were captured. The order tracking process was done with a Tachless approach, previously discussed in section 2.5. Additional verification of angular speed was done by using the 1x tachometer installed on the test rig, by connecting the TTL digital voltage of the tachometer to channel 4 of NI 9230. The waveform, MOPA, and Phase Demodulation techniques were also applied to the captured tacho-voltage signal were also applied.

Through the different cases, the outer race one results as the most straightforwardly diagnosable, whereas, the rolling element fault case becomes the most challenging. Apparently, the former is due to an advanced state of fault. When the bearing with a combination of faults was analyzed, strange patterns were observed on the Enhanced Envelope Order-Spectrum and the newIESFO where strong signs of slippage were noticed.

To classify those observations during the results of this chapter, the labels summarized in Table 6-1 were used. Those labels were proposed by [22] and used to classify the results obtained of analyze the famous Western University Bearing data set. In the explanation column of Table 6-5 minor adaptations were added.

Table 6-1. Diagnosis Categories

DIAGNOSTIC CATEGORY	DIAGNOSIS SUCCESS	EXPLANATION
Y1	Yes	Fault clearly diagnosable by the classical behaviour on the Squared Envelope Spectrum (or Enhanced Envelope Spectrum).
Y2	Yes	Fault is diagnosable, but there is abnormal behavior on Squared Envelope Spectrum (or Enhanced Envelope Spectrum).
P1	Partial	Fault probably diagnosable, Squared Envelope Spectrum shows discrete components at fault characteristic orders but they are not dominant. i.e. The peaks at the Fault Characteristic Orders are far from the statistical threshold.
P2	Partial	Fault potentially diagnosable, Squared Envelope Spectrum shows smeared components which could coincide with fault characteristic orders.
N1	No	Fault is not diagnosable. There is no evidence of Fault Characteristic Order on the Squared Envelope Spectrum, but there is some evidence of other problematics
N2	No	Fault is not diagnosable and not distinguishable for noise.

## 6.1 Outer Race Fault.

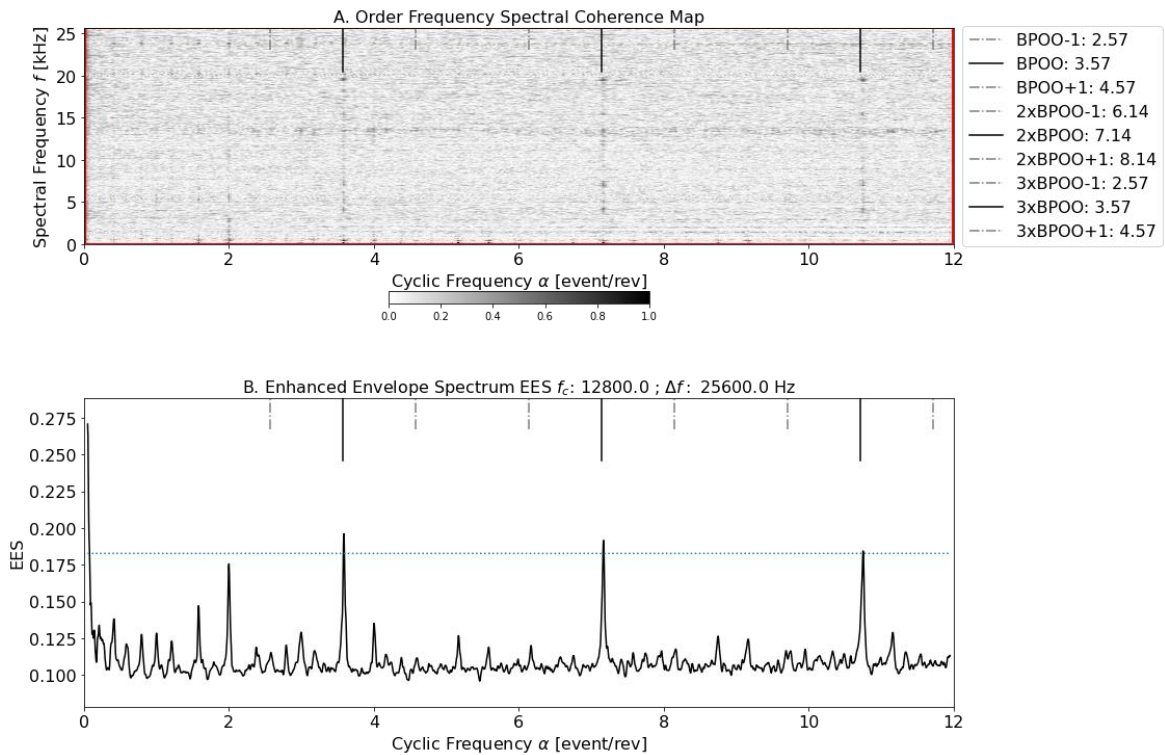
From the outer race fault case, all experiments done resulted in clear symptoms of failures, i.e. discrete components at BPOO were present. Those discrete components exceeded the statistical threshold considerably. Even the signals captured on Bearing 1, which was the healthy bearing, reflected the shown OR failure symptoms, coming from the vibrational response of Bearing 2. Table 6-2 resumes the experimentation results. In general, it results clear the fault observed at outer race, in all the runs. The results are further illustrated in annexes of section 9.6.

Table 6-2. Outer Race Fault Case - Experimental Results

Num.	Range Speed	Acceleration	Load	Bearing 1	Bearing 2
OR-1	14 – 30 Hz	High (6 Hz/s)	5 kg static	Y1	Y1
OR-2	30 – 25 Hz	High (6 Hz/s)	5 kg static	Y1	Y1
OR-3	8 – 18 Hz	Low (3 Hz/s)	5 kg static	Y1	Y1
OR-4	21 – 32 Hz	Low (3 Hz/s)	5 kg static	Y1	Y1
OR-5	22 – 39 Hz	High (6 Hz/s)	0 kg	Y1	Y1
OR-6	37 – 14 Hz	High (6 Hz/s)	0 kg	Y1	Y1
OR-7	17 – 30 Hz	Low (3 Hz/s)	0 kg	Y1	Y1
OR-8	22 – 38 Hz	Low (3 Hz/s)	0 kg	Y1	Y1

To illustrate the results obtained for the case of Outer Race Fault, consider Figure 6-1-A, where the OFSCoh map for the signal captured on bearing 1, under OR-3 conditions is shown. In the figure, the Spectral Coherence is plotted against spectral frequency  $-f$  and cyclic order  $-\alpha$ . Some vertical patterns at BPOO and its harmonics could be observed. In addition, some vertical contrasts are observable at 2x order. However, none relevant horizontal band is observed at naked eye. The Enhance Envelope Order Spectrum –EES is shown in Figure 6-1-B. The three first harmonics of BPOO exceed the statistical threshold and a particular peak rise at 2x order. The EES drawn in Figure 6-1-B is a clear pattern of Outer Race Fault.

Figure 6-1 Run OR-3 B1 signal. A. OFSCoh Map B. Enhanced Envelope Order Spectrum.



This particular case, i.e. OR-3 Bearing 1 signal, results convenient for illustrating the benefits of correct demodulation as it was discussed previously in section 4.1. To explore this, consider the IESFOgram illustrated in Figure 6-2-A, where the binary-three optimization selects the spectral range comprehended between 800 and 2400 Hz as the optimum spectral range. The result of using this spectral range for demodulation is shown in the IESFO plotted in Figure 6-2-B. Although there are peaks at BPOO and its harmonics, they are accompanied by some other peaks at uninterpretable orders, which also exceed the statistical threshold.

Similarly, the use of newIESFO and IESFO are shown in Figure 6-3. The use of newIESFO selects the spectral frequency range between 18400 and 21600 Hz, as it is illustrated in Figure 6-3-A. The order-spectrum obtained by the use of IESFOgram is shown in Figure 6-3-B. Clearly, it shows patterns of having a failure at outer race, since peaks at BPOO and its harmonics are clear and not disturbed by others uninterpretable orders. Notice also the fact that no peaks at synchronous components are observable in Figure 6-3-B.

Figure 6-2. Run OR-3 B1 A. IESFOgram B. IESFO.

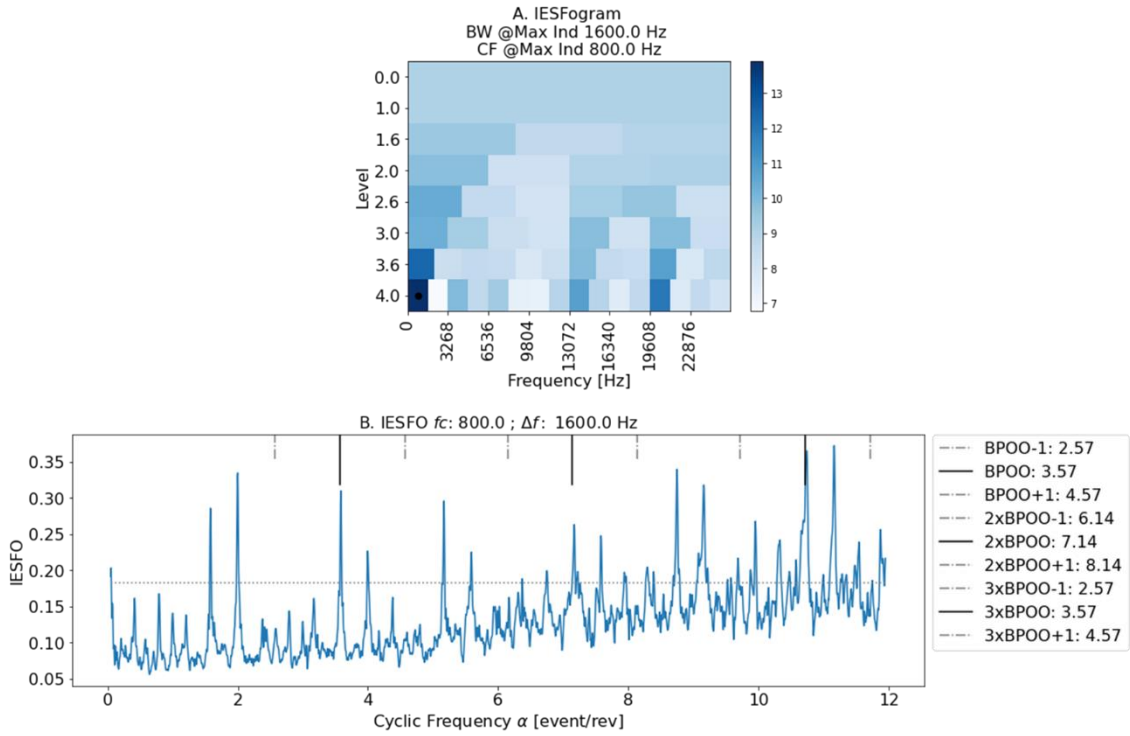
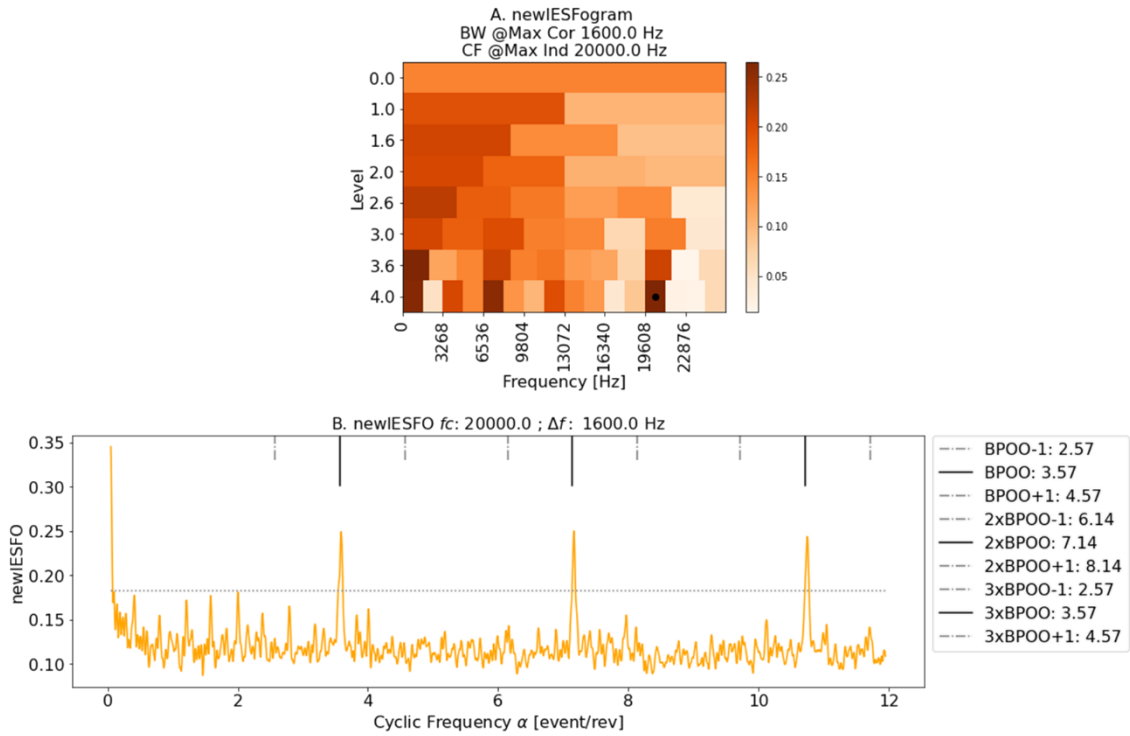
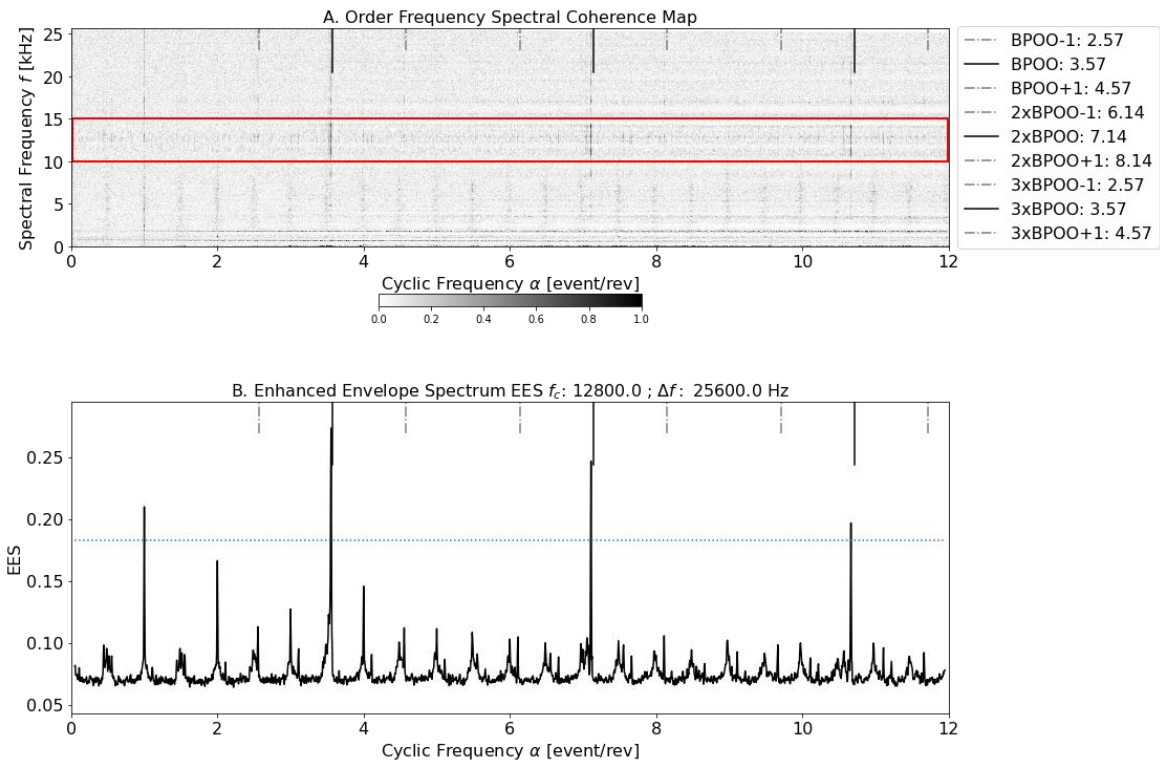


Figure 6-3. Run OR-3 B1. A. newIESFOgram, B. newIESFO.



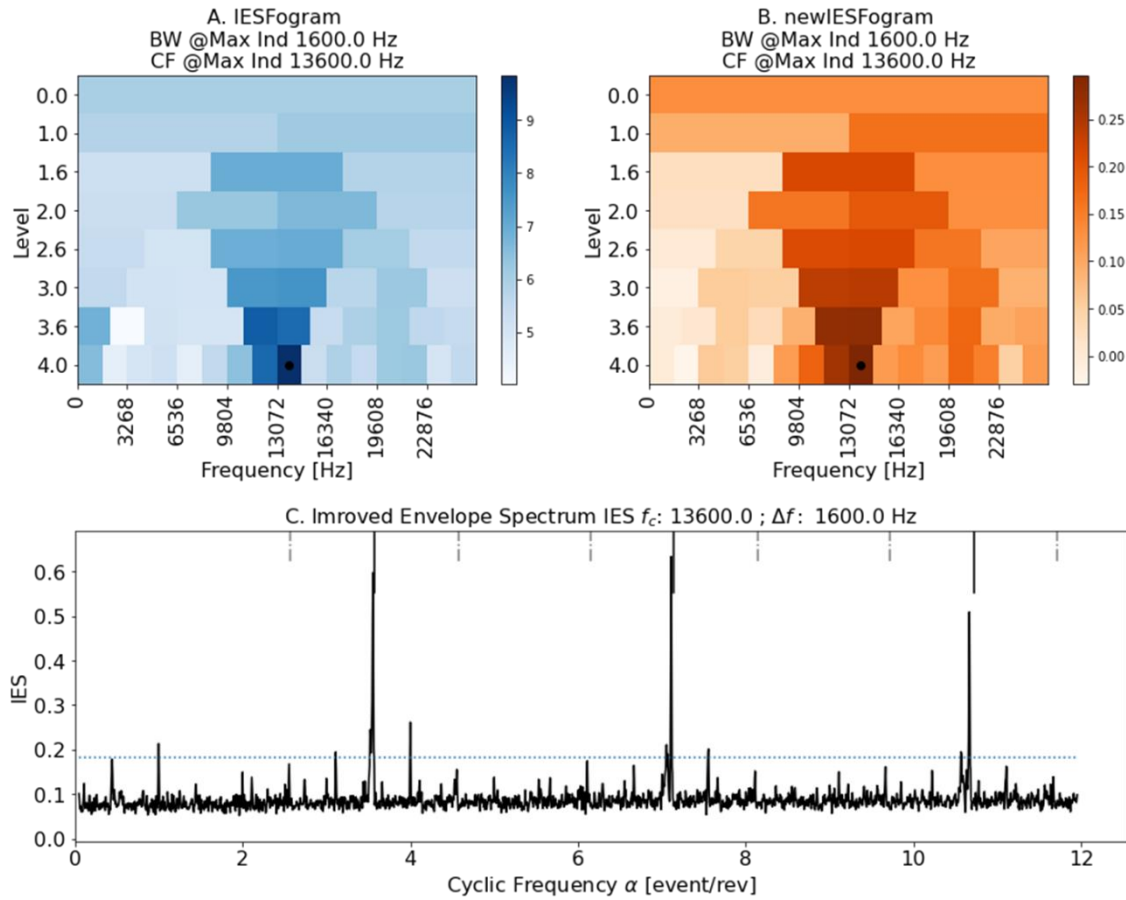
Additionally, consider the run signal captured on bearing1, under the conditions established on OR-5. The OFSCoh map and the EES are illustrated in Figure 6-4. In the OFSCoh map, Noticeable vertical patterns are observable at the first three harmonics of BPOO. Some other vertical contrasts are observed at synchronous orders such as 1x and 2x. An horizontal contrast could be noticed if the attention is focused on 10-15 kHz spectral band, as it is highlighted by the box drawn in the figure.

Figure 6-4. Run OR-5 B1 signal. A. OFSCoh Map B. Enhanced Envelope Order Spectrum.



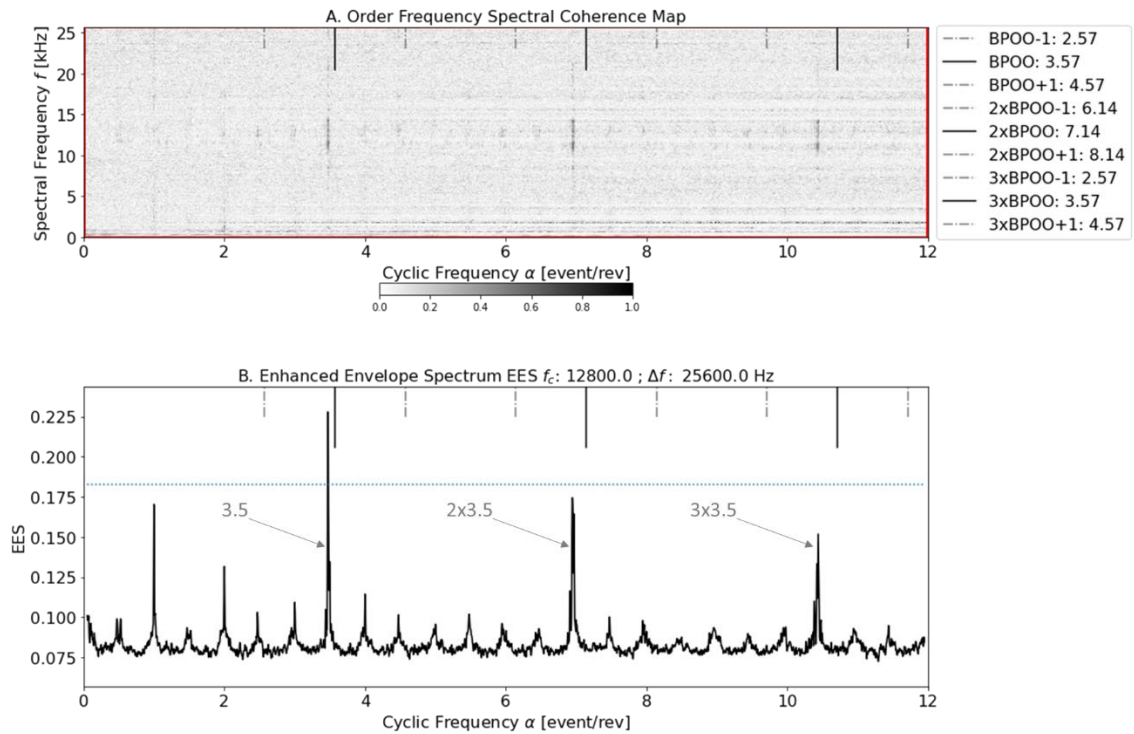
As a matter of fact, the spectral bands dictated by IESFO and newIESFO coincide with the spectral range previously highlighted, as it is shown in Figure 6-5-A and Figure 6-5-B. The IES obtained by demodulate the OFSCoh map according to the spectral frequency range between 12.8 kHz and 14.4 kHz is illustrated in Figure 6-5-C. Some improvement could be seen by comparing this latter IES with the EES of Figure 6-4-B, the most pinpointed is the range by which the statistical threshold is overcome. Clearly, after demodulation, the peaks at BPOO and harmonics are stronger, while conserving the importance of some synchronous orders such as 1x, 4x.

Figure 6-5. Run OR-5 B1 signal. A. IESFOgram B. newIESFOgram. C. Improved Envelope Order Spectrum.



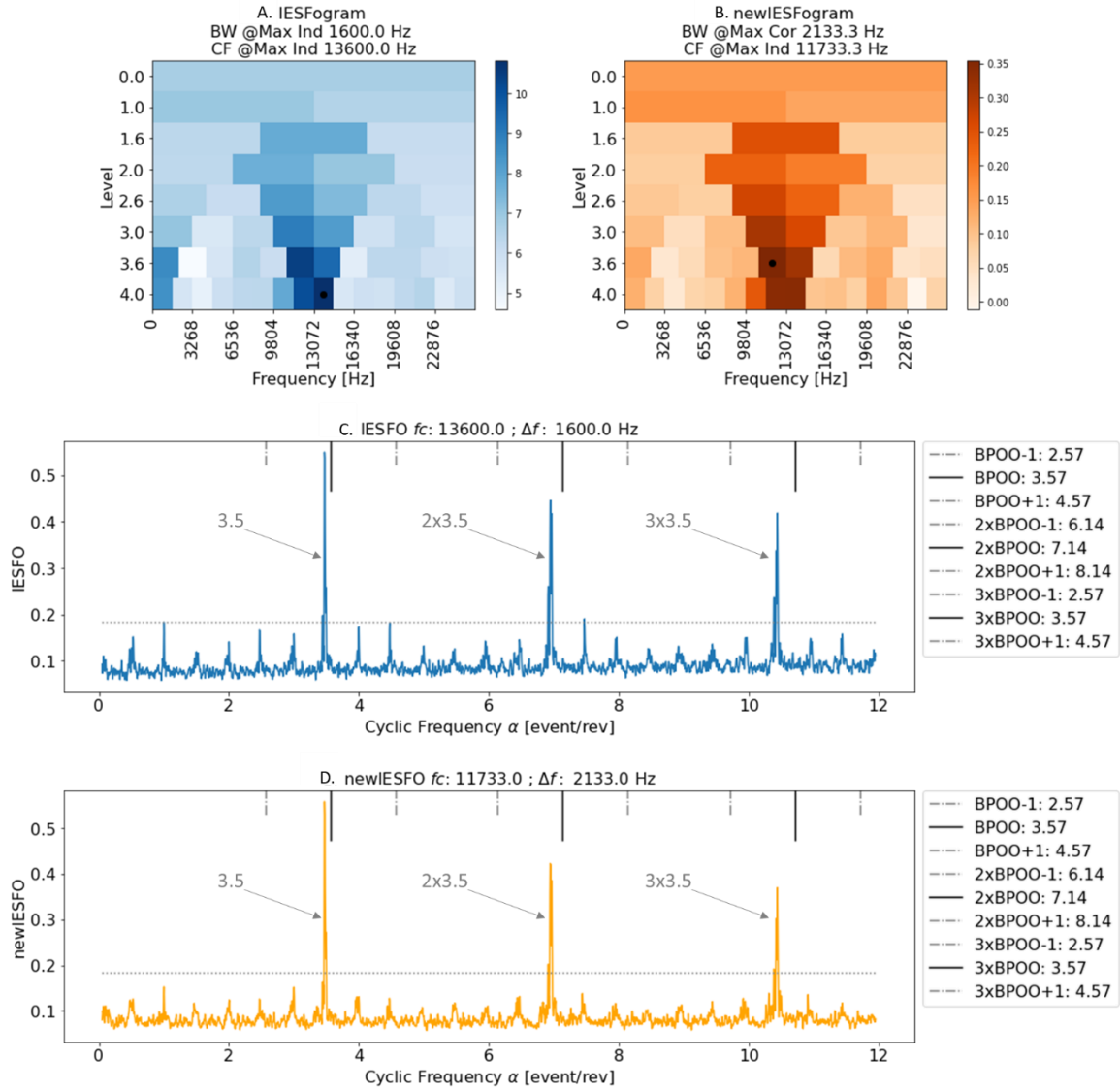
For the signal of OR-6 captured on bearing 1, the OFSCoh is illustrated in Figure 6-6-A. A clear spectral band rises around 13 kHz with some vertical visible lines. Nonetheless, those vertical lines do not coincide precisely with BPOO and its harmonics, instead, coincide with 3.5x order and harmonics. The situation is further illustrated in EES of Figure 6-6-B. It appears the BPOO discrete components tend to slice to coincide with 3.5x order, slicing roughly 2 percent. This in fact is tending to coincide with a synchronous order such as 7x as the second harmonic of 3.5x.

Figure 6-6. Run OR-6 B1 signal. A. OFSCoh Map B. Enhanced Envelope Order Spectrum



Especially care should be taken prior to using an optimization based on IESFOgram or newIESFOgram, since those methods use a pre-defined cyclic order in order to optimize their visualization in the Improved Envelope Spectrum. If the slice is taken into account, both, IESFOgram and newIESFOgram bring out roughly the same demodulation band comprehended between 12.8 and 14.4 kHz. IESFOgram, newIESFOgram, and IES for this case are shown in Figure 6-7.

Figure 6-7. Run OR-6 B1 signal. A. IESFOgram B. newIESFOgram C. IESFO D. newIESFO



It is also important to note the improvement in IES achieved by the use of newIESFO in Figure 6-7-D, in comparison with the EES shown in Figure 6-6-B. In the first case all three harmonics of BPOO exceeds the statistical threshold while for the EES is only true for the first harmonic.

## 6.2 Inner Race Fault.

For inner race faults, the diagnosis on signals captured on bearing 2 pedestal were clear in the major part of cases. However, the results for signals captured on bearing 1 pedestal were not clear in many cases. The results are summarized in Table 6-3 where the different running are listed with their corresponding range of speed, acceleration, and load. The Bearing 1 and Bearing 2 columns list the



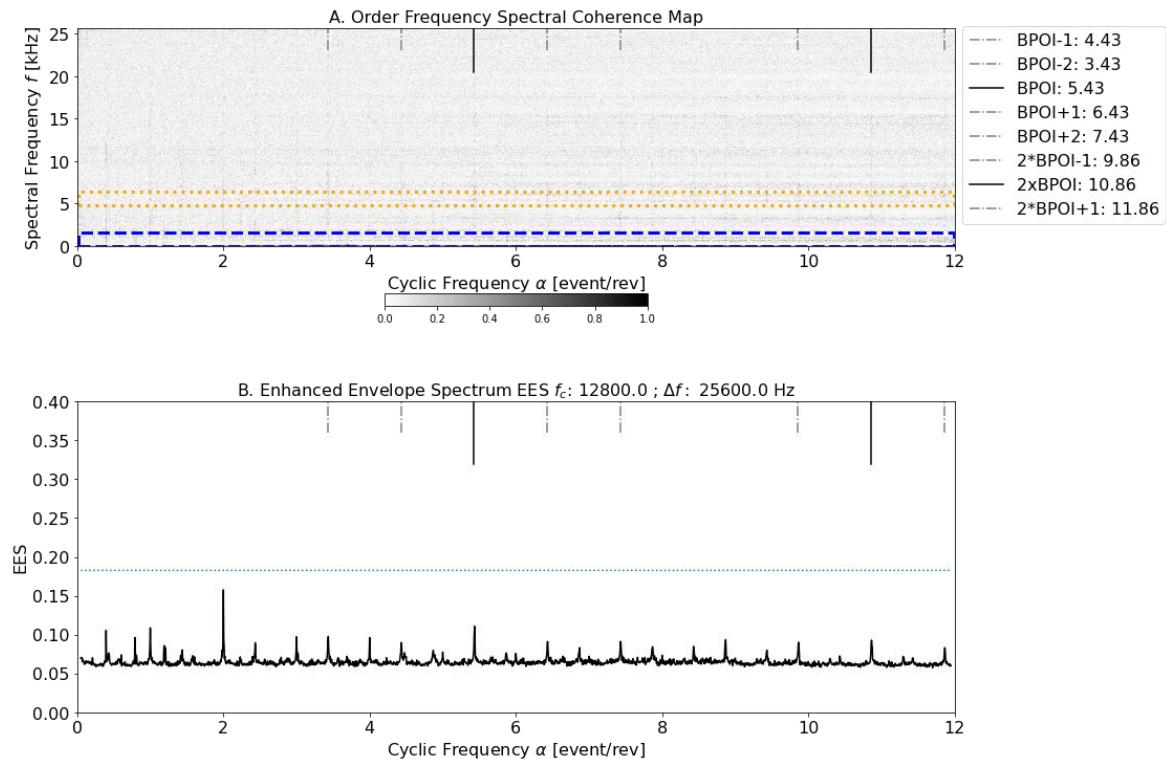
resulting diagnosis, according to the criteria exposed previously in Table 6-1. Those results are further illustrated on annex of section 9.6.

Table 6-3. Inner Race Fault Case - Experimental Results

Num.	Range Speed	Acceleration	Load	Bearing 1	Bearing 2
IR-1	29 – 38 Hz	High (6 Hz/s)	5 kg static	P1	Y1
IR-2	29 – 11 Hz	High (6 Hz/s)	5 kg static	N2	Y1
IR-3	13 – 29 Hz	Low (3 Hz/s)	5 kg static	N2	Y2
IR-4	29 – 13 Hz	Low (3 Hz/s)	5 kg static	N1	Y2
IR-5	21 – 38 Hz	High (6 Hz/s)	0 kg	P1	Y2
IR-6	37 – 14 Hz	High (6 Hz/s)	0 kg	N1	Y2
IR-7	15 – 28 Hz	Low (3 Hz/s)	0 kg	N1	Y2
IR-8	30 – 38 Hz	Low (3 Hz/s)	0 kg	Y1	Y2

To illustrate the results summarized on Table 6-3, consider the signal for IR-1 case, captured on pedestal 1. The SCoh map and the EES is shown in Figure 6-8. In the EES, peaks at discrete order of BOPI and  $2 \times \text{BPOI}$  are observable, however, their magnitude are far from the statistical threshold. This explains the P1 label assigned to this particular signal.

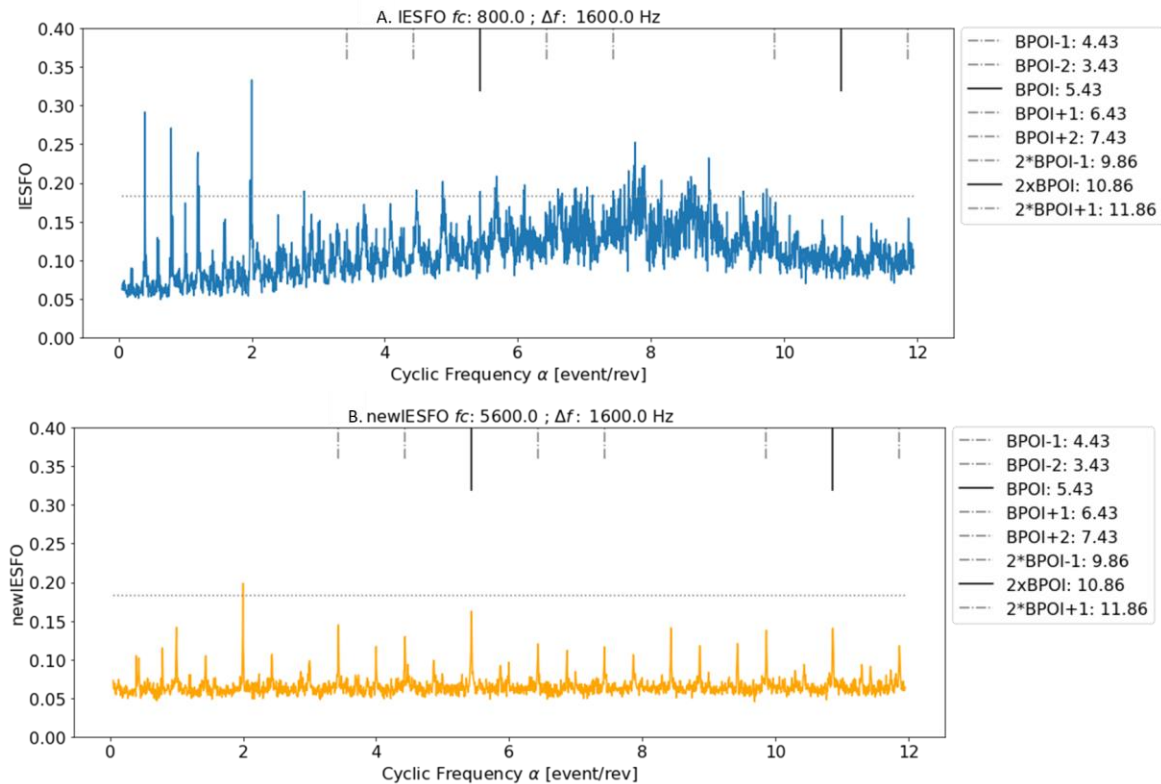
Figure 6-8. Run IR-1 B1 signal. A. OFSCoh Map B. Enhanced Envelope Order Spectrum.



Although the EES does not bring out a clear spectrum for establishing failure in the inner race, some improvements could be managed after demodulation. In Figure 6-8-A, a blue-dashed box has been drawn to denote the demodulation spectral range dictated by the IESFOgram. Similarly occurs for

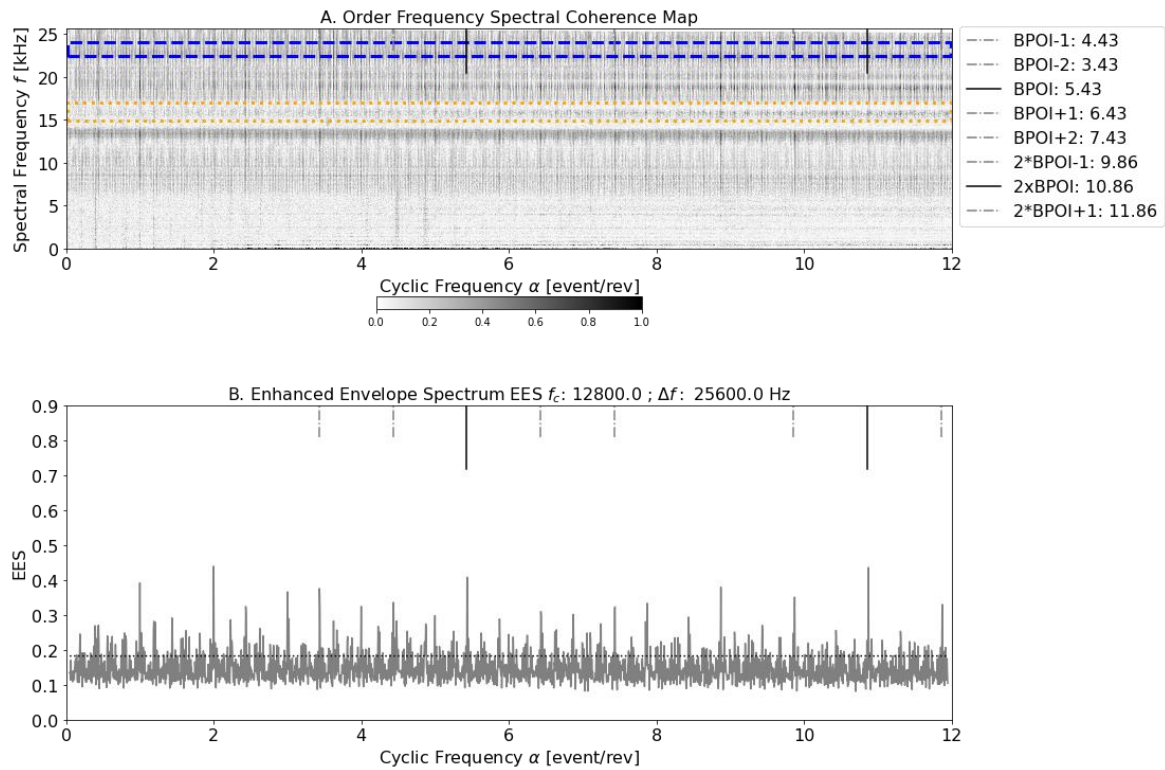
the orange dotted box, which highlights the spectral demodulation band marked by the newIESFO. The IESFO and newIESFO for IR-1 B1 signal are shown in Figure 6-9. Particularly, the use of IESFO, shown in Figure 6-9-A, does not help in any manner since the floor noise is so noticeable, even though the  $1 \times \text{BPOI}$  component exceeds the statistical threshold. On the other hand, the use of newIESFO allows to increase the magnitude of the discrete components at BPOI and  $2 \times \text{BPOI}$  orders, while keep the discreteness of those components. Additionally, it allows identifying side-lobes spaced at synchronous orders.

Figure 6-9 Run IR-1 B1 signal. A. IESFO. B. newIESFO



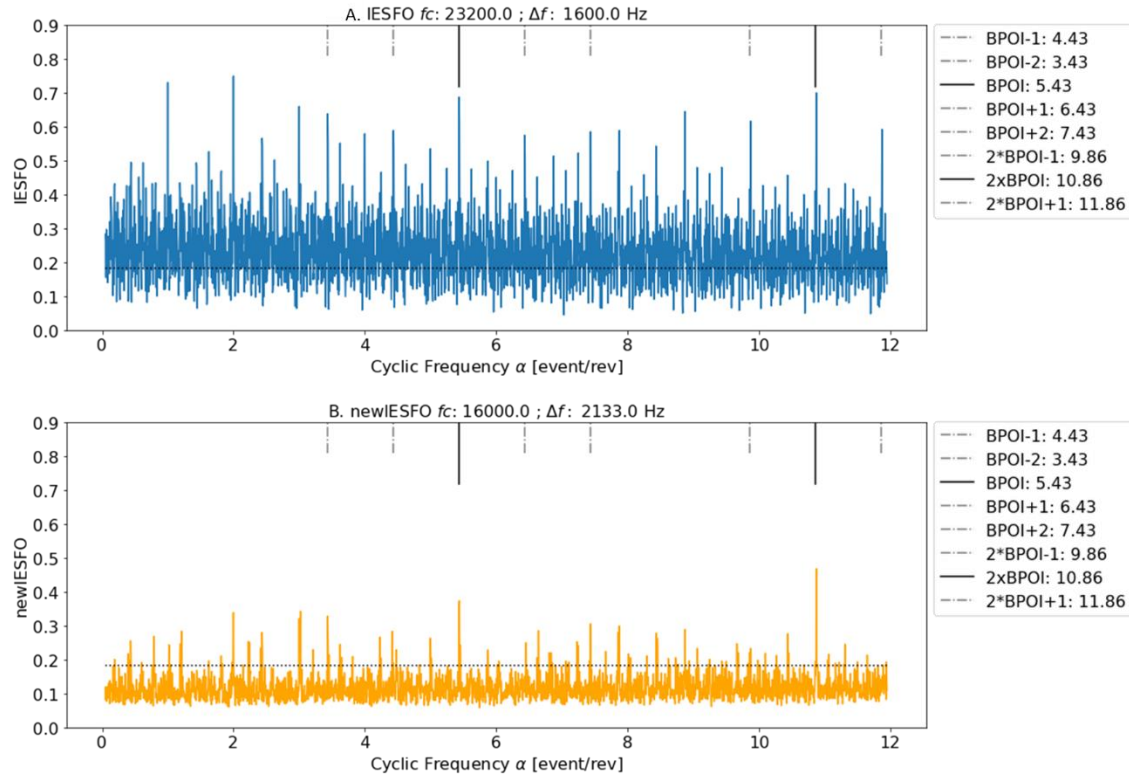
Similar analysis could be achieved for signal IR-1 captured on pedestal of bearing 2, which is the bearing with the fault at its inner race. The OFSCoh map is shown in Figure 6-10-A, while the resulting Enhanced Envelope Order Spectrum is shown in Figure 6-10-B. Discrete peaks at BPOI and  $2 \times \text{BPOI}$ , exceeding the threshold are noticeable, however, the appearance of the spectrum does not match the one expected for an incipient inner race fault.

Figure 6-10. Run IR-1 B2 signal. A. OFSCoh Map B. Enhanced Envelope Order Spectrum.



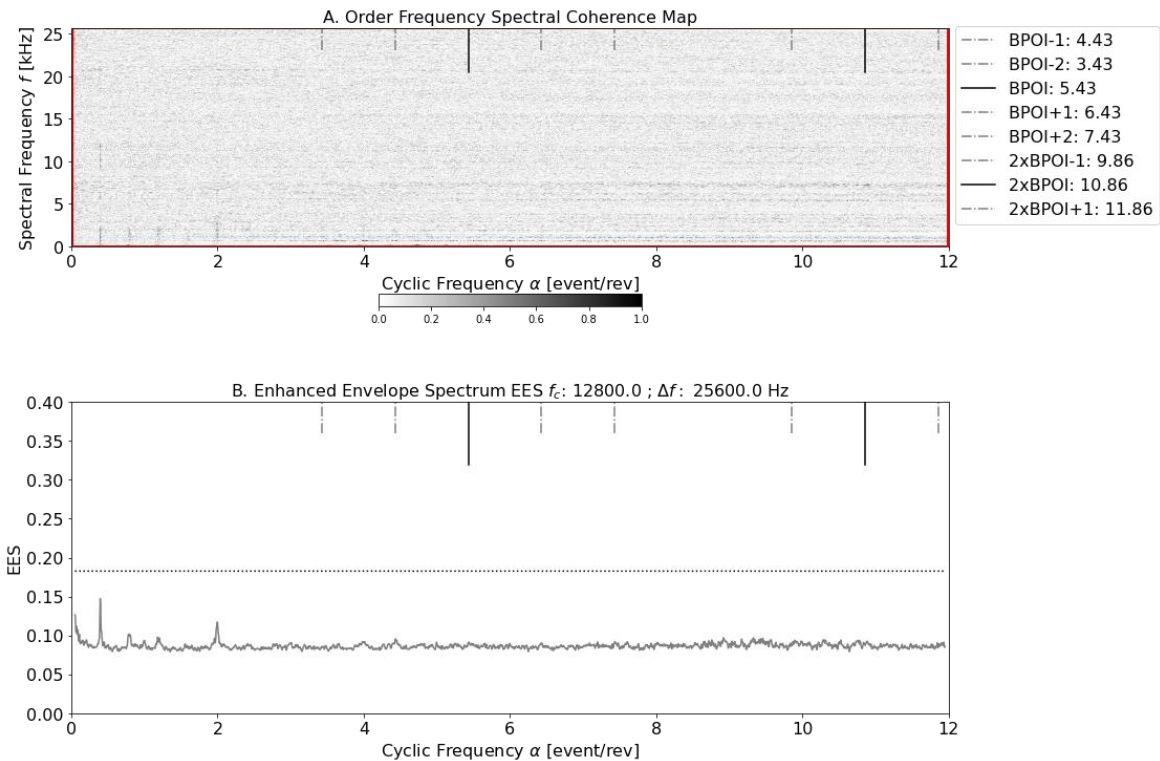
In Figure 6-10-B is noticeable the floor noise, and consequently, is desirable to have a spectrum with higher relevance at BPOI and its harmonics. The situation could be improved by using the demodulation dictated by the newIESFOgram (while IESFOgram does not appear useful for this case). The spectral frequency ranges dictated by IESFOgram and newIESFOgram are shown in Figure 6-10-A, sketched with the dashed blue box, and the dotted orange one, respectively. The newIESFO is then obtained by using a demodulation band lied between 14.93 and 17.07 kHz. Figure 6-11 illustrates the spectrograms obtained after demodulation. The newIESFOgram, shown in Figure 6-11-B shows that the BPOI and 2xBPOI overcomes the statistical threshold and some of the synchronous lobe-sides.

Figure 6-11. Run IR-1 B2 signal. A. IESFO. B. newIESFO.



Now consider the signal sampled on pedestal 1, under IR-2 conditions. This is illustrated in Figure 6-12. As it is seen, there is no evidence of any considerable vertical pattern in Figure 6-12-A neither a clear peak at BPOI nor 2xBPOI in the IES of the Figure 6-12-B. In fact, neither IESFO nor newIESFO could broadcast a relevant spectral frequency range at which signs of inner race fault could be obtained. This indicates the energy of the strikes at faulty bearing, i.e. bearing 2, got vanished along the path until the pedestal of bearing 1. The former discussion explains the label N1 set in Table 6-3 for the IR-2 row.

Figure 6-12. Run IR-2 B1 signal. A. OFSCoh Map B. Enhanced Envelope Order Spectrum.



In contrast, when the signal captured on bearing 2 is considered, clear peaks at BPOO and harmonics are observable in the EES. This is illustrated in the OFSCoh map and the EES in Figure 6-13. Even peaks spaced at synchronous orders exceed the statistical threshold. The spectral frequency ranges dictated by IESFO and newIESFO are illustrated in Figure 6-13-A by the drawn boxes. Particularly, the newIESFO's result turned out the most useful for demodulation given the clearness reflected in newIESFO as it is exposed on Figure 6-14. Although the EES per se results in a clear sign of inner race fault, the newIESFO increase the magnitude of relevant orders a little.

Figure 6-13. Run IR-2 B2 signal. A. OFSCoh Map B. Enhanced Envelope Order Spectrum.

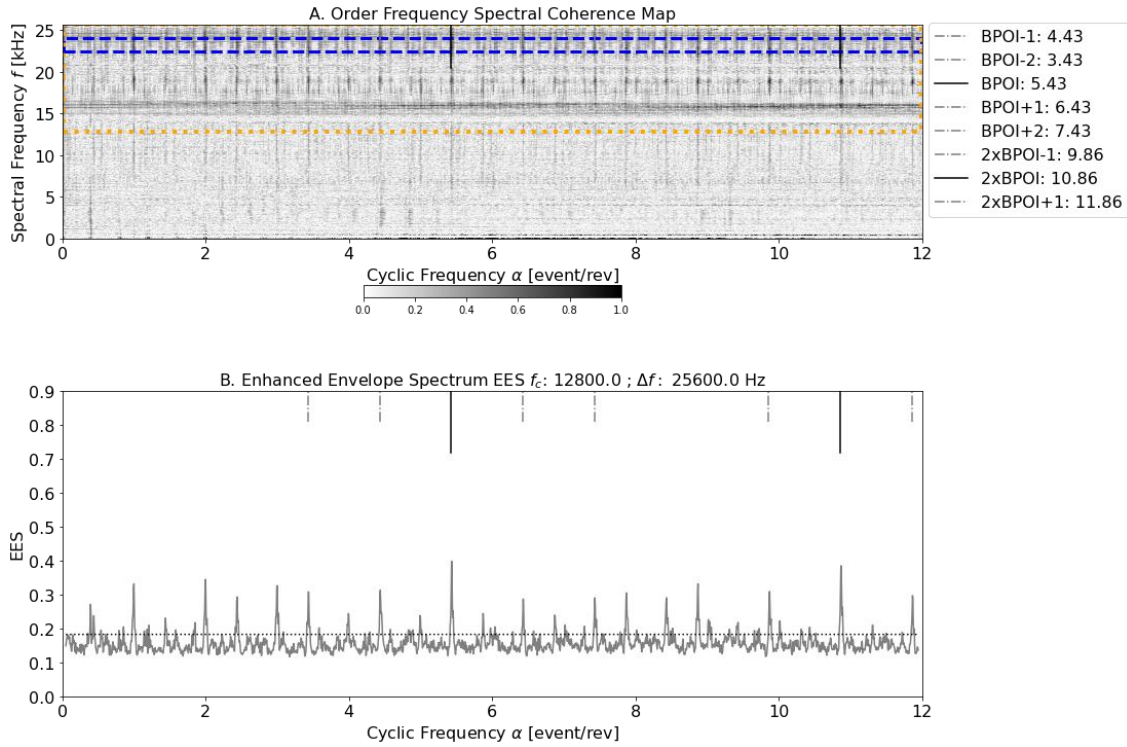
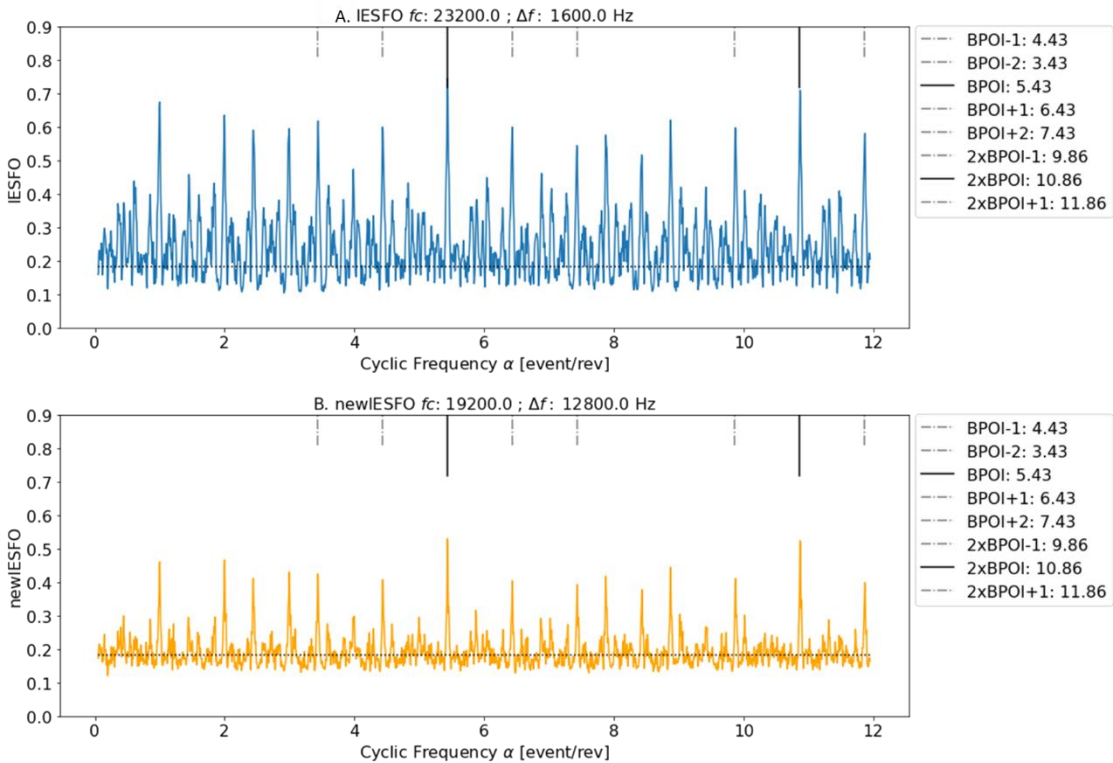


Figure 6-14. Run IR-2 B2 signal. A. IESFO. B. newIESFO.





### 6.3 Rolling Element Fault.

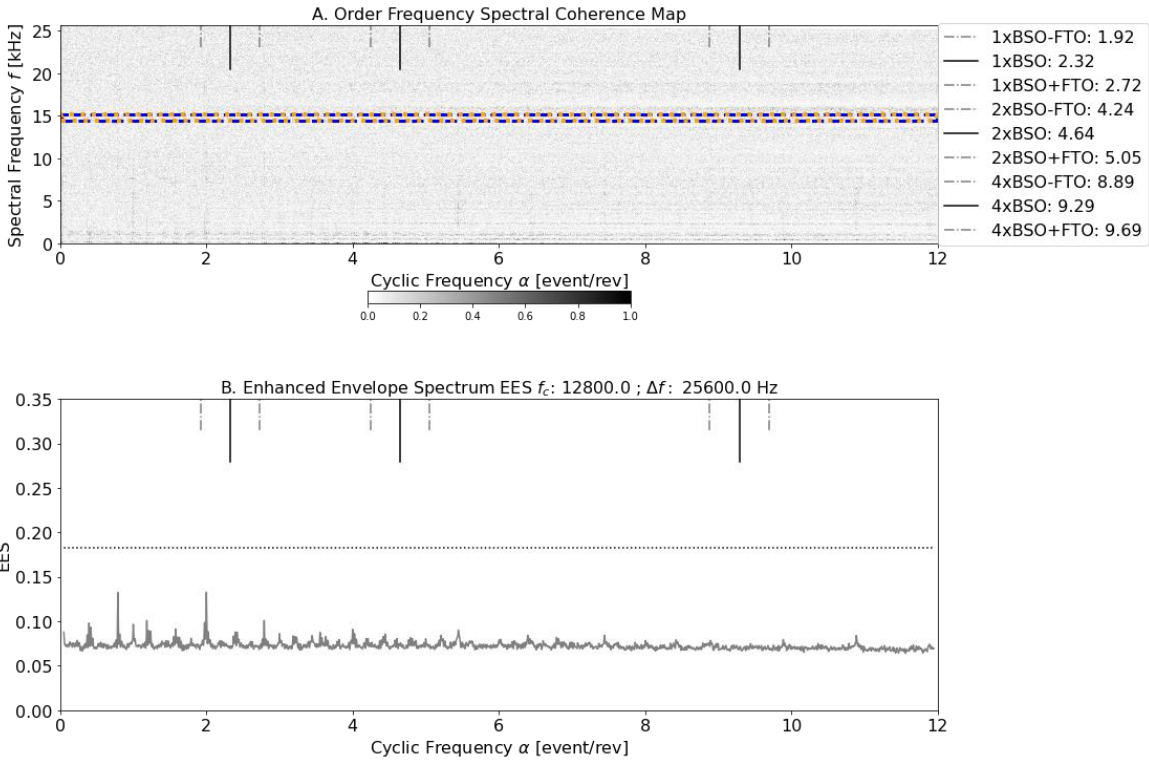
Eight runs were analyzed, as shown in Table 6-4. The experiments BF-1 to BF-4 were done with a loader mounted on the center of the shaft. Whereas experiments BF-5 to BF-8 were done without load applied to shaft. The diagnosis on rolling element resulted the most challenging case. In any of the cases analyzed was possibly to diagnostic the classical pattern of Envelope Order-Spectrum with peaks at BSO, with sidebands on the fundamental train order FTO. However at FTO and harmonics of FTO were evident in almost all cases. For the signals captured on pedestal of Bearing 1, i.e. healthy bearing, it was not possibly to stablish clearly the pattern of fault.

Table 6-4. Ball Fault - Experimental Results

Num.	Range Speed	Acceleration	Load	Bearing 1	Bearing 2
BF-1	20 – 38 Hz	High (6 Hz/s)	5 kg static	P1	Y2
BF-2	29 – 11 Hz	High (6 Hz/s)	5 kg static	P1	P1
BF-3	19 – 35 Hz	Low (3 Hz/s)	5 kg static	P1	Y2
BF-4	38 – 21 Hz	Low (3 Hz/s)	5 kg static	P1	Y2
BF-5	21 – 38 Hz	High (6 Hz/s)	0 kg	P1	Y2
BF-6	35 – 16 Hz	High (6 Hz/s)	0 kg	P1	Y2
BF-7	14 – 28 Hz	Low (3 Hz/s)	0 kg	N2	Y2
BF-8	30 – 38 Hz	Low (3 Hz/s)	0 kg	P1	Y2

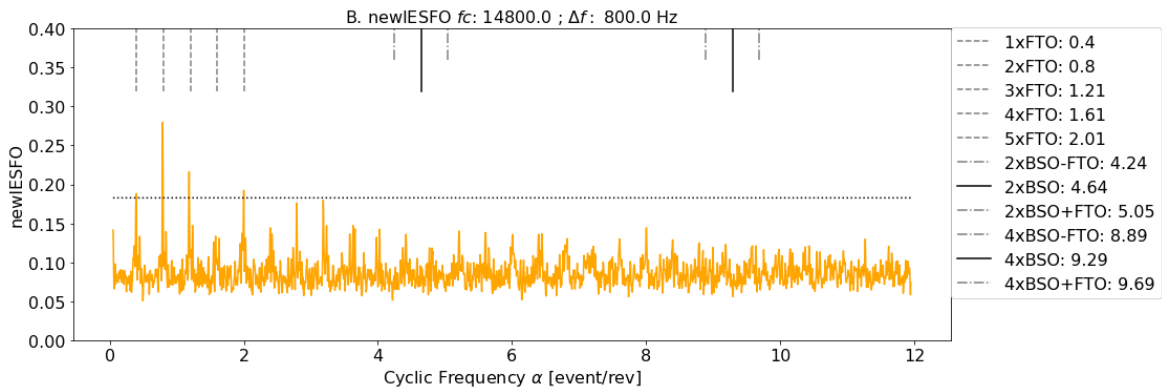
To exemplify the results, let consider the signal captured on Bearing 2, under conditions of BF-1 run. The spectral correlation and the Enhanced Envelope Spectrum (EES) is shown in Figure 6-15. The EES shows a series of peaks at the cage characteristic order FTO and their harmonics. The 2x order own a high magnitude, which could be attributable to the coincidence with the 5<sup>th</sup> harmonic of FTO ( $5 \times 0.402 \approx 2.01$ ), which is highly probably to fall in 2x if slippage happens. In fact, if slippage is so considerable, the 6<sup>th</sup> FTO harmonic ( $6 \times 0.402 = 2.41$ ) could also be misinterpreted as the BSO (2.32).

Figure 6-15 Run BF-1 B1 signal. A. OFSCoh Map B. Enhanced Envelope Order Spectrum.



By using the IESFOgram or newIESFOgram approaches for search FTO discrete components, both use the same demodulation band, comprehended between 14.4 and 15.2 kHz as the optimum range. This spectral frequency range has been illustrated in Figure 6-15-A with the plotted boxes in the OFSCoh map. The newIESFO (equivalent to IESFO for this case) is shown in Figure 6-16. Notice that 2xBFO peaks is near the statistical threshold, however, in a similar manner to exposed on EES of Figure 6-15-B, the most prominent components are located at harmonics of FTO.

Figure 6-16 Run BF-1 B2 signal. newIESFO.

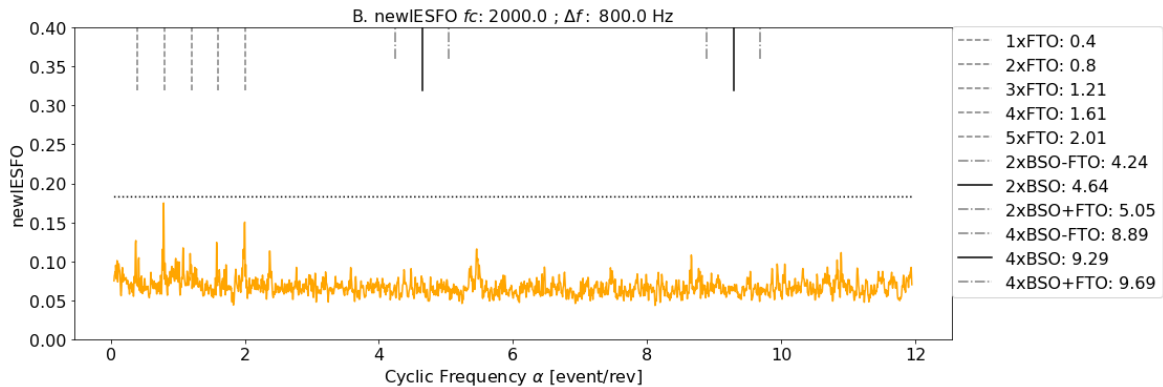




As the classical pattern of bearing element fault (peaks at BSO with FTO sidebands, see Figure 2-1) does not match with the one exposed in Figure 6-16, this case (Bearing 2 of BF-1) is labeled as Y2. It means that failure could be diagnosed but further considerations are needed to clarify this behavior. As mentioned on previous paragraph, similar results, i.e. peaks at FTO but not peaks at BSO were reported by the analysis exposed in [22] on a constant speed test rig, and the experimentation done by [54] on a similar test rig. Although this situation is not the classical pattern of a rolling element bearing, it is a characteristic pattern when damage is pronounced and the periodicity of BSO is loosed and the energy is smeared on low orders multiples of FTO [8].

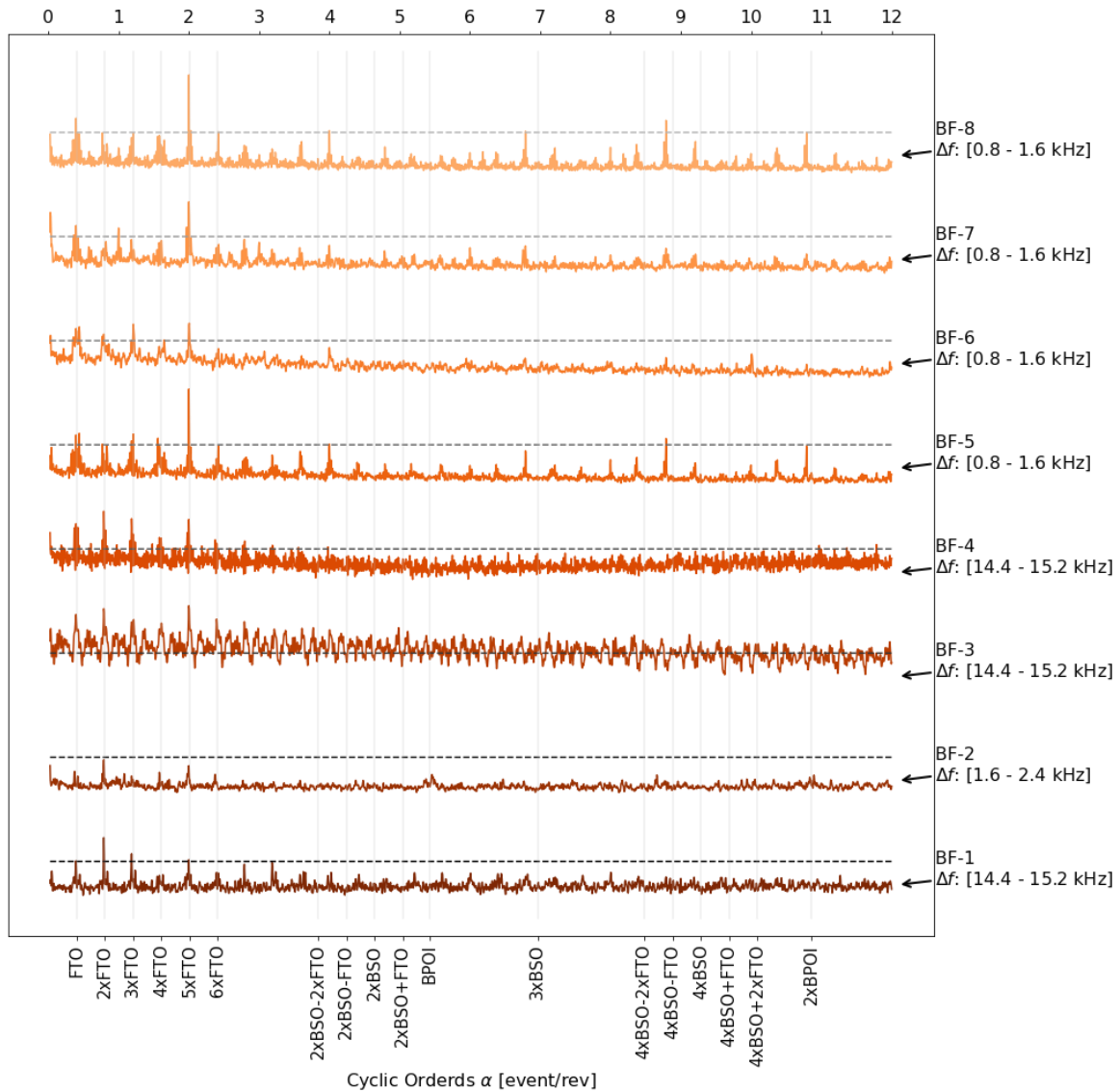
To further illustrate the results, consider the Figure 6-17. In this figure, the newIESFO is used to demodulate discrete components at FTO, on signal sampled on B2, for BF-2 run. Peaks at FTO are identifiable, however they magnitude do not exceed the statistical threshold plotted by the dashed line. In this sense, the result of the diagnosis is labeled as P1.

Figure 6-17. Run BF-2 B2 signal. newIESFO



More clear patterns of harmonics at FTO were observable at signals BF-5, BF-6, BF-7 and BF-8. Note that according to the Table 6-4 those signals were captured without the loader assembled in the shaft, this suggests FTO modulations become important when static load is not present or decimated. To further illustrates this, consider the Figure 6-18, where the newIESFO is plotted against cyclic orders. In the figure newIESFOgram demodulation approach has been used. The resulting spectral frequency range is labeled for each running. Particular cursors vertical lines have been set on the bottom axis while synchronous orders were set in top axis. Figure allows visualizing the influence of FTO and their harmonics, particularly for signals BF-5 to BF-8.

Figure 6-18 Different newIESFO for ball fault case, signals sampled on B2.



In general, the Rolling Element Fault case was not straightforward to diagnose. None of the signals captured on bearing one (1) showed a pattern of fault. Indeed, the crack seems to be in an advanced state, explaining the peaks at FTO and the lack of peaks at BSO, as explained by [8]. On the other hand, high values at cyclic frequency  $\alpha=0$  were also observed. The discussion of those tendencies was exposed in sections 5.3.2 and 5.3.3.

## 6.4 Combination Fault.

Experimental runs were also taken for the case of a bearing with a combination of faults. Those experimental runs were sampled under different load and speed conditions, as it is described in Table 6-5. The labels categories set on the columns Bearing1 and Bearing 2 were previously exposed on Table 6-1. Additional graphical results are shown in annex of section 9.9.

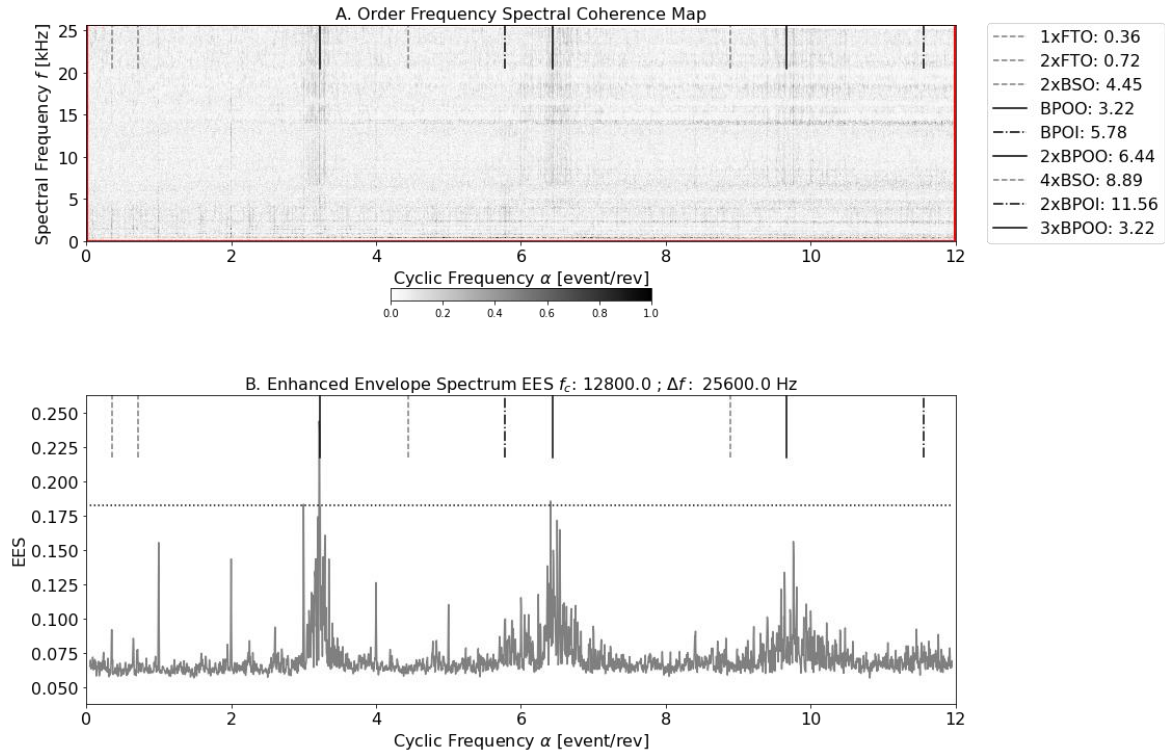
Table 6-5. Combination Fault - Experimental Results

Num.	Range Speed	Acceleration	Load	Bearing 1	Bearing 2
CF-1	4 – 25 Hz	High (6 Hz/s)	5 kg static	Y2	Y2
CF-2	26 – 38 Hz	High (6 Hz/s)	5 kg static	Y2	Y2
CF-3	19 – 36 Hz	Low (3 Hz/s)	5 kg static	Y1	Y1
CF-4	37 – 15 Hz	Low (3 Hz/s)	5 kg static	Y1	Y1
CF-5	14 – 28 Hz	High (6 Hz/s)	0 kg	N1	N1
CF-6	28 – 41 Hz	High (6 Hz/s)	0 kg	N1	N1
CF-7	16 – 29 Hz	Low (3 Hz/s)	0 kg	N1	N1
CF-8	30 – 38 Hz	Low (3 Hz/s)	0 kg	N1	N1

In general, faults were easily diagnosable for the case on which the shaft was mounted with the static loader. On the other hand, for the cases at which the shaft had not attached a load, the diagnosis process reveals clear cyclostationary components, but at orders different from expected. In both cases, a high slippage were observed. It is the thought of the author that the combination of fault works as high impulsivity noise among the different characteristic faulty orders.

To illustrate the aforementioned, let consider the vibration captured on bearing 2, under the conditions described on run CF-2. The OFSCoh map is shown in Figure 6-19-A. Clear vertical stripped pattern is evidential near to nominal BPOO among almost the entire spectral frequency range. However, it results important to highlight the smearing at the harmonics of BPOO, in fact, the BPOO was manually set as 3.215, in contrast with the theoretical 3.572 reported by bearing manufacturer (Table 3-1). The Enhanced Envelope (Order-)Spectrum is illustrated on Figure 6-19-B, peaks at 1xBPOO and 2xBPOO clearly exceed the statistical threshold drawn by the horizontal dashed line in the figure. None other fault characteristic order appears to be relevant, however, synchronous orders are noticeable

Figure 6-19 Run CF-2 B2 signal. A. OFSCoh Map B. Enhanced Envelope Order Spectrum.



From Figure 6-19, the setting of BPOO was further confirmed by a discrete component at 5.775, set as BPOI, which is consequent with the rule at which the sum of BPOO and BPOI should results equivalent to number of rolling elements. The aforementioned deduction comes from the relations established on Table 2-1, as it is exposed in Equation 6-1.

$$\text{Equation 6-1} \quad BPOO + BPOI = \frac{N}{2} \left( 1 - \frac{d}{D} \cos(\theta) \right) + \frac{N}{2} \left( 1 + \frac{d}{D} \cos(\theta) \right) = N$$

An interesting aspect of the newIESFO approach appears since different demodulation bands are obtained as a function of the failure tempted to be diagnosed. This is illustrated in Figure 6-20, and Figure 6-21 where newIESFOgram was used for demodulate the signal intending to search for inner race fault and outer race fault, respectively. For the case of inner race searching a demodulation band between 2.13 and 4.27 kHz arose, while for the case of outer race fault, the spectral frequency lied in the 17.1 to 19.2 kHz range was selected. The pattern observed in Figure 6-20 allows to diagnose a failure at inner race but being skeptical by the lack of discreteness, whereas the newIESFO shown in Figure 6-21 reveals a clear fault at the outer race.

Figure 6-20. Run CF-2 B2 newIESFO for Inner-Race fault search

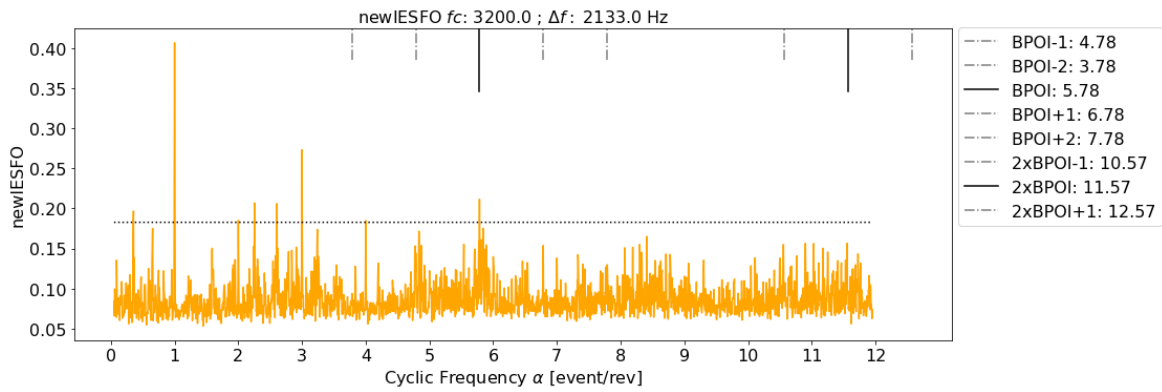
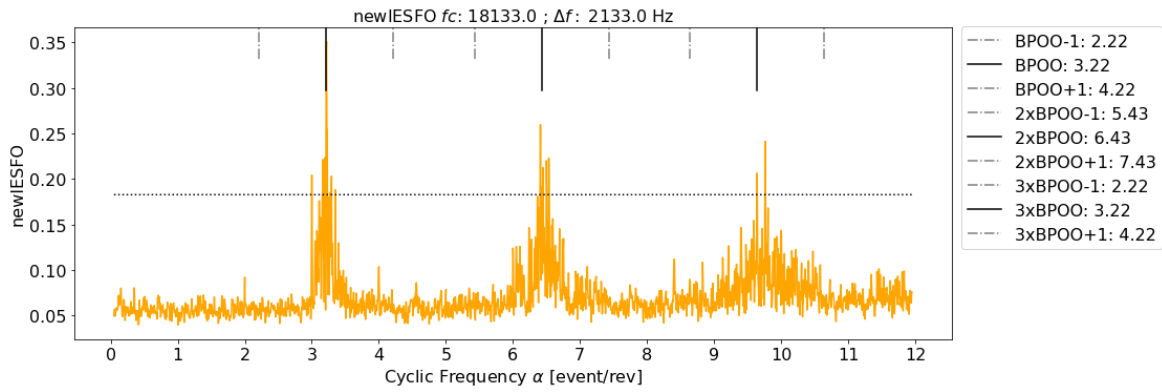
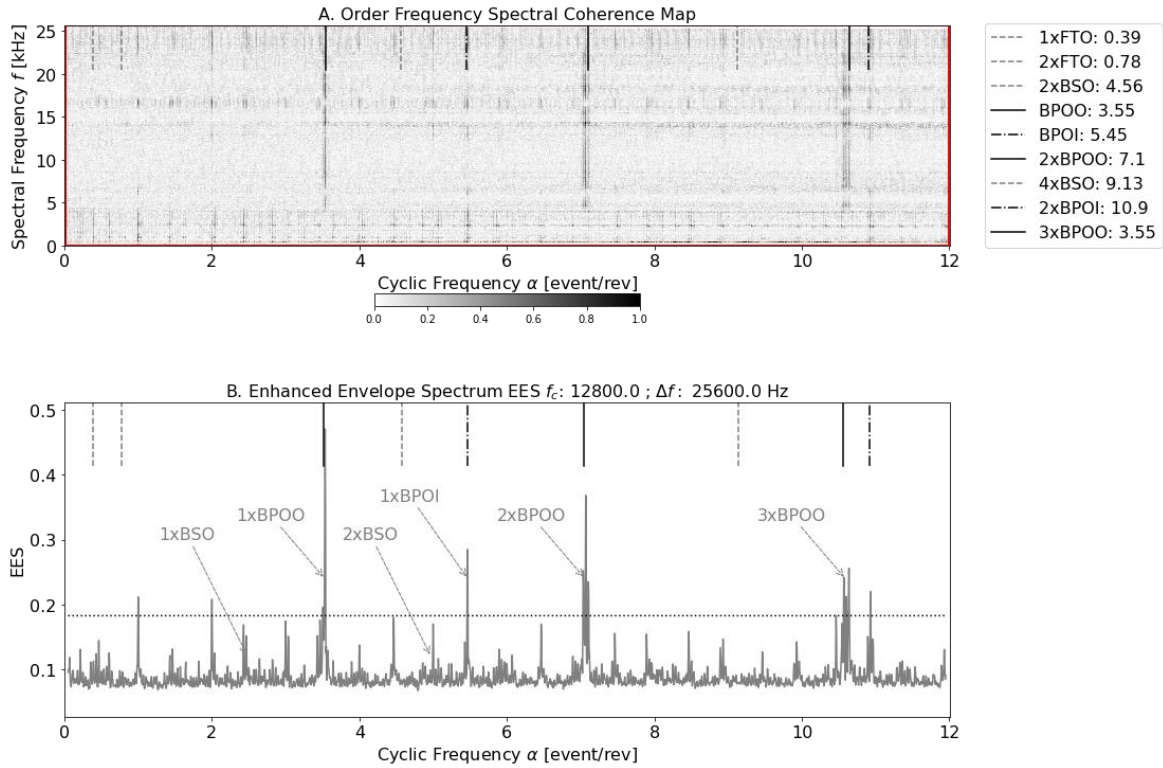


Figure 6-21. Run CF-2 B2 newIESFO for Outer-Race fault search



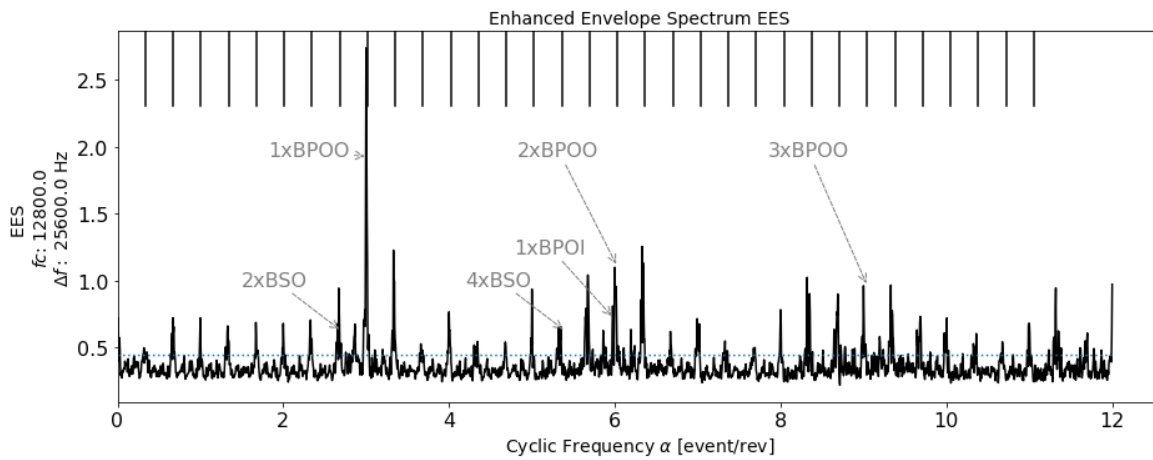
The result obtained on runs CF-3 and CF-4 were labeled as Y1 on both Bearings. To illustrate this, consider now the signal taken on bearing 2, under the conditions described for run CF-3, in such case the diverse fault were diagnosable by the high peaks at their corresponding Fault Characteristic Orders, as shown in the Enhanced Envelope Spectrum in Figure 6-22-B.

Figure 6-22. Run CF-3 B2 signal. Enhanced Envelope Order-Spectrum



When the shaft was mounted without load (CF-5 to CF-8), the Table 6-5 shows that diagnosis were no possible. However, particular situations were observed on experiments done without load. For instance, consider the case captured on B2 labeled as CF-6. The EES of Figure 6-23 shows a particular behaviour; in such all peaks are located at harmonics of 0.335.

Figure 6-23. Run CF-6 B2 signal. Enhanced Envelope Order-Spectrum



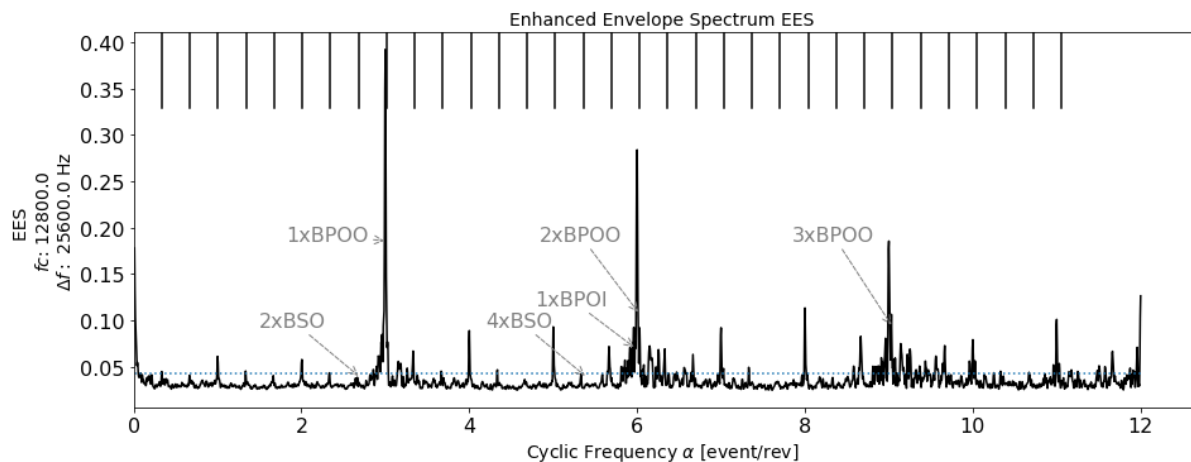
An explanation for this behaviour arise from the hypothesis the FTO take this value, either by an increase in contact angle from theoretical  $0^\circ$ , or by synchronism generated by the combination of multiple faults. The latter appears to be a reasonable explanation if the subsequent fault characteristic orders are computed from FTO as follows on Table 6-6.

Table 6-6. Fault Characteristic Orders as function of FTO

Fault Characteristic Order	Relation	Numerical Value	FTO - Harmonic
FTO	Hypothesis	0.335	1x
BPOO	$N \times FTO$	3.015	9x
BPOI	$N - N \times FTO$	5.985	$17.9x \approx 18x$
BSO	$\frac{2FTO(1 - FTO)}{1 - 2FTO}$	1.350	$4.03x \approx 4x$

The same behaviour is observable in the experiment labeled as ‘CF-8’, as illustrated in Figure 6-24. The peaks were observable just at harmonics of 0.335, which is why result tentative to think the FTO slice to 0.335. However, this assumption is not referenced in any other reference, and regardless the high value of EES at those discrete frequencies, those results are labeled as N1. This label was assigned since combination fault is neither easily diagnosable nor disagreeable, but there is evidence of discrete peaks revealing anomalies, i.e. excessive slippage, looseness or mounting mistakes. All the signals analyses on experiments Cf-5 to CF-8 presented the same behaviour.

Figure 6-24. Run CF-8 B2 signal. Enhanced Envelope Order-Spectrum



Along all the runs for the combination fault case, the BPOO was the most dominant fault characteristic order. A reasonable explanation is the direct contact that Outer-Race has with the Bearing Pedestal, and so, vibration do not suffer from path impedances prior to rise the accelerometer. Additionally, impacts at Outer Race should not be modulated, and so, their energy is not shared with modulation orders. This fact suggest that a diagnosis of incipient failures would be more diagnosable if the fault occurs at the outer race. On the other hand, the most challenging case occur when the incipient failure takes place at one of the rolling elements.

## **6.5 Conclusions of chapter.**

During this chapter, the method previously exposed on Figure 4-1 were applied through different experimental signals captured on test rig. For the major part of cases, fault were easily diagnosable but some aspects were also observed.

Diagnosis is straightforward when the fault is generated on outer race and Inner race, while is most difficult to be established when it is presented in the rolling element.

For the case of combination faults, slippage play an important role, since it could generates merging of different fault characteristic orders.

Experimental runs for rolling element shown that the fault was not in an incipient stage, which in fact causes the increase of cyclostationarity at orders such as 1-FTO and FTO. This was in accordance with the previous results exposed in section 5.3.2.

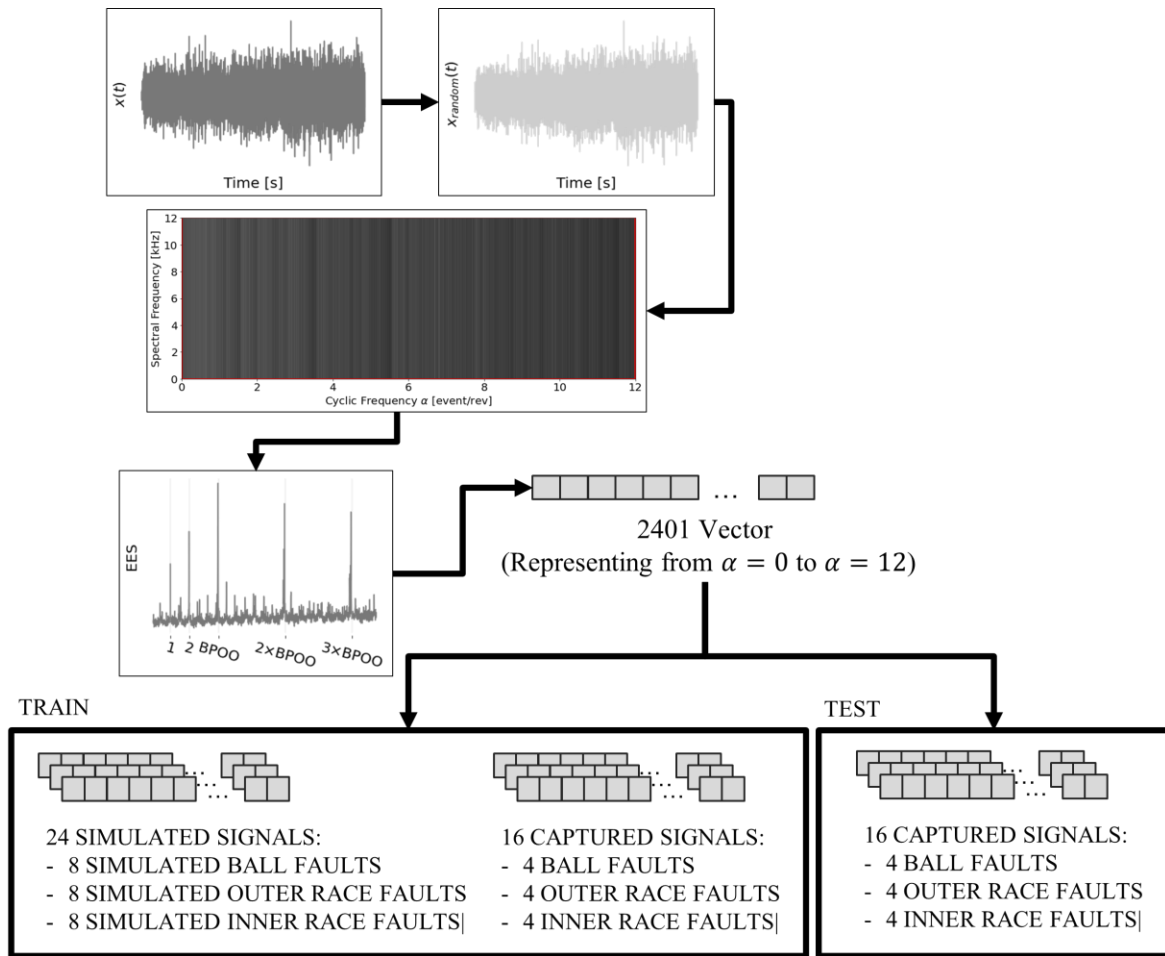
The use of newIESFO reveals in many cases, improvements on the diagnosis process, since it allows the analyst to get clearest order-envelope spectrum, by a correct demodulation. It also allows the identification of particular spectral frequencies for different types of fault, especially when a combination fault is intended to be diagnosed.

## **6.6 Classification Algorithm.**

In this section, the results of using a classification algorithm to diagnosis the fault in REB under variable speed are exposed. The algorithm was built by the use of data collected from test rig exposed on section, and simulated faults exposed on Figure 6-25.



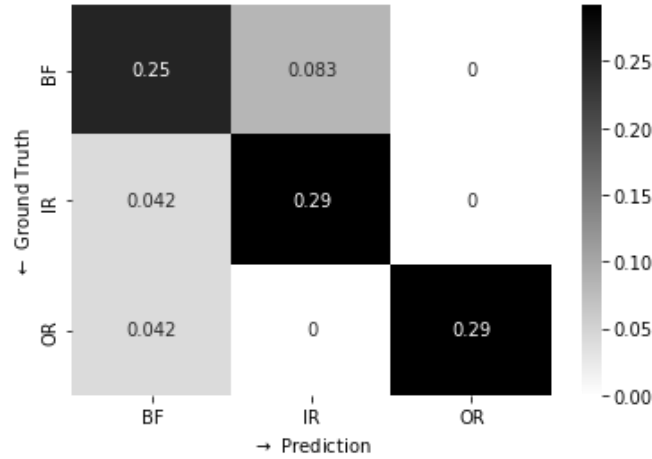
Figure 6-25. Data Set Estructure.



The architecture used is based on four dense layers attached to batch-normalization and 15% dropout. Each dense layer is activated by 'Relu' function. The first dense layer had 2401 units, corresponding to the entries on the EES of each signal, as it is illustrated on Figure 6-25. Subsequent dense layers own  $2^9$ ,  $2^5$  and 3 units on the last layer. Adam optimizer was used with a total of 8000 epochs.

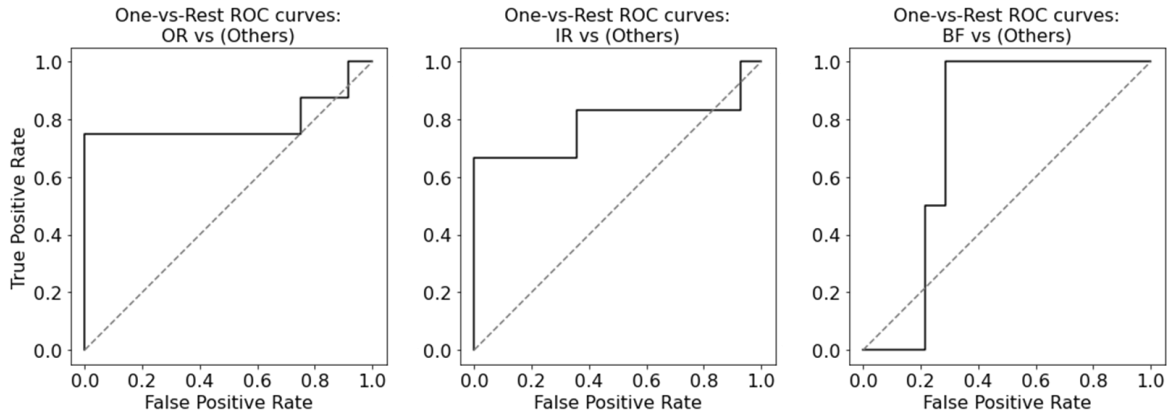
The data-set was normalized previously, since use of EES implies all values lie in the range between 0 and 1. Training process was achieved by use of Adam's optimizer, using hyper-parameters  $\alpha = 0.001$ ,  $\beta_1 = 0.9$ ,  $\beta_2 = 0.999$  and  $\varepsilon = 10^{-7}$ . After 5000 epochs, the maximum validation accuracy achieved is 0.83 as can be seen at the confusion matrix shown on Figure 6-26.

Figure 6-26. Confusion matrix for validation data



To further illustrate the performance of the classification algorithm, one class vs others ROC strategy is used, where each one of the failure types is compared against the others. The results are shown in Figure 6-27, where the base identity line have drawn for a threshold of 0.5.

Figure 6-27. ROC Performance illustration.



This classification method allows to classify faults on REB even with different fault, loads and rotational speed conditions. It is important to note the use of EES is a form to standardize the condition in such way a particular peak at fault characteristic order should be identified. It is also shown the possibility of build classification algorithms mainly by the use of simulated signals. This results in a big advantage for the use of learning algorithms in practical situations for machinery maintenance, since is not common to find data failures while is more common to have signals coming from healthy states of the machinery.

## 7. Conclusions and Recommendations

Diagnosis of REB under non-stationary regimens, and particularly, under variable speed represents a challenge for Condition Vibration Monitoring. Through this work, a method for diagnosing REB failure was proposed and tested on test rig experiments. The experimental tests were achieved under different loads and speed conditions. Some of the samples taken on the test rig show presence of incipient failures. Particularly, some of the REB tested do not shown presence of incipient failure, but the presence of smearing fault.

Additionally, a model for emulate REB faults was exposed and used for simulating faulty signals. Some runs were created using the simulation algorithm to validate the diagnosis method proposed. The simulation fault model allows to identify typical behavior for non-incipient failures, which in fact were observed during experimental runs where incipient failure was not the case.

The aims exposed in section 1.3 were achieved and closed by the next considerations.

- A model for the simulation of faults was built, which allows varying amplitude modulation function and correlating it with different load and speed conditions. By the use of the simulation fault model, some considerations were added in order to emulate different situations from incipient failures and analyze their effect on the diagnosis process. By the use of those considerations, it was possible to conclude about the experimental runs in such failures on REB under test do not seem to be incipient failures. Experimental signals were captured on the test rig, on both pedestals.
- A method for fault diagnosis were proposed. The proposed model was based on the Improved Envelope Order-Spectrum –IEOS, which is the most common used tool for Bearing Diagnosis. The IEOS were obtained by the use of order tracking, and cyclostationarity analysis.
- An algorithm to improve demodulation was proposed, based on newIESFO, which is a tool for selection the best spectral frequency range at which Improved Envelope Spectrum reveals presence of failure searched.
- The model proposed was used to diagnose a series of signals of REB faults, obtained from a test rig. The model was also used to diagnose faults on simulated REB fault signals. For the experimental signals model was able to diagnose correctly 77% of the cases. On the other hand, the model was able to diagnose correctly 84% of the simulated incipient failure signals.
- For the cases where non-incipient failures were suspected, the method proposed could identify patterns of failure, mainly dictated by presence of amplitude modulation governing orders on the Improved Envelope Order-Spectrum.

- A classification method based on a learning algorithm is exposed, showing some advantages by the use of simulation signals and a satisfactory performance based on metrics, reaching an overall precision of 84.2%, and an overall recall of 83.2%.
- The classification algorithm owns advantages from capturing different load, speed and acceleration conditions by unifying those using the Improved Envelope Order Spectrum – IEOS, and using it as the input for the algorithm. It would be desirable to amplify the signals available and increase the amount of data available for the training process.

## 8. References

- [1] R. Potter and M. Gribler, "Computed order tracking obsoletes older methods," *SAE Tech. Pap.*, no. 1, pp. 63–67, 1989.
- [2] R. B. Randall and J. Antoni, "Rolling element bearing diagnostics---A tutorial," *Mech. Syst. Signal Process.*, vol. 25, no. 2, pp. 485–520, 2011.
- [3] F. Bonnardot, R. B. Randall, and J. Antoni, "Enhanced unsupervised noise cancellation using angular resampling for planetary bearing fault diagnosis," *Int. J. Acoust. Vib.*, vol. 9, no. 2, pp. 51–60, 2004.
- [4] P. D. McFadden, "Interpolation techniques for time domain averaging of gear vibration," *Mech. Syst. Signal Process.*, vol. 3, no. 1, pp. 87–97, 1989.
- [5] C. Peeters *et al.*, "Review and comparison of tachless instantaneous speed estimation methods on experimental vibration data," *Mech. Syst. Signal Process.*, vol. 129, pp. 407–436, 2019.
- [6] P. D. McFadden and J. D. Smith, "Model for the vibration produced by a single point defect in a rolling element bearing," *J. Sound Vib.*, vol. 96, no. 1, pp. 69–82, 1984.
- [7] I. Howard, "A Review of Rolling Element Bearing Vibration 'Detection, Diagnosis and Prognosis,'" *DSTO-AMRL Report, DSTO-RR-00113*, no. October 1994, pp. 35–41, 1994.
- [8] B. P. Graney and K. Starry, "Rolling element bearing analysis," *Mater. Eval.*, vol. 70, no. 1, 2012.
- [9] D. Abboud, M. Elbadaoui, W. A. Smith, and R. B. Randall, "Advanced bearing diagnostics: A comparative study of two powerful approaches," *Mechanical Systems and Signal Processing*, vol. 114, pp. 604–627, 2019.
- [10] D. Abboud, J. Antoni, M. Eltabach, and S. Sieg-Zieba, "Angle\time cyclostationarity for the analysis of rolling element bearing vibrations," *Meas. J. Int. Meas. Confed.*, vol. 75, pp. 29–39, 2015.
- [11] N. K. Verma and T. S. S. Subramanian, "Cost benefit analysis of intelligent condition based maintenance of rotating machinery," *2012 7th IEEE Conference on Industrial Electronics and Applications (ICIEA)*. 2012.
- [12] B. Al-Najjar and I. Alsyouf, "Enhancing a company's profitability and competitiveness using integrated vibration-based maintenance: A case study," *Eur. J. Oper. Res.*, vol. 157, no. 3, pp. 643–657, 2004.
- [13] B. Al-Najjar, "The lack of maintenance and not maintenance which costs: A model to describe and quantify the impact of vibration-based maintenance on company's business," *Int. J. Prod. Econ.*, vol. 107, no. 1, pp. 260–273, May 2007.
- [14] R. B. Randall, *Vibration-based Condition Monitoring: Industrial, Aerospace and Automotive Applications*. John Wiley & Sons, 2011.
- [15] P. D. McFadden and J. D. Smith, "Vibration monitoring of rolling element bearings by the

- high-frequency resonance technique --- a review,” *Tribology International*, vol. 17, no. 1. pp. 3–10, 1984.
- [16] M. J. Dowling, “Application of non-stationary analysis to machinery monitoring,” in *1993 {IEEE} International Conference on Acoustics, Speech, and Signal Processing*, 1993, vol. 1, pp. 59–62 vol.1.
- [17] D. Rémond, J. Antoni, and R. B. Randall, “Editorial for the special issue on Instantaneous Angular Speed ({IAS}) processing and angular applications,” *Mechanical Systems and Signal Processing*, vol. 44, no. 1–2. pp. 1–4, 2014.
- [18] *{OREDA}: Offshore Reliability Data Handbook*. OREDA Participants, 2009.
- [19] M. El Hachemi Benbouzid, “A review of induction motors signature analysis as a medium for faults detection,” *IEEE Trans. Ind. Electron.*, vol. 47, no. 5, pp. 984–993, 2000.
- [20] R. R. Schoen, T. G. Habetler, F. Kamran, and R. G. Bartfield, “Motor bearing damage detection using stator current monitoring,” *IEEE Trans. Ind. Appl.*, vol. 31, no. 6, pp. 1274–1279, 1995.
- [21] C. Peeters, P. Guillaume, and J. Helsen, “Vibration-based bearing fault detection for operations and maintenance cost reduction in wind energy,” *Renew. Energy*, vol. 116, pp. 74–87, 2018.
- [22] W. A. Smith and R. B. Randall, “Rolling element bearing diagnostics using the Case Western Reserve University data: A benchmark study,” *Mech. Syst. Signal Process.*, vol. 64–65, pp. 100–131, 2015.
- [23] J. Antoni, F. Bonnardot, A. Raad, and M. El Badaoui, “Cyclostationary modelling of rotating machine vibration signals,” *Mech. Syst. Signal Process.*, vol. 18, no. 6, pp. 1285–1314, 2004.
- [24] E. Mendel *et al.*, “Automatic bearing fault pattern recognition using vibration signal analysis,” *IEEE Int. Symp. Ind. Electron.*, pp. 955–960, 2008.
- [25] D. Wang, X. Zhao, L. L. Kou, Y. Qin, Y. Zhao, and K. L. Tsui, “A simple and fast guideline for generating enhanced/squared envelope spectra from spectral coherence for bearing fault diagnosis,” *Mech. Syst. Signal Process.*, vol. 122, no. January, pp. 754–768, 2019.
- [26] O. Janssens *et al.*, “Convolutional Neural Network Based Fault Detection for Rotating Machinery,” *J. Sound Vib.*, vol. 377, pp. 331–345, 2016.
- [27] W. Zhang, M. P. Jia, L. Zhu, and X. A. Yan, “Comprehensive Overview on Computational Intelligence Techniques for Machinery Condition Monitoring and Fault Diagnosis,” *Chinese J. Mech. Eng. (English Ed.)*, vol. 30, no. 4, pp. 782–795, 2017.
- [28] R. Zhang, H. Tao, L. Wu, and Y. Guan, “Transfer Learning With Neural Networks for Bearing Fault Diagnosis in Changing Working Conditions,” *IEEE Access*, vol. 5, pp. 14347–14357, 2017.
- [29] J. Antoni, “The spectral kurtosis: A useful tool for characterising non-stationary signals,” *Mech. Syst. Signal Process.*, vol. 20, no. 2, pp. 282–307, 2006.

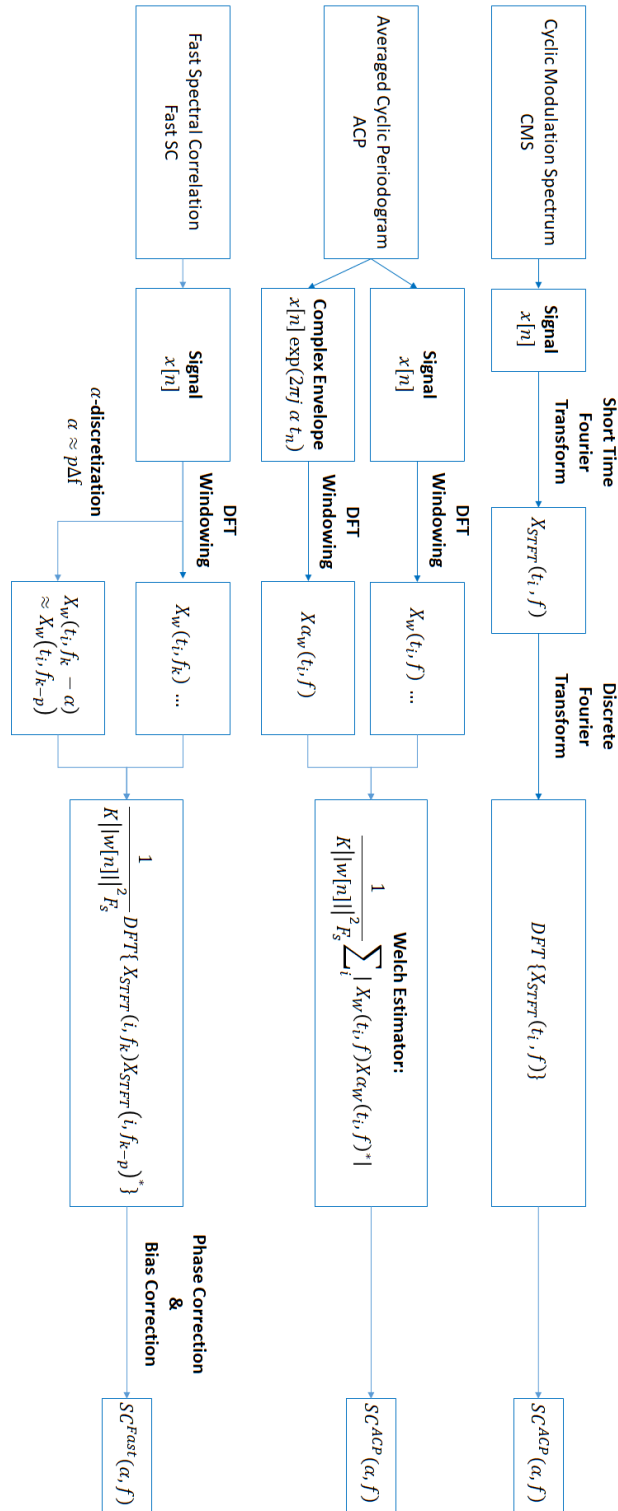
- 
- [30] J. Antoni and R. B. Randall, “The spectral kurtosis: Application to the vibratory surveillance and diagnostics of rotating machines,” *Mech. Syst. Signal Process.*, vol. 20, no. 2, pp. 308–331, 2006.
- [31] J. Antoni, “Fast computation of the kurtogram for the detection of transient faults,” *Mech. Syst. Signal Process.*, vol. 21, no. 1, pp. 108–124, 2007.
- [32] R. B. Randall, J. Antoni, and S. Chobsaard, “The relationship between spectral correlation and envelope analysis in the diagnostics of bearing faults and other cyclostationary machine signals,” *Mech. Syst. Signal Process.*, vol. 15, no. 5, pp. 945–962, 2001.
- [33] A. C. McCormick and A. K. Nandi, “Cyclostationarity in Rotating Machine Vibrations 1 Introduction 2 Wide-sense Cyclostationarity,” *Mech. Syst. Signal Process.*, vol. 12, no. 2, pp. 225–242, 1998.
- [34] J. Antoni, “Cyclic spectral analysis in practice,” *Mech. Syst. Signal Process.*, vol. 21, no. 2, pp. 597–630, 2007.
- [35] M. D. Coats and R. B. Randall, “Order-Tracking with and without a tacho signal for gear fault diagnostics,” *Aust. Acoust. Soc. Conf. 2012, Acoust. 2012 Acoust. Dev. Environ.*, no. November, pp. 447–454, 2012.
- [36] K. R. Fyfe and E. D. S. Munck, “Analysis of computed order tracking,” *Mech. Syst. Signal Process.*, vol. 11, no. 2, pp. 187–205, 1997.
- [37] S. J. Idehara, A. Luiz, A. Mesquita, U. A. Miranda, M. D. Jr, and D. Ph, “Order tracking methods analysis,” no. 1, 2003.
- [38] S. Schmidt, P. S. Heyns, and J. P. de Villiers, “A tacholess order tracking methodology based on a probabilistic approach to incorporate angular acceleration information into the maxima tracking process,” *Mech. Syst. Signal Process.*, vol. 100, pp. 630–646, 2018.
- [39] J. Urbanek, T. Barszcz, and J. Antoni, “A two-step procedure for estimation of instantaneous rotational speed with large fluctuations,” *Mech. Syst. Signal Process.*, vol. 38, no. 1, pp. 96–102, 2013.
- [40] Q. Leclère, H. André, and J. Antoni, “A multi-order probabilistic approach for Instantaneous Angular Speed tracking debriefing of the CMMNO?14 diagnosis contest,” *Mech. Syst. Signal Process.*, vol. 81, pp. 375–386, 2016.
- [41] D. Abboud, J. Antoni, S. Sieg-Zieba, and M. Eltabach, “Deterministic-random separation in nonstationary regime,” *J. Sound Vib.*, vol. 362, pp. 305–326, 2016.
- [42] P. Borghesani, P. Pennacchi, R. B. Randall, N. Sawalhi, and R. Ricci, “Application of cepstrum pre-whitening for the diagnosis of bearing faults under variable speed conditions,” *Mech. Syst. Signal Process.*, vol. 36, no. 2, pp. 370–384, 2013.
- [43] D. Abboud, S. Baudin, J. Antoni, D. Rémond, M. Eltabach, and O. Sauvage, “The spectral analysis of cyclo-non-stationary signals,” *Mech. Syst. Signal Process.*, 2016.
- [44] G. D’Elia, Z. Daher, and J. Antoni, “A novel approach for the cyclo-non-stationary analysis of speed varying signals,” *Proc. ISMA 2010 - Int. Conf. Noise Vib. Eng. Incl. USD 2010*, pp. 2801–2814, 2010.

- [45] W. A. Smith, R. B. Randall, X. de C. du Mée, and P. Peng, "Use of cyclostationary properties to diagnose planet bearing faults in variable speed conditions," in *10th {DST} group international conference on health and usage monitoring systems, 17th Australian aerospace congress*, 2017, pp. 26–28.
- [46] J. Berntsen, A. Brandt, and K. Gryllias, "Enhanced demodulation band selection based on Operational Modal Analysis (OMA) for bearing diagnostics," *Mech. Syst. Signal Process.*, vol. 181, no. July, p. 109300, 2022.
- [47] A. Mauricio, D. Helm, M. Timusk, J. Antoni, and K. Gryllias, "Novel Cyclo-Nonstationary Indicators for Monitoring of Rotating Machinery Operating Under Speed and Load Varying Conditions," *J. Eng. Gas Turbines Power*, vol. 144, no. 4, Apr. 2022.
- [48] A. Mauricio *et al.*, "Bearing diagnostics under strong electromagnetic interference based on Integrated Spectral Coherence," *Mech. Syst. Signal Process.*, vol. 140, p. 106673, 2020.
- [49] M. Nakhaeinejad and M. D. Bryant, "Dynamic modeling of rolling element bearings with surface contact defects using bond graphs," *J. Tribol.*, vol. 133, no. 1, pp. 1–12, 2011.
- [50] J. D. Arango and A. Restrepo-Martinez, "Rolling Element Bearing Diagnosis by Improved Envelope Spectrum : Optimal Frequency Band Selection," vol. 15, no. 8, pp. 322–330, 2021.
- [51] A. Mauricio, W. A. Smith, R. B. Randall, J. Antoni, and K. Gryllias, "Improved Envelope Spectrum via Feature Optimisation-gram (IESFOgram): A novel tool for rolling element bearing diagnostics under non-stationary operating conditions," *Mech. Syst. Signal Process.*, vol. 144, p. 106891, 2020.
- [52] F. Cong, J. Chen, G. Dong, and M. Pecht, "Vibration model of rolling element bearings in a rotor-bearing system for fault diagnosis," *J. Sound Vib.*, vol. 332, no. 8, pp. 2081–2097, 2013.
- [53] L. R. Kahn, "Single-Sideband Transmission by Envelope Elimination and Restoration," *Proc. IRE*, vol. 40, no. 7, pp. 803–806, 1952.
- [54] C. Mishra, A. K. Samantaray, and G. Chakraborty, "Ball bearing defect models: A study of simulated and experimental fault signatures," *J. Sound Vib.*, vol. 400, no. July, pp. 86–112, 2017.



## **9. Annex**

## 9.1 Annex: Spectral Correlation Estimators



## 9.2 Annex: Spectral Correlation Statistical Threshold

During this annex the statistical threshold is discussed for the Order Frequency Spectral Correlation function – OFSC. During this section, we consider the Welch Estimator is intend to be used (see section 9.1) [34].

Consider the signal  $x[n]$  and signal  $y[n]$ , each of one with a total of  $L$  samples. Those signals would be windowed with a window function  $w[n]$ , with a total of  $N_w$  samples and sliding  $R$  samples per each slice of window. Welch estimator, benefits from STFT representation, as indicates in Equation 9-1 for signal  $x[n]$ .

$$\text{Equation 9-1} \quad X[t_i; f] = \sum_{n=iR}^{iR+N_w-1} x[n]w[n - iR] \exp(-2\pi jfn)$$

Where  $N_w$  represents the amount of samples considered for  $w[n]$ ,  $R$  represents the samples sliced by each windowing step and  $K$  would be defined as the amount of windowing steps, estimated as exposed in Equation 9-2.

$$\text{Equation 9-2} \quad K = \left\lfloor \frac{L-N_w}{R} \right\rfloor + 1$$

where  $\lfloor \cdot \rfloor$  stands for roof function, i.e. the lower nearest integer from  $\cdot$ .

Welch estimator for spectral correlation between signals  $x[n]$  and  $y[n]$  takes the form exposed on Equation 9-3.

$$\text{Equation 9-3} \quad \widehat{SC}_{XY}(f; \alpha; L) = \frac{1}{KF_s} \sum_{i=0}^{K-1} X^*[t_i; f] Y[t_i; f + \alpha]$$

To define the variance of the estimator for  $SC(\alpha, f)$  the variance reduction factor  $\varepsilon$  play an important role. It is defined as follows.

$$\text{Equation 9-4} \quad \varepsilon = \sum_{i=-K+1}^{K-1} \mathcal{R}_w[kR]^2 \left( \frac{K-|i|}{K^2} \right)$$

Where  $\mathcal{R}_w$  represents the autocorrelation function of the window  $w[n]$ .  $\mathcal{R}_w$  is deifned as indicates Equation 9-5.

$$\text{Equation 9-5} \quad \mathcal{R}_w[k] = \sum_{n=-\infty}^{\infty} w[n - k]w[n]$$

An interesting result is established in [34], is that for a hann window, when  $R \leq N_w/3$ , it happens that

$$\text{Equation 9-6} \quad \varepsilon \approx \|\mathcal{R}_w\|^2 / L$$

where  $\|\cdot\|$  stands for  $L_2$  norm.

If  $L$  is large enough, the variance of welch SC estimator becomes

Equation 9-7 
$$\widehat{Var} \left\{ \widehat{SC}_{XY}(\alpha; f; L) \right\} \approx \varepsilon X(f)Y(f + \alpha)$$

Where  $X(f)$  and  $Y(f)$  stands for the power spectral density of signals  $x[n]$  and  $y[n]$ . This result makes possible to establish an hypothesis test for the presence of cyclo-stationarity at a particular  $\alpha$ . This hypothesis test is built from  $H_0$  hypothesis as follows.

$H_0$ : signal y and x are jointly Cyclo-stationary.

$H_1$ : Reject null hypothesis

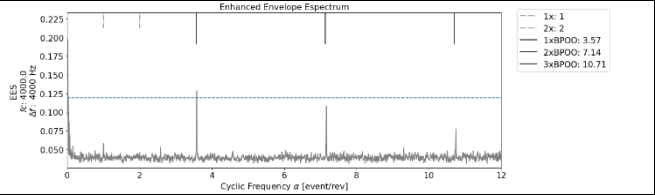
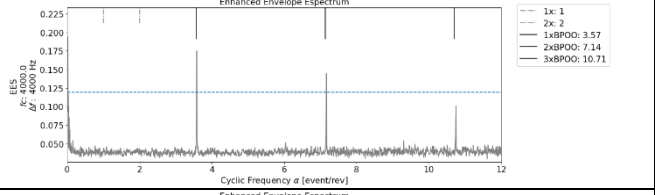
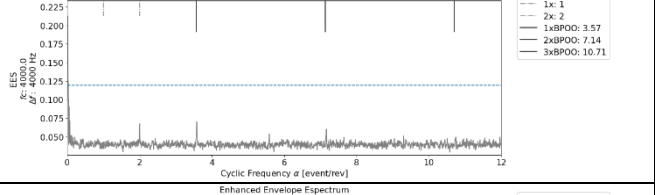
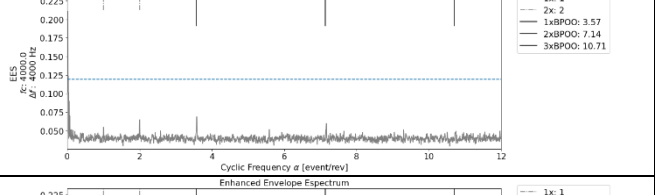
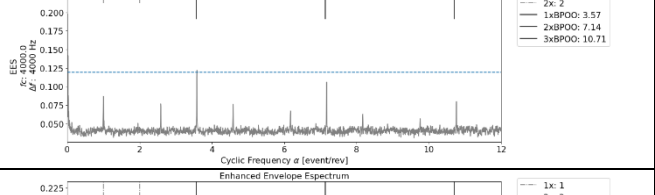
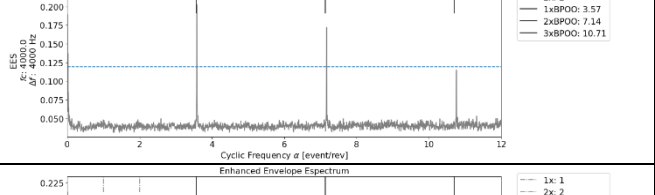
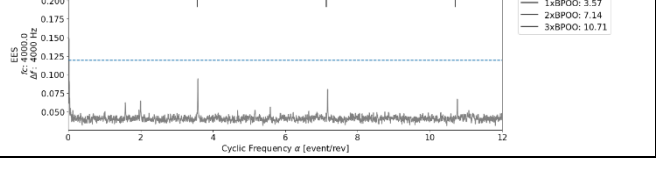
The criteria for rejection  $H_0$  has been established as follows [34].

Reject  $H_0$  if there exists a (non singleton) frequency interval “ $I$ ” where.

Equation 9-8 
$$\left| \widehat{SC}_{XY}(\alpha; f; L) \right|^2 \geq \frac{1}{2} \chi_{1-p,2}^2 \widehat{Var} \left\{ \widehat{SC}_{XY}(\alpha; f; L) \right\} \quad \forall f \in I$$

Equation 9-8 results extremely useful to establish the validation of cyclostationary content of a particular signal. It establish that an statistical threshold could be established with a p-value from consider a chi-squared distribution with 2 degree of freedom.

### 9.3 Annex: Chapter 5 - Outer Race Simulated Signals Summary.

Run Label	Static Load [N]	Static Unbalance [kg m]	Acceleration Freq. range	FROM 2000 to 6000 Hz demodulation
S-OR-1	10	0.00015	3 Hz s <sup>-1</sup> 10 – 25 Hz	
S-OR-2	60	0.00015	3 Hz s <sup>-1</sup> 10 – 25 Hz	
S-OR-3	10	0.01500	3 Hz s <sup>-1</sup> 10 – 25 Hz	
S-OR-4	60	0.01500	3 Hz s <sup>-1</sup> 10 – 25 Hz	
S-OR-5	10	0.00015	6 Hz s <sup>-1</sup> 10 – 40 Hz	
S-OR-6	60	0.00015	6 Hz s <sup>-1</sup> 10 – 40 Hz	
S-OR-7	10	0.01500	6 Hz s <sup>-1</sup> 10 – 40 Hz	

S-OR-8	60	0.01500	$6 \text{ Hz s}^{-1}$ 10 – 40 Hz	<p>Enhanced Envelope Spectrum</p> <p>Y-axis: EES (g/4000 Hz) from 0.050 to 0.225                  X-axis: Cyclic Frequency <math>\alpha</math> (event/rev) from 0 to 12</p> <p>Legend:                  --- 1x: 1                  --- 2x: 2                  --- 1xBPOO: 3.57                  --- 2xBPOO: 7.14                  --- 3xBPOO: 10.71</p>
--------	----	---------	-------------------------------------	---

## 9.4 Annex: Chapter 5 - Inner Race Simulated Signals Summary.

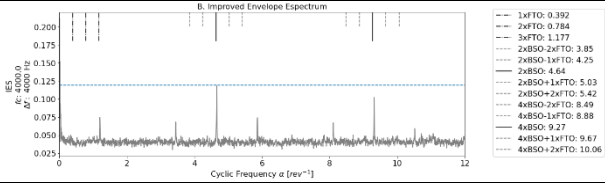
Run Label	Static Load [kg]	Dynamic Load [kg m]	Acceleration Freq. range	FROM 0 Hz to 12800 Hz demodulation
S-IR-1	1	0.00015	3 Hz s <sup>-1</sup> 10 – 25 Hz	
S-IR-2	6	0.00015	3 Hz s <sup>-1</sup> 10 – 25 Hz	
S-IR-3	1	0.01500	3 Hz s <sup>-1</sup> 10 – 25 Hz	
S-IR-4	6	0.01500	3 Hz s <sup>-1</sup> 10 – 25 Hz	
S-IR-5	1	0.00015	6 Hz s <sup>-1</sup> 10 – 40 Hz	
S-IR-6	6	0.00015	6 Hz s <sup>-1</sup> 10 – 40 Hz	
S-IR-7	1	0.01500	6 Hz s <sup>-1</sup> 10 – 40 Hz	

S-IR-8	6	0.01500	$6 \text{ Hz s}^{-1}$ 10 – 40 Hz	
--------	---	---------	-------------------------------------	--



## 9.5 Annex: Chapter 5 – Ball Fault Simulated Signals Summary.

Run Label	Static Load [kg]	Dynamic Load [kg m]	Acceleration Freq. range	FROM 2000 to 6000 Hz demodulation
S-BF-1	1	0.00015	3 Hz s <sup>-1</sup> 10 – 25 Hz	
S-BF-2	6	0.00015	3 Hz s <sup>-1</sup> 10 – 25 Hz	
S-BF-3	1	0.01500	3 Hz s <sup>-1</sup> 10 – 25 Hz	
S-BF-4	6	0.01500	3 Hz s <sup>-1</sup> 10 – 25 Hz	
S-BF-5	1	0.00015	6 Hz s <sup>-1</sup> 10 – 40 Hz	
S-BF-6	6	0.00015	6 Hz s <sup>-1</sup> 10 – 40 Hz	
S-BF-7	1	0.01500	6 Hz s <sup>-1</sup> 10 – 40 Hz	

S-BF-8	6	0.01500	$6 \text{ Hz s}^{-1}$ 10 – 40 Hz	 <p>B. Improved Envelope Spectrum</p> <p>Amplitude: 0.200, 0.175, 0.150, 0.125, 0.100, 0.075, 0.050, 0.025</p> <p>Cyclic Frequency <math>\alpha</math> [rev<sup>-1</sup>]: 0, 2, 4, 6, 8, 10, 12</p> <p>Legend:</p> <ul style="list-style-type: none"> <li>1xFTO: 0.392</li> <li>2xFTO: 0.784</li> <li>3xFTO: 1.177</li> <li>2xBSO+2xFTO: 3.85</li> <li>2xBSO+1xFTO: 4.75</li> <li>2xBSO: 4.64</li> <li>2xBSO+1xFTO: 5.03</li> <li>2xBSO+2xFTO: 5.42</li> <li>4xBSO+2xFTO: 8.69</li> <li>4xBSO+1xFTO: 8.88</li> <li>4xBSO: 9.27</li> <li>4xBSO+1xFTO: 9.67</li> <li>4xBSO+2xFTO: 10.06</li> </ul>
--------	---	---------	-------------------------------------	---

## 9.6 Annex: Chapter 6 - Outer Race Faults Summary.

Num.	Range Speed	Acc.	Load	Bearing 1 / Bearing 2
OR-1	14 – 30 Hz	6 Hz/s	5 kg static	
OR-2	30 – 25 Hz	6 Hz/s	5 kg static	
OR-3	8 – 18 Hz	3 Hz/s	5 kg static	

OR-4	21 – 32 Hz	3 Hz/s	5 kg static	
OR-5	22 – 39 Hz	6 Hz/s	0 kg	
OR-6	37 – 14 Hz	6 Hz/s	0 kg	

OR-7	17 – 30 Hz	3 Hz/s	0 kg	
OR-8	22 – 38 Hz	3 Hz/s	0 kg	

### 9.7 Annex: Chapter 6 - Inner Race Faults Summary.

Num.	Range Speed	Acc.	Load	Bearing 1 / Bearing 2
IR-1	29 – 38 Hz	6 Hz/s	5 kg static	
IR-2	29 – 11 Hz	High (6 Hz/s)	5 kg static	
IR-3	13 – 29 Hz	Low (3 Hz/s)	5 kg static	

IR-4	29 – 13 Hz	Low (3 Hz/s)	5 kg static	
IR-5	21 – 38 Hz	High (6 Hz/s)	0 kg	
IR-6	37 – 14 Hz	High (6 Hz/s)	0 kg	

IR-7	15 – 28 Hz	Low (3 Hz/s)	0 kg	
IR-8	30 – 38 Hz	Low (3 Hz/s)	0 kg	



## 9.8 Annex: Chapter 6 – Rolling Element Faults Summary.

Num.	Range Speed	Acc.	Load	Bearing 1 / Bearing 2
BF-1	20 – 38 Hz	6 Hz/s	5 kg static	
BF-2	29 – 11 Hz	6 Hz/s	5 kg static	
BF-3	19 – 35 Hz	3 Hz/s	5 kg static	

BF-4	38 – 21 Hz	3 Hz/s	5 kg static	
BF-5	21 – 38 Hz	6 Hz/s	0 kg	
BF-6	35 – 16 Hz	6 Hz/s	0 kg	

BF-7	14 – 28 Hz	3 Hz/s	0 kg	
BF-8	30 – 38 Hz	3 Hz/s	0 kg	

## 9.9 Annex: Chapter 6 – Combination Faults Summary.

Num.	Range Speed	Acc.	Load	Bearing 1 / Bearing 2
CF-1	4.4 – 24.6 Hz	6 Hz/s	5 kg	
CF-2	26.4 - 37.7 Hz	6 Hz/s	5 kg	

<p>CF-3</p>	<p>18.7 – 35.8 Hz</p>	<p>3 Hz/s</p>	<p>5 kg</p>	<p>Enhanced Envelope Spectrum EES</p> <p>EES [U<sup>2</sup>/m<sup>2</sup>] f<sub>c</sub>: 10000 Hz Δf: 120000 Hz</p> <p>Cyclic Frequency α [event/rev]</p> <p>Enhanced Envelope Spectrum EES</p> <p>EES [U<sup>2</sup>/m<sup>2</sup>] f<sub>c</sub>: 10000 Hz Δf: 120000 Hz</p> <p>Cyclic Frequency α [event/rev]</p>
<p>CF-4</p>	<p>37.5 - 15.1 Hz</p>	<p>3 Hz/s</p>	<p>5 kg</p>	<p>Enhanced Envelope Spectrum EES</p> <p>EES [U<sup>2</sup>/m<sup>2</sup>] f<sub>c</sub>: 10000 Hz Δf: 120000 Hz</p> <p>Cyclic Frequency α [event/rev]</p> <p>Enhanced Envelope Spectrum EES</p> <p>EES [U<sup>2</sup>/m<sup>2</sup>] f<sub>c</sub>: 10000 Hz Δf: 120000 Hz</p> <p>Cyclic Frequency α [event/rev]</p>

<p>CF-5</p>	<p>13.6 - 27.6 Hz</p>	<p>6 Hz/s</p>	<p>0 kg static</p>	
<p>CF-6</p>	<p>40.8 - 28.1 Hz.</p>	<p>6 Hz/s</p>	<p>0 kg static</p>	

